Mean-field theory and projective symmetry group classifications of quantum spin liquids

im Fachbereich Physik der Freien Universität Berlin eingereichte Dissertation zur Erlangung des Grades eines Doktors der Naturwissenschaften

von

Jonas Sonnenschein

Dahlem Center for Complex Quantum Systems

October 9, 2020

First referee: Prof. Dr. Johannes Reuther
Second referee: Prof. Dr. Piet Brouwer
Date of the defense: September 21, 2020

Eidesstattliche Erklärung

Ich erkläre hiermit an Eides statt, dass ich die vorliegende Arbeit selbstständig und ohne Benutzung anderer als der angegebenen Hilfsmittel angefertigt habe; die aus fremden Quellen direkt oder indirekt übernommenen Gedanken sind als solche kenntlich gemacht. Die Arbeit wurde bisher in gleicher oder ähnlicher Form keiner anderen Prüfungskommission vorgelegt und auch nicht veröffentlicht.

Ort, Datum *Jonas Sonnenschein*

Abstract

Quantum spin liquids are novel phases of matter whose physical properties cannot be captured within the conventional framework of phase transitions. These quantum states are characterized by excitations, called spinons, carrying a fractional value of the integer spin. A description based on a mean-field approximation leads to effective gauge theory. Due to this gauge freedom symmetry group operations act via projective symmetry group (PSG) representations, which can be used to classify quantum states beyond the conventional method. This introducing discussion is found in Chapters 2-6.

A preceding PSG classification on the square lattice, which took spin rotational symmetry breaking terms into account, showed that the resulting mean-field states could exhibit topologically non-trivial spinon bands. In Chapter 7, only those elements of this Classification are studied, which lead to short-ranged mean-field models. The mutual effect of spinons and visons is scrutinized by adding static configurations of a background gauge field. Spinons and visons form composite objects, which in the case of topological spinon bands, are described by Majorana zero modes. An exact mapping corroborates the relation to topological superconductors and vortices. The effect of multiple visons is investigated, and a possible experimental signature is exposed.

Chapter 8 explains how spinon mean-field theory can be used to derive a phenomenological effective model for the compound $Ca_{10}Cr_7O_{28}$. A material that was recently proposed as a quantum spin liquid. This low-energy theory consists of spinon hopping processes. The underlying bilayer kagome structure can be simplified to an effective honeycomb lattice. The dynamical spin structure factor is calculated and compared to neutron scattering data. It is discussed how f-wave pairing of spinons can explain small deviations from a linear temperature dependency observed in heat capacity measurements at the low temperatures. This pairing mechanism breaks the $U(1)$ invariance group of the pure hopping model and renders a coherent picture of $Ca_{10}Cr_7O_{28}$ being a $\mathbb{Z}_2$ quantum spin liquid.

Chapter 9 carries out a PSG classification for the simple-, body centered-, and face centered cubic lattices. Despite a large number of possible PSG representations, only very few describe short-ranged mean-field states. These mean-field models are constructed up to third neighbor couplings and calculated in a self-consistent manner. It is found that the energy is lower for non-trivial sign patterns induced by non-trivial representations of the symmetry generators. Higher neighbor extensions, including pairing terms, yield lower mean-field ground state energies compared to extensions with only hopping terms. For the fcc lattice, a first neighbor state could be identified, which exhibits symmetry protected zero-energy modes.

Kurzfassung

Quantenspinflüssigkeiten (QSF) sind neuartige Materiephasen, deren Eigenschaften nicht im herkömmlichen Sinne als Phasenübergängen beschrieben werden können. Diese Quantenzustände sind durch Anregungen gekennzeichnet, die Spinonen genannt werden, und nur einen Teil des ganzzahligen Spins tragen. Eine Beschreibung, die auf einer Mittelfeldnäherung (MF) basiert, führt zu einer effektiven Eichentheorie. Aufgrund dieser Eichfreiheit wirken Symmetriegruppen durch projektive Darstellungen (PSG), welche zur Klassifizierung von Quantenzuständen verwendet werden können, was über die herkömmliche Methode hinausgeht. Diese einleitende Diskussion finden Sie in Kapitel 2-6.

Eine vorherige PSG-Klassifizierung auf dem Quadratgitter unter Berücksichtigung von Termen, die Spinrotationssymmetrie brechen, zeigte, dass Zustände topologisch nicht triviale Spinonbänder aufweisen können. In Kapitel 7 dieser Arbeit werden nur die PSG-Elemente untersucht, die zu kurzreichweitiger Nachbarwechselwirkung führen. Die gegenseitige Wirkung von Spinonen und Visonen wird durch Hinzufügen statischer Konfigurationen eines Hintergrundfeldes untersucht. Spinonen und Visonen bilden Objekte, die im Fall von topologischen Spinonbändern durch Majorana-Nullmoden beschrieben werden. Die Beziehung zu topologischen Supraleitern wird durch eine genaue Abbildung bekräftigt. Die Wirkung mehrerer Visonen wird untersucht und eine mögliche experimentelle Signatur vorgeschlagen.

In Kapitel 8 wird ein phänomenologisches Modell der Spinon für den Kristall $Ca_{10}Cr_7O_{28}$ erzeugt. Dieses Material wurde kürzlich als mögliches QSF vorgeschlagen. Die Niedrigenergietheorie besteht aus Spinon-Hüpfprozessen und vereinfacht die doppelschichtige Kagome Gitterstruktur zu einem Wabengitter. Der dynamische Spinstrukturfaktor wird berechnet und mit Neutronenstreudaten verglichen. Eine f-Paarung der Spinonen kann eine kleine Abweichung der linearen Temperaturabhängigkeit erklären, die bei Wärmekapazitätsmessungen beobachtet wurde. Dieser Mechanismus bricht die $U(1)$ Invarianz und liefert ein kohärentes Bild von $Ca_{10}Cr_7O_{28}$ als $\mathbb{Z}_2$ QSF.

Kapitel 9 führt eine PSG-Klassifizierung für das einfache, körperzentrierte und flächenzentrierte kubische Gitter durch. Trotz der großen Anzahl möglicher Darstellungen beschreiben nur sehr wenige kurzreichweitige Zustände. Diese Modelle werden bis zu Drittnachbarkopplungen konstruiert und auf selbstkonsistente Weise berechnet. Die Energie für nicht triviale Vorzeichen der Amplituden ist geringer, als es für uniforme Vorzeichen der Fall ist. Höhere Nachbarerwechselwirkungen, die Paarungsterme einschließen, ergeben niedrigere Grundzustandsenergien, als Erweiterungen, die nur Hüpfterme enthalten. Ein interessanter Zustand konnte für erster Nachbarn auf dem flächenzentriert kubischen Gitter identifiziert werden. Dieser Zustand weist symmetriegeschützte Nullenergiemoden auf.

Publications

In the course of the doctoral studies the author made the following publications:

- Jonas Sonnenschein and Johannes Reuther, Topological spinon bands and vison excitations in spin-orbit coupled quantum spin liquids *Phys. Rev. B, 96: 235113*, Dec 2017

- Jonas Sonnenschein, Christian Balz, Ulrich Tutsch, Michael Lang, Hanjo Ryll, Jose A. Rodriguez-Rivera, A. T. M. Nazmul Islam, Bella Lake, and Johannes Reuther, Signatures for spinons in the quantum spin liquid candidate $Ca_{10}Cr_7O_{28}$, *Phys. Rev. B, 100: 174428*, Nov 2019

- Jonas Sonnenschein, Aishwarya Chauhan, Yasir Iqbal and Johannes Reuther, Projective symmetry group classifications of quantum spin liquids on the simple cubic, body centered cubic, and face centered cubic lattices, *Phys. Rev. B 102, 125140*, Sep 2020

The author also contributed to the following publication which is not discussed in this thesis:

- Max Hering, Jonas Sonnenschein, Yasir Iqbal and Johannes Reuther, Characterization of quantum spin liquids and their spinon band structures via functional renormalization, *Phys. Rev. B, 99: 100405(R)*, Mar 2019

Contents

1. Introduction

It has been almost an entire century since Lev Landau formulated his famous theory of phase transitions [1]. The beauty of this theory is its simplicity, which leads, nevertheless, to a very rich and diverse realm of applicability. The power lies in its unifying character, enabling the classification of many different physical phases regardless of any microscopic details. In its heart, it explains that conceptually the melting of ice is the same as the transition from a ferromagnet to a paramagnet. In both examples, it is possible to define an order parameter which discerns the two phases. In the magnetic example, this order parameter can be defined as the thermodynamic average of the magnetization per spin [2]. In the paramagnetic phase, the local spins can point in any direction, and each individual spin does not notice in which direction its neighbor is pointing; the order parameter becomes zero after performing the average. However, in the ferromagnetic phase, the local magnetic moments are all correlated and point in the same direction yielding a finite order parameter. The corresponding energy function remains invariant under the symmetry operation, which rotates all spins. Any state vector describing the system in the paramagnetic phase also obeys this symmetry. This is not true for the ferromagnetic case where the presence of the finite order parameter breaks the symmetry. The relation between an order parameter and the breaking of symmetry is the main idea behind Landau's theory. Yet there are physical states of matter which are not tractable by this classification scheme. In this regard, the discovery of a fractional quantum Hall state in the early eighties [3, 4] marked the beginning of a new era. Since then, more and more phases of matter have been identified, which evade a conventional description by the principle of symmetry breaking. Another prominent unconventional phase is the quantum spin liquid state [5, 6, 7, 8, 9]. This state escapes magnetic order down to absolute zero temperature and poses an insuperable challenge to Landau's theory. These discoveries did not daunt the community of condensed matter scientists but quickened their spirit, and shortly after, the development of a modern framework started. Some topological invariants replaced the obsolete order parameter, and the concept of topological order or quantum order was introduced [5, 10, 11]. Some of these aspects will be further discussed throughout this thesis with special regards to the quantum spin liquid phase and its classification using projective symmetry group representations (PSG) [5].

Many of these unusual states are found in materials called Mott insulators [12]. Applying conventional Bloch theory to these materials shows that the Fermi level intersects their half-filled energy bands. Usually, this would lead to the conclusion that the material conducts electric currents. Yet these odd insulators are characterized by a very strong interaction between their electrons such that, besides some possible modes which exist at the surface, the mutual Coulomb repulsion prevents the movement of electrons and damps the transport of electric charge. In the extreme limit of very large coupling strength $U \to \infty$, the commonly used Hubbard model can be replaced by the antiferromagnetic Heisenberg model at exactly half-filling [13, 14]. Thus these insulators are described on a microscopic scale by their magnetic features. In a seminal work, Phil Anderson recognized that some of these unconventional insulators show, in fact, fascinating magnetic properties [15]. Guided by the observation that for one-dimensional spin chains, a gain in energy can be achieved by pairing neighboring spins into singlet bonds, instead of forming a Néel ordered state, he proposed that such a singlet bond state could also be relevant in higher-dimensional systems. He named this state the resonating valance bond state (RVB). RVB states were thought to be most relevant for geometrically frustrated lattice, e.g., an equilateral triangle, where quantum fluctuations prevent the forming of magnetically ordered states. Unfortunately, experimental evidence at that time purported Néel ordering, and the RVB idea was put aside for a while.

In the late eighties, copper oxide compounds, a certain type of unconventional insulators, received a great deal of attention after the discovery of high critical temperature (T_c) superconductors [16, 17]. Shortly before their experimental discovery, some numerical work based on perturbative calculations on the Hubbard and Anderson model suggested that for substantial electron repulsion, antiferromagnetically coupled spins develop an attractive potential, which can lead to their condensation [18]. This sparked a renaissance of the RVB idea. It was hoped that by starting from a description of a Mott insulator at exactly half-filling, the superconducting phase could be accessed by hole doping [19, 20, 21]. The parent state of the Mott insulator is governed by the antiferromagnetic Heisenberg model. Until today, this attempt could not unveil the mechanism leading to high-T_c superconductors, but it resulted, at least, in the formulation of mean-field theory for antiferromagnetic Heisenberg systems which lie in the core of this thesis [22, 23, 24, 25, 26, 27]. These theories use a fermionic representation of the spin operators [28], allowing for a decoupling suited to describe non-magnetic states. However, fermions are not the only ingredients as bosonic gauge fields are emerging. The resulting interplay between these fermionic and bosonic degrees of freedom pave the way for a plethora of exotic phenomena [29, 30, 5, 31]. One of these curiosities, which will become an essential motive in this thesis, is the aspect of fractionalization. This effect was initially observed for fractional quantum Hall states in which, due to a coupling

between electrons to magnetic flux, quasi-particles arise, which can carry a fractionalized value of the electric charge. This immediately leads to unusual exchange statistics [32, 33, 34]. Every excitation carries an integer spin quantum number for the pristine Heisenberg model in its usual spin representation. Yet in the alternative formulation, it turns out that there is a possible way in which such an excitation decays into two quasi-particles, each carrying only a fraction of the initial integer spin. These spin-1/2 quasi-particles are called spinons. The mechanism which leads to this decomposition is similar[1] to the one behind the confinement of quarks [35]. The gauge field acts effectively as a potential in which the fermions feel a binding force. Depending on the strength of this force, they are either confined to a certain region or can be arbitrarily far separated by only investing a finite amount of energy. In modern terms, these fractionalized spinon particles' very existence can be seen as the defining property of a quantum spin liquid [36]. Objects with unconventional exchange statistics [37, 38, 39], sometimes called anyons because they are neither bosons nor fermions, are actively studied, as they may provide a platform for protected quantum computation [40, 31, 41].

From a pragmatic perspective, the moment to investigate the intriguing behavior of quantum spin liquid phases could not be better. Many aspects have been theoretically formulated in a rather general and abstract way and could until very recently not escape the realm of platonic shadows due to the lack of existing materials. This is about to change. In the last years, experimental techniques improved, and physicists became able to artificially engineer materials from the drawing board. This advancement results in the discovery of more and more compounds hosting properties, which are in accordance with the theoretical description of spin liquids. One of the most prominent specimens is the mineral $ZnCu_3(OH)_6Cl_2$, also called Herbertsmithe, named after the mineralogist Herbert Smith. The magnetically active ions of this crystal are arranged in single layer kagome lattices whose geometrical structure consists of equilateral triangles and for which the antiferromagnetic Heisenberg model suggested the existence of a quantum spin liquid phase [42]. Using inelastic neutron scattering, a commonly used method in the study of frustrated magnetism, which will be further explained in Chapter 6, experimenters found comportment, which indicates the existence of fractionalized spinons [43, 44]. Even though the material α-$RuCl_3$, whose ions form a honeycomb lattice structure, develops a magnetic order at low temperatures [45] it is actively studied thanks to its proximity to the Kitaev spin liquid model [31, 46, 47, 48, 49]. In Chapter 8, another important material will be introduced in more detail. The material has the chemical structure $Ca_{10}Cr_7O_{28}$ and shows striking features as it produces a frustrating mechanism through the interplay of ferro- and antiferromagnetic couplings [50, 51, 52]. The

[1] Similar, but reversely acting since quarks are confined, and spinons are deconfined

serendipitous coincident of its discovery permitted the author to test the theoretical formulation against new experimental data.

The following treaties are organized into nine chapters. Chapter 2 to 6 will build and explain the fundamental framework which is used in the main part (Chapter 7 to 9). These core chapter will present the principle work which was performed during the doctoral studies of the author. Chapter 10 summarizes the relevant findings and concludes this thesis.

The first chapter introduces an enhanced mean-field theory for antiferromagnetic Heisenberg spin systems based on a fermionic representation of the spin operators. This enhanced theory valid as an effective low-energy description includes phase fluctuations to the bare mean-field solution, resulting in the emergence of gauge fields. The origin of these gauge fields, as well as their analytic structure, will be discussed. The low-energy theory consisting of fermionic and gauge fields can be further reduced if fermionic modes are massive. This reduction will lead to a pure gauge theory, which will be discussed in the second chapter. These gauge theories come in different flavors depending on local invariance transformations. In the most simple theory, called the $\mathbb{Z}_2$ gauge theory, this invariance group consists of only two elements. The corresponding Hamiltonian contains two parameters that, depending on their mutual relations, determine the model's phase. Two possible phases exist, which will be explained. The question of how these phases relate to the phenomenon of fractionalization and the physics of quantum spin liquids will be answered. Chapter 4 introduces the concept of projective symmetry groups (PSG). The necessity to use a projective representation for symmetry groups, which is a ramification of redundancy introduced by the mapping from the spin representation to the fermionic one, is further elucidated. It will also be shown how the invariance group, a normal subgroup in the entire PSG, can be used to derive arguments about the stability of particular mean-field models. The next chapter further elaborates on the PSG concept and gives step-by-step instruction to construct gauge inequivalent representations. These representations can be used for a classification of quantum phases, which goes beyond the classical Landau formalism. The consequence which arises for a mean-field theory in the case that spin rotational symmetry is broken will be commented on. This case becomes vital for materials that contain strong spin-orbit interactions. The last chapter of these preliminaries discusses the experimental set up of inelastic neutron scattering experiments. It furthers clarifies how the measurable quantities can be related to the dynamical spin structure factor. This structure factor is then calculated within the framework of the initially introduced mean-field theory.

The first research project published in Ref. [53] is outlined in Chapter 7. It starts explaining an existing PSG classification of spin-orbit coupled mean-field models

that preceded this project. This classification [54] calculated 1488 possible representations for which the resulting spinon models may contain topologically non-trivial bands. The aim of the follow-up work presented in this thesis is to reduce the number of relevant representation by taking some physically motivated arguments into account. It will be shown that for models that include only first neighbor couplings, the band topology is always trivial. Taking second neighbors into considerations almost inevitably yields mean-field models whose band dispersion shows exotic features. Two of these models, which show resemblance to the Bernevig-Hughes-Zhang model [55], are scrutinized. In the second part, these two models and one which represents a first neighbor model are employed to study the interplay of spinons and visons. Visons are the second type of excitations which govern the low-energy physics of quantum spin liquids. These excitations can be understood as discrete versions of magnetic fluxes. In order to disentangle an interacting theory of spinons and visons, a static approximation of the underlying gauge fields will be explained. Within this approximation, different configurations of visons are considered, and by diagonalization of a simple lattice problem, one obtains information about the spinon-vison model. The confining behavior of these models will be studied. It is found that spinons and visons form bound states. The resulting quasi-particles can be identified as Majorana zero modes, which will be rigorously related to the binding of fermionic modes by vortices observed in field-theoretic models and in the context of $p+ip$ superconductors [56, 57, 58]. Finally, an experimental signature is proposed. The presence of multiple visons induces this signature expressed by the formation of characteristic peaks in the low-energy spectrum. It is suggested that the number of visons can be linked to the temperature, and hence varying the temperature might be sufficient to gather information on the spinon band properties.

The second doctoral research project culminating in Ref. [59] dealt with the already mentioned spin liquid candidate $Ca_{10}Cr_7O_{28}$ and is the content of Chapter 8. This compound was recently discovered. Inelastic neutron scattering experiments and heat capacity measurements provided experimental data that are discussed in this work. After introducing the material and its magnetic structure, an effective mean-field model that uses a particular basis will be explained. This basis is motivated by the different magnetic couplings observed in $Ca_{10}Cr_7O_{28}$. These couplings do not only differ in type (ferro, or antiferromagnetic), but also in strength. The mean-field model allows evaluating the dynamical structure factor, which can be related to measured neutron scattering data. The model is capable to physically explain some of the key features found in the neutron measurement. Based on heat capacity data, it is further discussed that a weak pairing mechanism modifies the otherwise linear temperature dependency of the heat capacity in the low-temperature limit. It will be explained why the pairing is of an f-wave type. The importance of such a pairing term and the relation to a $\mathbb{Z}_2$ quantum spin liquid will be elucidated.

The third and final work, published in Ref. [60], is explained in Chapter 9. In this work, a PSG classification is executed for several three-dimensional space groups. These space groups, defining the simple cubic lattice, the body centered cubic lattice and the face centered cubic lattice, share a common O_h point group. The symmetry conditions and the respective projective representations of the O_h group are discussed. It will be explained how, based on the simple cubic classification, one can achieve the classifications for the body- and face centered cubic lattice. Using the body centered cubic case as an example it will be illustrated how the PSG representations and their implied symmetry conditions can be used to build symmetric short-ranged mean-field models. Such models are further discussed for the body and face centered lattice where up to third neighbor couplings are taken into account. The resulting spinon states are calculated based on a Hartree-Fock self-consistent procedure. Finally, the resulting states are discussed with regard to their energy dispersions, and the dynamical spin structure factor is evaluated in perspective to yield some guidance for future experiments.

2. Parton approach

This chapter introduces the framework which will be used throughout the rest of this thesis. Instead of using the fundamental spin representation, spin operators will be represented by second quantized operators. A priori not known which dispersion behavior one wishes to describe, it turns out that a fermionic representation is more convenient than a bosonic one. The advantage over a bosonic description is that fermions do not condense at low temperatures and hence can be used to capture the physics of gapless excitations. This fermionic description allows for the development of a mean-field theory.

2.1. First order mean-field theory

One of the main goals of this entire work is to get a better understanding of spin systems, which can often be described by the Heisenberg Hamiltonian

$$H = \sum_{(\mathbf{r}\mathbf{r}')} J_{\mathbf{r}\mathbf{r}'} \mathbf{S}_{\mathbf{r}} \mathbf{S}_{\mathbf{r}'}, \tag{2.1}$$

defined on a lattice whose sites are denoted by $\mathbf{r}$, and with spin operators $\mathbf{S}_{\mathbf{r}}$ defined on each lattice site. The coupling constant shall be positive $J_{\mathbf{r}\mathbf{r}'} > 0$ such that the spins favor antiferromagnetic alignment. The bracket indicates that the sum runs over possible neighbor pairings. Instead of using the common spin representation, it turns out to be convenient to choose a fermionic representation[28]

$$S^{\mu}_{\mathbf{r}} = \sum_{\alpha\beta} \frac{1}{2} f^{\dagger}_{\alpha\mathbf{r}} \sigma^{\mu}_{\alpha\beta} f_{\beta\mathbf{r}}, \tag{2.2}$$

whereas $f^{\dagger}_{\alpha\mathbf{r}}$ ($f_{\alpha\mathbf{r}}$) creates (annihilates) a fermion on lattice site $\mathbf{r}$ of spin projection $\alpha = \{\uparrow, \downarrow\}$ and $\sigma^{\mu}_{\alpha\beta}$ denotes in the case of spin$-\frac{1}{2}$ one of the Pauli matrices for $\mu = \{x, y, z\}$. The fermionic operators fulfill the usual anti-commutation relations $\left\{f^{\dagger}_{\alpha\mathbf{r}}, f^{\dagger}_{\beta\mathbf{r}'}\right\} = \{f_{\alpha\mathbf{r}}, f_{\beta\mathbf{r}'}\} = 0$ and $\left\{f^{\dagger}_{\alpha\mathbf{r}}, f_{\beta\mathbf{r}'}\right\} = \delta_{\alpha\beta}\delta_{\mathbf{r}\mathbf{r}'}$. One may later identify these fermions as quasi-particles called spinons. This mapping provokes a severe issue since it enlarges the local Hilbert space. In the original problem, every lattice site is singly occupied by either a particle with spin-up or one with spin-down, but in the fermionic representation, one includes unphysical states that are empty or doubly

occupied by one spin-up and one spin-down fermion. If one hopes for an adequate description of the initial spin problem, it is evident that these unphysical states have to be excluded. The relevant states can be identified as they obey the one particle per site constraint

$$\begin{aligned}\sum_{\alpha} f^{\dagger}_{\alpha\mathbf{r}} f_{\alpha\mathbf{r}} &= 1 \\ \sum_{\alpha\beta} \epsilon_{\alpha\beta} f_{\alpha\mathbf{r}} f_{\beta\mathbf{r}} &= 0,\end{aligned} \tag{2.3}$$

where $\epsilon_{\alpha\beta}$ denotes the Levi-Civita-Symbol. The second condition is a direct consequence of the first one and the fermionic anti-commutation relations. At this point, it might seem odd to use this representation. Why bothering with a representation in which one has to deal with this unhandy constraint after all? To understand this better it is helpful to consider how the Heisenberg Hamiltonian (2.1) transforms under this mapping (2.2).

$$\begin{aligned}H =& \sum_{(\mathbf{r}\mathbf{r}')} \sum_{\alpha\beta} \sum_{\alpha'\beta'} J_{\mathbf{r}\mathbf{r}'} \frac{1}{4} \left(f^{\dagger}_{\mathbf{r}\alpha} \sigma_{\alpha\beta} f_{\mathbf{r}\beta}\right) \left(f^{\dagger}_{\mathbf{r}'\alpha} \sigma_{\alpha'\beta'} f_{\mathbf{r}'\beta'}\right) \\ =& \sum_{(\mathbf{r}\mathbf{r}')} \frac{J_{\mathbf{r}\mathbf{r}'}}{4} \left(\sum_{\alpha\beta} 2 f^{\dagger}_{\mathbf{r}\alpha} f_{\mathbf{r}\beta} f^{\dagger}_{\mathbf{r}'\beta} f_{\mathbf{r}'\alpha} - \sum_{\alpha\alpha'} f^{\dagger}_{\mathbf{r}\alpha} f_{\mathbf{r}\alpha} f^{\dagger}_{\mathbf{r}'\alpha'} f_{\mathbf{r}'\alpha'} \right) \\ =& \sum_{(\mathbf{r}\mathbf{r}')} \sum_{\alpha\beta} -\frac{J_{\mathbf{r}\mathbf{r}'}}{2} \left(-f^{\dagger}_{\mathbf{r}\alpha} f_{\mathbf{r}\beta} \delta_{\alpha\beta} - f^{\dagger}_{\mathbf{r}\alpha} f_{\mathbf{r}'\alpha} \delta_{\mathbf{r}\mathbf{r}'} + f^{\dagger}_{\mathbf{r}\alpha} f_{\mathbf{r}'\alpha} f^{\dagger}_{\mathbf{r}'\beta} f_{\mathbf{r}\beta} + \frac{1}{2} f^{\dagger}_{\mathbf{r}\alpha} f_{\mathbf{r}\alpha} f^{\dagger}_{\mathbf{r}'\beta} f_{\mathbf{r}'\beta} \right) \\ \sim& \sum_{(\mathbf{r}\mathbf{r}')} \sum_{\alpha\beta} -\frac{J_{\mathbf{r}\mathbf{r}'}}{2} \left(f^{\dagger}_{\mathbf{r}\alpha} f_{\mathbf{r}'\alpha} f^{\dagger}_{\mathbf{r}'\beta} f_{\mathbf{r}\beta} + \frac{1}{2} f^{\dagger}_{\mathbf{r}\alpha} f_{\mathbf{r}\alpha} f^{\dagger}_{\mathbf{r}'\beta} f_{\mathbf{r}'\beta} \right).\end{aligned} \tag{2.4}$$

In the second line the identity $\sigma_{\alpha\beta}\sigma_{\alpha'\beta'} = 2\delta_{\alpha\beta'}\delta_{\alpha'\beta} - \delta_{\alpha\beta}\delta_{\alpha'\beta'}$ was used. The constant terms $f^{\dagger}_{\mathbf{r}\alpha} f_{\mathbf{r}\beta}\delta_{\alpha\beta}$ and $f^{\dagger}_{\mathbf{r}\alpha} f_{\mathbf{r}'\alpha}\delta_{\mathbf{r}\mathbf{r}'}$ merely shift the chemical potential, and can be neglected for the moment. The resulting Hamiltonian is unfortunately quartic in the fermionic operators and cannot be solved. Nevertheless, it enables one to do a mean-field decoupling. At this point, the use of the fermionic representation becomes clearer. Surely, one could have done the mean-field decoupling already in the spin representation. Yet this is only possible for magnetically ordered states $\langle S^z \rangle \neq 0$ [11]. The new representation obviates this limitation and thus becomes convenient in the study of non-magnetic phases. In the fermionic basis, there are many ways to decouple the interacting Hamiltonian (2.4). As usually done in mean-field theory, one replaces a given operator by its mean value plus a small fluctuating term - for concreteness take the bilinear $f^{\dagger}_{\mathbf{r}\alpha} f_{\mathbf{r}'\beta}$ and replace it by $\left\langle f^{\dagger}_{\mathbf{r}\alpha} f_{\mathbf{r}'\beta} \right\rangle + \delta f^{\dagger}_{\mathbf{r}\alpha} f_{\mathbf{r}'\beta}$. The first

term in the last line of Eq. (2.4) can then be factorized

$$\begin{aligned} f^\dagger_{\mathbf{r}\alpha} f_{\mathbf{r}'\alpha} f^\dagger_{\mathbf{r}'\beta} f_{\mathbf{r}\beta} &= \left(\left\langle f^\dagger_{\mathbf{r}\alpha} f_{\mathbf{r}'\alpha}\right\rangle + \delta f^\dagger_{\mathbf{r}\alpha} f_{\mathbf{r}'\alpha}\right)\left(\left\langle f^\dagger_{\mathbf{r}'\beta} f_{\mathbf{r}\beta}\right\rangle + \delta f^\dagger_{\mathbf{r}'\beta} f_{\mathbf{r}\beta}\right) \\ &= \left\langle f^\dagger_{\mathbf{r}\alpha} f_{\mathbf{r}'\alpha}\right\rangle \left\langle f^\dagger_{\mathbf{r}'\beta} f_{\mathbf{r}\beta}\right\rangle + \left\langle f^\dagger_{\mathbf{r}\alpha} f_{\mathbf{r}'\alpha}\right\rangle \delta f^\dagger_{\mathbf{r}'\beta} f_{\mathbf{r}\beta} + \delta f^\dagger_{\mathbf{r}\alpha} f_{\mathbf{r}'\alpha} \left\langle f^\dagger_{\mathbf{r}'\beta} f_{\mathbf{r}\beta}\right\rangle + \delta f^\dagger_{\mathbf{r}\alpha} f_{\mathbf{r}'\alpha} \delta f^\dagger_{\mathbf{r}'\beta} f_{\mathbf{r}\beta} \\ &\approx -\left|\chi_{\mathbf{r}\mathbf{r}'}\right|^2 + \left(\delta f^\dagger_{\mathbf{r}\alpha} f_{\mathbf{r}'\alpha} \chi_{\mathbf{r}'\mathbf{r}} + h.c.\right). \end{aligned} \tag{2.5}$$

The approximation consists of neglecting the term quadratic in the fluctuations. Further, the mean value, as well as the constraint (2.3), are replaced by their ground state expectation values $\chi_{\mathbf{r}\mathbf{r}'} = \left\langle f^\dagger_{\mathbf{r}\alpha} f_{\mathbf{r}'\alpha}\right\rangle$ and $\left\langle \sum_\alpha f^\dagger_{\alpha\mathbf{r}} f_{\alpha\mathbf{r}}\right\rangle = 1$. Thus the constraint becomes scleronomous, and it can be enforced in the Hamiltonian formalism by adding a site-dependent Lagrange multiplier $a_\mathbf{r}$ term. The second term of the last line in Eq. (2.4) corresponds to a non-local density-density interaction, which in the one-particle per site limit merely yields a constant term which will be omitted. Note that this decoupling neglects magnetic ordered terms, which could be traced back to $\langle \mathbf{S}_\mathbf{r}\rangle \mathbf{S}_{\mathbf{r}'}$. Hence, as already mentioned, the resulting model may be used to study non-magnetic phases. The mean-field Hamiltonian to zeroth order[1] is then given by [11]

$$H_{\mathrm{mf}} = \sum_{(\mathbf{r}\mathbf{r}')} \sum_\alpha \frac{J_{\mathbf{r}\mathbf{r}'}}{2} \left(\left|\chi_{\mathbf{r}\mathbf{r}'}\right|^2 - \left(f^\dagger_{\mathbf{r}\alpha} f_{\mathbf{r}'\alpha} \chi_{\mathbf{r}'\mathbf{r}} + h.c.\right)\right) + \sum_\mathbf{r} \sum_\alpha a_\mathbf{r} \left(f^\dagger_{\mathbf{r}\alpha} f_{\mathbf{r}\alpha} - 1\right). \tag{2.6}$$

Being quadratic in the field operators, this Hamiltonian is readily diagonalized by a Fourier transformation given that it is translationally invariant. The ground state energy is given by the minimum of the energy functional $E_{\mathrm{gs}}(\chi, a) = \langle \Psi^0(\chi, a)| H_{\mathrm{mf}}(\chi, a) |\Psi^0(\chi, a)\rangle$, where the superscript 0 denotes the ground state wave function. The extremal condition $\frac{\delta E}{\delta \chi_{\mathbf{r}\mathbf{r}'}} = 0$ can be used to find the self-consistent amplitudes $\chi_{\mathbf{r}\mathbf{r}'}$. The constraint may also be formulated as an extremal condition $\frac{\delta E}{\delta a_\mathbf{r}} = 0$.

Mean-field theory may serve as a good starting point for analyzing the system in question, but the approximation made in Eq. (2.5) is entirely uncontrolled. Thus the solution of the mean-field Hamiltonian (2.6) might not be stable as soon as fluctuations are taken into account. To study the dynamics of fluctuations it is helpful to use a path integral representation [11, 2]. The partition function can be written as

$$Z = \int \mathcal{D}[f^\dagger]\mathcal{D}[f]\mathcal{D}[\chi^*]\mathcal{D}[\chi] e^{-S[f^\dagger, f, \chi^*, \chi]}. \tag{2.7}$$

Note that the fermionic fields now correspond to Grassmann variables. The constraint can be implemented by imposing single occupancy via a multiplier field. This

[1] It will become clear later what zeroth-order means.

is achieved by inserting a delta distribution that enforces single occupancy. Using the Fourier representation of the delta distribution then inserts the multiplier field $a_{\mathbf{r}}$

$$\delta\left(\sum_{\alpha}(f^{\dagger}_{\mathbf{r}\alpha}f_{\mathbf{r}\alpha}-1)\right)=\int da_{\mathbf{r}}e^{i\sum_{\alpha}(f^{\dagger}_{\mathbf{r}}f_{\mathbf{r}}-1)a_{\mathbf{r}}}. \tag{2.8}$$

This gives the same term, as it was argued for the derivation of Eq. (2.6)[2]. The euclidean action is given by

$$\begin{aligned} &S=L_0+H\\ &=\int d\tau\sum_{\mathbf{r},\alpha}f^{\dagger}_{\mathbf{r}\alpha}\left(\frac{\partial}{\partial\tau}-\mu+ia_{\mathbf{r}}\right)f_{\mathbf{r}\alpha}+\sum_{(\mathbf{r}\mathbf{r}'),\alpha}\frac{J_{\mathbf{r}\mathbf{r}'}}{2}\left(|\chi_{\mathbf{r}\mathbf{r}'}|^2-\left(f^{\dagger}_{\mathbf{r}\alpha}f_{\mathbf{r}'\alpha}\chi_{\mathbf{r}'\mathbf{r}}+h.c.\right)\right). \end{aligned} \tag{2.9}$$

In this representation, the fields $\chi_{\mathbf{r}\mathbf{r}'}$ correspond to auxiliary fields that have been included by a Hubbard-Stratonovitch transformation decoupling the interaction of the full Hamiltonian (2.4). One can obtain the same result, as it was derived using the mean-field decoupling Eq. (2.5), by assuming the Hubbard-Stratonovitch fields to be static. Note that including full dynamical decoupling fields yields an exact representation of the interacting problem.

In the static limit, one can obtain the equations of motion of the fermions in the usual way. Their dispersion will depend on the static value of $\chi^0_{\mathbf{r}\mathbf{r}'}$. Small variations from a saddle-point can be parametrized by introducing amplitude $\delta\chi_{\mathbf{r}\mathbf{r}'}$ and phase $\theta_{\mathbf{r}\mathbf{r}'}$ fluctuations around $\chi^0_{\mathbf{r}\mathbf{r}'}=|\chi^0_{\mathbf{r}\mathbf{r}'}|$ such that in the vicinity the dispersion is governed by $\chi_{\mathbf{r}\mathbf{r}'}=(\chi^0_{\mathbf{r}\mathbf{r}'}+\delta\chi_{\mathbf{r}\mathbf{r}'})e^{i\theta_{\mathbf{r}\mathbf{r}'}}$. It is found that the amplitude fluctuations will lead to an energy gap in the dispersion [24, 27, 14], and can be neglected if one seeks to study the behavior close to the saddle-point. The action (2.9) including these fluctuations becomes

$$\begin{aligned} S=&\int d\tau\sum_{\mathbf{r},\alpha}f^{\dagger}_{\mathbf{r}\alpha}\left(\frac{\partial}{\partial\tau}-\mu+ia_{\mathbf{r}}\right)f_{\mathbf{r}\alpha}\\ &+\sum_{(\mathbf{r}\mathbf{r}'),\alpha}\frac{J_{\mathbf{r}\mathbf{r}'}}{2}\left(|\chi_{\mathbf{r}\mathbf{r}'}|^2-\left(\chi^0_{\mathbf{r}'\mathbf{r}}f^{\dagger}_{\mathbf{r}\alpha}f_{\mathbf{r}'\alpha}e^{i\theta_{\mathbf{r}'\mathbf{r}}}+h.c.\right)\right), \end{aligned} \tag{2.10}$$

where the fermionic fields, which are free in the pure mean-field theory, now couple to the phase fluctuations. This action is invariant under a local transformation of $f_{\mathbf{r}\alpha}\to f_{\mathbf{r}\alpha}e^{i\phi_{\mathbf{r}}}$, if the phase fluctuations transform according to $\theta_{\mathbf{r}'\mathbf{r}}\to\theta_{\mathbf{r}'\mathbf{r}}+\phi_{\mathbf{r}}-\phi_{\mathbf{r}'}$, and the multiplier field $a_{\mathbf{r}}\to a_{\mathbf{r}}+\frac{\partial}{\partial\tau}\phi_{\mathbf{r}}$. These transformation properties define a

[2]Note the factor i appears in the euclidean action.

$U(1)$ gauge theory with an emergent gauge field $\phi_{\mathbf{r}}$ whose spatial components are connected to the phase fluctuations $\theta_{\mathbf{r}'\mathbf{r}}$, and the temporal component is connected to the multiplier field $a_{\mathbf{r}}$ [20, 22, 23]. It is important to keep in mind that the action (2.10) describes a low-energy effective theory valid only in the vicinity of a specific saddle-point, which is determined by the means of mean-field theory. The advantage is that in its realm of validity, fluctuations are correctly taken into account. Therefore, this approach is sometimes called first-order mean-field theory, whereas the pure self-consistent calculation of the saddle-point is entitled zeroth-order [11].

2.2. Local gauge invariance

This is quite a remarkable result. The initial theory of spins can be described by a low-energy effective fermionic theory coupled to emerging gauge fields. The reason for this lies in the mapping (2.2). One immediately realizes that this mapping is invariant under a local $U(1)$ transformation of the fermions. Yet it turns out that the invariance group of Eq. (2.2) is, as a matter of fact, lager than $U(1)$ [23, 25]. This can be best seen by using a matrix notation for the fermions [23]

$$\Psi_{\mathbf{r}} = \begin{pmatrix} f_{\mathbf{r}\uparrow} & f_{\mathbf{r}\downarrow} \\ f^{\dagger}_{\mathbf{r}\downarrow} & -f^{\dagger}_{\mathbf{r}\uparrow} \end{pmatrix}. \tag{2.11}$$

The spin operator written as

$$S^{\mu}_{\mathbf{r}} = \frac{1}{2} \operatorname{Tr}\left[\Psi^{\dagger}_{\mathbf{r}} \Psi_{\mathbf{r}} (\sigma^{\mu})^{T}\right], \tag{2.12}$$

reveals the invariance under a local transformation $\Psi_{\mathbf{r}} \to W_{\mathbf{r}} \Psi_{\mathbf{r}}$, with $W_{\mathbf{r}} \in SU(2)$. This transformation is not equal to a general spin rotation, which is given by right multiplication $\Psi_{\mathbf{r}} \to \Psi_{\mathbf{r}} V$ with $V \in SU(2)$, which becomes apparent by recalling the cyclic permutation invariance of the trace, and the transformation rules of the $SU(2)$ representation of spin-1/2. Written in this matrix form, one can conveniently expresses the interacting term of the Heisenberg Hamiltonian as

$$\mathbf{S}_{\mathbf{r}} \mathbf{S}_{\mathbf{r}'} = -\frac{1}{8} \operatorname{Tr}\left[\Psi_{\mathbf{r}} \Psi^{\dagger}_{\mathbf{r}'} \Psi_{\mathbf{r}'} \Psi^{\dagger}_{\mathbf{r}}\right]. \tag{2.13}$$

As anticipated, this term is invariant under the global spin rotation V as a reminiscent of the fundamental spin representation in which the Heisenberg model is invariant under a global rotation of all spins. However, in this fermionic picture, one additionally has a local freedom $W_{\mathbf{r}}$, which was not present in the spin picture. The origin of this $SU(2)$ invariance roots in the fact that besides the usual $U(1)$ symmetry, which means that the total number of fermions is conserved, an additional

particle-hole symmetry is present. This particle-hole symmetry is specified by

$$\begin{aligned} f_{\mathbf{r}\uparrow} &= f_{\mathbf{r}\uparrow}\cos\varphi + f^{\dagger}_{\mathbf{r}\downarrow}\sin\varphi \\ f_{\mathbf{r}\downarrow} &= f_{\mathbf{r}\downarrow}\cos\varphi - f^{\dagger}_{\mathbf{r}\uparrow}\sin\varphi, \end{aligned} \tag{2.14}$$

which leaves the spin operator under the mapping (2.2) invariant. If one defines a doublet of the form $\psi_{\mathbf{r}} = (f_{\mathbf{r}\uparrow}, f^{\dagger}_{\mathbf{r}\downarrow})^T$, the $U(1)$ transformation becomes $\psi_{\mathbf{r}} \rightarrow e^{i\phi\sigma^3}\psi_{\mathbf{r}}$, and the particle-hole transformation $\psi_{\mathbf{r}} \rightarrow e^{i\varphi\sigma^2}\psi_{\mathbf{r}}$. However, these two transformations do not commute and by applying a second $U(1)$ transformation one finds

$$\psi_{\mathbf{r}} \rightarrow e^{i\theta\sigma^3}e^{i\varphi\sigma^2}e^{i\phi\sigma^3}\psi_{\mathbf{r}}, \tag{2.15}$$

where the different angles θ, φ, ϕ are the Euler-angle that define a rotation in $SU(2)$ [61].

Now that the reason for the local invariance has been clarified, it is time to understand its ramifications a bit better. There are many different fermionic configurations, namely all that can be connected via local $SU(2)$ transformations, that represent the same spin configuration. This is directly related to the fact that the spin-to-fermion mapping enlarges the local Hilbert space. As it was explained above, any physical solution needs to be projected to the sub-space of single occupancy Eq. (2.3), which in the matrix representation can be formulated as

$$\mathrm{Tr}\left[\Psi^{\dagger}_{\mathbf{r}}\sigma^{\mu}\Psi_{\mathbf{r}}\right] = 0. \tag{2.16}$$

Note that contrary to the spin operator (2.12), the constraint does not transform trivially under the local transformation $W_{\mathbf{r}}$, but it transforms trivially under the global spin rotation that was defined by the right multiplication V [61]. Ultimately, many fermionic states describe the same physical spin state. These fermionic states form a sub-space, and transformations that act within this sub-space are called gauge transformations. Theories of this type appear in many different physics domains and can be summarized by the two following statements: (1) Many apparently different states describe the same physical state due to a redundancy in the description. (2) This redundancy comes along with a constraint [62, 63, 11]. Due to these many states that describe the same physical situation, one has to be careful by performing averages. Usually, one can prevent overcounting by fixing a gauge. Yet this is not possible in the case of non-abelian gauge theories. These theories have to be treated by more involved methods as for example, the Fadeev-Popov method [64].

2.3. $SU(2)$ mean-field theory

A theory that respects the full $SU(2)$ invariance group can be formulated. This theory provides a generalization of the previously explained $U(1)$ theory. In order

to derive the first-order mean-field theory, including the full $SU(2)$ gauge group, one starts from the matrix representation of the Heisenberg Hamiltonian (2.13). Similar to the previously studied $U(1)$ scenario this term is quartic in the field operators $\Psi_{\mathbf{r}}$, and it needs to be decoupled by a suitable Hubbard-Stratonovitch transformation, which now introduces matrix-valued auxiliary fields on the bonds defined as

$$\frac{8}{J}u_{\mathbf{rr}'} = \Psi_{\mathbf{r}}\Psi_{\mathbf{r}'}^{\dagger} = \begin{pmatrix} f_{\mathbf{r}\uparrow}f_{\mathbf{r}'\uparrow}^{\dagger} + f_{\mathbf{r}\downarrow}f_{\mathbf{r}'\downarrow}^{\dagger} & f_{\mathbf{r}\uparrow}f_{\mathbf{r}'\downarrow} - f_{\mathbf{r}\downarrow}f_{\mathbf{r}'\uparrow} \\ -f_{\mathbf{r}\uparrow}^{\dagger}f_{\mathbf{r}'\downarrow}^{\dagger} + f_{\mathbf{r}\downarrow}^{\dagger}f_{\mathbf{r}'\uparrow}^{\dagger} & f_{\mathbf{r}\uparrow}^{\dagger}f_{\mathbf{r}'\uparrow} + f_{\mathbf{r}\downarrow}^{\dagger}f_{\mathbf{r}'\downarrow} \end{pmatrix} = \begin{pmatrix} -\chi_{\mathbf{rr}'}^{\dagger} & -\Delta_{\mathbf{rr}'}^{\dagger} \\ -\Delta_{\mathbf{rr}'} & \chi_{\mathbf{rr}'} \end{pmatrix}. \tag{2.17}$$

The decoupled Hamiltonian can then be written as

$$H = \frac{8}{J}\sum_{\langle \mathbf{rr}' \rangle} \mathrm{Tr}\left[u_{\mathbf{rr}'}^{\dagger}u_{\mathbf{rr}'} + \Psi_{\mathbf{r}}^{\dagger}u_{\mathbf{rr}'}\Psi_{\mathbf{r}'} + h.c.\right] + \sum_{\mathbf{r}} \mathrm{Tr}\left[\Psi_{\mathbf{r}}^{\dagger}\left(a_{\mathbf{r}}^{\mu}\sigma_{\mu}\right)\Psi_{\mathbf{r}}\right]. \tag{2.18}$$

Using the time-independent mean value for the fields $u_{\mathbf{rr}'}^{0}$ yields the zero-order mean-field theory. The entries of the vector $a_{\mathbf{r}}^{\mu}$ are the Lagrange multipliers that enforce the constraint (2.16). As before, by including phase fluctuations over the saddle-point values $u_{\mathbf{rr}'} = |u_{\mathbf{rr}'}^{0}|e^{ia_{\mathbf{rr}'}^{\mu}\sigma_{\mu}}$, one can formulate an effective low-energy theory in which the vector fields, represented by $a_{\mathbf{rr}'}^{\mu}\sigma_{\mu}$ transforming according to an emerging $SU(2)$ gauge theory, and couple to the matter fields $\Psi_{\mathbf{r}}$. Depending on the explicit decoupling scheme and the resulting saddle-point, the $SU(2)$ group can be broken such that the effective low-energy theory has a different invariance group, which will be further explained in Chapter 4. The most important specimens in the context of quantum spin liquids are effective theories that include either a $U(1)$ or $\mathbb{Z}_2$ invariance group.

This entire procedure yields an exact representation of the low-energy behavior of the full interacting theory close to a given saddle-point. Unfortunately, like the quartic theory from the beginning, it cannot be solved analytically. However, if one could argue that the excitations of the emergent fields have a finite gap in energy (Chapter 4 will further elaborate this point), which implies that the phase fluctuations require a certain amount of energy, then sufficiently below this energy, one could go back to the zeroth-order mean-field theory, i.e., replacing $u_{\mathbf{rr}'}$ by its mean value $u_{\mathbf{rr}'}^{0}$. As described above, in this limit, one can find the spinon dispersion governed by the free fermionic fields. In the following step, one can integrate over these fermionic fields yielding a theory that only includes the remaining gauge fields. In Chapter 3, the simplest of such a theory, namely the $\mathbb{Z}_2$ gauge theory, will be explained in more depth. Solving this final problem would provide the ultimate solution to the full interacting problem[3]. Generally, these theories can be very complicated. Even though the auxiliary fields $u_{\mathbf{rr}'}$ do not have an explicit dynamical

[3]Yet still only in a low-energy limit

term in the action[4] a gradual integration over the fermions, in an RG sense, can introduce the dynamics of the gauge fields as explained by the Gross-Neveu model [25, 65]. Another way that can incorporate dynamics to the auxiliary fields comes from a rigorous treatment of the one-particle per site constraint. This will be further discussed in Chapter 7.

[4]Compare to Eq. (2.9)

3. Lattice gauge theory

In this chapter, the concept of lattice gauge theories is explained in a nutshell. This will mainly be done using the most simple specimen, the $\mathbb{Z}_2$ lattice gauge theory [66, 35, 30]. This theory plays a major role in the description of quantum spin liquids [6, 9, 31] as it leads directly to a deconfinement of spinons, which will be shown below. It is a relatively simple model to explain the concept of topological order [67, 26] and appears in the theory of quantum information [40]. Sometimes it turns out to be helpful to compare with the ordinary $U(1)$ gauge theory, as this theory might be more familiar to most of the readers, and, especially, to motivate the analytic form of the $\mathbb{Z}_2$ Hamiltonian emphasis lies on the $U(1)$ theory in its discretized lattice version. This chapter only scratches on the surface of this vast field. Further readings can be found in many textbooks [11, 36, 14], larger reviews [68, 31], and a plethora of lecture notes.

3.1. Gauge theory on a lattice

In Chapter 2, it was argued that a lattice gauge theory describes the low-energy physics of quantum spin liquids. The exact derivation depends on many details and shall not be addressed. Instead, it is assumed that after integrating out the fermionic fields, the Lagrangian L governing the path integral depends solely on the field $e^{a_\mu \tau^\mu} \sim \mathbf{A}$, where the notation $\mathbf{A}$ is chosen to emphasize the analogy to the vector potential as it is used in electrodynamics. Contrary to electrodynamics and reminiscent to the character of the underlying phase fluctuations, which led to the emergence of the gauge fields $A_i \in [0, 2\pi]$ takes only values within a compact interval. It shall further be possible that L can be decomposed into kinetic part $T(\dot{\mathbf{A}})$ and a potential $U(\mathbf{A})$ such that $L(\mathbf{A}) = T(\dot{\mathbf{A}}) - U(\mathbf{A})$. In electrodynamics, the kinetic energy is given by

$$T = \int d^3r \frac{\epsilon_0 \dot{\mathbf{A}}^2}{2} = \int d^3r \frac{\epsilon_0 (\mathbf{E} + \nabla\psi)^2}{2}, \tag{3.1}$$

where $\mathbf{E}$ is the electric field, ψ the temporal component of the vector field and ϵ_0 the vacuum permittivity. In the discrete setting one can identify

$$a^0_{\mathbf{r}} = \psi(\mathbf{x})|_{\mathbf{x}=\mathbf{r}}, \quad a_{\mathbf{r}\mathbf{r}'} = \int_{\mathbf{r}}^{\mathbf{r}'} d\mathbf{x}\mathbf{A}(\mathbf{x}), \tag{3.2}$$

where $\mathbf{x}$ is a point in space and $\mathbf{r}$ is a position on the lattice. One finds then the lattice kinetic term as [11]

$$T = \sum_{\langle \mathbf{r}\mathbf{r}' \rangle} \frac{e^2_{\mathbf{r}\mathbf{r}'}}{4J}, \tag{3.3}$$

with J some coupling parameter and the electric flux through a link $e_{\mathbf{r}\mathbf{r}'} = \dot{a}_{\mathbf{r}\mathbf{r}'} + a^0_{\mathbf{r}} - a^0_{\mathbf{r}'}$. The potential term is a function of the magnetic flux $\Phi = \oint_{\delta S} \mathbf{A}(\mathbf{r}) d\mathbf{r}$ that should further respect, at least in the compact theory, the periodicity of the field $a_{\mathbf{r}\mathbf{r}'} \sim a_{\mathbf{r}\mathbf{r}'} + 2\pi$. On a lattice, the potential is given by [11]

$$U = g \sum_{\mathbf{p}} \cos(\Phi_{\mathbf{p}}), \tag{3.4}$$

with g being another coupling parameter. The lattice flux is given on a square lattice by

$$\Phi_{\mathbf{r}} = a_{\mathbf{r},\mathbf{r}+\hat{e}_x} + a_{\mathbf{r}+\hat{e}_x,\mathbf{r}+\hat{e}_x+\hat{e}_y} + a_{\mathbf{r}+\hat{e}_x+\hat{e}_y,\mathbf{r}+\hat{e}_y} + a_{\mathbf{r}+\hat{e}_y,\mathbf{r}}. \tag{3.5}$$

The resulting Lagrangian is invariant under a $U(1)$ gauge transformation given by

$$a_{\mathbf{r}\mathbf{r}'}(t) \to a_{\mathbf{r}\mathbf{r}'}(t) - \phi_{\mathbf{r}}(t) + \phi_{\mathbf{r}'}(t), \quad a^0_{\mathbf{r}}(t) \to a^0_{\mathbf{r}}(t) + \dot{\phi}_{\mathbf{r}}(t), \tag{3.6}$$

for $\phi_{\mathbf{r}}(t)$ an arbitrary function of time on the lattice.

A quantum theory can be derived by determining the canonical momentum $\pi_i = \frac{\partial L}{\partial \dot{A}_i}$ and promoting the Poisson brackets to the commutator $\{\pi_i, A_j\} \to [\pi_i, A_j] = -i\delta_{ij}$[1], while $\hbar = 1$. The resulting lattice Hamiltonian is

$$H = \frac{1}{4J} \sum_{\langle \mathbf{r}\mathbf{r}' \rangle} e^2_{\mathbf{r}\mathbf{r}'} - g \sum_{\mathbf{r}} \cos(\Phi_{\mathbf{r}}). \tag{3.7}$$

Eventually, before going to the $\mathbb{Z}_2$ scenario, one final remark should be made about charge conservation and the quantization of the electric flux. Dealing with a compact theory requires that a wave function has to respect the periodicity of the field $\Psi(a_{\mathbf{r}\mathbf{r}'}) = \Psi(a_{\mathbf{r}\mathbf{r}'} + 2\pi)$. Using a plain wave *Ansatz* $\Psi(a_{\mathbf{r}\mathbf{r}'}) \to \Psi_m(a_{\mathbf{r}\mathbf{r}'}) \propto e^{-ima_{\mathbf{r}\mathbf{r}'}}$ and the fact that the electric flux is conjugate to $a_{\mathbf{r}\mathbf{r}'}$ readily leads to

$$e_{\mathbf{r}\mathbf{r}'}\Psi_m(a_{\mathbf{r}\mathbf{r}'}) = i\frac{\partial}{\partial a_{\mathbf{r}\mathbf{r}'}}\Psi_m(a_{\mathbf{r}\mathbf{r}'}) = m\Psi_m(a_{\mathbf{r}\mathbf{r}'}). \tag{3.8}$$

This means that the eigenvalues of $e_{\mathbf{r}\mathbf{r}'}$ have to be quantized. Yet this does not necessarily imply that they are integer. The physical theory is made of bilinear

[1] In the Coulomb gauge the electric field is the conjugate variable $[e_{\mathbf{r}\mathbf{r}'}, a_{\mathbf{r}\mathbf{r}'}] = -i\delta_{\mathbf{r}\mathbf{r}'}$.

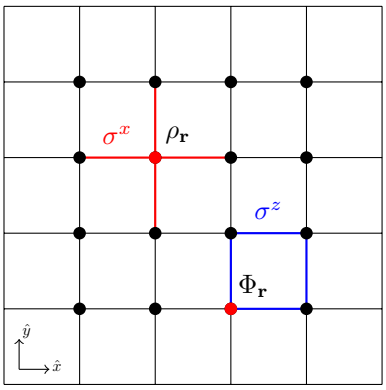

Figure 3.1: Illustration of the charge operator $\rho_{\mathbf{r}}$ and the flux operator $\Phi_{\mathbf{r}}$ on a square lattice. The red sites indicate the position on which each operator is applied. The blue bonds correspond to an σ^z operation and the red bonds to an operation of σ^x.

terms $\Psi^*\Psi$ such that the periodicity requires merely $\Psi^*(a_{\mathbf{rr}'} + 2\pi) = e^{-i\theta}\Psi^*(a_{\mathbf{rr}'})$ and $\Psi(a_{\mathbf{rr}'} + 2\pi) = e^{i\theta}\Psi(a_{\mathbf{rr}'})$ which could also allow half-integer values.

Motivated by Gauss-law $\nabla\mathbf{E} = \rho$ one defines the electric lattice charge as $q_{\mathbf{r}} = \sum_\mu e_{\mathbf{r},\mathbf{r}+\hat{e}_\mu}$ where $\sum_\mu$ denotes the sum over all adjacent sites connected to $\mathbf{r}$. Using the transformation Eq. (3.6) and the definition of the electric flux indicate that charge is a gauge invariant quantity. With the electric flux quantized, the electric charge is also quantized. Furthermore, one can show that $[q_{\mathbf{r}}, H] = 0$, which means that these local charges are conserved quantities, and the Hamiltonian can be block diagonalized. These locally conserved quantities are not surprising as it was already observed that the theory is invariant under a local gauge transformation. One can thus identify these charge operators as the generators of this gauge transformation [62].

3.2. $\mathbb{Z}_2$ Lattice gauge theory

The $\mathbb{Z}_2$ theory is obtained by restricting the image of the bond variables to two distinct values $e^{a_\mu \tau^\mu} \in \{-1, 1\}$. The Hamiltonian is

$$H = -\Gamma \sum_{\langle \mathbf{rr}' \rangle} \sigma^x_{\mathbf{rr}'} - \lambda \sum_{\text{plaquets}} \prod_{\square} \sigma^z_{\mathbf{rr}'}. \tag{3.9}$$

Here σ^x, σ^z are operators represented by the corresponding Pauli matrices and defined on the links of the underlying lattice. The notation $\prod_\square \sigma^z_{\mathbf{rr}'}$ indicates the product of all bond operators following a closed loop around an elementary plaquette, i.e., on a square lattice $\prod_\square \sigma^z_{\mathbf{rr}'} = \sigma^z_{\mathbf{r},\mathbf{r}+\hat{e}_x}\sigma^z_{\mathbf{r}+\hat{e}_x,\mathbf{r}+\hat{e}_x+\hat{e}_y}\sigma^z_{\mathbf{r}+\hat{e}_x+\hat{e}_y,\mathbf{r}+\hat{e}_y}\sigma^z_{\mathbf{r}+\hat{e}_y,\mathbf{r}}$. This is illustrated in Fig. 3.1. These plaquette terms are the discrete equivalent of the magnetic flux $\Phi_{\mathbf{r}}$. Γ, and λ are some coupling parameters. Similar to the $U(1)$ theory, one can define electric charges $\rho_{\mathbf{r}} = \prod_\mu \sigma^x_{\mathbf{r},\mathbf{r}+\hat{e}_\mu}$, where the product is taken over all from site $\mathbf{r}$ emanating bond operators, e.g., $\rho_{\mathbf{r}} = \sigma^x_{\mathbf{r},\mathbf{r}+\hat{e}_x}\sigma^x_{\mathbf{r},\mathbf{r}+\hat{e}_y}\sigma^x_{\mathbf{r},\mathbf{r}-\hat{e}_x}\sigma^x_{\mathbf{r},\mathbf{r}-\hat{e}_y}$ on the square lattice, as shown in Fig. 3.1. These operators commute with $\sigma^x_{\mathbf{rr}'}$, the

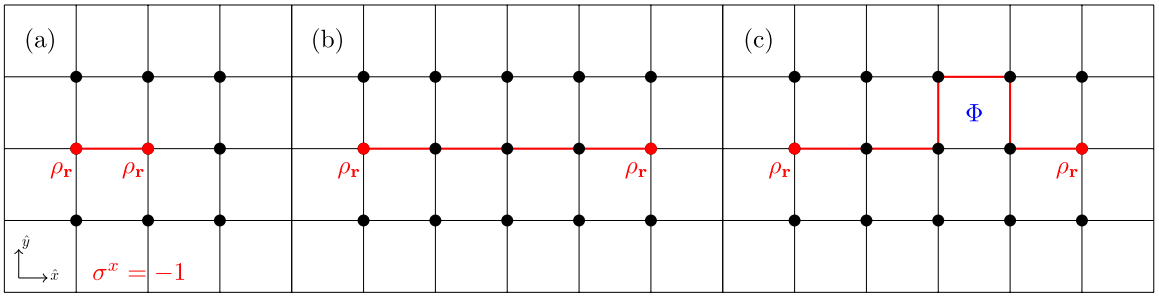

Figure 3.2.: The ground state of the confining phase is given by the uniform configuration for which every $\sigma^x_{\mathbf{r}\mathbf{r}'} = +1$ and $\rho_{\mathbf{r}} = +1$ represented by a black line or respectively a dot. (a) Two charges $\rho = -1$ are inserted by changing $\sigma^x = -1$ as denoted by the red link. (b) insertion of neighboring negative links separates the two charges. (c) the application of the plaquette term Φ flips the values of all adjacent links. This distorts the string connecting the two charges.

plaquette operators $[\rho_{\mathbf{r}}, \prod_{\square} \sigma^z_{\mathbf{r}\mathbf{r}'}] = 0$, and hence with the entire Hamiltonian. Consequently, analog to the $U(1)$ case the electric flux and the magnetic flux are gauge invariant quantities, and the Hamiltonian can be block diagonalized according to different charge sectors.

3.2.1. Confining phase $\Gamma \gg \lambda$

To start the analysis, one assumes the limit $\Gamma \to \infty$. The second term in Eq. (3.9) becomes irrelevant and the ground state is formed by the unique configuration $\sigma^x_{\mathbf{r}\mathbf{r}'} = +1$ on all bonds. The electric charge operator is also uniform $\rho_{\mathbf{r}} = +1$ on all sites. This sector is called the charge-free sector. Flipping one variable $\sigma^x_{\mathbf{r}_0\mathbf{r}_1} \to -1$ creates two electric charges as illustrated in Fig. 3.2. Such a bond flip provokes an energy penalty of 2Γ. Nevertheless, as this configuration belongs to a different charge sector, it cannot be directly compared to the charge-free state. Flipping a second bond adjacent to one of the two charges does not include further charge. Yet it increases the energy again by 2Γ. Including more and more negative bonds, neighboring the previous ones, separates the two charges while remaining in the same charge sector. This spatial separation of the two initial charges disturbs the initial configuration along a string, as depicted in Fig. 3.2. If one defines the string length between the two charges as ℓ, then the separation energy can be expressed via $\epsilon_\ell = 2\Gamma\ell$. By lowering Γ but remaining in the regime $\Gamma \gg \lambda$, the second term in the Hamiltonian (3.9) can be treated perturbatively. The σ^z operators will induce fluctuations. However, it does not change the charge sector as $\rho_{\mathbf{r}}$ commutes with the magnetic flux. Analogously, by inducing two spatially separated charges, one gets some insight on the effect of this perturbing term. Applying the plaquette operator

flips the σ^x variables around the plaquette. If now this happens on a plaquette adjacent to the separating string of the two charges, the string gets twisted, and its length is extended by 2ℓ, as shown in Fig. 3.2 on a square latte. On the one hand, this twisting gives an energy gain of λ by applying the plaquette term. On the other hand, it is punished by extending the length of the string. The separation energy of the two charges is usually expressed via $\epsilon_\ell = \sigma\ell$, where $\sigma = 2\Gamma - \mathcal{O}(\lambda/\Gamma)$ is called the string tension [14]. As long as the limit $\Gamma \gg \lambda$ is maintained, the term 2Γ will be the dominant contribution, and the energy cost of separating two charges grows monotonically. In this regime, charges are always confined to a local region. One speaks of the confining phase. The point in parameter space where $\sigma = 0$ marks a phase transition, which is exactly tractable [66, 35, 68].

3.2.2. Deconfining phase $\Gamma \ll \lambda$

In the opposite extreme where $\lambda \to \infty$ the first term of Eq. (3.9) becomes negligible. The ground state configuration is determined by a state in which all plaquettes are $\prod_\square \sigma^z_{\mathbf{r}\mathbf{r}'} = +1$. Yet this description does not lead to a unique configuration since the product of the bond variables, measured in the σ^z-basis, is positive if an even number of negative bonds are included. Following Kitaev's arguments on deriving the ground state [40] one picks the charge-free sector, $\rho_\mathbf{r} = +1$ for all $\mathbf{r}$. Because all charge sectors obey the same physics, this is a convenient choice since the absence of charges simplifies the analysis. The ground state has then to fulfill two criteria

$$\prod_\square \sigma^z_{\mathbf{r}\mathbf{r}'} |\Psi\rangle = |\Psi\rangle\,, \quad q_\mathbf{r} |\Psi\rangle = |\Psi\rangle\,, \quad \forall \square, \mathbf{r}. \tag{3.10}$$

A local constraint can formulate the charge condition: Every link is assigned an in-going or out-going arrow according to the σ^x values (measured in the corresponding σ^x basis). An arrow pointing in either positive x or y direction corresponds to $\sigma^x = +1$ whereas $\sigma^x = -1$ if it points in a negative direction. The charge condition requires an even number of in- and out-going arrows on every lattice site, as shown in the first row of Fig. 3.3. In the second row of Fig. 3.3 a different representation is constructed in which $\sigma^x = -1$ values are drawn by a blue lines on the lattice. Any configuration which fulfills the charge condition has to be represented by closed blue loops. Since no particular loop configuration can be preferred over the others, the ground state can be understood as a coherent superposition of all loop configurations. Sometimes this state is called a loop or string-net condensate [69, 11]. Acting on such a state with the operator $\prod_\square \sigma^z_{\mathbf{r}\mathbf{r}'}$ flips all arrows around the plaquette to the opposite direction, yielding a loop configuration in the other representation again. Therefore, the loop condensate is an eigenstate of the plaquette operator. Focusing on the charge sector with two test charges, in order to compare with the previous

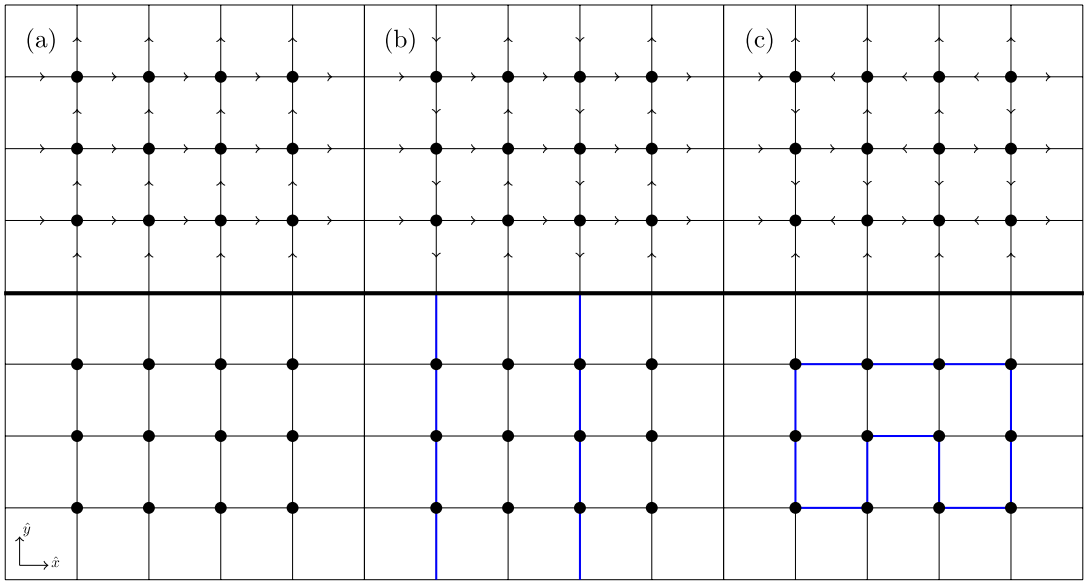

Figure 3.3.: Different ground state configurations (a)-(c) of the deconfining phase in the charge free sector. The first row shows the configuration in the arrow representaion the second row corresponds to a presentation for which $\sigma^x_{\mathbf{r}\mathbf{r}'} = -1$ bonds are colored in blue. In the later representation valid configuration must contain closed loops as shown in (c). Note that these loops can extend to infinity as illustrated in (b).

case, shows that a superposition of loop configurations can equally describe the ground state configuration for this sector with the difference that one open string, connecting the two test charges, is included. In the superposition, this string can have any possible length, and one concludes that there is no confinement of charges. Evidently, this phase is called the deconfining phase. An excitation in this phase is induced by a single bond flip $\sigma^z_{\mathbf{r}_0\mathbf{r}_1} \to -1$, creating two frustrated plaquettes. These objects are the discrete version of vortices in the $U(1)$ theory, and sometimes called visons [30]. Analog to the charge excitation in the confining phase, these flux excitations can be separated by further flipping adjacent bonds.

Keeping $\Gamma \ll \lambda$ the electric term can be added perturbatively. One finds that the strength of an induced effective interaction between charges exponentially decays with the distance between the charges such that the deconfining property remains robust[14].

3.2.3. Topological ground state degeneracy

The deconfined phase has an additional property, which is remarkable. If the system is considered on a topologically non-trivial object, a torus, for instance, one finds that different low-energy sectors cannot be mutually connected by any local operation.

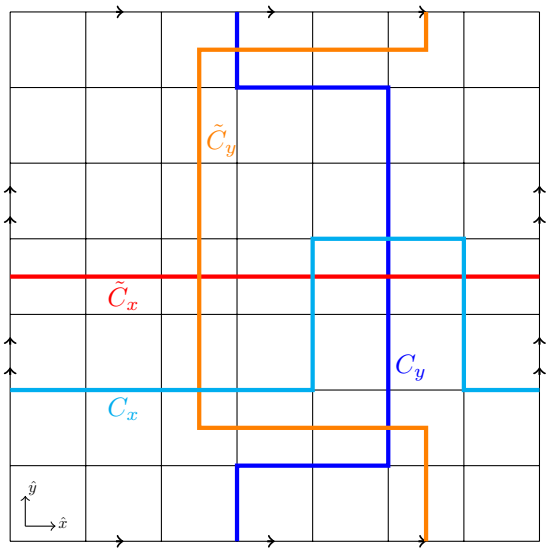

Figure 3.4: Different non-contractible loops on a torus. The arrows indicate which edges have to be identified. The loops $\tilde{C}$ live on the dual lattice and define the 't Hooft operators V_x and V_y. The corresponding operation on the original lattice is given by all $\sigma^x_{\mathbf{rr}'}$ for which $\mathbf{r}' - \mathbf{r}$ is intersected by the loop. The loops C correspond to the operator W_x and W_y. Their action applies $\sigma^z_{\mathbf{rr}'}$ on all links which belong to the respective loop.

The reason for this lies in the fact that in addition to the local gauge operators, other operators exist which commute with the Hamiltonian. These operators are given on a torus by

$$V_x = \prod_{\tilde{C}_x} \sigma^x_{\mathbf{rr}'}, \quad V_y = \prod_{\tilde{C}_y} \sigma^x_{\mathbf{rr}'}, \tag{3.11}$$

where and $\tilde{C}_x$, $\tilde{C}_y$ denote non-contractible loops along one direction of the torus on the dual lattice as illustrated in Fig. 3.4. These operators are sometimes referred to as 't Hooft loop operators. The sites of the dual lattice are defined on the centers of the plaquettes of original lattice [14]. The operation $\prod_{\tilde{C}_x} \sigma^x_{\mathbf{rr}'}$ means that $\sigma^x_{\mathbf{rr}'}$ acts on every link of the original lattice which is intersected by the loop of the dual lattice. Since these operators form closed loops, they always act on two edges of every plaquette. Thus one finds that $[V_x, H] = [V_y, H] = 0$. In the confining phase, it was argued that the ground state is given by $\sigma^x_{\mathbf{rr}'} = +1$ on all bonds. This is fine for $V_x = V_y = +1$. However, to have, for instance, $V_x = -1$, at least one bond must be negative; such a configuration receives an energetic penalty of large Γ. Therefore, it cannot be degenerate with the ground state. Things are different in the deconfined phase. Defining operators which measure a $\mathbb{Z}_2$ flux through the holes of the torus as

$$W_x = \prod_{C_x} \sigma^z_{\mathbf{rr}'}, \quad W_y = \prod_{C_y} \sigma^z_{\mathbf{rr}'}, \tag{3.12}$$

where C_x, C_y define non-contractible loops, this time, on the original lattice. One can easily show that the V and W operators anti-commute for different directions, and commute for the same direction

$$\{W_x, V_y\} = \{W_y, V_x\} = [W_x, V_x] = [W_y, V_y] = 0. \tag{3.13}$$

In the limit $\Gamma = 0$ one finds that the ground state Eq. (3.10) is an eigenstate $W_{x,y} |\Psi\rangle = \pm |\Psi\rangle$. The state $V_x |\Psi\rangle$ is an eigenstate of W_y with the opposite eigenvalue. Yet $V_x |\Psi\rangle$ is degenerate with the ground state. Similarly, $V_y |\Psi\rangle$ and $V_y V_x |\Psi\rangle$ are degenerate with the ground state, but can be distinguished according to their eigenvalues of W_x, W_y. Therefore, the ground state on the torus is fourfold degenerate, while each state corresponds to the presence or absence of a $\mathbb{Z}_2$ flux through the holes of the torus. One can construct linear combinations $(1 \pm V_x) |\Psi\rangle$ and $(1 \pm V_y) |\Psi\rangle$, which have eigenvalues $V_x = \pm 1$ and $V_y = \pm 1$, in contrast to the confining phase. If $0 < \Gamma \ll \lambda$, these states are no longer degenerate. Yet the splitting in energy is exponentially suppressed $\sim e^{-|\ln \Gamma| L}$ where L is one of the circumferences of the torus [14]. Importantly, there are no local operators that could induce tunneling from one state to another. Such an operation has to wind around the entire torus. This robustness may be an important ingredient to build a quantum computer, and it sparked a great interest in studying $\mathbb{Z}_2$ quantum spin liquids.

3.3. Concluding remarks

The previous analysis results can be summarized in a phase diagram of the two dimensional $\mathbb{Z}_2$ theory, which is shown in Fig. 3.5. The discerning quantity is the string tension σ, a function of the couplings λ/Γ. The two different phases can be interpreted in the context of quantum spin liquids as follows: The deconfining phase corresponds to one phase for which spinons exists as fractionalized spin$-1/2$ excitations. The confining phase is characterized by spin-1 excitations, also called magnons or spin-waves. Contrarily, the two-dimensional $U(1)$ lattice gauge theory has only a single confining phase, as shown in Fig. 3.5 [70, 68, 14]. Note that this prohibits the existence of a spin liquid phase only in the pure gauge theory Eq. 3.7. In a theory where also matter degrees of freedom enter the effective low-energy description, it is still not known what the exact phase diagram looks like. Some studies suggest that it could be possible that deconfinement appears despite a gauge field of a $U(1)$ type. Other studies say the converse [71, 72, 73, 74, 75]. However, this ongoing debate will not be answered in this thesis.

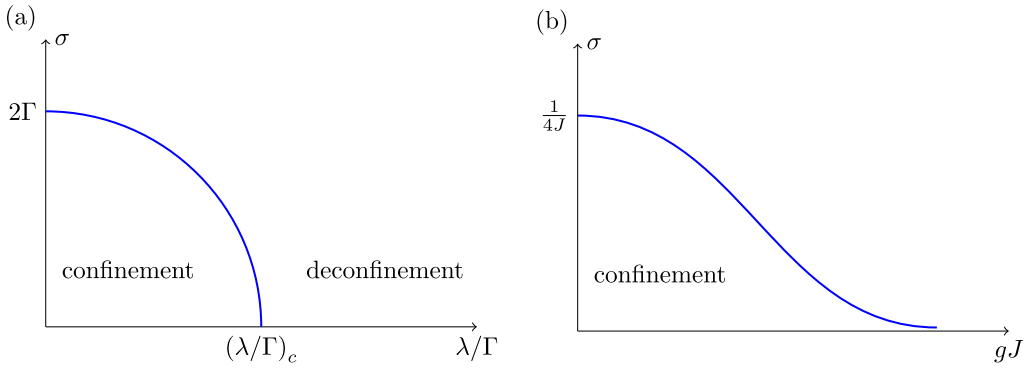

Figure 3.5.: Phase diagram for the $\mathbb{Z}_2$ and $U(1)$ lattice gauge theories in two dimensions. (a) string tension σ as a function of the coupling strength λ/Γ for the $\mathbb{Z}_2$ lattice gauge theory Eq. (3.9). Two different phases exist which are separated by a phase transition occurring at $(\lambda/\Gamma)_c$. (b) shows the string tension σ as a function of the coupling strength gJ for the $U(1)$ lattice gauge theory Eq. (3.7). Only one phase exist in which charges are in a confining potential.

4. Projective symmetry groups (PSG)

In Chapter 2, it was explained that writing the spin problem in a fermionic representation incorporates a redundancy that is manifested by a class of transformations that leave the physical state vector invariant. In this chapter, a different type of transformation is taken into account. These transformations explicitly change the state vectors and can be very useful to reduce the problem's complexity. If such a transformation relates two different state vectors, one speaks of a symmetry. Symmetry transformations can be understood as groups and have been exhaustively studied in mathematics, yielding large machinery called group theory from which especially the sub-field representation theory is of major interest for physics. Scrutinizing the symmetries of a system and, in particular, what happens if these symmetries are broken has been a compelling strategy. This method has been applied in literally every domain of theoretical physics in the last century [76, 77, 62, 63]. Therefore, it might be worth investigating the ramifications that arise due to a redundancy in the description and how symmetry and gauge transformation mutually affect each other. Yet, there is another interesting point that will be addressed. If one wants to study systems like quantum spin liquids that do not break any symmetry, the usual classification scheme proposed by Lev Landau is futile. It turns out that for these cases replacing the group structure by a projective group structure can be very helpful. This group extension leads to the entirely new concept of topological order or quantum order, which can then be used to classify different quantum states. These advances were mostly developed by Xiao-Gang Wen [67, 5, 10].

In Chapter 2, it was further argued that in the case that the emergent gauge field has an excitation gap, one can rely on the results of zeroth-order mean-field theory as an effective low-energy description. The projective symmetry description provides a framework to systematically study which saddle-points the emergent fields exhibit an excitation gap.

4.1. Extension of the symmetry group

As explained in Chapter 2 gauge transformations act as $\Psi_{\mathbf{r}} \to W_{\mathbf{r}}\Psi_{\mathbf{r}}$ on a spinor $\Psi_{\mathbf{r}}$, with $W_{\mathbf{r}} \in SU(2)$, which can equivalently be formulated as the action on the auxiliary fields (2.17) as $u_{\mathbf{r}\mathbf{r}'} \to W_{\mathbf{r}} u_{\mathbf{r}\mathbf{r}'} W_{\mathbf{r}}^{\dagger}$. These simultaneous transformations leave the spin operator and thus the Heisenberg Hamiltonian invariant and hence

do not change the physical content of the theory. This does not hold any longer as soon as the auxiliary field takes a static value such that the operator matrix is replaced by a complex matrix $u^0_{\mathbf{rr'}}$, which is what happens in mean-field theory. The gauge transformation then acts solely on the spinor. The Hamiltonian is only invariant if $W^\dagger_{\mathbf{r}} u^0_{\mathbf{rr'}} W_{\mathbf{r'}} = u^0_{\mathbf{rr'}}$. Any generic mean-field matrix does not commute $u^0_{\mathbf{rr'}} \neq W^\dagger_{\mathbf{r}} u^0_{\mathbf{rr'}} W_{\mathbf{r'}}$ for arbitrary $W_{\mathbf{r}} \in SU(2)$. However, a subgroup might exist $\mathcal{G} \subset SU(2)$ for which the equality still holds. This subgroup is called the *invariant gauge group* (IGG) and is defined as

$$\mathcal{G} = \left\{ W_{\mathbf{r}} | W^\dagger_{\mathbf{r}} u^0_{\mathbf{rr'}} W_{\mathbf{r'}} = u^0_{\mathbf{rr'}}, \quad W_{\mathbf{r}} \in SU(2) \right\}. \tag{4.1}$$

These types of transformations are called pure gauge transformations. Note that this group has at least two elements since, besides the identity, $W_{\mathbf{r}} = -\tau^0$ for all sites $\mathbf{r}$ fulfills this relation.

The action of a given symmetry group of the underlying lattice $\mathcal{S}$ can be written as $\Psi_{\mathbf{r}} \to T(\Psi_{\mathbf{r}})$ or equivalently $u_{\mathbf{rr'}} \to T(u_{\mathbf{rr'}})$, where T is a group element of $\mathcal{S}$. Certainly, this prescription by itself is of minor value to study invariance properties of the Hamiltonian since one has the freedom to apply further gauge transformations. Combining these two operations yields what is called the *projective symmetry group* (PSG). In order to be invariant, a Hamiltonian, which shall be specified by its mean-field matrix $u^0_{\mathbf{rr'}}$ and a multiplier field $a^\mu_{\mathbf{r}} \sigma_\mu$, has to fulfill

$$\begin{aligned} &G^\dagger_{T(\mathbf{r})} u^0_{T(\mathbf{r})T(\mathbf{r'})} G_{T(\mathbf{r'})} = u^0_{\mathbf{rr'}}, \\ &G^\dagger_{T(\mathbf{r})} a^\mu_{T(\mathbf{r})} \sigma_\mu G_{T(\mathbf{r})} = a^\mu_{\mathbf{r}} \sigma_\mu, \quad G_{T(\mathbf{r}))} \in SU(2). \end{aligned} \tag{4.2}$$

The gauge transformations G_T are not unique as a transformation under any element of $\mathcal{G}$ also comply with Eq. (4.2). In fact, the invariance group is a normal subgroup [76] of the PSG, which allows a factorization according to

$$PSG = SG \ltimes IGG. \tag{4.3}$$

Since the IGG depends on a particular *Ansatz*, the PSG does so, too. This dependency allows to use PSGs to define an equivalence relation between different *Ansätze*. Thus *Ansätze* sharing the same PSG belong to an equivalence class. These classes are said to be universal in the sense that a stable *Ansatz* is robust against generic perturbations. One can now assign a quantum phase to each class. Similar to the symmetry protected topological phases (STP), these phases are protected by their PSG [11, 5]. This equivalence relation will be explained further in Chapter 5.

4.2. Invariance group and gauge fields

Unfortunately, the entire reasoning stems on the ground that the mean-field solution is a valid candidate. So far, no tool has been presented that could help to identify a

stable mean-field *Ansatz*. In fact, the IGG provides such a device. The elements of $\mathcal{G}$ generate the gauge fields under which the fluctuations transform. To make this statement more precise, assume that inside $\mathcal{G}$ a subgroup exists being parametrized by a compact value as it is the case for a $U(1)$ theory

$$\left\{ W_{\mathbf{r}} = e^{i\theta n_{\mathbf{r}}^{\mu}\sigma_{\mu}} | \quad \theta \in [0, 2\pi[\,, |\mathbf{n}| = 1 \right\} \subset \mathcal{G}. \tag{4.4}$$

Using the local $SU(2)$ gauge freedom it is possible to rotate the coordinate system of the spinor space on each site such that $G_{\mathbf{r}} W_{\mathbf{r}}^{(\theta)} G_{\mathbf{r}}^{\dagger} = e^{i\theta\sigma^3}$ with $G_{\mathbf{r}} \in SU(2)$. In this new gauge, a mean-field matrix transforms according to $u_{\mathbf{rr}'}^0 \to \tilde{u}_{\mathbf{rr}'}^0 = G_{\mathbf{r}} u_{\mathbf{rr}'}^0 G_{\mathbf{r}'}^{\dagger}$. To see what happens beyond the mean-field level fluctuations should be taken into account. As mentioned in Chapter 2 this can be achieved by replacing $u_{\mathbf{rr}'} = u_{\mathbf{rr}'}^0 e^{ia_{\mathbf{rr}'}\sigma^3}$, whereas for simplicity consider only fluctuations in the σ^3 direction. The gauged $\tilde{u}_{\mathbf{rr}'}$ then transforms under a local $U(1)$ transformation, which is parametrized by the elements of $\mathcal{G}$ as in Eq. (4.4), according to

$$\begin{aligned} \tilde{u}_{\mathbf{rr}'} &\to e^{i\theta_{\mathbf{r}}\sigma^3} \tilde{u}_{\mathbf{rr}'} e^{-i\theta_{\mathbf{r}'}\sigma^3} = e^{i\theta_{\mathbf{r}}\sigma^3} \tilde{u}_{\mathbf{rr}'}^0 e^{ia_{\mathbf{rr}'}\sigma^3} e^{-i\theta_{\mathbf{r}'}\sigma^3} = G_{\mathbf{r}} W_{\mathbf{r}}^{(\theta_{\mathbf{r}})} u_{\mathbf{rr}'}^0 G_{\mathbf{r}'}^{\dagger} e^{ia_{\mathbf{rr}'}\sigma^3} e^{-i\theta_{\mathbf{r}'}\sigma^3} \\ &= G_{\mathbf{r}} u_{\mathbf{rr}'}^0 W_{\mathbf{r}'}^{(\theta_{\mathbf{r}})} G_{\mathbf{r}'}^{\dagger} e^{ia_{\mathbf{rr}'}\sigma^3} e^{-i\theta_{\mathbf{r}'}\sigma^3} = \tilde{u}_{\mathbf{rr}'}^0 e^{i\theta_{\mathbf{r}}\sigma^3} e^{ia_{\mathbf{rr}'}\sigma^3} e^{-i\theta_{\mathbf{r}'}\sigma^3}. \end{aligned} \tag{4.5}$$

Is was used that $W_{\mathbf{r}}^{(\theta_{\mathbf{r}})} u_{\mathbf{rr}'}^0 = u_{\mathbf{rr}'}^0 W_{\mathbf{r}'}^{(\theta_{\mathbf{r}})}$, which is a consequence of $W_{\mathbf{r}}^{(\theta_{\mathbf{r}})}$ being a member of the IGG, and that $e^{i\theta_{\mathbf{r}}\sigma^3} G_{\mathbf{r}} = G_{\mathbf{r}} W_{\mathbf{r}}^{(\theta_{\mathbf{r}})}$, which follows from the special gauge that is used. Thus one finds the transformation rule $a_{\mathbf{rr}'} \to a'_{\mathbf{rr}'} = a_{\mathbf{rr}'} + \theta_{\mathbf{r}} - \theta_{\mathbf{r}'}$ for the fluctuations, which includes the elements of $\mathcal{G}$ [11, 5, 36]. The lesson to learn from this result becomes clear by realizing that the transformation Eq. (4.5) did not change anything on the mean-field level, as it is generated by the IGG, and both descriptions result the same physical state. Therefore, the resulting energies should be equal $E(u_{\mathbf{rr}'}^0, e^{ia_{\mathbf{rr}'}\sigma^3}) = E(u_{\mathbf{rr}'}^0, e^{i(a_{\mathbf{rr}'} + \theta_{\mathbf{r}} - \theta_{\mathbf{r}'})\sigma^3})$. Expanding both sides in $a_{\mathbf{rr}'}$ up to second order and comparing coefficients shows that $(a_{\mathbf{rr}'})^2$ has to vanish [5, 11]. Usually, quadratic terms couple to the mass, which means that these $a_{\mathbf{rr}'}$ fields have to be massless. Thus they participate in the low-energy regime of the system. One immediately sees that by restricting $\theta \in \{0, \pi\}$ the argument does not longer hold, and one expects the $a_{\mathbf{rr}'}$ field to become massive.

5. Algebraic PSGs

Projective symmetry groups provide a framework to classify symmetric quantum spin liquids according to a given symmetry group, similar to the ordinary symmetry classification. The main difference lies in the group extension, which carries over to the representations of the symmetry group. In order to find gauge inequivalent members of every class, it is necessary to identify representations of the projective symmetry group, which are not related by a gauge transformation. Each PSG representation then offers a way to construct a symmetric mean-field *Ansatz*, which according to its transformation properties, should differ from another mean-field *Ansatz* built upon a non-equivalent representation. Therefore, the equivalence relation can be defined as the transformation properties of a mean-field state, and a class representative is simply the constructed *Ansatz*. The set of gauge inequivalent PSG representations is sometimes called the algebraic PSG, and those that genuinely lead to distinct mean-field states are called the invariant PSG [5, 11].

This chapter will explain how algebraic PSGs are, in principle, derived for a given lattice. Lattices can be described through a symmetry group $\mathcal{S}$ which contains translation operators

$$T_\mu : \mathbf{r} \to \mathbf{r} + \hat{e}_\mu, \tag{5.1}$$

where $\mathbf{r}$ points on given site of the lattice and $\hat{e}_\mu$ denotes a Cartesian basis vector in direction μ, e.g. $\mu \in \{x, y, z\}$ in three dimensions. Furthermore, $\mathcal{S}$ includes a point group $\mathcal{O}$ whose elements act via linear transformations

$$O : \mathbf{r} \to M_O(\mathbf{r}), \tag{5.2}$$

here M_O denotes the matrix representation of the point group operator O. If it becomes clear from the context O and its representation, M_O will be denoted equally. Finally, time-reversal symmetry $\mathcal{T}$ shall be included, which, contrary to the other operators, acts via an anti-unitary operator directly on the Hilbert space. The extension of the symmetry group is considered to be $\mathcal{G} = \mathbb{Z}_2$. At the end of this chapter, it will also be considered how the entire theory differs if spin rotational symmetry is broken. It will be discussed in short how the decoupling changes by taking triplet channels into account. This further requires representations which explicitly act within the spin space.

5.1. Uniform gauge and lattice translations

In order to find the gauge inequivalent representations, it is first necessary to filter out the gauge freedom such that it becomes possible to determine true differences. This can be done by fixing the gauge, which means in particular to reduce the local freedom. Yet gauge fixing does not mean that further gauge transformations are forbidden. However, bookkeeping becomes possible as soon as some reference is assigned and usually later gauge transformations have a global effect. A particular gauge that turns out to be convenient is the uniform gauge. Here it will be explained for a three-dimensional cubic lattice. Before this gauge is explained any further, it is essential to see how the gauge part of a PSG representation changes under a pure gauge transformation. Assume that for a given symmetry operation, $G_O O$ is an element of the PSG, which means by definition (4.2) that[1]

$$G_O^\dagger(O(\mathbf{r}))u_{O(\mathbf{r})O(\mathbf{r}')}G_O(O(\mathbf{r})) = u_{\mathbf{r}\mathbf{r}'}. \tag{5.3}$$

If now two different $u_{\mathbf{r}\mathbf{r}'}$ are related by a gauge transformation $W_\mathbf{r}$ the G_O matrix transforms according to

$$G_O(\mathbf{r}) \to W^\dagger_{O^{-1}(\mathbf{r})}G_O(\mathbf{r})W_\mathbf{r}, \tag{5.4}$$

which can easily be verified by inserting identities $W^\dagger_{O(\mathbf{r})}W_{O(\mathbf{r})} = \mathbb{1}$ in Eq. (5.3), and using the invariance properties. Turning back to the uniform gauge in which one wants the gauge transformation belonging to translations G_{T_μ} to be as simple as possible, i.e. ideally, they are given by the unit matrix. In three dimensions, one starts the gauging process at a given site $\mathbf{r}_0 = (x_0, y_0, z_0)$. One seeks a gauge such that $\tilde{G}_{T_x}(\mathbf{r}_0) = \tau^0$, where τ^0 is the identity matrix. This operation fixes the gauge transformation on a neighboring site determined by Eq. (5.4) as

$$\begin{aligned}\tilde{G}_{T_x}(\mathbf{r}_0) &\stackrel{!}{=} \tau^0 = W^\dagger_{T_x^{-1}(\mathbf{r}_0)}G_{T_x}(\mathbf{r}_0)W_{\mathbf{r}_0} \\ &\implies W_{\mathbf{r}_0-\hat{e}_x} = G_{T_x}(\mathbf{r}_0)W_{\mathbf{r}_0}.\end{aligned} \tag{5.5}$$

Repeating this procedure n times, fixes the gauge transformation on the other sites to the left of $\mathbf{r}_0$ as $W_{\mathbf{r}_0-n\hat{e}_x} = G_{T_x}(\mathbf{r}_0-(n-1)\hat{e}_x)\dots G_{T_x}(\mathbf{r}_0)W_{\mathbf{r}_0}$. The inverse operation T_x^{-1} yields a similar result for all sites to the right of $\mathbf{r}_0$ such that for the entire line $\tilde{G}_{T_x}(x, y_0, z_0) = \tau^0$ is fixed. This exhausted the gauge freedom of all sites except for $W_{\mathbf{r}_0}$. The same procedure can be done for G_{T_y} for lines along the y-direction starting from an arbitrary point of the line $\mathbf{r}_1 = \{\mathbf{r}|(x, y_0, z_0), x \in \mathbb{Z}\}$. This assigns the gauge transformations $\tilde{G}_{T_y}(\mathbf{r}_2) = \tau^0$ in the plane $\mathbf{r}_2 = \{\mathbf{r}|(x, y, z_0), x, y \in \mathbb{Z}\}$.

[1] The superscript of $u^0_{\mathbf{r}\mathbf{r}'}$ is not indicated any longer and it is tacitly assumed to deal with mean-field matrices.

Finally, one fixes $\tilde{G}_{T_z}(\mathbf{r}) = \tau^0$ for the entire lattice by starting at given any point of the plane $\mathbf{r}_2$. Thus the entire lattice has been gauged besides the starting point $\mathbf{r}_0$. Therefore, the local gauge freedom has been reduced to a remaining global one $W_{\mathbf{r}_0}$. In the following all matrices are given in this gauge and the tilde will be omitted.

Having the gauge fixed, it remains to find the other representations matrices since so far only G_{T_z} is known for the entire lattice. The other representations can be found by identifying invariant elements of the PSG. These elements correspond to the stabilizer group of a lattice site. Sometimes this group is also called the little group; a term mostly used in the literature of relativistic quantum mechanics [62, 76]. Consider the operation $T_y T_z T_y^{-1} T_z^{-1} = id$, which follows a closed loop and yields an invariance condition for every lattice site. This condition requires that $G_{T_y} T_y G_{T_z} T_z T_y^{-1} G_{T_y}^{-1} T_z^{-1} G_{T_z}^{-1} \in \mathcal{G}$, which means for a representation that

$$\begin{aligned} &G_{T_y}(\mathbf{r}) G_{T_z}(\mathbf{r} - \hat{e}_y) G_{T_y}^{-1}(\mathbf{r} - \hat{e}_z) G_{T_z}^{-1}(\mathbf{r}) = \pm\tau^0 = \eta_{z_y}\tau^0 \\ &\implies G_{T_y}(\mathbf{r}) = \eta_{z_y} G_{T_y}(\mathbf{r} - \hat{e}_z), \end{aligned} \tag{5.6}$$

with $\eta_{z_y} = \pm 1$. The representations for lattice sites belonging to $\mathbf{r}_2$ have already been fixed, which means that $G_{T_y}(\mathbf{r}_2) = \tau^0 = \eta_{z_y} G_{T_y}(\mathbf{r}_2 - \hat{e}_z)$. Hence a valid representation is given by

$$G_{T_y}(\mathbf{r}) = \eta_{z_y}^{z_0+z} \tau^0, \tag{5.7}$$

which fulfills all necessary requirements. Similarly, one determines the representation of G_{T_x} by employing $T_x T_z T_x^{-1} T_z^{-1}$ and $T_x T_y T_x^{-1} T_y^{-1}$, which are again little group elements. This yields

$$G_{T_x}(\mathbf{r}) = \eta_{z_x}^{z_0+z} \eta_{y_x}^{y_0+y} \tau^0 \tag{5.8}$$

with two different sign parameters $\eta_{z_x} = \pm$ and $\eta_{z_y} = \pm$. The site $\mathbf{r}_0$ is arbitrary and, without loosing any generality, it can be chosen to be the origin. The PSG representations of the symmetry group $\mathcal{S} = \{T_x, T_y, T_z\}$ are then given by

$$G_{T_x}(\mathbf{r}) = \eta_{z_x}^z \eta_{y_x}^y \tau^0, \quad G_{T_y}(\mathbf{r}) = \eta_{z_y}^z \tau^0, \quad G_{T_z}(\mathbf{r}) = \tau^0, \quad \forall \mathbf{r}. \tag{5.9}$$

These representations are distinguished by the different $\eta = \pm 1$ values yielding $2^3 = 8$ different algebraic PSGs which are gauge inequivalent. The two dimensional case $\mathcal{S} = \{T_x, T_y\}$ can be obtained by setting $z = 0$ and neglecting the third generator T_z resulting in two distinct representations given by

$$G_{T_x}(\mathbf{r}) = \eta_{y_x}^y \tau^0, \quad G_{T_y}(\mathbf{r}) = \tau^0, \quad \forall \mathbf{r}. \tag{5.10}$$

5.2. Point group and time-reversal symmetry

Until now, the symmetry group does not contain any point group elements. However, for most lattices, such point group elements have to be taken into account; see for instance Appendix A.1, where the point group generators of the square lattice are given or in Chapter 9 where some three-dimensional lattices and their corresponding points groups are shown. These additional group elements need their projective representations, which can be derived by the same procedure as the translations that were not fixed by the local gauge transformations. One identifies little group elements of a given site $\mathbf{r}$ by successively applying symmetry operations starting and ending at this site. These operations then form closed paths, which lead to conditions on the representations. Starting the path with one particular point group generator O followed by a translation T_μ yields an equation that relates the representation $G_O(\mathbf{r})$ with one of its neighbors $G_O(\mathbf{r}+\hat{e}_\mu)$. Repeating this step with all other translations gives a set of equations determining the translation properties of representation G_O.

To make this procedure more concrete consider as an example a rotation of 120° around the $(1,1,1)$-axis, which belongs in the point group of cubic crystal systems. This rotation acts by permuting the entries of $\mathbf{r}$

$$P : \mathbf{r} = (x, y, z) \to (z, x, y) \tag{5.11}$$

One little group element is $PT_xP^{-1}T_y^{-1}$ requiring that

$$G_P P G_{T_x} T_x P^{-1} G_P^{-1} T_y^{-1} G_{T_y}^{-1} \in \mathcal{G}. \tag{5.12}$$

This further leads to

$$\begin{aligned} &G_P(x,y,z)G_{T_x}(y,z,x)G_P^{-1}(x,y-1,z)G_{T_y}^{-1}(x,y,z) = \eta_{y_P}\tau^0 \\ \implies\ &G_P(x,y,z) = \eta_{y_x}^z \eta_{z_x}^x \eta_{z_y}^z \eta_{y_P} G_P(x,y-1,z), \end{aligned} \tag{5.13}$$

where the gauge transformations (5.9) were used. Similarly, one finds for the other directions

$$G_P(x,y,z) = \eta_{z_x}^z \eta_{y_x}^y \eta_{x_P} G_P(x-1,y,z) \tag{5.14}$$

$$G_P(x,y,z) = \eta_{z_y}^x \eta_{z_P} G_P(x,y,z-1). \tag{5.15}$$

To find a closed solution of $G_P(x,y,z)$, one creates all possible elementary loops around the origin employing the translational conditions. These loops dictate some

consistency conditions:

$$\begin{aligned}
G_P(0,0,0) &= \eta_{x_P} G_P(1,0,0) \\
G_P(1,0,0) &= \eta_{z_x}\eta_{y_P} G_P(1,1,0) = \eta_{x_P} G_P(0,0,0) \\
G_P(1,1,0) &= \eta_{y_x}\eta_{x_P} G_P(0,1,0) = \eta_{z_x}\eta_{y_P}\eta_{x_P} G_P(0,0,0) \\
G_P(0,1,0) &= \eta_{y_P} G_P(0,0,0) = \eta_{y_x}\eta_{z_x}\eta_{y_P} G_P(0,0,0).
\end{aligned} \tag{5.16}$$

From the last equation it can be learned that $\eta_{y_x} = \eta_{z_x}$ to guarantee consistency of the representations. Taking the other directions into account reveals that all parameters have to be equal $\eta_{y_x} = \eta_{z_x} = \eta_{z_y} \equiv \eta_X$. Any given loop operation can be decomposed into elementary loops[2] and, therefore, such an operation should be equivalent to the identity operation. Yet if all loops are identity operations, then there cannot be any path dependence. Hence one can get a solution for $G_P(\mathbf{r})$, with $\mathbf{r}$ arbitrary, by a successive application of elementary steps, starting from the origin for which $G_P(0,0,0) \equiv g_P$ with $g_P \in SU(2)$. Finally, one obtains the unique solution

$$G_P(\mathbf{r}) = \eta_X^{x(y+z)} \eta_{x_P}^x \eta_{y_P}^y \eta_{z_P}^z g_P. \tag{5.17}$$

Generally, site-dependent representations of the point group generators can be expressed in the form $G_O(\mathbf{r}) = \eta^{f(\mathbf{r})} g_O$, where $\eta = \pm 1$, $f(\mathbf{r})$ a local function, and a global matrix representation $g_O \in SU(2)$. These g_O are not general matrices as they have to fulfill some more conditions. One condition can be obtained by taking the point group generators' cyclic character into consideration since they form Z_n subgroups on their own. For example, P is a three-fold cyclic group with $P^3 = id$. This condition requires the matrix representation to cope with $g_P^3 = \pm\tau^0$. Furthermore, these matrix representations are specified by taking mutual commutation relation of the point group generators into account. In the example above, it was already encountered that the η sign factors of translations, initially independent, became dependent on each other after the point group generator P was incorporated into the symmetry group. This always happens when a generator is included in the group algebra that does not commute with other group elements, and it will usually affect the projective representations of the previously determined ones. The number of all independent algebraic relations of the matrix representations of the point group generators g_O times the number of independent sign factors η_O yields the number of algebraic PSGs.

Time-reversal symmetry $\mathcal{T}$ can also be included to $\mathcal{S}$. This operation is, however, special compared to the other group elements as it acts by an anti-unitary operator.

[2] Similar to the principle behind Stokes' theorem

On the physical spin operator $\mathbf{S_r}$ it acts according to

$$\mathcal{T} : \mathbf{S_r} \to -\mathbf{S_r}, \tag{5.18}$$

which is readily verified by recalling that the spin can be interpreted as an internal angular momentum $\mathbf{r} \times \mathbf{p}$. In the fermionic spin-1/2 representation it is represented by an anti-untitary operator $\kappa\mathcal{U}$ with κ denoting the operator of a complex conjugation $\kappa : i \to -i$ and $\mathcal{U}$ a unitary transformation [78]. Thus it transforms the fermions as

$$\mathcal{T} : \begin{pmatrix} f_\uparrow \\ f_\downarrow \end{pmatrix} \to i\sigma^2 \begin{pmatrix} f_\uparrow \\ f_\downarrow \end{pmatrix}. \tag{5.19}$$

One sees that each fermion transforms as $\mathcal{T} : f_\uparrow \to f_\downarrow$ and $\mathcal{T} : f_\downarrow \to -f_\uparrow$. The action on a spinor $\psi_\mathbf{r} = (f_{\mathbf{r}\uparrow}, f^\dagger_{\mathbf{r}\downarrow})^T$ is then given as

$$\mathcal{T} : \psi_\mathbf{r} \to i\tau^2\kappa\psi_\mathbf{r}. \tag{5.20}$$

It is then convenient to chose a global gauge, which transforms $\psi_\mathbf{r} \to i\tau^2\psi_\mathbf{r}$. In this gauge time-reversal acts on the spinor as a simple complex conjugation $\mathcal{T} : \psi_\mathbf{r} \to (\psi_\mathbf{r})^*$. This has the advantage that it commutes with other gauge transformations [11, 61]. Time-reversal acts then on a mean-field matrix or a multiplier field according to

$$\mathcal{T} : u_{\mathbf{r}\mathbf{r}'} \to -u_{\mathbf{r}\mathbf{r}'} \tag{5.21}$$

$$\mathcal{T} : a_\mu(\mathbf{r})\tau^\mu \to -a_\mu(\mathbf{r})\tau^\mu. \tag{5.22}$$

This leads to a condition on the PSG elements

$$-G^\dagger_\mathcal{T}(\mathbf{r})u_{\mathbf{r}\mathbf{r}'}G_\mathcal{T}(\mathbf{r}) = u_{\mathbf{r}\mathbf{r}'}, \tag{5.23}$$

which differs by a sign compared to the usual PSG equations given in Eq. (5.3). The determination of the site-dependent representations for time-reversal can be achieved in the same way as for the other point group generators.

In Chapter 9, this procedure is further explained as it is used to determine the projective representations for several three-dimensional lattices.

5.3. Flux operator and invariance group

Once the projective representations are determined it is possible to construct a mean-field *Ansatz*, whose projected wave function respects all required symmetries, and thus might be a valid candidate describing a symmetric quantum spin liquid state. To avoid a complicated analysis concerning the stability of such an *Ansatz*, the

constructions in this work are all based upon a $\mathbb{Z}_2$ invariant subgroup, which can be related to gapped excitations of the emergent gauge field, as explained in Chapter 4. Yet there is one caveat. The constructed mean-field state can, nevertheless, belong to a larger invariance subgroup [5, 11]. In fact, the analytic form of a mean-field matrix $u_{\mathbf{r}\mathbf{r}'}$ cannot reveal anything about the underlying gauge group, as it obviously depends on the chosen gauge. However, some quantities can be made of these matrices called flux operators or Wilson loop operators defined as [23, 22]

$$P_{\mathbf{r}} = \prod_{\square} u_{\mathbf{r}\mathbf{r}'} = u_{\mathbf{r}\mathbf{r}_1} u_{\mathbf{r}_1\mathbf{r}_2} \dots u_{\mathbf{r}_{N-1}\mathbf{r}}, \tag{5.24}$$

with $\square$ denoting a closed path. Note the analogy to the flux terms that were introduced in Chapter 3. These operators transform under a gauge transformation $P_{\mathbf{r}} \to W_{\mathbf{r}}^{\dagger} P_{\mathbf{r}} W_{\mathbf{r}}$, which is a recognizable similarity transformation. It follows that the spectrum of these operators remains untouched; hence their determinant and trace are gauge invariant quantities. These operators are also subjects to a consistency condition, which can be stated as follows: Using the defining invariance equation of $\mathcal{G}$, which can be written as $W_{\mathbf{r}} = u_{\mathbf{r}\mathbf{r}_1} W_{\mathbf{r}_1} u_{\mathbf{r}\mathbf{r}_1}^{-1}$ or similarly on a neighboring site as $W_{\mathbf{r}_1} = u_{\mathbf{r}_1\mathbf{r}_2} W_{\mathbf{r}_2} u_{\mathbf{r}_1\mathbf{r}_2}^{-1}$, etc., one finds for a closed loop that

$$\begin{aligned} W_{\mathbf{r}} &= u_{\mathbf{r}_1\mathbf{r}_2} \dots u_{\mathbf{r}_{N-1}\mathbf{r}} W_{\mathbf{r}} (u_{\mathbf{r}_1\mathbf{r}_2} \dots u_{\mathbf{r}_{N-1}\mathbf{r}})^{-1} = P_{\mathbf{r}} W_{\mathbf{r}} P_{\mathbf{r}}^{-1} \\ &\implies [W_{\mathbf{r}}, P_{\mathbf{r}}] = 0. \end{aligned} \tag{5.25}$$

Since this should be true for any closed loop, it follows that a local gauge transformation must commute with all possible $P_{\mathbf{r}}$ operators. This condition can be used to determine the proper invariance group of an *Ansatz*, which is given by the smallest subgroup $\mathcal{G} \subset SU(2)$, such that $W_{\mathbf{r}} \in \mathcal{G}$ commutes with all possible flux operators for all $\mathbf{r}$. Since these operators inherit their translational transformation rules from the underlying $u_{\mathbf{r}\mathbf{r}'}$ matrices, it becomes trivial in the unitary gauge to determine $P_{\mathbf{r}'}$ for $\mathbf{r}' \neq \mathbf{r}$ as soon as $P_{\mathbf{r}}$ is known. It remains to check all possible $P_{\mathbf{r}}$ for one particular site. Again, this problem can be reduced, as one seeks to understand if and how these operators restrain the form of $W_{\mathbf{r}}$. A convenient representation for $SU(2)$ matrices is given by $W_{\mathbf{r}} = \alpha_0 \tau^0 + i\boldsymbol{n}\boldsymbol{\tau}$. Here $\boldsymbol{\tau}$ is the Pauli vector and $\boldsymbol{n} = (\alpha_1, \alpha_2, \alpha_3)$. The coefficients are real and normalized such that $\sum_{i=0}^{3} \alpha_i^2 = 1$. In order to reduce this form, such that $W_{\mathbf{r}} \in \mathbb{Z}_2$, the vector term has to vanish $\boldsymbol{n} \stackrel{!}{=} 0$. The flux operator appears in two different guises $P_{\mathbf{r}}^{(o)} = ip_0\tau^0 + \boldsymbol{p}\boldsymbol{\tau}$ or $P_{\mathbf{r}}^{(e)} = q_0\tau^0 + i\boldsymbol{q}\boldsymbol{\tau}$ which can be verified using an expanded form of the mean-field matrices $u_{\mathbf{r}\mathbf{r}'} = ia_0\tau^0 + \boldsymbol{a}\boldsymbol{\tau}$. The label o corresponds to a loop containing an odd number of links and e to an even number. Note that all coefficients are real but contrary to the $SU(2)$ case, they are not subject to any normalization constraint. In these representations one easily sees that for $P^{(o)}$ the condition to break the invariance to $\mathbb{Z}_2$ is $\boldsymbol{p}\boldsymbol{n} = 0$. Analog for $P^{(e)}$

one finds $\boldsymbol{q} \times \boldsymbol{n} = 0$. Due to the symmetry constraints on the mean-field matrices, it is uncommon that a single loop operator already exists eliminating all necessary degrees of freedom of $\boldsymbol{n}$. In order for multiple different flux operators to break the invariance they have to be linearly independent such that $a_1\boldsymbol{p_1} + a_2\boldsymbol{p_2} + \ldots = 0$ is only true if $a_1 = a_2 = \ldots = 0$.

5.4. Broken spin-rotational symmetry

Until now, the entire discussion was based on decoupling in the singlet spin channel, i.e., all terms in the Hamiltonian are invariant under rotations in spin space. In a more realistic scenario, regarding real materials, one should include spin-orbit coupling terms, which will break this invariance. Such a decoupling of the triplet channels includes spin-dependent hopping- $(f^\dagger_{\mathbf{r}\uparrow}f_{\mathbf{r}'\uparrow} - f^\dagger_{\mathbf{r}\downarrow}f_{\mathbf{r}'\downarrow})$ and triplet pairing- $(f^\dagger_{\mathbf{r}\uparrow}f^\dagger_{\mathbf{r}'\downarrow} - f^\dagger_{\mathbf{r}\downarrow}f^\dagger_{\mathbf{r}'\uparrow})$ terms. These terms are still invariant under a $U(1)$ spin rotation. Spin-flip hopping- $(f^\dagger_{\mathbf{r}\alpha}f_{\mathbf{r}'\beta})$, with $\alpha \neq \beta$, and spin-polarized p-wave pairing- $(f^\dagger_{\mathbf{r}\alpha}f^\dagger_{\mathbf{r}'\alpha})$ terms break this invariance entirely. Starting from a generic model, a corresponding decoupling leads to a generalized mean-field matrix

$$\begin{aligned}\tilde{u}_{\mathbf{r}\mathbf{r}'} &= \begin{pmatrix} \left\langle f^\dagger_{\mathbf{r}\uparrow}f_{\mathbf{r}'\uparrow}\right\rangle & \left\langle f^\dagger_{\mathbf{r}\uparrow}f^\dagger_{\mathbf{r}'\downarrow}\right\rangle & \left\langle f^\dagger_{\mathbf{r}\uparrow}f_{\mathbf{r}'\downarrow}\right\rangle & -\left\langle f^\dagger_{\mathbf{r}\uparrow}f^\dagger_{\mathbf{r}'\uparrow}\right\rangle \\ -\left\langle f^\dagger_{\mathbf{r}\downarrow}f^\dagger_{\mathbf{r}'\uparrow}\right\rangle^* & -\left\langle f^\dagger_{\mathbf{r}\downarrow}f_{\mathbf{r}'\downarrow}\right\rangle^* & -\left\langle f^\dagger_{\mathbf{r}\downarrow}f^\dagger_{\mathbf{r}'\downarrow}\right\rangle^* & \left\langle f^\dagger_{\mathbf{r}\downarrow}f_{\mathbf{r}'\uparrow}\right\rangle^* \\ \left\langle f^\dagger_{\mathbf{r}\downarrow}f_{\mathbf{r}'\uparrow}\right\rangle & \left\langle f^\dagger_{\mathbf{r}\downarrow}f^\dagger_{\mathbf{r}'\downarrow}\right\rangle & \left\langle f^\dagger_{\mathbf{r}\downarrow}f_{\mathbf{r}'\downarrow}\right\rangle & -\left\langle f^\dagger_{\mathbf{r}\downarrow}f^\dagger_{\mathbf{r}'\uparrow}\right\rangle \\ \left\langle f^\dagger_{\mathbf{r}\uparrow}f^\dagger_{\mathbf{r}'\uparrow}\right\rangle^* & \left\langle f^\dagger_{\mathbf{r}\uparrow}f_{\mathbf{r}'\downarrow}\right\rangle & \left\langle f^\dagger_{\mathbf{r}\uparrow}f^\dagger_{\mathbf{r}'\downarrow}\right\rangle & -\left\langle f^\dagger_{\mathbf{r}\uparrow}f_{\mathbf{r}'\uparrow}\right\rangle^* \end{pmatrix} \\ &= \begin{pmatrix} u^s_{\mathbf{r}\mathbf{r}'} + u^{t_1}_{\mathbf{r}\mathbf{r}'} & u^{t_2}_{\mathbf{r}\mathbf{r}'} + u^{t_3}_{\mathbf{r}\mathbf{r}'} \\ -u^{t_2}_{\mathbf{r}\mathbf{r}'} + u^{t_3}_{\mathbf{r}\mathbf{r}'} & u^s_{\mathbf{r}\mathbf{r}'} - u^{t_1}_{\mathbf{r}\mathbf{r}'} \end{pmatrix}, \end{aligned} \tag{5.26}$$

which couples bilinears of the 4 dimensional spinors $\Psi_{\mathbf{r}} = (f_{\mathbf{r}\uparrow}, f^\dagger_{\mathbf{r}\downarrow}, f_{\mathbf{r}\downarrow}, -f^\dagger_{\mathbf{r}\uparrow})^T$. The 4×4 matrix can be rewritten in terms of 2×2 matrices with real parameters $\alpha, \beta, \gamma, \delta$, as it was done in the second line of Eq. (5.26). These 2×2 matrices are given by

$$\begin{aligned} u^s_{\mathbf{r}\mathbf{r}'} &= i\alpha^0_{\mathbf{r}\mathbf{r}'}\tau^0 + \sum_{i=1}^{3}\alpha^i_{\mathbf{r}\mathbf{r}'}\tau^i, \\ u^{t_1}_{\mathbf{r}\mathbf{r}'} &= \beta^0_{\mathbf{r}\mathbf{r}'}\tau^0 + i\sum_{i=1}^{3}\beta^i_{\mathbf{r}\mathbf{r}'}\tau^i, \\ u^{t_2}_{\mathbf{r}\mathbf{r}'} &= i\gamma^0_{\mathbf{r}\mathbf{r}'}\tau^0 + \sum_{i=1}^{3}\gamma^i_{\mathbf{r}\mathbf{r}'}\tau^i, \\ u^{t_3}_{\mathbf{r}\mathbf{r}'} &= \delta^0_{\mathbf{r}\mathbf{r}'}\tau^0 + i\sum_{i=1}^{3}\delta^i_{\mathbf{r}\mathbf{r}'}\tau^i. \end{aligned}, \tag{5.27}$$

where τ^i are the three Pauli matrices and τ^0 is the 2×2 identity matrix. Here $u^s_{\mathbf{rr'}}$ describes the singlet case, which was studied so far. $u^{t_1}_{\mathbf{rr'}}$ are triplet terms which are invariant under a $U(1)$ spin-rotation. The other triplet terms, that entirely break spin-rotational symmetry, are the off-diagonal elements $u^{t_2}_{\mathbf{rr'}}$ and $u^{t_3}_{\mathbf{rr'}}$. The decoupled mean-field Hamiltonian can be written as

$$H = \frac{1}{2}\sum_{(\mathbf{rr'})} \left(\Psi^\dagger_{\mathbf{r}} \tilde{u}_{\mathbf{rr'}} \Psi_{\mathbf{r'}} + H.c.\right) + \frac{1}{2}\sum_{\mathbf{r}}\sum_{i=1}^{3} a_l \Psi^\dagger_{\mathbf{r}} \left(\tau^0 \otimes \tau^i\right) \Psi_{\mathbf{r}}. \tag{5.28}$$

In order to find projective representations of these mean-field models, it is necessary to understand how gauge transformations act on the extended 4-dimensional spinor space. Note that the four-spinor can be decomposed as $\Psi_{\mathbf{r}} = (\psi_{\mathbf{r}}, i\tau^2\psi^*_{\mathbf{r}})$, with $\psi_{\mathbf{r}} = (f_{\mathbf{r}\uparrow}, f^\dagger_{\mathbf{r}\downarrow})^T$ the two-spinor whose transformation properties are known to be $\psi_{\mathbf{r}} \to W_{\mathbf{r}}\psi_{\mathbf{r}}$. Focusing on the lower two components which are related by time-reversal in its pristine form[3].

$$\begin{aligned}
\begin{pmatrix} f_\downarrow \\ -f^\dagger_\uparrow \end{pmatrix} &= \left[\left(i\tau^2 \begin{pmatrix} f_\uparrow \\ f^\dagger_\downarrow \end{pmatrix}\right)^T\right]^\dagger \to \left[\left(i\tau^2 W \begin{pmatrix} f_\uparrow \\ f^\dagger_\downarrow \end{pmatrix}\right)^T\right]^\dagger \\
&= \left[\left(f^\dagger_\uparrow, f_\downarrow\right) \underbrace{(-i)\tau^2 i\tau^2}_{\mathbb{1}} W^\dagger (-i)\tau^2\right]^T \\
&= \left[\left(f_\downarrow, -f^\dagger_\uparrow\right) \underbrace{i\tau^2 W^\dagger (-i)\tau^2}_{W^T}\right]^T = W \begin{pmatrix} f_\downarrow \\ -f^\dagger_\uparrow \end{pmatrix}.
\end{aligned} \tag{5.29}$$

Hence a gauge transformation in this basis is block diagonal, and given by

$$\Psi_{\mathbf{r}} \to \tilde{W}_{\mathbf{r}}\Psi_{\mathbf{r}} \quad \text{with} \quad \tilde{W}_{\mathbf{r}} = \begin{pmatrix} W_{\mathbf{r}} & 0 \\ 0 & W_{\mathbf{r}} \end{pmatrix}, \tag{5.30}$$

with $W_{\mathbf{r}} \in SU(2)$ a 2×2 matrix. Another important consequence of breaking spin-rotational symmetry is that terms describing the spin-orbit coupling can break a symmetry. Therefore, true invariance can only be guaranteed if a combined transformation on the lattice and the spin degree of freedom leaves the Hamiltonian invariant. This means that one has to find point group representations acting on the spin space. A rotation corresponding to an element of the symmetry group acts on the four-spinor as

$$\Psi_{\mathbf{r}} \to \mathcal{D}_{\mathcal{S}}\Psi_{\mathcal{S}(\mathbf{r})}. \tag{5.31}$$

[3]That means without changing the gauge (see Eq. (5.20)).

The structure of $\mathcal{D}_\mathcal{S}$ can be specified since the first and third component transform as regular spin-1/2 objects

$$\begin{pmatrix} f_\uparrow \\ f_\downarrow \end{pmatrix} \to \tilde{\mathcal{D}} \begin{pmatrix} f_\uparrow \\ f_\downarrow \end{pmatrix}, \tag{5.32}$$

with $\tilde{\mathcal{D}} = \begin{pmatrix} \gamma_1 & \gamma_2 \\ -\gamma_2^* & \gamma_1^* \end{pmatrix}$ with $\gamma_i \in \mathbb{C}$ and $|\gamma_| + |\gamma_2| = 1$. The remaining components transform as

$$\begin{aligned} \begin{pmatrix} f_\downarrow^\dagger \\ -f_\uparrow^\dagger \end{pmatrix} &= \left[\left(i\tau^2 \begin{pmatrix} f_\uparrow \\ f_\downarrow \end{pmatrix} \right)^T \right]^\dagger \to \left[\left(i\tau^2 \tilde{\mathcal{D}} \begin{pmatrix} f_\uparrow \\ f_\downarrow \end{pmatrix} \right)^T \right]^\dagger \\ &= \left[\left(f_\uparrow^\dagger, f_\downarrow^\dagger \right) \underbrace{i\tau^2(-i)\tau^2}_{\mathbb{1}} \tilde{\mathcal{D}}^\dagger i\tau^2 \right]^T \\ &= \left[\left(f_\downarrow^\dagger, -f_\uparrow^\dagger \right) \underbrace{(-i)\tau^2 \tilde{\mathcal{D}}^\dagger i\tau^2}_{\tilde{\mathcal{D}}^T} \right]^T = \tilde{\mathcal{D}} \begin{pmatrix} f_\downarrow^\dagger \\ -f_\uparrow^\dagger \end{pmatrix}. \end{aligned} \tag{5.33}$$

Thus the four dimensional representation can be decomposed

$$\mathcal{D} = \begin{pmatrix} \gamma_1 & 0 & \gamma_2 & 0 \\ 0 & \gamma_1 & 0 & \gamma_2 \\ -\gamma_2^* & 0 & \gamma_1^* & 0 \\ 0 & -\gamma_2^* & 0 & \gamma_1^* \end{pmatrix}. \tag{5.34}$$

The entries depend on the corresponding point group element. In Appendix A.1, the usual spin representations for the point group generators of the square lattice are given.

Including spin-rotations, the defining PSG equation becomes

$$\tilde{G}^\dagger_{\mathcal{S}(\mathbf{r})} \mathcal{D}^\dagger_\mathcal{S} \tilde{u}_{\mathcal{S}(\mathbf{r})\mathcal{S}(\mathbf{r}')} \mathcal{D}_\mathcal{S} \tilde{G}_{\mathcal{S}(\mathbf{r}')} = \tilde{u}_{\mathbf{r}\mathbf{r}'}. \tag{5.35}$$

Yet it turns out that the irreducible representations are unaffected by the spin rotations: Consider two elements of the point group, and for simplicity assume that they commute. $\mathcal{O}_{ab} = \mathcal{S}_a^{-1}\mathcal{S}_b^{-1}\mathcal{S}_a\mathcal{S}_b$ is hence an element of the invariance group which becomes

$$\begin{aligned} \mathcal{D}_{\mathcal{O}_{ab}} \tilde{G}_{\mathcal{O}_{ab}}(\mathbf{r}) = &\left(\tilde{G}_{\mathcal{S}_a}(\mathcal{S}_b^{-1}(\mathcal{S}_a(\mathcal{S}_b(\mathbf{r})))) \right)^\dagger \mathcal{D}^\dagger_{\mathcal{S}_a} \left(\tilde{G}_{\mathcal{S}_b}(\mathcal{S}_a(\mathcal{S}_b(\mathbf{r}))) \right)^\dagger \mathcal{D}^\dagger_{\mathcal{S}_b} \\ &\times \mathcal{D}_{\mathcal{S}_a} \tilde{G}_{\mathcal{S}_a}(\mathcal{S}_a(\mathcal{S}_b(\mathbf{r})) \mathcal{D}_{\mathcal{S}_b} \tilde{G}_{\mathcal{S}_b}(\mathcal{S}_b(\mathbf{r})) \end{aligned} \tag{5.36}$$

in terms of PSG elements. As spin rotations and gauge transformations do not act on the same subspace they commute which leads to

$$\begin{aligned}\mathcal{D}_{\mathcal{O}_{ab}}\tilde{G}_{\mathcal{O}_{ab}}(\mathbf{r}) =&\mathcal{D}^{\dagger}_{\mathcal{S}_a}\mathcal{D}^{\dagger}_{\mathcal{S}_b}\mathcal{D}_{\mathcal{S}_a}\mathcal{D}_{\mathcal{S}_b}\\ &\times\left(\tilde{G}_{\mathcal{S}_a}(\mathcal{S}_b^{-1}(\mathcal{S}_a(\mathcal{S}_b(\mathbf{r})))\right)^{\dagger}\left(\tilde{G}_{\mathcal{S}_b}(\mathcal{S}_a(\mathcal{S}_b(\mathbf{r}))\right)^{\dagger}\\ &\times\tilde{G}_{\mathcal{S}_a}(\mathcal{S}_a(\mathcal{S}_b(\mathbf{r}))\tilde{G}_{\mathcal{S}_b}(\mathcal{S}_b(\mathbf{r})).\end{aligned} \tag{5.37}$$

For the square lattice, it follows that, for all combinations, $\mathcal{D}_{\mathcal{O}_{ab}} = \mathcal{D}^{\dagger}_{\mathcal{S}_a}\mathcal{D}^{\dagger}_{\mathcal{S}_b}\mathcal{D}_{\mathcal{S}_a}\mathcal{D}_{\mathcal{S}_b} = \pm\mathbb{1}_{4\times4}$ [54]. Since a global sign factor is irrelevant, one concludes that the algebraic conditions, which define the PSG, are the same for the spin rotational symmetric and the broken case.

The derivation of the gauge inequivalent representations in the spin-rotational broken case follows the same scheme, as explained previously. In Appendix A.2, the relevant PSG equations are given, which are needed to construct the symmetric mean-field matrices used in Chapter 7. The entire projective symmetry group analysis for the square lattice with spin rotational symmetry broken is explained in Ref. [54].

6. Neutron scattering and dynamical structure factor

So far, much effort was made to develop a theoretical framework. In this regard, the following chapter digresses from the main route as some experimental concepts will be treated. These concepts are nevertheless important for any advancement of the physical understanding, which can only be achieved via a synthesis of theory and experimental evidence. From a theoretician's point of view, it is seemingly easy to write down a state which prevails from conventional ordering down to absolute zero temperature, but quantum spin liquids are notoriously hard to identify in an experiment. How is it possible to measure something absent? One way of doing so employs neutron scattering. Here it will be briefly explained what the measured quantities are and how to connect them to the theoretical framework, which was introduced in the previous chapters.

6.1. Neutron scattering experiments

As the name already suggests, neutrons are scattered at a sample of a given material in a neutron scattering experiment. This is schematically illustrated in Fig. 6.1. The reason to use neutrons is that any electrically charged projectile and electromagnetic radiation would immediately interact with the charged particles of the material itself. This causes two problems: These interactions shade the pristine properties that one seeks to understand, and secondly, the penetration depth is relatively short

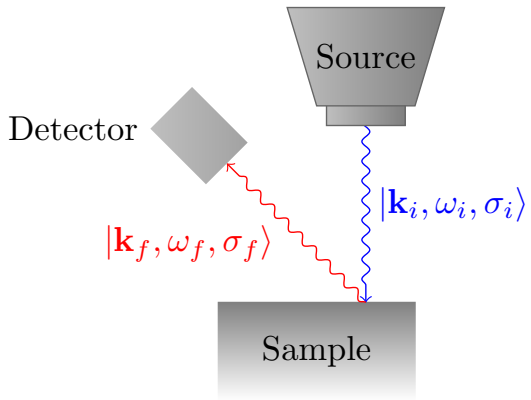

Figure 6.1: Schema of the experimental set up. The incoming neutron is initialized in the source with wave function $|\mathbf{k}_i, \omega_i, \sigma_i\rangle$, denoted in blue. After a scattering event occurred in the sample material the outgoing neutron, denoted in red, is specified by wave function $|\mathbf{k}_f, \omega_f, \sigma_f\rangle$ which is recorded in the detector.

such that only the interface of the sample is accessible. As in any other scattering experiment an initial state $|\mathbf{k}_i, \omega_i, \sigma_i\rangle$ prepared with momentum $\mathbf{k}$, energy ω, and a spin quantum number σ undergoes a transformation in the scattering process and the finial state $|\mathbf{k}_f, \omega_f, \sigma_f\rangle$ can be measured. This transformation can be described in terms of a time-dependent perturbation series induced by a scattering potential $V(\mathbf{r})$. The initial and final states are considered to be asymptotically free [62, 78, 2]. The difference in momenta, energy, and spin

$$\begin{aligned} \Delta\mathbf{q} &= \mathbf{k}_i - \mathbf{k}_f \\ \Delta E &= \frac{\hbar^2}{2m}\left(k_i^2 - k_f^2\right)^2 \\ \Delta\sigma &= \sigma_i - \sigma_f \end{aligned} \tag{6.1}$$

provide the information of the sample due to the conservation of energy and momentum. Here m denotes the neutron mass. Since neutrons are spin-1/2 particles, the transferred spin is integer-valued. In a real experiment, one fixes the wavelength of the incoming particle. The detecting apparatus is then adjusted such that it measures within a solid angle $\Delta\Omega$ the scattering angle and in a certain range ΔE the energy transfer. These quantities are combined in the partial differential cross-section

$$\frac{d^2\sigma}{d\Omega dE} = r_0^2 \frac{k_f}{k_i}\phi(\mathbf{q}, \omega, \sigma), \tag{6.2}$$

which measures the number of scattered neutrons into the solid angle $d\Omega$ in a range of energy $E + dE$ per seconds and per unit flux. The parameter r_0 gives a characteristic length scale and $\phi(\mathbf{q}, \omega, s)$ is a function that can be further specified [36, 78].

Two possible scattering events can occur. In the first one, the neutron is scattered at an atomic nucleus, e.g., phonon or Bragg scattering. The second event, which is of greater importance for the present discussion, describes the scattering by a magnetic moment or a spin. The relevant scattering potential can be described by a magnetic field $\mathbf{B}(t, \mathbf{r})$, which is induced by the orbital angular momentum and the spin of the sample. Yet as the experiment is measured in the momentum basis for which the potential becomes the Fourier transform $\mathbf{B}(\omega, \mathbf{q})$ some ramifications have to be taken into account. According to Maxwell's equation $\nabla\mathbf{B} = 0$, one finds that the Fourier transform has to be perpendicular to the scattering vector $\mathbf{q}$. Thus the neutrons can only resolve transversal components. To guarantee this analytically one can include an orientation factor that projects onto the perpendicular subspace $(\delta_{\alpha\beta} - \hat{q}_\alpha \hat{q}_\beta)$ where $\hat{\mathbf{q}} = \frac{\mathbf{q}}{|\mathbf{q}|}$ denotes a unit vector and α labels the different components. A second problem lies in the fact that the objects evoking the magnetic field are not fully localized, and the neutron is subject to a scattering density distribution. However, as shown by the Wigner-Eckart theorem, one can replace such a density distribution

by an effective point like field [36]. This leads to a modification that can be included by a magnetic form factor f, which depends on the type of atoms within the sample.

In order to relate to theoretical accessible quantities, one treats the magnetic field in linear response theory revealing the relevant correlation function [36, 2]

$$\mathcal{S}^{\alpha\beta}(\mathbf{q},\omega) = \int_{-\infty}^{\infty} \frac{dt}{2\pi} e^{i\omega t} \frac{1}{N} \sum_{\mathbf{r}\mathbf{r}'} e^{i\mathbf{q}(\mathbf{r}-\mathbf{r}')} \left\langle S^{\alpha}_{\mathbf{r}}(t) S^{\beta}_{\mathbf{r}'}(0) \right\rangle, \tag{6.3}$$

which is called the dynamical structure factor. In this equation $\mathbf{r}$ denote different lattice sites, N is the total number of sites, $\mathbf{S}$ represents the spin operator, and $\mathbf{q}, \omega$ is the energy and momentum of the incoming neutron. Taking further the additional orientation and form factor into account, one finds that the partial differential cross-section is given by [36]

$$\frac{d^2\sigma}{d\Omega dE} = r_0^2 \frac{k_f}{k_i} f(\mathbf{q})^2 \sum_{\alpha\beta} \left(\delta_{\alpha\beta} - \hat{q}_\alpha \hat{q}_\beta\right) \mathcal{S}^{\alpha\beta}(\mathbf{q},\omega). \tag{6.4}$$

The following theoretical discussions will, however, put more emphasis on the dynamical structure factor without modification. Yet comparing to real experimental data, these remarks should be kept in mind.

6.2. Dynamical structure factor

The dynamical structure factor can be calculated within the mean-field theory explained in Chapter 2. Without specifying a particular saddle-point, here it is assumed that the effective Hamiltonian has a generic form including hopping $\chi_{\mathbf{r}\mathbf{r}'}$ and pairing $\Delta_{\mathbf{r}\mathbf{r}'}$ amplitudes

$$H = \sum_{\mathbf{r}\mathbf{r}',\sigma,\sigma'} \left[\chi_{\mathbf{r}\mathbf{r}'} f^{\dagger}_{\mathbf{r}\sigma} f_{\mathbf{r}'\sigma} + \Delta^{*}_{\mathbf{r}\mathbf{r}'} f^{\dagger}_{\mathbf{r}\sigma} f^{\dagger}_{\mathbf{r}'\sigma'} \epsilon_{\sigma\sigma'} + H.c. \right]. \tag{6.5}$$

Defining a doublet via $\Psi_{\mathbf{r}} = (f_{\mathbf{r}\uparrow}, f^{\dagger}_{\mathbf{r}\downarrow})$ it can be written in compact form

$$H = \sum_{\mathbf{r}\mathbf{r}'} \Psi^{\dagger}_{\mathbf{r}} u_{\mathbf{r}\mathbf{r}'} \Psi_{\mathbf{r}'}. \tag{6.6}$$

The lattice might consists of multiple atoms within a unit cell and can be separated according to $\mathbf{r} = \mathbf{R} + \delta\mathbf{r}$, where the vectors $\mathbf{R}$ form a Bravais lattice and $\delta\mathbf{r}$ denotes the position within one unit cell. By Fourier transformation

$$\Psi^{\dagger}_{\mathbf{R},\delta\mathbf{r}} = \frac{1}{\sqrt{N_B}} \sum_{\mathbf{k}} e^{-i\mathbf{R}\mathbf{k}} \Psi^{\dagger}_{\mathbf{k},\delta\mathbf{r}}, \tag{6.7}$$

where N_B denotes the number of Bravais lattice sites, the Hamiltonian can be written in a block diagonal form

$$H = \sum_{\mathbf{k}} \sum_{\delta\mathbf{r}\delta\mathbf{r}'} \Psi^\dagger_{\mathbf{k},\delta\mathbf{r}} u_{\mathbf{k};\delta\mathbf{r},\delta\mathbf{r}'} \Psi_{\mathbf{k},\delta\mathbf{r}'}, \tag{6.8}$$

with $u_{\mathbf{k};\delta\mathbf{r},\delta\mathbf{r}'} = \sum_{\Delta_R} e^{i\Delta_R\mathbf{k}} u_{\Delta_R;\mathbf{r},\mathbf{r}'}$ and $\Delta_R = \mathbf{R}' - \mathbf{R}$. Each block can be further diagonalized by $\mathcal{D}_\mathbf{k} u_{\mathbf{k};\delta\mathbf{r},\delta\mathbf{r}'} \mathcal{D}^\dagger_\mathbf{k} = \xi_\mathbf{k}\delta_{\mathbf{r}\mathbf{r}'}$ yielding

$$H = \sum_{\mathbf{k},\delta\mathbf{r}} \xi_{\mathbf{k},\delta\mathbf{r}} \tilde{\Psi}^\dagger_{\mathbf{k},\delta\mathbf{r}} \tilde{\Psi}_{\mathbf{k},\delta\mathbf{r}}. \tag{6.9}$$

In order to derive the corresponding two-point correlator, it is convenient to choose an imaginary-time representation. The real-time representation can afterward be obtained by analytic continuation [2]. Going to momentum space the dynamical structure factor becomes

$$\mathcal{S}^{\alpha\beta}(\mathbf{q}, i\omega_n \to \omega + i\eta) = \int_{-\beta}^{\beta} d\tau e^{i\omega_n\tau} \frac{1}{N_u} \sum_{\delta\mathbf{r},\delta\mathbf{r}'} e^{i\mathbf{q}(\delta\mathbf{r}-\delta\mathbf{r}')} \left\langle S^\alpha_{-\mathbf{q},\delta\mathbf{r}}(\tau) S^\beta_{\mathbf{q},\delta\mathbf{r}'}(0) \right\rangle, \tag{6.10}$$

here N_u denotes the number of atoms in one unit cell. Using the parton mapping (2.2) of the spin operators the momentum space representation is found as

$$S^\alpha_{\mathbf{q},\delta\mathbf{r}} = \frac{1}{2\sqrt{N_B}} \sum_{\mathbf{k}} \left(f^\dagger_{\mathbf{k},\delta\mathbf{r},a} \sigma^\alpha_{ab} f_{\mathbf{k}+\mathbf{q},\delta\mathbf{r},b} \right). \tag{6.11}$$

In the following, it will be assumed that the system is invariant under rotations in spin space such that it suffices to consider the $\mathcal{S}^{zz}$ component of the spin-spin correlation function. After a Wick contraction and the neglect of constant terms, this correlator can be expressed by

$$\left\langle S^z_{-\mathbf{q},\delta\mathbf{r}}(\tau) S^z_{\mathbf{q},\delta\mathbf{r}'}(0) \right\rangle = -\frac{1}{4} \sum_{\mathbf{k}} \mathrm{Tr} \left\{ \bar{\bar{\mathcal{G}}}_{\delta\mathbf{r},\delta\mathbf{r}'}(\mathbf{k},\tau) \bar{\bar{\mathcal{G}}}_{\delta\mathbf{r}',\delta\mathbf{r}}(\mathbf{k}+\mathbf{q},-\tau) \right\}. \tag{6.12}$$

Here Nambu-Green's functions were used

$$\begin{aligned} \bar{\bar{\mathcal{G}}}_{\delta\mathbf{r},\delta\mathbf{r}'}(\mathbf{k},\tau) &= -\left\langle T_\tau \Psi_{\mathbf{k},\delta\mathbf{r}}(\tau) \Psi^\dagger_{\mathbf{k},\delta\mathbf{r}'}(0) \right\rangle \\ &= \begin{pmatrix} \mathcal{G}_{\delta\mathbf{r},\delta\mathbf{r}',\uparrow\uparrow}(\mathbf{k},\tau) & \mathcal{F}_{\delta\mathbf{r},\delta\mathbf{r}',\uparrow\downarrow}(-\mathbf{k},\tau) \\ \mathcal{F}^*_{\delta\mathbf{r},\delta\mathbf{r}',\downarrow\uparrow}(\mathbf{k},\tau) & \mathcal{G}^*_{\delta\mathbf{r},\delta\mathbf{r}',\downarrow\downarrow}(-\mathbf{k},\tau) \end{pmatrix}, \end{aligned} \tag{6.13}$$

T_τ denotes the time ordering operator, the simple Green's function is defined as

$$\mathcal{G}_{\delta\mathbf{r},\delta\mathbf{r}',\uparrow\uparrow}(\mathbf{k},\tau) = -\left\langle T_\tau f_{\mathbf{k},\delta\mathbf{r},\uparrow}(\tau) f^\dagger_{\mathbf{k},\delta\mathbf{r}',\uparrow}(0) \right\rangle \tag{6.14}$$

and the anomalous Green's function as

$$\mathcal{F}^{*}_{\delta\mathbf{r},\delta\mathbf{r}',\downarrow\uparrow}(\mathbf{k},\tau) = -\left\langle T_\tau f^{\dagger}_{-\mathbf{k},\delta\mathbf{r},\downarrow}(\tau) f^{\dagger}_{\mathbf{k},\delta\mathbf{r}',\uparrow}(0)\right\rangle. \tag{6.15}$$

Choosing the basis Eq. (6.9), in which the Hamiltonian becomes diagonal, yields

$$\bar{\bar{\mathcal{G}}}_{\delta\mathbf{r},\delta\mathbf{r}'}(\mathbf{k},\tau) = \mathcal{D}^{\dagger}_{\mathbf{k}}\tilde{\mathcal{G}}(\mathbf{k},\tau)\delta_{\delta\mathbf{r},\delta\mathbf{r}'}\mathcal{D}_{\mathbf{k}}. \tag{6.16}$$

$\tilde{\mathcal{G}}(\mathbf{k},\tau)$ is now diagonal and can be further evaluated by taking the imaginary time derivative which yields

$$\partial_\tau \tilde{\mathcal{G}}_{\delta\mathbf{r},\delta\mathbf{r}}(\mathbf{k},\tau) = -\,\delta(\tau)\left\langle \tilde{\Psi}_{\mathbf{k},\delta\mathbf{r}}(\tau)\tilde{\Psi}^{\dagger}_{\mathbf{k},\delta\mathbf{r}}(0)\right\rangle - \Theta(\tau)\left\langle \left[H, \tilde{\Psi}_{\mathbf{k},\delta\mathbf{r}}\right](\tau)\tilde{\Psi}^{\dagger}_{\mathbf{k},\delta\mathbf{r}}(0)\right\rangle. \tag{6.17}$$

The commutator can be easily evaluated using Eq. (6.9) as

$$\left[H, \tilde{\Psi}_{\mathbf{k},\delta\mathbf{r}}\right](\tau) = -\xi_{\mathbf{k},\delta\mathbf{r}}\tilde{\Psi}_{\mathbf{k},\delta\mathbf{r}}(\tau). \tag{6.18}$$

The last two results and a transformation into Matsubara frequency space can be used to derive the spin-spin correlator as [79, 2]

$$\begin{aligned}&\frac{1}{\beta}\sum_{\mathbf{k},i\Omega_n}\mathrm{Tr}\left\{\bar{\bar{\mathcal{G}}}_{\delta\mathbf{r},\delta\mathbf{r}'}(\mathbf{k},i\Omega_n)\bar{\bar{\mathcal{G}}}_{\delta\mathbf{r}',\delta\mathbf{r}}(\mathbf{k}+\mathbf{q},i\omega_n+i\Omega_n)\right\}e^{i\Omega_n\eta} \qquad (6.19)\\ =&\frac{N_B}{\beta}\sum_{i\Omega_n}\int\frac{d^2k}{(2\pi)^2}\mathrm{Tr}\left\{\mathcal{D}^{\dagger}_{\mathbf{k}}\tilde{\mathcal{G}}(\mathbf{k},i\Omega_n)\mathcal{D}_{\mathbf{k}}\mathcal{D}^{\dagger}_{\mathbf{k}+\mathbf{q}}\tilde{\mathcal{G}}(\mathbf{k}+\mathbf{q},i\Omega_n+i\omega_n)\mathcal{D}_{\mathbf{k}+\mathbf{q}}\right\}e^{i\Omega_n\eta}.\end{aligned}$$

The sum over the Matsubara frequencies in this expression can be evaluated using

$$\frac{1}{\beta}\sum_{i\Omega_n} f(i\Omega_n)e^{i\Omega_n\eta} = \sum_j \operatorname*{Res}_{z=z_j}\left[f(z)\right] n_F(z_j)e^{z_j\eta}, \tag{6.20}$$

with $n_F(z)$ being the Fermi distribution. One finds that

$$\begin{aligned}&\frac{1}{\beta}\sum_{i\Omega_n}\mathrm{Tr}\left\{\mathcal{D}^{\dagger}_{\mathbf{k}}\tilde{\mathcal{G}}(\mathbf{k},i\Omega_n)\mathcal{D}_{\mathbf{k}}\mathcal{D}^{\dagger}_{\mathbf{k}+\mathbf{q}}\tilde{\mathcal{G}}(\mathbf{k}+\mathbf{q},i\Omega_n+i\omega_n)\mathcal{D}_{\mathbf{k}+\mathbf{q}}\right\}e^{i\Omega_n\eta}\\ &= O(\mathbf{k},\mathbf{q},a,b)\left(n_F(\xi^b_{\mathbf{k}+\mathbf{q}}) - n_F(\xi^a_{\mathbf{k}})\right)\left(\frac{1}{\xi^b_{\mathbf{k}+\mathbf{q}} - \xi^a_{\mathbf{k}} - \omega} + i\pi\delta\left(\xi^b_{\mathbf{k}+\mathbf{q}} - \xi^a_{\mathbf{k}} - \omega\right)\right)\end{aligned} \tag{6.21}$$

where a representation of the δ-function $\delta(x) = \frac{1}{\pi}\frac{\eta}{x^2+\eta^2}$ was used, and ω_n has been analytically continued. The Latin indices label the bands according to the number of atoms within the unit cell and the Nambu space. The function $O(\mathbf{k},\mathbf{q},a,b)$ accounts

for the transformations $\mathcal{D}_{\mathbf{k}}$. In the following only the imaginary part is kept. The zz- component of the structure factor can then be evaluated as

$$\mathcal{S}^{zz}(\mathbf{q},\omega) = \frac{\pi}{4N_u}\sum_{a,b}\int \frac{d^2k}{(2\pi)^2} f(\mathbf{k},\mathbf{q},a,b)\left(n_F(\xi^a_{\mathbf{k}}) - n_F(\xi^b_{\mathbf{k}+\mathbf{q}})\right)\delta\left(\xi^b_{\mathbf{k}+\mathbf{q}} - \xi^a_{\mathbf{k}} - \omega\right). \tag{6.22}$$

The function

$$f(\mathbf{k},\mathbf{q},a,b) = \left|\sum_{\kappa}\phi^*_{a\kappa}(\mathbf{k})\phi_{b\kappa}(\mathbf{k}+\mathbf{q})e^{i\mathbf{q}\mathbf{R}_\kappa}\right|^2 \tag{6.23}$$

accounts for the exponential functions $e^{i\mathbf{q}(\delta\mathbf{r}-\delta\mathbf{r}')} = e^{i\mathbf{q}\mathbf{R}_\kappa}$ as well as for the similarity transformations $\mathcal{D}_{\mathbf{k}}$, which consist of the eigenfunctions $\phi_{a\kappa}(\mathbf{k})$, the sum over κ runs over all possible vectors $\delta\mathbf{r} - \delta\mathbf{r}'$ in one unit cell.

The factor $\left(n_F(\xi^a_{\mathbf{k}}) - n_F(\xi^b_{\mathbf{k}+\mathbf{q}})\right)$ in the dynamical structure factor (6.22) describes particle-hole like transitions. Such a transition occurs if an occupied state of momentum $\mathbf{k}$ in the spinon spectrum can be connected to a vacant state of momentum $\mathbf{k}+\mathbf{q}$. The delta function $\delta\left(\xi^b_{\mathbf{k}+\mathbf{q}} - \xi^a_{\mathbf{k}} - \omega\right)$ assures that energy is conserved. Each transition receives additionally a certain weight according to the overlap of the spinon wave functions involved in the process. This weight is given by the function $f(\mathbf{k},\mathbf{q},a,b)$. The integral counts all possible processes which together determine the spin structure factor.

6.3. Concluding remarks

Now that the experimental technique and the measured quantities are known, one can answer the initial question of how a quantum spin liquid can be measured. One does not expect significant peaks in the momentum resolved structure factor since such signals would correspond to a certain periodicity in real space, which implies a magnetically ordered state. For instance, in an anti-ferromagnetically ordered state, one expects that magnons govern the low-energy regime. These quasiparticles carry spin-1, and their dispersion is linear. The neutron can only scatter if it has the right energy and momentum such that it coincides with the magnon dispersion. It can excite exactly one magnon. The resulting signal reflects this one particle spectrum characterized by a sharp line. On the other hand, a signal homogeneously spread over the entire Brillouin zone suggests a paramagnetic phase in which the spins inside the sample point in random directions. For the collective behavior of spinons, governing the low-energy regime of a quantum spin liquid phase, one anticipates a relatively homogeneous signal and shows a non-trivial momentum dependency different from the diffusive signature of a simple paramagnet. The main difference

compared to magnons is that due to the conservation of total spin, neutrons can only excite a pair of spinons. As a result, the scattering experiment identifies a two particle spinon continuum. These characteristics will be explained in more depth in Chapters 8 and 9, where the dynamical structure factor is calculated for several models. Truth be told, a smoking gun evidence of a quantum spin liquid phase can currently not be made by neutron scattering experiments on their own. In order to get a broader picture, further indications, for instance, the temperature dependency of the heat capacity, should be taken into account. The ultimate proof may eventually be given by braiding experiments that could reveal once and for all the entanglement properties of a topologically degenerate spin liquid ground state.

7. Topological spinon bands and vison excitations in spin-orbit coupled quantum spin liquids

The following chapter is intended to explain the author's work, which culminated in the publication [53].

In the past decades, topological aspects have become very prominent in condensed matter physics. The underlying concepts borrowed from a seemingly abstract realm of mathematics dealing with continuous deformations disclose themselves as powerful tools by characterizing and classifying new phases of matter. Some of the most prominent specimens are the integer [80, 81] and fractional [3, 4] quantum Hall effects, the topological insulator [82, 83, 84] and, of course, quantum spin liquids [67, 10]. The strength of these approaches are, in fact, the capability of abstraction. It enables one to make rigorous arguments about physical states, ignoring most of the microscopic details. It is often possible to reduce one of the key properties to a single number called a topological invariant. One can vaguely discern between two fields in which these concepts arise. The first one treats electronic band structures of weekly interacting electrons. In this realm of almost free electrons, symmetries can protect certain states against any generic but symmetry preserving perturbation. Based on the classifications of different symmetry groups, one is capable of tracking down phases in which these states either exist or do not [85, 86]. Topology enters as it is impossible to continuously deform one phase into the other. One speaks of trivial topology if a deformation of a given state to the vacuum state exists. It is further possible to assign topological indexes to each phase. The second area deals with strongly interacting electronic systems in which approximating electrons as almost free is impossible. Here topologically distinct ground states arise, tightly related to fractional excitations [39, 38, 67, 26, 87]. Quantum spin liquids and fractional quantum Hall states are prominent members of the second field. Interestingly, there are scenarios for which both concepts apply at the same time [88, 89, 90, 91]. The current chapter also describes such a scenario.

As explained in the preliminary chapters of this thesis, the fundamental constituents of $\mathbb{Z}_2$ spin liquids can be described by fermionic spinons and visons, a bosonic flux excitation. A deconfined spinon can be effectively treated as a free

fermion [39, 38, 92]. If spin-orbit coupling effects are explicitly taken into account for the interaction's decoupling, it becomes possible to construct spinon mean-field states whose dispersion can exhibit non-trivial topology [93, 94, 54, 95].

In reference [54], an exhaustive classification using the concept of PSGs has been made on a square lattice. It was found that by breaking spin rotational invariance, 1488 new PSG representations appeared. These new representations are distinct from the 272 PSGs initially found in a classification on the square lattice based on a decoupling that did not include spin rotational symmetry breaking terms [5]. This massive amount of possible states exacerbates a detailed case study. Yet in this classification, all possible symmetry respecting states are counted regardless of their bond distance. In the presented work, these classified representations are scrutinized to identify those that lead to short-ranged states in which only the nearest neighbors terms enter the effective mean-field model. By this means, a feasible number of states could be identified, which are analyzed with the main focus on finding spinon bands exhibiting a non-trivial topology. It is found that states including only nearest-neighbor bonds, cannot develop a topology different from the vacuum. However, including second neighbor bonds can immediately lead to non-trivial spinon bands. Except for minor modifications, the corresponding mean-field Hamiltonians resemble the Bernevig-Hughes-Zhang (BHZ) model [55]; a model that describes a topological insulator.

Furthermore, the effects of visons are taken into account. Including a single pair of visons revealed their binding potential to spinon modes, which in the case of a topologically non-trivial spinon band, leads to modes whose energy is asymptotically vanishing in dependence of the distance between the visons forming the pair. This phenomenon has already been observed in the context of vortices coupled to fermions and, in particular, in the case of $p+ip$ superconductors [56, 57, 58, 96]. The relation between these models and the spinon-vison case could be made rigorous by finding a mapping from the present case to the Bogoliubov-de Gennes Hamiltonian, including a vortex. Finally, the comportment of a vison gas has been investigated. Therefore, multiple visons are introduced and randomly distributed over the entire lattice. This setting mimics the effect of an increasing temperature as the required energy to excite the gauge field can be supplied by thermal fluctuations. It was found that the spinon modes bound to the visons can form bands on their own, which usually emerge at low energies. The corresponding energy distribution shows some clear peaks which emerge within the band gap. Such a formation of bands and the corresponding signature in the energy distribution could be an identifying feature useful for future experiments.

7.1. Short-range couplings and topological spinon states

A PSG classification for mean-field models, including singlet and triplet channels, as explained in Chapter 5, reveals all different ways of representing the gauge transformation corresponding to the symmetry generators of the square lattice. The symmetry group generators and the corresponding spin representations are explained in Appendix A.1. For each channel, one finds a different set of requirements that a mean-field *Ansatz* has to obey in accordance with the lattice symmetry. These equations can be found in the Appendix A.2. In order to identify short-range states it is convenient to label the $u^X_{\mathbf{r}\mathbf{r}'}$ matrices according to the distance between site $\mathbf{r}$ and $\mathbf{r}'$. Here X labels the different channels s, t_1, t_2, t_3. The coupling matrices can be written as

$$u^X_{\mathbf{r}\mathbf{r}'} = \eta^{x\delta y} u^X_{\delta\mathbf{r}}, \tag{7.1}$$

with $\eta = \pm 1$ a sign factor which appears in the representations of lattice translations. First neighbor states can be found by limiting the possible coupling vectors to $\delta\mathbf{r}_1 = \{(\pm 1, 0), (0, \pm 1)\}$. This reduces drastically the number of representations that lead to a non-vanishing *Ansatz*. The remaining states are required to have an invariance group of a $\mathbb{Z}_2$ type. As explained in Chapter 5 this requirement can be formulated as in Eq. (5.25) in terms of loop operators $P_{\mathbf{r}}$. It was in particular shown that there exist two distinct analytic expressions: $P^{(e)}_{\mathbf{r}}$ and $P^{(o)}_{\mathbf{r}}$. Since the present case deals with multiple channels, one must extend this requirement to the four-dimensional spinor space. The generalized loop operators are generated analog to the two-dimensional case except that the generalized $\tilde{u}_{\mathbf{r}\mathbf{r}'}$, defined in Eq. (5.27), enter the product along the loop. One finds that the generalized loop operator can be written as

$$\tilde{P}_{\mathbf{r}} = \begin{pmatrix} P^a_{\mathbf{r}} & P^b_{\mathbf{r}} \\ P^c_{\mathbf{r}} & P^d_{\mathbf{r}} \end{pmatrix}. \tag{7.2}$$

Each block $P^\mu_{\mathbf{r}}$ is expressed by a two dimensional loop operator whereas the label $\mu = \{a, b, c, d\}$ indicates that every individual operator is independently given by either $P^{(e)}_{\mathbf{r}}$ or $P^{(o)}_{\mathbf{r}}$. The condition for the invariance group can be formulated similarly to the one for the singlet channel explained in Chapter 5. By using the fact that the four-dimensional gauge transformation Eq. (5.30) can be made block diagonal, one finds that

$$[W_{\mathbf{r}}, (P^\mu_{\mathbf{r}})] = 0, \tag{7.3}$$

with $W_{\mathbf{r}}$ a two-dimensional gauge transformation. This means that $W_{\mathbf{r}}$ must commute with each block component $P^\mu_{\mathbf{r}}$ simultaneously. Eventually, there are only 28 different PSGs for nearest neighbors realizing a $\mathbb{Z}_2$ invariance group. These PSGs are listed in Appendix A.3.

The difference of the PSG classifications for the spin rotational invariant and the broken case manifests itself through the symmetry operation

$$\mathcal{P}_z : z \to -z. \tag{7.4}$$

By using the fact that the four-dimensional gauge transformation Eq. (5.30) can be made block diagonal, one finds that The corresponding local representation matrix can, like the other symmetry generators, be expressed as $G_{\mathcal{P}_z}(\mathbf{r}) = \eta_{\mathcal{P}_z}^{f(\mathbf{r})} g_{\mathcal{P}_z}$, with a sign factor $\eta_{\mathcal{P}_z} = \pm 1$, an integer-valued function of the lattice coordinates $f(\mathbf{r})$, and a site-independent $SU(2)$ matrix $g_{\mathcal{P}_z}$. Under the assumption that $\mathcal{P}_z$ has a non-trivial implementation, i.e. $g_{\mathcal{P}_z} \neq \tau^0$, which is a necessary condition for the finite off-diagonal elements u^{t_2}, u^{t_3}, one finds that time-reversal has to have an implementation $g_{\mathcal{T}} = \tau^0$. Unfortunately, this representation does not support any Kramer's pairs, and the resulting spinon band models can be identified as members of the Altland-Zirnbauer class BDI, which has no topological index in two dimensions [97, 85]. Ten different Altland-Zirnbauer classes classify random matrices according to their transformation properties of time-reversal, particle-hole and chiral symmetry. Based on these classes, one can create a periodic table that tells immediately whether a $d-$ dimensional system can host a topological invariant. By including second nearest neighbor bonds, it is found that $\mathbb{Z}_2$ states exist having neither $\mathcal{P}_z$ nor $\mathcal{T}$ implemented by a unity matrix. If $g_{\mathcal{T}} = i\tau^2$, Kramer's theorem applies, and these states belong to class DIII. In this class, it is possible to define a $\mathbb{Z}_2$ topological invariant in two dimensions, which discerns between two phases where one phase can host Majorana zero modes as it will be further explained below. The major difference compared to the first neighbor case is that now closed loops can be made by including diagonal bonds. This results in the freedom to create even and odd-numbered loops simultaneously, whereas the first neighbor bonds only allow even-numbered loops. These two different loop operators are most likely not linearly dependent and thus break the invariance group.

The characteristics of the first neighbor state are multifarious. Their dispersion can exhibit band gaps, nodal Dirac points, or entire Fermi surfaces. Even mean-field models belonging to the same PSG depend on multiple amplitudes altering the spectral comportment entirely. This impedes any general statement and to gain more insight becomes cumbersome. One possible route to follow is self-consistent calculations, which could reduce the size of the parameter space spanned by the different amplitudes. This approach will not be further elaborated here. Instead, one specimen shall be introduced and studied in more detail, leaving the other open for future studies. The defining PSG is given by

$$\begin{aligned} g_{\mathcal{P}_z} = i\tau^3, \quad g_{\mathcal{T}} = \tau^0, \quad g_{\mathcal{P}_{xy}} = i\tau^3, \quad g_{\mathcal{P}_x} = i\tau^1, \quad g_{\mathcal{P}_y} = i\tau^1 \\ \eta_{\mathcal{P}_z} = 1, \quad \eta_{\mathcal{T}} = -1, \quad \eta = \pm 1, \quad \eta_{\mathcal{P}_x} = -1, \quad \eta_{\mathcal{P}_y} = -1. \end{aligned} \tag{7.5}$$

Among the first neighbor states this state has the unique property that spin-up and spin-down sectors decouple. Therefore, an appropriate basis is[1] $\Psi_{\mathbf{k}} = (f_{\mathbf{k}\uparrow}, f^\dagger_{\mathbf{k}\uparrow}, f_{\mathbf{k}\downarrow}, f^\dagger_{\mathbf{k}\downarrow})^T$. The matrix $\tilde{u}_{\mathbf{k}}$ then becomes block-diagonal. The resulting mean-field Hamiltonian can be written in momentum space as

$$H_{\mathbf{k}} = \sum_{\mathbf{k}} \Psi^\dagger_{\mathbf{k}} \begin{pmatrix} h^1_{\mathbf{k}} & 0 \\ 0 & h^2_{\mathbf{k}} \end{pmatrix} \Psi_{\mathbf{k}} \quad \text{with} \tag{7.6}$$

$$h^1_{\mathbf{k}} = \begin{pmatrix} (\alpha+\beta)\cos k_x + (\alpha-\beta)\cos k_y & -(\gamma-\delta)\sin k_x + i(\gamma+\delta)\sin k_y \\ (-\gamma+\delta)\sin k_x + i(\gamma+\delta)\sin k_y & -(\alpha+\beta)\cos k_x + (\alpha-\beta)\cos k_y \end{pmatrix}$$

$$h^2_{\mathbf{k}} = \begin{pmatrix} (\alpha-\beta)\cos k_x + (\alpha+\beta)\cos k_y & -(\gamma+\delta)\sin k_x + i(\gamma-\delta)\sin k_y \\ -(\gamma+\delta)\sin k_x + i(\gamma-\delta)\sin k_y & (-\alpha+\beta)\cos k_x - (\alpha+\beta)\cos k_y \end{pmatrix}$$

$\alpha, \beta, \gamma, \delta$ are real valued parameters that correspond to the certain hopping and pairing amplitudes. These two blocks $h^1_{\mathbf{k}}, h^2_{\mathbf{k}}$ are not mutually related by a single symmetry operation. The spectrum, shown in Fig. 7.1, exhibits a bandgap that is persistent in the generic case that all parameters have different finite values. Fine-tuning, however, $\delta = \gamma$ induces a band touching point. Putting the system on a cylinder induces edge modes that appear along the ends of the cylinder. These edge modes are created by only one of the blocks depending on whether the x or y direction is periodic. However, as this state belongs in the topological trivial class BDI these boundary states are unprotected. It is seen in Fig. 7.1 that they are separated from the bulk band. Applying a generic perturbation shows that these states can merge in the bulk continuum, and they vanish. This *Ansatz* will reappear latter in order to study the effect of visons.

As there are no topological spinon bands found for mean-field models, including first neighbor bonds only, it is inevitable to include further second nearest neighbor bonds. This, unfortunately, increases the number of possible candidates tremendously. To circumvent an extended analysis of all of these states additional criteria are imposed. In order to assure protected Kramer modes time-reversal shall be implemented as $g_{\mathcal{T}} = i\tau^2$. As a second condition, only states are considered whose second neighbor bonds do not include any triplet terms. This simplification might be justified because usually, spin-orbit effects are small in realistic materials and can be treated in perturbation theory resulting in small modifications. One expects further that the coupling strengths decrease with distance as they correspond to overlap integrals. These two effects combined should yield very small amplitudes in the triplet channels. A third condition is motivated by having less computational effort, and it is required that the mean-field model can be written in a block diagonal form. After rejecting possible states according to these limitations, only two

[1] The tilde $\tilde{\Psi}$ will be omitted in the following chapter and one should always think of the four dimensional spinor space.

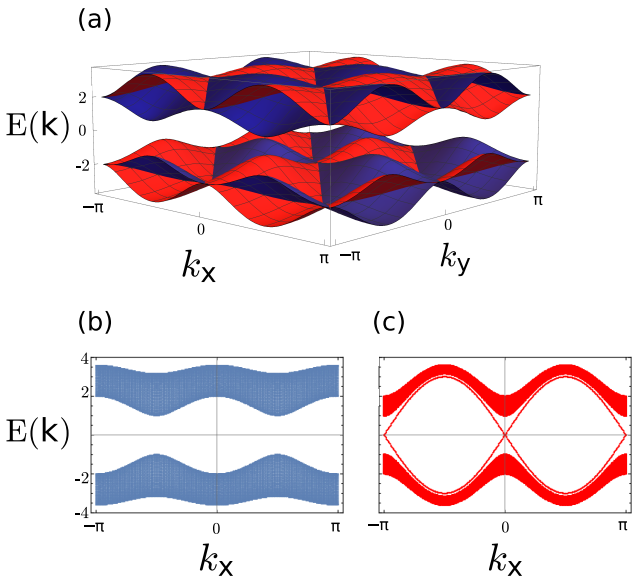

Figure 7.1.: Spinon-band structure of the nearest neighbor Hamiltonian in Eq. (7.6) using the parameters $\alpha = \beta = \gamma = 1$ and $\delta = 2$. The $h^1_{\mathbf{k}}$ bands ($h^2_{\mathbf{k}}$ bands) are plotted in red (blue) color. (a) Spinon bands for periodic boundary conditions in x and y directions. (b) Band structure of the $h^1_{\mathbf{k}}$ block for a cylinder edge along the x direction. (c) Band structure of the $h^2_{\mathbf{k}}$ block for a cylinder edge along the x direction. Note that for an edge along one of the lattice directions, only one block shows topologically trivial edge states. (Figure taken from [53])

candidates remain. The first one is defined through its transformation behavior of the following PSG

$$\begin{aligned} g_{\mathcal{P}_z} = i\tau^3, \quad g_{\mathcal{T}} = i\tau^2, \quad g_{\mathcal{P}_{xy}} = \tau^0, \quad g_{\mathcal{P}_x} = \tau^0, \quad g_{\mathcal{P}_y} = \tau^0 \\ \eta_{\mathcal{P}_z} = 1, \quad \eta_{\mathcal{T}} = 1, \quad \eta = 1, \quad \eta_{\mathcal{P}_x} = 1, \quad \eta_{\mathcal{P}_y} = 1. \end{aligned} \tag{7.7}$$

The mean-field Hamiltonian is given in the spinor basis $\Psi_{\mathbf{k}} = (f_{\mathbf{k}\uparrow}, f^\dagger_{\mathbf{k}\uparrow}, f_{\mathbf{k}\downarrow}, f^\dagger_{\mathbf{k}\downarrow})^T$, which decouples the different spin sectors, as

$$H_{\mathbf{k}} = \sum_{\mathbf{k}} \Psi^\dagger_{\mathbf{k}} \begin{pmatrix} h_{\mathbf{k}} & 0 \\ 0 & h^*_{-\mathbf{k}} \end{pmatrix} \Psi_{\mathbf{k}} \quad \text{with} \tag{7.8}$$

$$h_{\mathbf{k}} = \begin{pmatrix} \alpha\left(\cos k_x + \cos k_y\right) + \beta \cos k_x \cos k_y & \gamma\left(i \sin k_x - \sin k_y\right) \\ \gamma\left(i \sin k_x + \sin k_y\right) & -\alpha\left(\cos k_x + \cos k_y\right) - \beta \cos k_x \cos k_y \end{pmatrix}.$$

The parameters α, β, γ are real numbers and can be identified as hopping and pairing amplitudes. The upper and lower blocks are related by time-reversal symmetry $\mathcal{T}$: $h_{\mathbf{k}} \to h^*_{-\mathbf{k}}$. This model has an astonishing resemblance with the Bernevig-Hughes-Zhang (BHZ) model [55]. The BHZ model is an effective model initially formulated to describe the quantum spin Hall effect and a topological phase transitions in HgTe. Its basis is made of s- and p-orbitals $\Psi_{BHZ} = (s_\uparrow, \frac{1}{\sqrt{2}}(p_x + ip_y)_\uparrow, s_\downarrow, \frac{1}{\sqrt{2}}(p_x + ip_y)_\downarrow)^T$. Therefore, the $i \sin k_x + \sin k_y$ term, which is linearized in the BHZ model $k_x + ik_y$, has a different interpretation in these two models. In the BHZ model it describes a momentum dependent spin-orbit coupling whereas in the spinon model it represents a p-wave condensation of spinons. In this regard, one can think of this model as a description of two copies of a topological spinon superconductor related by time-reversal symmetry [98, 99, 100]. This term's physical importance is that it induces a spin-momentum locking in both models, which is the reason for a topological band structure as it results in edge modes with different chirality. The exact meaning of this will be further explained below in the text. The major difference between these two models is the $\beta \cos k_x \cos k_y \tau^3$ term in the spinon model which is a quadratic term in the BHZ model $\left[M - B(k_x^2 + k_y^2)\right] \tau^3$. These terms can be related to an effective mass arising in a linearized theory around the Γ point in both models. Importantly, the mass has an opposite sign for the upper and lower bands. Away from the Γ point, the $\cos k_x \cos k_y$ term is capable of inducing a second transition point, which is lacking in the BHZ model. This can be understood by considering the phase diagram of the spinon model, which is shown in Fig. 7.2. Fixing the amplitudes $\alpha = \gamma = 1$ sets the global energy scale and the size of the gap. Yet, it does not affect the transition points. These points depend on β, which can be seen when β is varied between $(0, 3)$[2]. For $\beta = 0$ the system is gapless with band touching

[2] A sign reversed image of the phase diagram is obtained by a reflection $\beta \to -\beta$

points at $\mathbf{k} = (\pm\pi, 0)$ and $\mathbf{k} = (0, \pm\pi)$. Increasing β opens a bandgap. One finds two bands that are twice degenerate, corresponding to the spin-up and spin-down block. The two blocks have non-trivial Chern numbers $n_\uparrow = 1$ and $n_\downarrow = -1$ which yields a non-trivial $\mathbb{Z}_2$ invariant $\nu = \frac{n_\uparrow - n_\downarrow}{2}|_{\mathrm{mod}_2} = 1$ [101, 97]. This is because both blocks are mutual images under time-reversal. The spectrum of the system put on a cylinder shows two degenerate modes emerging within the bulk gap. Note that the degeneracy comes from the fact that the cylinder has two edges. Focusing on only one edge, one finds that these modes are simultaneously protected by $\mathcal{P}_z$ and $\mathcal{T}$ [54]. Due to the already mentioned spin-momentum locking, one mode has a fixed spin projection and moves to the right, whereas the other mode has the opposite spin and moves to the left. After assigning Majorana operators to these modes, γ_R for the right mover and γ_L for the left mover, one finds that time-reversal acts as $\mathcal{T} : \gamma_R \to \gamma_L$ and $\mathcal{T} : \gamma_L \to -\gamma_R$. A possible mass term, capable of gapping these modes out, would couple to $i\gamma_R\gamma_L$ and is hence forbidden by time-reversal. Similarly, one finds that $\mathcal{P}_z : \gamma_R \to \gamma_R$ and $\mathcal{P}_z : \gamma_L \to -\gamma_L$. Thus, to evoke a possible mass term, both symmetries need to be broken simultaneously.

Setting $\beta = 2$ shows that a second transition occurs for which the bulk gap closes at momenta $\mathbf{k} = (\pm\pi, \pm\pi)$. After this transition point the Chern numbers of the upper and lower bulk bands have increased $n_\uparrow = 2$ and $n_\downarrow = -2$. The resulting topological invariant indicates a trivial phase $\nu = 0$. This phase persists for $\beta \to \infty$. Yet, at this point, the $\mathbb{Z}_2$ invariant might be misleading. It is seen in the spectrum on a cylinder that additional edge modes appear, which pass through zero energy at momenta $k_x = \pi$. The corresponding Majorana operators are denoted by η_R, η_L. Similar to the γ_R, γ_L, these modes cannot couple to a mutual mass term as $i\eta_R\eta_L$ is prohibited by time-reversal symmetry. Any coupling between different modes $i\eta_L\gamma_R$ requires a finite momentum transfer $\Delta k_x = \pi$ which can only appear if translational symmetry in x direction is broken. Therefore, this model could be regarded as a crystalline topological spinon superconductor [102, 103].

The second model belongs to the PSG

$$\begin{aligned} g_{\mathcal{P}_z} = i\tau^3, \quad g_{\mathcal{T}} = i\tau^2, \quad g_{\mathcal{P}_{xy}} = \tau^0, \quad g_{\mathcal{P}_x} = i\tau^3, \quad g_{\mathcal{P}_y} = i\tau^3 \\ \eta_{\mathcal{P}_z} = 1, \quad \eta_{\mathcal{T}} = -1, \quad \eta = 1, \quad \eta_{\mathcal{P}_x} = -1, \quad \eta_{\mathcal{P}_y} = -1. \end{aligned} \tag{7.9}$$

The corresponding mean-field Hamiltonian reads

$$H_{\mathbf{k}} = \sum_{\mathbf{k}} \Psi^\dagger_{\mathbf{k}} \begin{pmatrix} h_{\mathbf{k}} & 0 \\ 0 & h^*_{-\mathbf{k}+(\pi,\pi)^T} \end{pmatrix} \Psi_{\mathbf{k}} \quad \text{with} \tag{7.10}$$

$$h_{\mathbf{k}} = \begin{pmatrix} \alpha\left(-\cos k_x + \cos k_y\right) + \beta \cos k_x \cos k_y & \gamma\left(i \sin k_x - \sin k_y\right) \\ \gamma\left(-i \sin k_x + \sin k_y\right) & -\alpha\left(-\cos k_x + \cos k_y\right) - \beta \cos k_x \cos k_y \end{pmatrix},$$

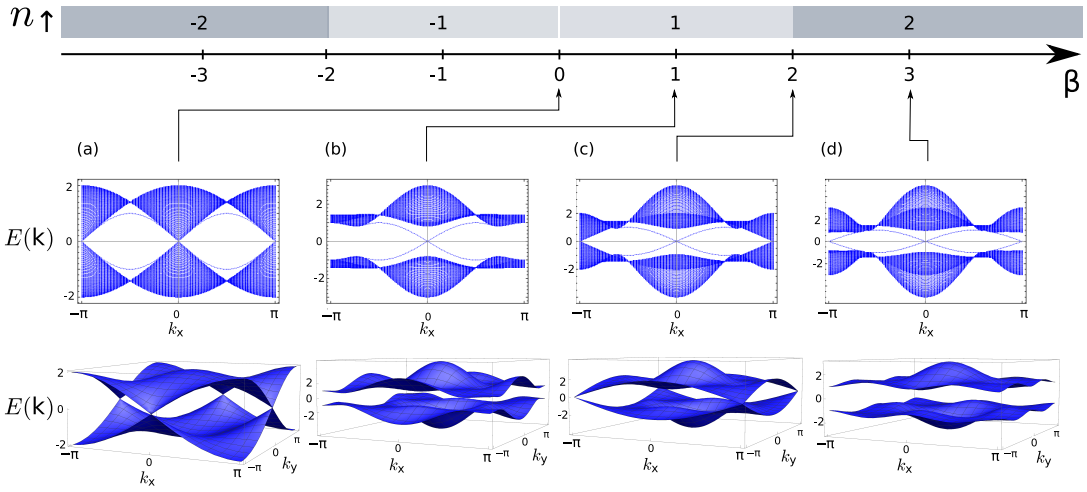

Figure 7.2.: Top: Phase diagram of the topological spinon bands for the mean-field Hamiltonian in Eq. (7.8) using $\alpha = 1$. Chern numbers $n_\uparrow$ of the block $h_\mathbf{k}$ are indicated in each phase. Note that the phase diagram is independent of γ. (a)-(d) Spinon band structures for $\beta = 0, 1, 2, 3$ and $\alpha = \gamma = 1$ where the upper plots correspond to a cylinder geometry with an edge along the x-axis and the lower plots are for a torus geometry. All spinon bands are doubly degenerate with respect to the spin degree of freedom. (Figure taken from [53])

in the spin decoupled spinor basis $\Psi_\mathbf{k} = (f_{\mathbf{k}\uparrow}, f^\dagger_{\mathbf{k}\uparrow}, f_{\mathbf{k}\downarrow}, f^\dagger_{\mathbf{k}\downarrow})^T$, with $\alpha, \beta, \gamma \in \mathbb{R}$. Due to a negative sign factor $\eta_\mathcal{T} = -1$, the representation of time-reversal becomes site dependent $G_\mathcal{T}(\mathbf{r}) = (-1)^{x+y} i\tau^2$. This leads to a momentum shift of the time-reversed block $\mathbf{k} \to \mathbf{k} + (\pi, \pi)^T$. Besides this modification the spectral and topological properties are equivalent to the previously discussed model (compare Eq. (7.8) and Fig. 7.2) and shall not be repeated.

7.2. Vison excitations

7.2.1. Static approximation

Up to now, the existence of a dynamic gauge field was entirely ignored. As explained in Chapter 2, this corresponds to the zeroth-order mean-field theory in which spinons are treated as free fermions. This bare mean-field theory yields reasonable solutions only in very specific cases. One of the scenarios in which mean-field results become trustworthy is linked to the emergence of a $\mathbb{Z}_2$ gauge field. In the previous section, all mean-field Hamiltonians were constructed such that the invariance group is $\mathbb{Z}_2$, and this should lead to a $\mathbb{Z}_2$ gauge field as described in Chapter 4. Therefore, the effective low-energy theory should resemble a $\mathbb{Z}_2$ lattice gauge theory as introduced

in Chapter 3. If one considers $\mathbb{Z}_2$ phase fluctuations $\sigma^z_{\mathbf{rr}'} = \pm 1$ and replaces $u_{\mathbf{rr}'} = \sigma^z_{\mathbf{rr}'} u^0_{\mathbf{rr}'}$ as discussed in Chapter 2 one obtains

$$H = \sum_{(\mathbf{rr}')} \left(\Psi^\dagger_{\mathbf{r}} \sigma^z_{\mathbf{rr}'} u_{\mathbf{rr}'} \Psi_{\mathbf{r}'} + h.c \right). \tag{7.11}$$

This model is invariant under a combined transformation

$$\mathcal{G} : \Psi_{\mathbf{r}} \to -\Psi_{\mathbf{r}}, \quad \sigma^z_{\mathbf{rr}'} \to -\sigma^z_{\mathbf{rr}'}, \tag{7.12}$$

where $\mathbf{r}'$ represents all relevant nearest neighbors as indicated in Fig. 7.3, and thus defines a $\mathbb{Z}_2$ gauge theory [30]. It was explained in Chapter 3 that the pure $\mathbb{Z}_2$ gauge theory has two different phases: the first phase confines two charges locally while in the second phase, charges are free entities. If one identifies the physical spinon as the charge, the deconfining phase describes the spin liquid phase. Note that the spinon field operator $\Psi_{\mathbf{r}}$ is gauge dependent and hence not a physical quantity. Motivated by the pure gauge theory, one expresses the local gauge transformation as

$$\mathcal{S}_{\mathbf{r}} = \prod_{\mathbf{r}' \in \mathrm{Star}(\mathbf{r})} \sigma^x_{\mathbf{rr}'}, \tag{7.13}$$

where $\sigma^x_{\mathbf{rr}'}$ induces a sign flip of the fluctuating bond variables $\sigma^z_{\mathbf{rr}'}$, if both σ^x and σ^z are understood as Pauli operators. The star of $\mathbf{r}$ contains all connected neighbor sites as illustrated in Fig. 7.3. The gauge transformation acts then according to

$$\mathcal{G} : \Psi_{\mathbf{r}} \to -\Psi_{\mathbf{r}}, \quad \sigma^z_{\mathbf{rr}'} \to \mathcal{S}_{\mathbf{r}} \sigma^z_{\mathbf{rr}'} \mathcal{S}_{\mathbf{r}}. \tag{7.14}$$

In the discussion of Chapter 3, the charge-free sector was selected. For the problem at hand, fixing the sector has to respect the one particle per site condition, which can be expressed by the constraint [30, 36]

$$\mathcal{S}_{\mathbf{r}} (-1)^{f^\dagger_{\mathbf{r}\uparrow} f_{\mathbf{r}\uparrow} + f^\dagger_{\mathbf{r}\downarrow} f_{\mathbf{r}\downarrow}} = -1. \tag{7.15}$$

This requirement has to hold for all $\mathbf{r}$, and importantly it does not commute with the Hamiltonian (7.11). Thus it evokes a connection between the $\sigma^z_{\mathbf{rr}'}$ and the $\Psi_{\mathbf{r}}$ operators, which otherwise could be treated separately. This leads, unfortunately, to a complicated many-body problem similar to the initial spin model.

A pure gauge theory can, at least in principle, be derived from Eq. 7.11 by integrating over the $\Psi_{\mathbf{r}}$ fields. This can be done if the free spinon models exhibit a bandgap. Respecting the constraint (7.15) generates $\sigma^x_{\mathbf{rr}'}$ terms in the resulting model. The pure gauge theory should contain all possible gauge invariant terms, i.e., they are made of operators which locally commute with the generator of gauge transformation Eq. (7.14) [68, 104, 11]. These terms can be interpreted as electric

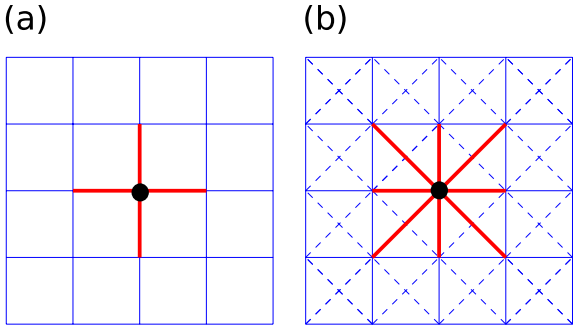

Figure 7.3: Effect of a local gauge transformation $\mathcal{S}_{\mathbf{r}}$ [Eq. (7.15)] acting on a site $\mathbf{r}$ denoted by a black dot: All bond variables $\sigma^z_{\mathbf{r}\mathbf{r}'}$ are flipped ($\sigma^z_{\mathbf{r}\mathbf{r}'} \to -\sigma^z_{\mathbf{r}\mathbf{r}'}$) on links belonging to the star of $\mathbf{r}$ illustrated by red lines. (a) For a nearest neighbor mean-field model the star consists of four bonds emanating from $\mathbf{r}$. When second neighbor mean-field amplitudes are added (dashed lines), the gauge fields $\sigma^z_{\mathbf{r}\mathbf{r}'}$ are also defined on diagonal links, such that the gauge transformation acts on all bonds highlighted in (b). (Figure taken from [53])

and magnetic fluxes. Therefore, one expects that the resulting gauge theory is given by a Hamiltonian

$$\begin{aligned} H_{\text{gauge}} = &- h_1 \sum_{\langle \mathbf{r}\mathbf{r}' \rangle} \sigma^x_{\mathbf{r}\mathbf{r}'} - h_2 \sum_{\langle\langle \mathbf{r}\mathbf{r}' \rangle\rangle} \sigma^x_{\mathbf{r}\mathbf{r}'} - K_1 \sum_{\text{plaquette}} \prod_{\square} \sigma^z_{\mathbf{r}\mathbf{r}'} \\ &- K_2 \Bigg(\sum_{\measuredangle} \prod_{\measuredangle} \sigma^z_{\mathbf{r}\mathbf{r}'} + \sum_{\measuredangle} \prod_{\measuredangle} \sigma^z_{\mathbf{r}\mathbf{r}'} \\ &+ \sum_{\measuredangle} \prod_{\measuredangle} \sigma^z_{\mathbf{r}\mathbf{r}'} + \sum_{\measuredangle} \prod_{\measuredangle} \sigma^z_{\mathbf{r}\mathbf{r}'} \Bigg) - \dots . \end{aligned} \tag{7.16}$$

The simple brackets $\langle \mathbf{r}\mathbf{r}' \rangle$ indicate a summation of nearest neighbor pairs while $\langle\langle \mathbf{r}\mathbf{r}' \rangle\rangle$ denotes second neighbors. The $\square$ symbol represents an elementary plaquette of the square lattice as already introduced in Chapter 3. Analog the symbols $\measuredangle, \measuredangle, \measuredangle, \measuredangle$ denote the plaquettes encircled by two first neighbor bonds and one diagonal second neighbor bond. The terms proportional to h_2 and K_2 extend the simple gauge theory such that it respects higher plaquette terms as they arise for models with second neighbor mean-field amplitudes. As discussed in Chapter 3 the ground state of the deconfined phase is characterized by a configuration in which all plaquette terms are uniform $\prod_{\square} \sigma^z_{\mathbf{r}\mathbf{r}'} = 1 = \prod_{\measuredangle} \sigma^z_{\mathbf{r}\mathbf{r}'} = \dots$. This is not a unique description in terms of the bond variables, and the true ground state is a coherent superposition of extensively many different configurations. The elementary excitations in this phase correspond to frustrated plaquette terms which means that the product becomes negative $\prod_{\square} \sigma^z_{\mathbf{r}\mathbf{r}'} = -1 = \prod_{\measuredangle} \sigma^z_{\mathbf{r}\mathbf{r}'} = \dots$. In order to study these vison excitations, one has, in principle, to deal with a highly entangled fluctuating ground state. To simplify this intricate problem an approach is pursued in which only one configuration is considered. Using the mean-field model (7.11) for which fluctuations are taken into account by one configuration of the $\sigma^z_{\mathbf{r}\mathbf{r}'}$ field but ignoring

the constraint Eq. (7.15) such that these fluctuations are deprived of their dynamics will make an investigation feasible. This might seem a rather drastic approach, but confinement properties, in particular, should not depend on these dynamical properties. Furthermore, in the case of an exactly soluble spin model, it was shown that the gauge field configurations are indeed static [31, 11].

7.2.2. Vison deconfinement in selected PSG solutions

In the static approximation, different mean-field spinon models are considered to scrutinize the confinement behavior of visons. A fixed configuration of $\sigma^z_{\mathbf{r}\mathbf{r}'} u_{\mathbf{r}\mathbf{r}'}$ bonds on a square lattice is assumed. The $u_{\mathbf{r}\mathbf{r}'}$ are chosen according to the symmetric models derived in a previous section of this chapter. The resulting Hamiltonian (7.11) can be diagonalized, revealing the quasi-particle spectrum. This has to be done for each configuration anew. Starting with a flux free configuration in which all $\sigma^z_{\mathbf{r}\mathbf{r}'} = 1$ one can insert a pair of vison by changing the value of one bond variable creating two visons on the adjacent plaquettes. Comparing the ground state energies of these two configurations supplies information about the magnetic coupling constant K of the pure gauge model Eq. (7.16). Note that in the static approximation, one cannot access the electric coupling h. By correctly inserting more and more negative bonds, one can separate the vison pair without adding more of them, as illustrated in Fig. 7.4. Note that if second neighbor bonds are included one has to flip additional diagonal bonds to avoid the creation of unwanted vison pairs. The confining potential $E(d)$ as a function of the distance between the individual visons is calculated by subtracting the flux free ground state energy from the ground state energies of a configuration containing one pair of visons, where d is the distance of the visons calculated in the metropolis norm. Here one block corresponds to one unit square of the lattice. These confining potentials are shown in Fig. 7.4 for the nearest neighbor model Eq. (7.6) and the BHZ like model Eq. (7.8) in two different phases $n_\uparrow = 1$ and $n_\uparrow = 2$. It is found that regardless of the specific spinon properties, the vison potential is constant for sufficiently large distances. This means that the creation of one pair requires a finite amount of energy. A separation does not require further energy. Hence the visons are, in fact, deconfined. This was already anticipated since the gauge transformation $\mathcal{S}_\mathbf{r}$ deforms the string connecting the vison pair. Therefore, the string operator should not be a measurable quantity. Interestingly, $E(d)$ reaches a constant value for very short distances. This supports the argument that in the pure gauge theory the leading terms are made by loops including only first K_1 and second neighbors K_2. Comparing the vison gap $E(d \to \infty)$ with the spinon gap Δ shows that they are of the same magnitude.

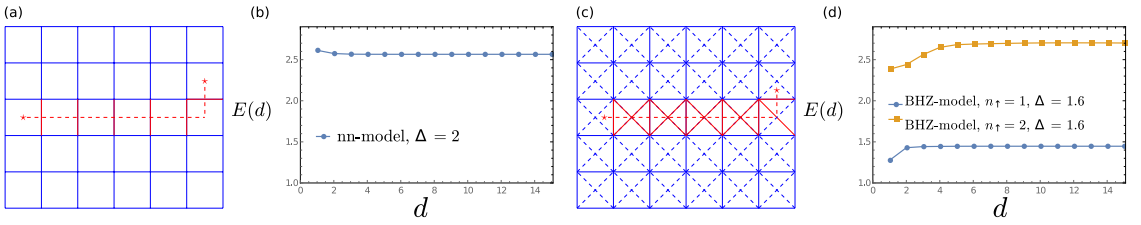

Figure 7.4.: (a) Possible gauge field configuration for a pair of separated visons (marked by stars) in the case of nearest neighbor mean-field models. The full red lines indicate bonds with $\sigma^z_{\mathbf{r}\mathbf{r}'} = -1$ while $\sigma^z_{\mathbf{r}\mathbf{r}'} = 1$ otherwise. Gauge fields $\sigma^z_{\mathbf{r}\mathbf{r}'} = -1$ occur on all bonds crossing the "gauge string" (dashed red line). The plaquettes at which the visons reside are threatened by a finite local flux. (b) Vison pair-excitation energy $E(d)$ as a function of the distance d for the nearest neighbor PSG solution in Eq. (7.6) using the parameters $\alpha = \beta = \gamma = 1$, $\delta = 2$. Here, d is defined in units of the nearest-neighbor lattice spacing and the separation is along a lattice direction. For comparison, the spinon bulk gap Δ is indicated in the figure. (c) Same as (a) but with additional second neighbor mean-field amplitudes. In this case also diagonal bond variables $\sigma^z_{\mathbf{r}\mathbf{r}'}$ need to be flipped along the gauge string. (d) Vison potentials $E(d)$ for the BHZ-like model [see Eq. (7.8)] in the phases with Chern numbers $n_\uparrow = 1$ (blue line with parameters $\alpha = \beta = \gamma = 1$) and $n_\uparrow = 2$ (yellow line with parameters $\alpha = \gamma = 1$, $\beta = 3$). (Figure taken from [53])

7.2.3. Spinon-vison bound states

In lattice gauge theory, electric charges and magnetic fluxes can form composite objects which obey certain fusion rules [31, 14]. These objects may have non-trivial exchange statistics. That means in the spin liquid context, the presence of a vison influences the spinon comportment and vice versa. Indeed it was numerically found that visons and spinon form bound states. In the spinon spectrum, states can be identified, which have a real-space probability distribution correlated to the vison positions, as shown in Fig. 7.5. Their corresponding eigenenergies appear within the spinon gap. These compound objects depend on the spinon mean-field model. In the case of a topologically non-trivial spinon band the vison-spinon pair's energy tends to zero if the visons of the pair are sufficiently far separated. This can be seen by taking the energy of such a mode $\epsilon(d)$ as a function of the separation distance, which can be seen in Fig. 7.5. The separation is defined analog to the previously explained example and counted in the units of square plaquettes. For the non-topological first neighbor spinon model Eq. (7.6), it is found that the appearing in-gap modes do not depend on the separation distance. In the BHZ like spinon model (7.8), for which only the positive part of the spectrum is taken into account as the negative part is connected by particle-hole symmetry, one finds in the phase with Chern number $n_\uparrow = 1$ two degenerate modes, each corresponding to one spin degree, that can be identified as

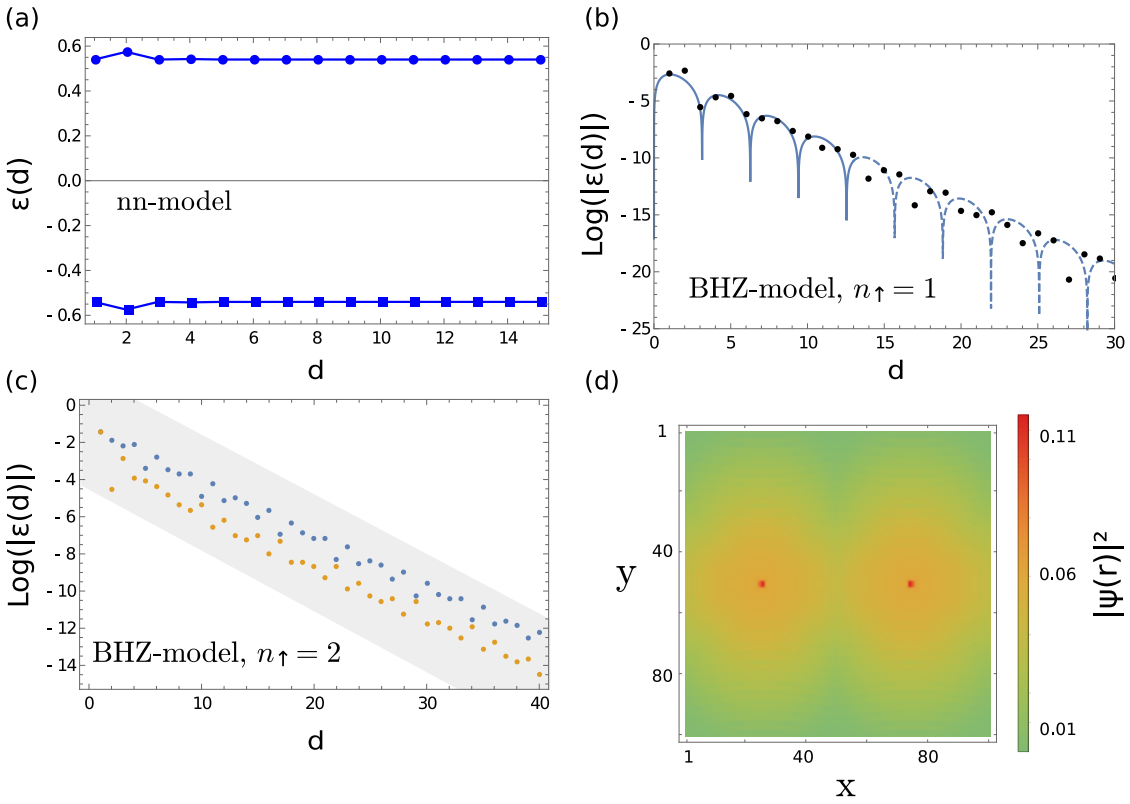

Figure 7.5.: (a)-(c) Excitation energies $\epsilon(d)$ of in-gap states as a function of the vison-pair separation d for (a) the nearest neighbor spin liquid in Eq. (7.6), (b) the BHZ-like spin liquid in the phase with $n_\uparrow = 1$ [see Eq. (7.8)] and (c) the BHZ-like spin liquid in the phase with $n_\uparrow = 2$. The corresponding mean-field parameters are the same as in Fig. 7.4. The plots in (b) and (c) use a logarithmic energy axis and only show the positive part of the spectrum (the negative part is an exact mirror image). Note that all depicted data points are degenerate with respect to the spin degree of freedom. In (b) we find indications for an oscillating modulation as indicated by a fit of $\epsilon(d)$ to a function $\sim e^{-ad}\cos(bd + \phi)$ with fit parameters a, b, ϕ (blue line). The quality of the fit becomes worse at larger d, see dashed blue line. (d) Real-space probability distribution of the spinon wave function corresponding to the zero-energy mode of the $n_\uparrow = 1$ BHZ-like system in (b). The locations of the vison cores are given by the red spots where the wave function is sharply peaked. (Figure taken from [53])

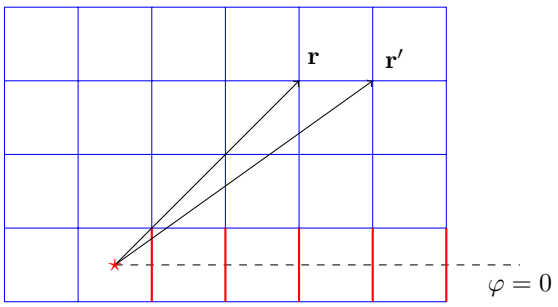

Figure 7.6: Possible gauge-field configuration $\sigma^z_{\mathbf{r}\mathbf{r}'}$ for a single vison, located at the origin (marked by a red star). Blue (red) bonds correspond to $\sigma^z_{\mathbf{r}\mathbf{r}'} = 1$ ($\sigma^z_{\mathbf{r}\mathbf{r}'} = -1$). Bonds with $\sigma^z_{\mathbf{r}\mathbf{r}'} = -1$ form a string along the $\varphi = 0$ line. For large $\mathbf{r}, \mathbf{r}' \gg 1$, the angle $\varphi_{\mathbf{r}} - \varphi_{\mathbf{r}'}$ between two coupled lattice sites $\mathbf{r}$, $\mathbf{r}'$ vanishes, see text for details. (Figure taken from [53])

spinon-vison pairs. The modes show an exponential decay in energy as the visons of the pair are spatially separated. The plots may suggest that the exponential decay is further modified by an oscillating function. Such behavior has also been observed in numerical studies of the Kitaev honeycomb model where included visons form superlattices [105, 106]. These oscillations are linked to fusion rules of the composite particles. If the model is in the phase for which $n_\uparrow = 2$ two additional degenerate modes appear. One also finds an exponential decay as the distance between the pair constituents increases. These localized modes can be linked to the previously discussed Majorana modes $\gamma_L, \gamma_R, \eta_L, \eta_R$ [107, 108]. Their existence can be understood by the following argument: The boundary of the frustrated plaquette describes a phase transition between a trivial phase, governing the interior of the vison core, and the topological phase surrounding it. The interface marks then the gap closing point. This effect is well known for fermionic systems coupled to a vortex [56], and a similar phenomenon has been explained for topological $p + ip$ superconductor [57, 109, 96]. The correspondence between the spinon-vison model and the one describing superconductors can be made rigorous by taking a continuum limit of the lattice model. To this end the BHZ like spinon model (7.8) in the phase $n_\uparrow = 1$ is expanded up to second-order around $\mathbf{k} = 0$. In the continuum limit, the real-space Hamiltonian is given by

$$H = \int d^2\mathbf{r}\, \Psi^\dagger(\mathbf{r}) \begin{pmatrix} h(\mathbf{r}) & 0 \\ 0 & h^*(\mathbf{r}) \end{pmatrix} \Psi(\mathbf{r}), \tag{7.17}$$

with

$$h(\mathbf{r}) = \begin{pmatrix} -\frac{1}{2m}\nabla^2 + \mu & \gamma\left(\partial_x + i\partial_y\right) \\ \gamma\left(\partial_x - i\partial_y\right) & \frac{1}{2m}\nabla^2 - \mu \end{pmatrix}. \tag{7.18}$$

The mass term can be expressed in terms of the lattice model parameters as $\frac{-1}{\alpha+\beta}$ and the chemical potential as $\mu = 2\alpha + \beta$. Each spin sector $h(\mathbf{r})$ has the typical Bogoliubov-de Gennes form of a triplet superconductor where γ denotes the pairing amplitude. In the lattice model, $\mathbf{k} = 0$ marked a band inversion point. This

topological property is correctly captured in the continuum model for which the mass changes sign in the lower band of Eq. (7.18). Going back to the lattice model

$$H = \sum_{\mathbf{r}\mathbf{r}'} \left[\Psi^\dagger_{\mathbf{r}} \sigma^z_{\mathbf{r}\mathbf{r}'} \begin{pmatrix} h_{\mathbf{r}\mathbf{r}'} & 0 \\ 0 & h^*_{\mathbf{r}\mathbf{r}'} \end{pmatrix} \Psi_{\mathbf{r}} + h.c. \right] \tag{7.19}$$

one can include a single vison at the origin by inserting a string of negative bonds that extend to $x \to \infty$. This, as illustrated in Fig. 7.6, shifts the second vison to infinity. To put the origin in the center of a plaquette all sites are labeled according to $\mathbf{r} = (0.5 + n_x, 0.5 + n_y)$ for $n_x, n_y \in \mathbb{Z}$. The string of negative bonds $\sigma^z_{\mathbf{r}\mathbf{r}'} = -1$ is then defined for all bonds connecting $\mathbf{r}, \mathbf{r}'$ where $x, x' > 0$ and $y > 0, y' < 0$. All other bonds are positive $\sigma^z_{\mathbf{r}\mathbf{r}'} = 1$. In the continuum model this string will cause a branch cut. In order to circumvent this obstruction consider the gauge transformation

$$\begin{pmatrix} f_{\mathbf{r}\uparrow} \\ f^\dagger_{\mathbf{r}\downarrow} \end{pmatrix} \to \begin{pmatrix} e^{i\frac{\varphi_{\mathbf{r}}}{2}} & 0 \\ 0 & e^{-i\frac{\varphi_{\mathbf{r}}}{2}} \end{pmatrix} \begin{pmatrix} f_{\mathbf{r}\uparrow} \\ f^\dagger_{\mathbf{r}\downarrow} \end{pmatrix} \tag{7.20}$$

which includes a phase variable $\varphi \in [0, 2\pi[$ given by the polar angle of $\mathbf{r}$ in the mathematical sense such that the x axis defines $\varphi = 0$. This transformation acts on the upper block of Eq, (7.19) as

$$h_{\mathbf{r}\mathbf{r}'} \to \begin{pmatrix} h^{11}_{\mathbf{r}\mathbf{r}'} e^{-i\frac{\varphi_{\mathbf{r}} - \varphi_{\mathbf{r}'}}{2}} & h^{12}_{\mathbf{r}\mathbf{r}'} e^{-i\frac{\varphi_{\mathbf{r}} + \varphi_{\mathbf{r}'}}{2}} \\ h^{21}_{\mathbf{r}\mathbf{r}'} e^{i\frac{\varphi_{\mathbf{r}} + \varphi_{\mathbf{r}'}}{2}} & h^{22}_{\mathbf{r}\mathbf{r}'} e^{i\frac{\varphi_{\mathbf{r}} - \varphi_{\mathbf{r}'}}{2}} \end{pmatrix} \tag{7.21}$$

where the superscripts denote the corresponding matrix elements of $h_{\mathbf{r}\mathbf{r}'}$. In this gauge, one can now approach the continuum limit. If $\mathbf{r}, \mathbf{r}' \gg 1$ the corresponding angles become equal, which leads to a transformation

$$h_{\mathbf{r}\mathbf{r}'} \to \begin{pmatrix} h^{11}_{\mathbf{r}\mathbf{r}'} & h^{12}_{\mathbf{r}\mathbf{r}'} e^{-i\varphi_{\mathbf{r}}} \\ h^{21}_{\mathbf{r}\mathbf{r}'} e^{i\varphi_{\mathbf{r}}} & h^{22}_{\mathbf{r}\mathbf{r}'} \end{pmatrix}. \tag{7.22}$$

For sites that are connected by a negative bond, the phase angle is $\varphi_{\mathbf{r}} = \delta\varphi$ and $\varphi_{\mathbf{r}'} = 2\pi - \delta\varphi$. In the continuum limit $\delta\varphi \to 0$ vanishes. For these bonds the transformation becomes

$$h_{\mathbf{r}\mathbf{r}'} \to -h_{\mathbf{r}\mathbf{r}'}. \tag{7.23}$$

Thus this construction has correctly included a continuous phase variable $\varphi(\mathbf{r})$ and the branch cut, leading to a winding number. The resulting continuum model includes one single vison and can be written as

$$h(\mathbf{r}) = \begin{pmatrix} -\frac{1}{2m}\nabla^2 + \mu & \gamma\left(\partial_x + i\partial_y\right) e^{-i\varphi(\mathbf{r})} \\ \gamma\left(\partial_x - i\partial_y\right) e^{i\varphi(\mathbf{r})} & \frac{1}{2m}\nabla^2 - \mu \end{pmatrix} \tag{7.24}$$

which represents the Bogoliubov-de Gennes Hamiltonian of a $p+ip$ superconductor coupled to a vortex in the pairing field. For this system the existence of Majorana zero modes has been analytically shown [56, 57, 96]. This discussion does not entirely capture the properties of the $n_\uparrow = 2$ phase as a second point of band inversion exists. One would have to do a second expansion around this point to derive the correct continuum model.

7.2.4. Vison gas

After gaining a grasp of the physics behind a single vison pair, in the following, the more realistic scenario will be studied in which a finite number of visons are initialized. This number has to be much smaller than the total number of plaquettes to remain in the same phase of the model. Two different vison populations are taken into account for which the vison density, given by the ratio of frustrated plaquettes to the total number of plaquettes, is fixed to 0.6% or 2%. This yields a mean distance of approximately ~ 14 to ~ 7.5 lattice spacing between the vison pairs. To avoid unwanted boundary effects the calculations are executed on a torus. The results for the three spinon models, already encountered in the last sections, are given in Fig. 7.7. In all examples, a clear peak in the bulk gap is seen. In the trivial nearest-neighbor model this peak is located at a finite energy $\epsilon \approx 0.52$, whereas, for both topological models, it appears around zero energy. A broadening of this peak at zero energy is observed at the higher density of 2%, which is more pronounced in the phase $n_\uparrow = 2$. This broadening is due to hybridization among the different zero modes. In the phase $n_\uparrow = 2$ hosts twice as many Majorana modes compared to the $n_\uparrow = 1$ phase. This explains the different broadening behavior. In both topological models, a second yet significantly smaller peak can be identified at $\epsilon \approx 0.26$, which can be related to two visons having a distance of one single plaquette. This peak is expected to be an artifact of the static approximation. If the gauge field dynamics are considered, visons may be subject to a mutual repulsive or attractive force that modifies the position and weight of this peak. In all three studied scenarios, such an in-gap peak might be a relevant signature that could be verified in an experiment, and its position could yield valuable information about the spinon band topology.

7.3. Conclusion

The first part of this work continued an analysis in order to identify and characterize spinon mean-field states exhibiting exotic band properties. The previous analysis [54] based on a projective symmetry group classification on the square lattice, in which it was explicitly assumed that spin-orbit effects break spin rotational symmetry, revealed too many states such that it became impossible to draw any unifying

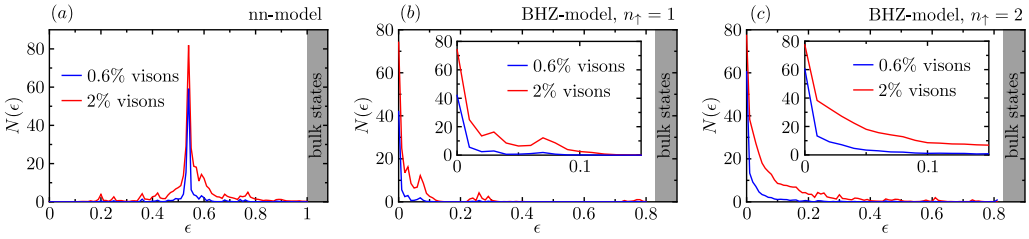

Figure 7.7.: Fermionic spinon density of states $N(\epsilon)$ in the bulk gap for a dilute gas of randomly arranged visons. The vison density is indicated for each curve. Using a system size of 100×100 lattice sites, $N(\epsilon)$ counts the number of states in each energy interval of length 0.01. All results are averaged over 100 different realizations. The thick gray line indicates the onset of the bulk gap. The data in (a) - (c) corresponds to the nearest-neighbor spin liquid, the BHZ-like model with $n_\uparrow = 1$ and the BHZ-like model with $n_\uparrow = 2$, respectively, with the same parameters as in Fig. 7.4. The insets in (b) and (c) show the density of states in the low-energy region. (Figure taken from [53])

conclusions. In order to circumvent this problem here only states were taken into account whose mean-field Hamiltonian includes only short-ranged coupling terms. This assumption reflects the expected behavior of realistic materials and, in this regard, makes the scenario even more plausible than the generic case where the coupling length is unrestricted. In the case where only nearest-neighbor sites couple, the number of relevant PSG representations is reduced from initially 1488 to 28. It was found that the corresponding mean-field models cannot bear topological spinon band features. This observation relies on a competition between different representation matrices and the requirement that the resulting spinon model contains only a $\mathbb{Z}_2$ invariance group. The invariance group is determined by the sub-space perpendicular to the direction of loop operators in the spinor space. These loop operators are products of coupling matrices along a closed path. Nearest-neighbor coupling matrices on the square lattice are not flexible enough to produce the necessary loop operators to break the gauge freedom down to $\mathbb{Z}_2$. Even for these 28 remaining candidates, it was not possible to find some unifying features. The band dispersion depends on too many parameters, and for a single model, different phases can be constructed according to the parameter tuning. One particular PSG is identified for which the mean-field Hamiltonian decouples in the spin sector. Including second neighbors paves the way for more complex loop operators, which immediately leads to possible $\mathbb{Z}_2$ states. As this also drastically increases the number of relevant PSGs, further assumptions were made, which led to only two distinct spinon models. Both models resemble the Bernevig-Hughes-Zhang model and host non-trivial spinon bands. For one of these models, the band properties are studied in detail, and the existence of protected Majorana modes is explained.

In the second part, the prior constructed spinon models are extended by coupling to a static gauge field. By choosing one proper configuration of this gauge field, one can mimic the effect of a vison. In this setting, the confining properties of spinon particles were studied. For all models, it could be affirmed that the resulting quasiparticles are subjects to a weak short-ranged potential, thus corroborating the assumption that the underlying physics should be governed by a $\mathbb{Z}_2$ lattice gauge theory in the deconfining phase. In the case of non-trivial spinon bands, it was further observed that visons bind to spinon modes, and the resulting composite objects can be described by a Majorana zero mode. This behavior, similarly observed in the context of $p + ip$ superconductors and vortices, could be made rigorous by a mapping from the present lattice model to a continuum theory. Finally, the effect of multiple visons was studied. These visons were randomly distributed over a given sample by keeping their density fixed. The resulting observation provides information about some features in the energy distribution, which can be used in future experiments to gain information about the spinon band topology.

8. Signatures for spinons in the quantum spin liquid candidate $Ca_{10}Cr_7O_{28}$

This chapter is dedicated to the theoretical work which was published in Ref. [59].

The idea of a quantum spin liquid and the theory behind hurries ahead of accessible experimental materials; First proposed in the early seventies by Phil Anderson [15], it took over thirty years until experiments caught up and revealed that in some organic salt compounds, the heat capacity grows linearly for low temperatures [110]. This would not be worth mentioning if these materials were usual conductors. For conductors, it is a well-established result by Sommerfeld's semiclassical extension of the Drude model. In the Sommerfeld model, quantum effects are taken into account using a Fermi distribution instead of a classical Boltzmann partition function [111]. Employing this theory, one can relate the fact that free electrons are ferimons to the linear temperature dependence of the heat capacity. Yet these organic salt compounds are insulators in which no electric charge is transported. This obstructs the usual arguing. It seems like there is something that behaves as a fermion but does not move electric charge. This something can be most likely identified by spinons [29, 112, 113]. κ-salt compounds are not the only materials showing spin liquid behavior and signatures of spinons. Other are for example Herbertsmithite which has a kagome lattice structure [43, 44, 114] [$ZnCu_3(OH)_6Cl_2$], $YbMgGaO_4$ forming a triangular lattice [115, 116, 117], and α-$RuCl_3$ which has gained a lot attention lately as it might realize the Kitaev honeycomb material [46, 48, 47, 118, 49]. However, until now, it is still under debate whether real spin liquid materials have been found. As often, an unambiguous interpretation of the experiments is not given. For instance, the properties observed in the case of $YbMgGaO_4$ might be merely induced by disorder [119]. Other materials initially related to quantum spin liquids eventually develop magnetic order as lower temperatures are approached. In this regard building, a bridge between possible experimental realizations and current theoretical development is of paramount importance for advancing the field.

The compound $Ca_{10}Cr_7O_{28}$ is another candidate that has been recently identified [50]. The crystal structure of this material and its essential properties will be explained in some depth. It will serve as a candidate to test the mean-field theory developed in Chapter 2. Based on the parton approach and the resulting mean-field theory, an effective spinon model is presented, which at one hand sim-

plifies the complex double layer crystal structure of the investigated material but, on the other hand, draws a coherent picture of the fundamental physics behind the measured data. The assumptions behind this model are explained and physically motivated. The model further allows for the evaluation of the dynamical structure factor which, as explained in Chapter 6, is the relevant quantity resolved by inelastic neutron scattering experiments. Many of the observed features found in the experiment are reproduced in the theoretical calculation, and it is possible to track down their physical origin. In the end, it is studied how a spinon pairing mechanism can explain measured deviations from a linear temperature dependence of the heat capacity. Such a pairing is in accordance with the prior developed spinon hopping model and completes the picture of $\mathbb{Z}_2$ quantum spin liquid.

8.1. $Ca_{10}Cr_7O_{28}$

Among spin liquid candidates, there is one particularly interesting, namely $Ca_{10}Cr_7O_{28}$ [50, 51]. Its crystal structure consists of a kagome bilayer built by the magnetic active Cr^{5+} ions, which is illustrated in Fig. 8.1. These ions carry spin-1/2. The intriguing fact is that their mutual couplings are ferro- as well as antiferromagnetic, as shown in Tab. 8.1. This leads to a rather unusual mechanism of frustration. Combining these different couplings yields a microscopic picture expressed by a Heisenberg Hamiltonian $H = \frac{1}{2}\sum_{\mathbf{r}\mathbf{r}'} \mathbf{S}_\mathbf{r}\mathbf{S}_{\mathbf{r}'}$. It was observed that couplings of a certain type form triangles, i.e., three spins are coupled either ferro- or antimagnetically. These triangles appear in an alternating order such that one triangle of a certain type is adjacent to the opposite type. Taking the spatial direction perpendicular to these planes into account shows that a stacking pattern arises where one ferromagnetic triangle lies on top of an antiferromagnetic one and vice versa. This combination results in the bilayer kagome structure. Importantly, an additional ferromagnetic coupling between these layers drives the mechanism of frustration. Supported by numerical studies, this material seems to refrain magnetic order even at zero temperature [50, 120, 121, 122].

J_0	J_{21}	J_{22}	J_{31}	J_{32}
$-0.08(4)$	$-0.76(5)$	$-0.27(3)$	$0.09(2)$	$0.11(3)$

Table 8.1.: Exchange couplings of $Ca_{10}Cr_7O_{28}$ as determined in Refs. [50, 51]. All couplings are given in meV.

As other spin liquid claimants, this material shows a linear temperature dependency of the heat capacity in an extended low-temperature range, as shown in Fig. 8.2. Data obtained by inelastic neutron scattering experiments represented

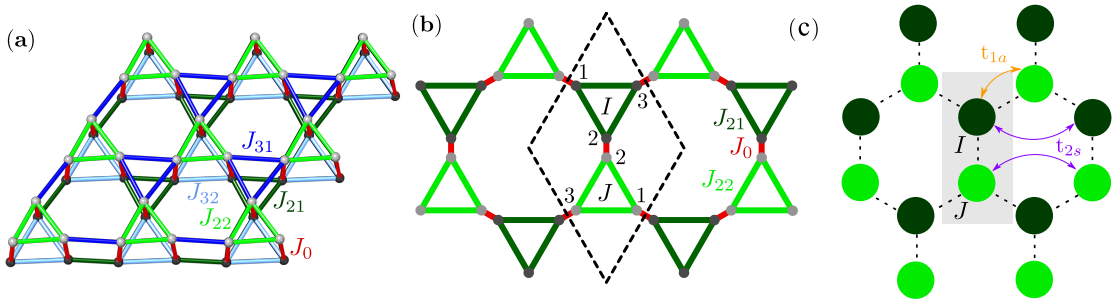

Figure 8.1.: (a) Bilayer kagome lattice as realized in $Ca_{10}Cr_7O_{28}$. The differently colored bonds carry the interactions J_0, J_{21}, J_{22}, J_{31}, and J_{32} as indicated in the figure, see also Table 8.1. (b) Effective decorated honeycomb lattice arising from a projection of the ferromagnetically coupled triangles (green triangles labeled I, J) of the bilayer kagome system into one plane. Bonds are colored and labeled in the same way as in (a), except the antiferromagnetic (blue) bonds which are not shown for reasons of clarity. Note that sites coupled by the vertical ferromagnetic interlayer couplings (red lines) almost coincide in their position after projection. We have, hence, increased their in-plane distance in this illustration for better visibility. Dark gray (light gray) dots denote sites in the lower (upper) plane. Dashed lines mark the boundaries of the unit cell and numbers label the sites within ferromagnetically coupled triangles. (c) Effective honeycomb lattice with hopping amplitudes t_{a1}, t_{s2} as they are used in the phenomenological model in Eq. (8.4). In this illustration, each green point corresponds to a ferromagnetic triangle. (Figure taken from [59])

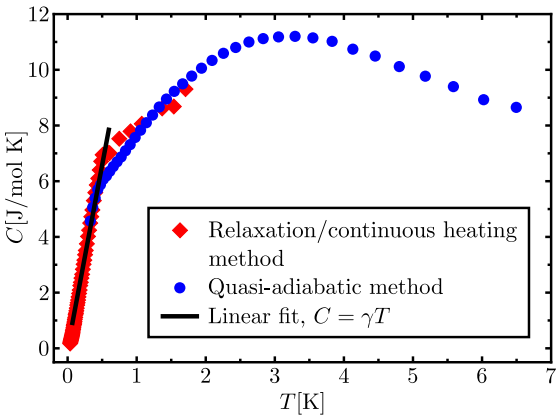

Figure 8.2: Measured heat capacity of $Ca_{10}Cr_7O_{28}$ in an extended temperature range. Shown are two different data sets corresponding to two different experimental methods that have been used for the measurement. The exact details of these methods are explained in Refs. [59, 50, 51, 52]. The black line indicates the approximate linear behavior at low temperatures. (Figure taken from [59])

in Fig. 8.3 show a very diffusive response in the low-temperature regime, which is not compatible with any sharp dispersive excitations. This indicates that no magnetic order is present and excludes spin-wave excitations, as discussed in Chapter 6. Besides the fact that no magnetic peaks can be identified[1] one sees, however, some structural features. For instance, one finds two distinct regions of finite intensity, best seen in subfigure Fig. 8.2(f). The low-energy region reaches roughly from $0 - 0.6\ meV$ and the high energy region from $0.8 - 1.5\ meV$. In the lower region, one observes V-shaped forms appearing around the Γ points. The plots of an extended region in momentum space for constant energies show in the low-energy region that the signal is mostly pronounced within the first Brillouin zone (black lines) Fig. 8.2(a, b). One sees further that for an increment of the energy, the signal vanishes at the zone center Γ. The largest intensity observed for the higher region in energy Fig. 8.2(c, d) lies outside of the first zone and tends towards the zone boundary of the extended Brillouin zone (red lines). As it will be explained in the suite of this chapter many of these signatures can be coherently explained by a spinon picture based on an effective mean-field theory.

8.2. Effective spinon model for $Ca_{10}Cr_7O_{28}$

Instead of carrying out a lengthy PSG analysis, as it is done in the other contributions to this thesis, which would reveal the symmetry dictated form of any possible *Ansatz* plus necessary information about the low-energy gauge group, in this work, a bolder tactic is chosen. Guided by the experimental evidence, it is suggested that $Ca_{10}Cr_7O_{28}$ is indeed a quantum spin liquid. Its fundamental excitations are fractional spin-1/2 objects such that the parton approach, introduced in Chapter 2, is the right formalism to describe these deconfined particles. The low-energy behavior is governed by a stable saddle-point solution obtained from a mean-field decoupling

[1] The peaks that are visible at the M points can be related to phonons.

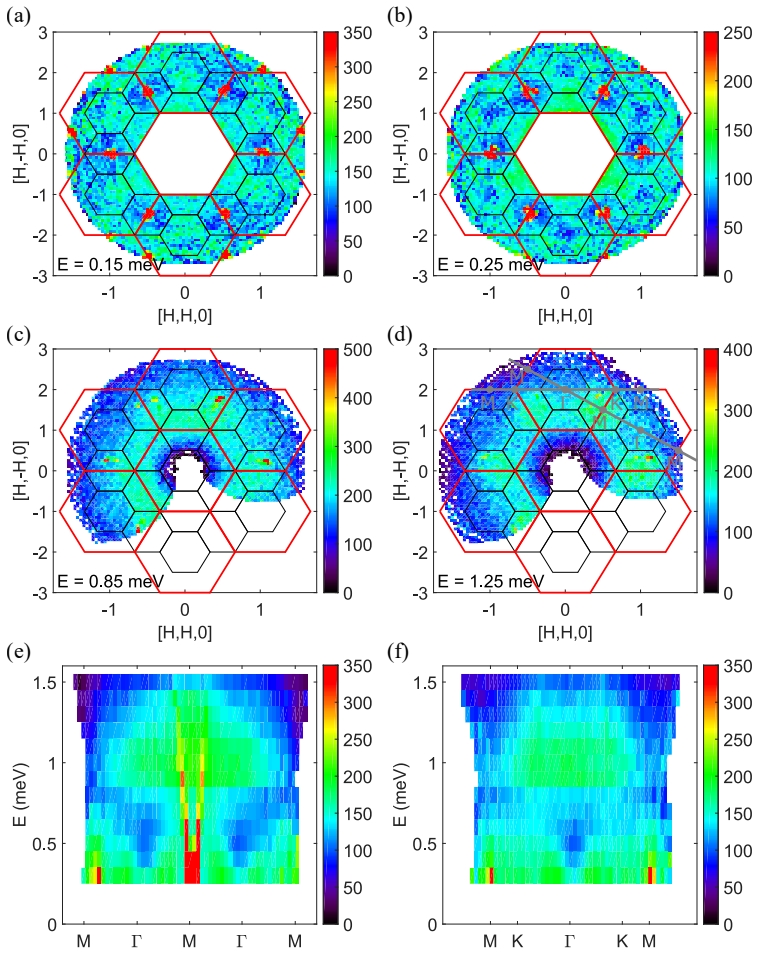

Figure 8.3.: Inelastic neutron scattering data of $Ca_{10}Cr_7O_{28}$. (a) - (d) Constant energy slices as a function of the momentum transfer in the kagome bilayer plane. The black (red) hexagons indicate the boundaries of the first (extended) Brillouin zone. The energy transfer is indicated in each plot. (e) - (f) Energy versus momentum slices along two high-symmetry directions within the kagome bilayer plane. The two momentum cuts are illustrated by the gray lines in (d). Note that the color scale is different in each subfigure. The sharp features appearing in red outside the color scale are phonons dispersing out of nuclear Bragg peaks. Note that the constant energy slices in (a) and (b) were measured with a final energy of $E_f = 2.5$ meV which leads to an overall lower intensity compared to the constant energy slices in (c) and (d) measured with $E_f = 3$ meV. For the energy versus momentum slices in (e) and (f) all data was taken with $E_f = 3$ meV. Furthermore, the data in these two plots was collected by integrating the signal over ± 0.2 r.l.u. in directions perpendicular to the respective cuts. (Figure taken from [59])

in which the spinons are expressed as free fermions. The gauge field can be safely approximated as being static. After this long list of rather keen assumptions, the dear reader's alarm bell should start ringing as there are doubtlessly many question marks behind every statement. However, the phenomenological spinon model presented here renders an astonishingly coherent description of the empirical findings.

The starting point of this phenomenological description is a generic mean-field Hamiltonian which can be written as [26, 5, 11]

$$H = \sum_{\mathbf{r}\mathbf{r}'} \left(t_{\mathbf{r}\mathbf{r}'} f^\dagger_{\mathbf{r}\alpha} f_{\mathbf{r}'\alpha} + \Delta_{\mathbf{r}\mathbf{r}'} f_{\mathbf{r}\uparrow} f_{\mathbf{r}'\downarrow} + h.c. \right) + \mu \sum_{\mathbf{r}} n_{\mathbf{r}}, \tag{8.1}$$

with spinon creation operators $f^\dagger_{\mathbf{r}\alpha}$, hopping amplitudes $t_{\mathbf{r}\mathbf{r}'}$, singlet pairing amplitudes $\Delta_{\mathbf{r}\mathbf{r}'}$ and a chemical potential μ. This model stems from a decoupling of the interacting Heisenberg Hamiltonian in the singlet channel only, which is in accordance with the experimental data [50]. Using Eq. 8.1 one can obtain the dynamical structure factor as described in Chapter 6. The remaining task then is to adjust the mean-field amplitudes such that it best fits the neutron data. Similar approaches have been made in the past for other materials like $YbMgGaO_4$, herbertsmithite, $Na_4Ir_3O_8$ and $Ba_3NiSb_2O_9$ [115, 94, 95, 123, 124, 125]. Yet for those materials, the Heisenberg model comprises only very few magnetic couplings $J_{\mathbf{r}\mathbf{r}'}$. Even though there is no one-to-one mapping between the coupling constants and the mean-field amplitudes, it is a plausible route to derive the corresponding mean-field amplitudes[2]. The difficulty of doing this for $Ca_{10}Cr_7O_{28}$ lies in the complicated structure of the spin model, which includes multiple ferro- and antiferromagnetic coupling constants. Instead of pursuing the goal of determining all possible hopping and pairing amplitudes, here a minimal model is presented, which reduces the number of relevant tuning parameters yet still capturing the key features of the experimental data. This reduction is based on the observation that in the kagome double layer crystal structure of $Ca_{10}Cr_7O_{28}$ one triangle per layer per unit cell exists in which the magnetic relevant Cr^{5+} ions are coupled ferromagnetically, represented by the green bonds in Fig. 8.1. These ferromagnetic couplings are at least twice as strong as their antiferromagnetic counterpart (compare Tab. 8.1). This observation suggests using a basis reflecting this comportment rather than using the individual spinon operators $f_{\mathbf{r}\alpha}$. The first basis vector is built as a symmetric superposition of the three ferromagnetically coupled sites of one layer defined as

$$c_{sI\alpha} = \frac{1}{\sqrt{3}} \left(f_{I1\alpha} + f_{I2\alpha} + f_{I3\alpha} \right). \tag{8.2}$$

The index $I \in \{1, 2\}$ corresponds to one specific triangle, the index α remains the spin degree, and s denotes the first basis vector as the symmetric superposition.

[2] Obviously, $t_{\mathbf{r}\mathbf{r}'}$ and $\Delta_{\mathbf{r}\mathbf{r}'}$ are gauge dependent quantities and hence cannot be directly matched with the physical $J_{\mathbf{r}\mathbf{r}'}$ constants.

This new operator $c_{sI\alpha}$, since it combines three ferromagnetically coupled spin-1/2 particles, can be regarded as a creation operator of an effective spin-3/2 object. These objects will be the relevant constituents for the low-energy regime. In order to span the entire vector space, two additional linear independent basis vectors are required which are chosen to be

$$\begin{aligned} c_{a1I\alpha} &= \frac{1}{\sqrt{2}}\left(f_{I1\alpha} - f_{I2\alpha}\right) \\ c_{a2I\alpha} &= \frac{1}{\sqrt{6}}\left(f_{I1\alpha} + f_{I2\alpha} - 2f_{I3\alpha}\right), \end{aligned} \tag{8.3}$$

where the indexes a_1, a_2 denote antisymmetric superpositons[3]. These spin-1/2 objects will be relevant for the high energy regime of the effective theory. A simple counting shows that after summing over the layer index I a basis given by $\{c_{s1\alpha}, c_{s2\alpha}, c_{a11\alpha}, \ldots\}$ correctly represents the 6 atomic unit cell for spin α.

Focusing on the basis vectors $c_{sI\alpha}$, it seems natural to redraw the lattice such that the bilayer kagome lattice becomes a honeycomb lattice effectively as illustrated in Fig. 8.1. Neglecting possible pairing terms for the time being it is suggested that an effective spinon hopping model can be built upon this honeycomb lattice using the c operators. Such a model can generically be written as

$$\begin{aligned} H = \sum_{\alpha} \Bigg[& \sum_{\langle IJ \rangle} t_{1s} c^{\dagger}_{sI\alpha} c_{sJ\alpha} + t_{1a}\left(c^{\dagger}_{a1I\alpha} c_{a1J\alpha} + c^{\dagger}_{a2I\alpha} c_{a2J\alpha}\right) \\ & + \sum_{\langle\langle IJ \rangle\rangle} t_{2s} c^{\dagger}_{sI\alpha} c_{sJ\alpha} + t_{2a}\left(c^{\dagger}_{a1I\alpha} c_{a1J\alpha} + c^{\dagger}_{a2I\alpha} c_{a2J\alpha}\right) + h.c. \\ & + \sum_{I} \mu_s c^{\dagger}_{sI\alpha} c_{sI\alpha} + \mu_a\left(c^{\dagger}_{a1I\alpha} c_{a1I\alpha} + c^{\dagger}_{a2I\alpha} c_{a2I\alpha}\right) \Bigg], \end{aligned} \tag{8.4}$$

where the amplitudes $t_{1s}, (t_{2s})$ describe hopping between (next) nearest neighbor sites of the c_s objects on the honeycomb lattice, correspondingly $t_{1a}, (t_{2a})$ for the c_{a1}, c_{a2} objects. The chemical potentials μ_s, μ_a are of paramount importance as they separate between the symmetric and antisymmetric sectors energetically. Thus one can distinguish between the dynamics of the spin-3/2 objects which emerge due to the comparably strong ferromagnetic coupling in one triangle and the spin-1/2 objects which reflect a single spin-flip within one of these triangles. As there is no physical argument about the exact structure of the antisymmetric sector the corresponding hopping amplitudes $t_{a1} = t_{a2} \equiv t_a$ and the chemical potential $\mu_{a1} = \mu_{a2} \equiv \mu_a$ are equal such that the Hamiltonian is symmetric under an exchange of

[3]Note that the new basis vector c_s, c_{a1}, c_{a2} correspond to the irreducible representations of the dihedral group D_3 describing the underlying equilateral triangle [76, 77].

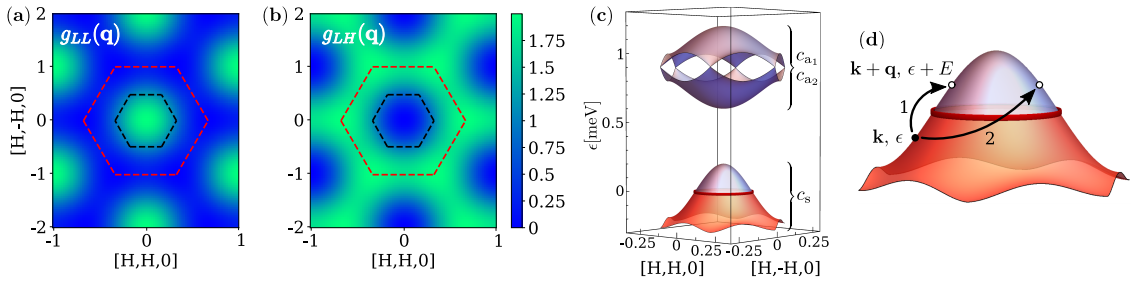

Figure 8.4.: (a), (b) Weight factors $g_{\mathrm{LL}}(\mathbf{q})$ and $g_{\mathrm{LH}}(\mathbf{q})$ of the dynamical spin structure factor $\mathcal{S}(\mathbf{q}, E)$ as defined in Eqs. (8.5)-(8.9) for the spinon hopping amplitudes given in Eq. (8.10). Here, $g_{\mathrm{LL}}(\mathbf{q})$ ($g_{\mathrm{LH}}(\mathbf{q})$) is the total weight factor for all particle-hole excitation processes within the low-energy bands formed by c_{s} (between the low-energy bands formed by c_{s} and the high-energy bands resulting from c_{a_1}, c_{a_2}). Black (red) dashed lines indicate the boundaries of the first (extended) Brillouin zone. (c) Spinon band structure for the same set of spinon hopping amplitudes [see Eq. (8.10)]. Low-energy (high energy) bands are marked by the corresponding spinon operators c_{s} (c_{a_1} and c_{a_2}) they result from. The red line marks the Fermi surface. Note that all bands are doubly degenerate. (d) Illustration of two different particle-hole excitations around the Fermi surface with a given energy E. Process 1 shows an excitation from an occupied state (full black dot) with momentum and energy $\mathbf{k}$, ϵ to an unoccupied state (open dot) with $\mathbf{k}+\mathbf{q}$, $\epsilon+E$ for the minimal momentum transfer $\mathbf{q}$ which linearly depends on the energy E. Process 2 is an example for a particle-hole excitation with larger momentum transfer. (Figure taken from [59])

the indices $a_1 \leftrightarrow a_2$. This division into low and high energy sectors can be related to a semi-classical study of $Ca_{10}Cr_7O_{28}$ where it has been observed that the spins develop different dynamics on short and long time-scales [120].

In fact, merely tuning the chemical potentials μ_s, μ_a, such that the Fermi energy cuts the energy bands of the symmetric sector, yielding a Fermi surface as indicated by the linear temperature dependence of the heat capacity, and pushing the bands of antisymmetric sector up in energy such that a gap in energy separates both sectors, already reveals some of the main features seen in the dynamical structure factor, remarkably, without any tuning of the remaining hopping amplitudes. Recalling the fermionic representation of the dynamical structure factor as explained in Chapter 6

$$\mathcal{S}^{zz}(\mathbf{q}, E) = \frac{\pi}{24} \sum_{a,b} \int \frac{d^2k}{(2\pi)^2} f(\mathbf{k}, \mathbf{q}, a, b) \left[n_a(\mathbf{k}) - n_b(\mathbf{k}+\mathbf{q})\right] \delta(\epsilon_b(\mathbf{k}+\mathbf{q}) - \epsilon_a(\mathbf{k}) - E), \tag{8.5}$$

here $n_a(\mathbf{k})$ denotes the occupation number of a band labeled by index a at momentum $\mathbf{k}$, $\epsilon_a(\mathbf{k})$ represents the corresponding energy. As there is a six atomic unit

cell[4] the band index takes the values $a = \{1, \ldots, 6\}$. The two lower bands correspond to the symmetric operators c_{sI} and the four others to c_{a1I}, c_{a2I}. The spin structure factor describes processes of spinon particle-hole excitations. The factor $n_a(\mathbf{k}) - n_b(\mathbf{k}+\mathbf{q})$ gives finite contributions to the integral for all possible ways of how an occupied particle state can connect to an empty hole state and vice versa, by conserving the energy E and momentum $\mathbf{q}$ of the incoming neutron, which is guaranteed by the delta function. This is depicted in Fig. 8.4. Up to now nothing has been said about the function $f(\mathbf{k}, \mathbf{q}, a, b)$. It turns out that this function plays an interesting role. In Chapter 6, it was identified as a product of different matrix elements of the unitary transformations which diagonalized the Hamiltonian. It can be written as

$$f(\mathbf{k}, \mathbf{q}, a, b) = \left| \sum_{\kappa} \phi^*_{a\kappa}(\mathbf{k}) \phi_{b\kappa}(\mathbf{k}+\mathbf{q}) e^{i\mathbf{q}\mathbf{R}_\kappa} \right|^2 \tag{8.6}$$

with $\phi_{a\kappa}(\mathbf{k})$ being an eigenstate of Eq. 8.4 at sublattice position κ of band a at momentum $\mathbf{k}$. The vector $\mathbf{R}_\kappa$ points to the position of κ within the unit cell. This means that f gives the overlap of the particle and hole wave functions. By first taking its momentum integrated form

$$g(\mathbf{q}, a, b) = \int \frac{d^2k}{(2\pi)^2} f(\mathbf{k}, \mathbf{q}, a, b) \tag{8.7}$$

one can separate it further according to different band indexes

$$g_{\mathrm{LL}}(\mathbf{q}) = \sum_{a,b=1,2} g(\mathbf{q}, a, b), \tag{8.8}$$

which takes processes of the low-energy part into account, and

$$g_{\mathrm{LH}}(\mathbf{q}) = \sum_{a=1,2} \sum_{b=3,4,5,6} g(\mathbf{q}, a, b), \tag{8.9}$$

which represents processes that involve one state of a lower band and one from a higher band. This separation reveals valuable information about particle-hole processes according to the involved sectors. As shown in Fig. 8.4, a process within the sector of the lower bands, corresponding to the symmetric sector, shows a high intensity around the Γ point within the first Brillouin zone. Yet any signal vanishes outside the first zone. This is due to the orthogonality of the eigenstates involved in this process. One immediately sees that $f(\mathbf{k}, \mathbf{q} = 0, a, b \neq a) = 0$ and $f(\mathbf{k}, \mathbf{q} = 0, a, b = a) = 1$. Therefore, g_{LL} has to have its maximum at $\mathbf{q} = \Gamma$. Analogously, one can argue that g_{LH}, describing a process in which a particle of the symmetric

[4] Since there is no spin dependency, only one spin sector is taken into account

type becomes a hole of the antisymmetric type, cannot have a finite signal at $\mathbf{q} = \Gamma$. The intensity distribution of g_{LH} is high outside the first Brillouin zone and vanishes inside. These general properties of g_{LL} and g_{LH}, as shown in Fig. 8.4, are robust and do not depend on the precise values of the hopping amplitudes as long as they are in a reasonable range such that the two sectors are well separated in energy. With this in mind, the response can be explained as follows: Starting at low energies the relevant processes involve particle-hole excitations close to the Fermi surface. These processes are entirely governed by the dynamics of the effective spin-3/2 objects defined by the symmetric superposition of ferromagnetically coupled spins. Neglecting anisotropic effects that could discern between different layers and hence between different triangles leads to degenerate low-energy bands. This further implies that the corresponding wave functions are parallel, and thus, the scattering function $f(\mathbf{k}, \mathbf{q}, a, b = a)$ has a high intensity inside the first Brillouin zone and the signal vanishes outside. If an incoming neutron's energy increases and becomes larger than the width of the lower band, the intensity goes to zero. A gap will be seen in the structure factor. As the energy further increases such that it becomes sufficiently large to connect the lower band with the upper ones, the relevant processes involve the symmetric as well as the antisymmetric sector. Since the corresponding wave functions become orthogonal, the signal has to disappear in the first Brillouin zone and becomes finite in the extended zone.

After having identified the mechanism behind the response function the lasting endeavor is to adjust the hopping amplitudes $t_{1s}, t_{2s}, t_{1a}, t_{2a}$ which will fix the band width of the upper and lower bands respectively. Unfortunately, there is no analytic relation known which could be exploited to find the right values such that the set of parameters, which is given below has been determined by the eagle eye method

$$\begin{aligned} &t_{1s} = 0,\ t_{2s} = 0.05 \text{ meV},\ t_{1a} = 0.1 \text{ meV},\ t_{2a} = 0, \\ &\mu_s = -0.1 \text{ meV},\ \mu_a = 0.9 \text{ meV}. \end{aligned} \tag{8.10}$$

This set describes a hopping of the symmetric objects c_s between next-nearest neighbors on the honeycomb lattice. This means that they reside in one layer of the double kagome lattice. The resulting dispersion thus resembles a hopping model on a triangular lattice. As this happens for both layers equally, the low-energy bands are twice degenerate. The prior assumption chooses the chemical potentials, i.e., the Fermi surface cuts the lower bands, and the upper bands have to be clearly separated by a sufficiently large gap. The corresponding dispersion can be seen in Fig. 8.4. Using these amplitudes the dynamical structure factor has been calculated, and the result is shown in Fig. 8.5 for different energy and momenta.

At this point, it should be stressed that these results are not meant to be a quantitative explanation of the experimental data, but rather a tentative to relate

physical aspects to the signatures of the experiment. Some general statements can be readily linked to the weight function, which has previously been discussed. Tracing out paths through the Brillouin zone (shown in subfigure (e) and (f)) clearly indicates the two regions dictated by g_{LL}, which ranges from energies between 0 meV to roughly 0.35 meV, and by g_{LH}, valid for energies between 0.7 meV up to 1.4 meV. Focusing first on the low-energy regime, one sees no signal precisely at the Γ point. This can be explained by the dispersion of the spinon bands. Any finite signal here would require the existence of an occupied and unoccupied level of parallel eigenvectors, i.e., both belonging to the symmetric sector. Since there is only one degenerate band, this is impossible. Moving slightly away from the Γ point, one sees cone-like shapes. The appearance of cones is caused by processes that happen very close to the Fermi surface. In this regime, the dispersion can be approximated as being linear such that the condition for an energy transfer becomes $E = v_{sp}|\mathbf{q}|$, with v_{sp} denoting the spinon Fermi velocity. The opening angle of the cone is thus directly related to v_{sp}. The combined effect of this finite Fermi velocity and the overlap of the particle-wave functions manifests in the structure factor plots for constant energy as rings of finite intensity, which appear around the Γ point in the first Brillouin zone (compare subfigure (a), (b)). Shifting the focus to the upper region shows that, as anticipated due to the orthogonal eigenvectors involved, a finite signal appears only between the first and extended Brillouin zone borders. Further characteristics depend on the precise choice of the hopping amplitudes. As this goes beyond the applicability of the model, it shall not be discussed here.

The spinon model juxtaposed to the neutron data in Fig. 8.3 shows that many of the measured signatures can be nicely explained, but there are clearly some shortcomings. In the low-energy region, the experimental data show a broad region of a homogeneously diffusive signal contrary to the spinon model for which the signal is rather sharply drawn. This discrepancy may be explained by the lack of visonic excitations, which are completely neglected in the pure spinon model. Yet they are expected to be present in a real quantum spin liquid, and coupling between visons and spinon can lead to a smearing of the signal as demonstrated in a study conducted on an antiferromagnetical monolayer kagome system [92]. A second point for which the spinon model cannot provide an adequate description is the response observed for high energies at the Γ point. As explained, due to the orthogonality of the wave functions involved in these high energetic processes, it is impossible within this spinon theory to obtain a finite signal in this region. A remedy may be found by including terms in the mean-field model, which take anisotropic effects into account. Such anisotropic terms are indeed compatible with the $Ca_{10}Cr_7O_{28}$ crystal as the triangles are slightly distorted. Another issue is that the pure spinon hopping model leads to a $U(1)$ invariance group for which it is not a priori known if the

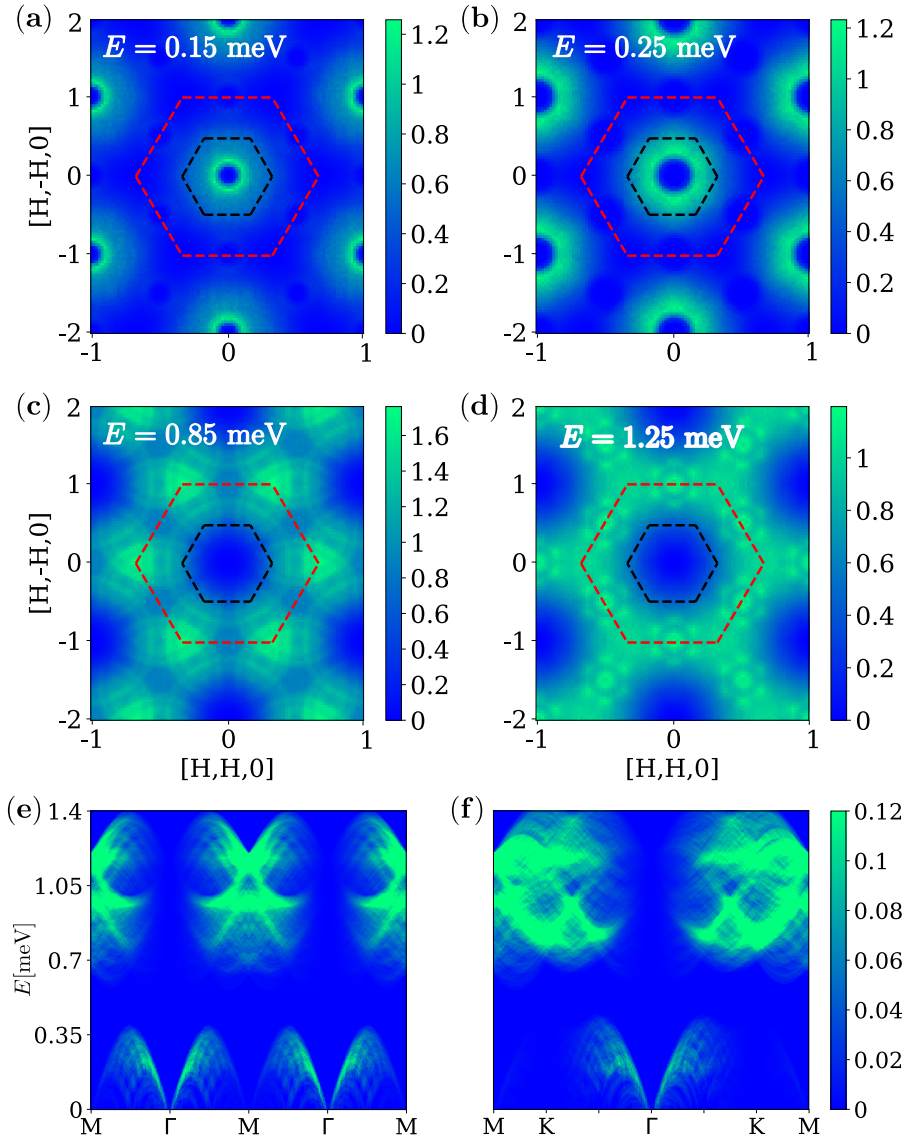

Figure 8.5.: Calculated spin-structure factor for the effective spinon model in Eq. (8.4) using the representation of $\mathcal{S}(\mathbf{q}, E)$ from Eq. (8.5) and the spinon parameters in Eq. (8.10). The plots (a)-(d) show the spin structure factor in momentum space for the same fixed energies E as for the experimental neutron data in Fig. 8.3 (a)-(d). Black (red) dashed lines indicate the boundaries of the first (extended) Brillouin zone. The figures (e) and (f) show $\mathcal{S}(\mathbf{q}, E)$ as a function of energy along two momentum space directions to compare with Fig. 8.3 (e) and (f), respectively. The data in (a)-(d) has been convoluted with a gaussian distribution function to match the experimental resolution while in (e) and (f) the finite energy resolution and perpendicular $\mathbf{q}$-integration have not been taken into account. Note that the magnetic form factor of the Cr^{5+} ions is not included in these plots. (Figure taken from [59])

saddle-point solution is stable [70, 73, 126, 72, 71]. One last caveat insinuates that the one-particle per site condition is violated since the four bands corresponding to the antisymmetric sector are empty, whereas the two lower bands are not entirely filled to guarantee the presence of a Fermi surface.

8.3. Heat capacity and spinon pairing

So far, besides the fact that the resulting spinon model should be following a linear temperature dependency of the heat capacity and therefore contained a Fermi surface, only the neutron scattering data were taken into account. Yet a closer look at the measured heat capacity, as presented in Fig. 8.6, shows small deviations from the linear behavior in a small range of the lowest recorded temperature. These deviations modify the functional dependency, which appears to be best approximated as quadratic in temperature T^2. One possible explanation for a low temperature modification is the presence of visons since they appear as gapless excitations within a $U(1)$ theory. Yet the resulting modification would rather suggest a $T^{2/3}$ dependence [127]. Another scenario could be when the spinons feel an attractive potential such that they start to pair similar to electrons in a superconductor. Such a spinon pairing $\Delta_{\mathbf{r}\mathbf{r}'}$ renders, in fact, a coherent picture. It leads to a breaking of the $U(1)$ gauge group, and the free fermion model becomes plausible as it is derived from a stable saddle-point solution. Visons acquirer an excitation gap and do not enter the lowest temperature regime. Even the one-particle-per-site condition might be fulfilled as the constraint can be reformulated in the $\mathbb{Z}_2$ case, which was explained in Chapter 4.

The overall heat capacity curve is then divided into three regions: (1) for very small temperature $T \leq 0.1\ K$ spinons feel an attractive potential and start to form Cooper pair like objects which condense. This opens a small gap, except for possible nodal points. (2) for small temperatures, $0.1\ K < T \leq 0.5\ K$ spinons behave as free fermions whose dispersion seemingly contains a Fermi surface. (3) for high temperatures, $0.5\ K < T$ thermal fluctuations are sufficiently large to excite phonons and visons. Also, impurity scattering becomes more and more important such that the linear temperature dependency of the heat capacity is lost.

These temperature regimes indicate that the neutron scattering data for which the energy resolution is in order of $0.1\ meV \simeq 1K \cdot k_B$ is not capable of resolving the pairing gap. Therefore, no tentative has been made to include such a pairing term into the previously discussed spinon model. Nevertheless, the heat capacity measurement is analyzed in order to make some statements about the pairing type. Based on this investigation, it is suggested that such a pairing has a momentum dependency, which is not in line with a naive s-wave paring leading to a constant gap $\Delta(\mathbf{k}) \equiv \Delta_s$. Such an s-wave pairing implies a temperature dependency of the

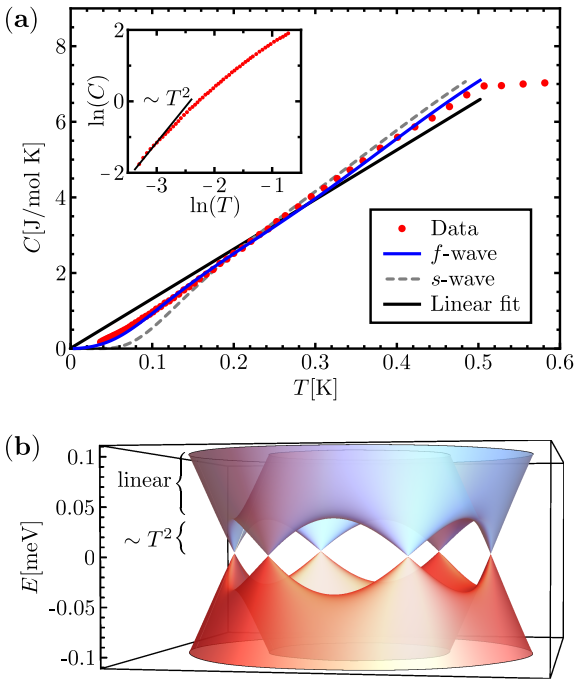

Figure 8.6: (a) Measured heat capacity of $Ca_{10}Cr_7O_{28}$ in an enlarged view of the low-temperature behavior of the measured heat capacity (see Fig. 8.2). Several fits are shown: Linear temperature dependence as obtained for an intact Fermi surface (black line), s-wave pairing model with a $\mathbf{k}$-independent gap $\Delta_s = 0.039$ meV (gray dashed line), and f-wave pairing model with the gap function in Eq. (8.11) using $\Delta_f = 0.039$ meV (blue line). Inset: Heat-capacity data in a double-logarithmic plot. For comparison, the black line shows a T^2 temperature dependence. (c) Low-energy spinon band structure for the f-wave pairing model in Eq. (8.11) with $\Delta_f = 0.039$ meV. The energy regimes which lead to a linear and quadratic temperature dependence of the heat capacity are indicated. (Figure taken from [59])

heat capacity as $c(T) \propto \exp(-\frac{\Delta_s}{k_B T})$ [111, 128]. As shown in Fig. 8.6, a better agreement is achieved by a momentum dependent f-pairing of the form

$$\Delta(\mathbf{k}) = \Delta_f |\sin(3\varphi_\mathbf{k} + \varphi_0)|. \tag{8.11}$$

Such an f-wave pairing does not entirely gap out the spectrum, but comprises six nodal Dirac points that comply with the kagome lattice's three-fold rotational symmetry. The momentum dependent polar angle is given by $\tan(\varphi_\mathbf{k}) = \frac{k_y}{k_x}$. The best fit for the available data is obtained by $\Delta_f = 0.039\ meV$, which is indeed one order of magnitude smaller than the step size of the dynamical structure factor plots in Fig. 8.3. The resulting picture is illustrated in Fig. 8.6: For a very high resolution in energy, one finds that the picture of a Fermi surface is not entirely correct and the lower bands exhibit nodal Dirac points. However, on energy scales larger than the size of the gap, these nodal points are invisible such that the Fermi surface picture yields good agreement with the observations.

8.4. Conclusion

The compound $Ca_{10}Cr_7O_{28}$ is a recently discovered material that shows some of the key features characterizing a quantum spin liquid candidate. Neutron scattering experiments indicate that even at very low temperatures, no sign of magnetic order

appears. However, one observes some underlying structure in the intensity spectrum, which hints at a collective behavior rather than a mere disorder response. The heat capacity measurement shows within an extended range a linear temperature dependency, a behavior that insinuates the presence of a Fermi surface. This is somewhat unusual for an electric charge insulating material. A small deviation from the linearity has also been observed in a short interval of the lowest measured temperature. All these facts suggest that a quantum spin liquid state is, in fact, a plausible scenario in order to describe the low-temperature behavior of $Ca_{10}Cr_7O_{28}$. This implies that one of the low-energy degrees of freedom corresponds to spinons if the current theory is correct. Since, as the heat capacity data suggests, these spinons should exhibit a Fermi surface, they are adequately represented by the fermionic parton theory introduced in Chapter 2.

This argument sets the stage for the presented mean-field spinon model. Instead of using the naive basis in which each site is represented by an individual spinon operator, the peculiar pattern of ferro- and antiferromagnetic couplings measured for the material $Ca_{10}Cr_7O_{28}$ suggests the choice of different basis elements. The crystal of $Ca_{10}Cr_7O_{28}$ can be partitioned into different triangles. Within a given triangle spins couple either ferro- and antiferromagneticly. Since the ferromagnetical couplings are dominant in strength, a new basis is introduced, which contains states that combine these three ferromagnetically coupled spins into one symmetric superposition. For the resulting spin-3/2 objects, it appears natural to draw an effective honeycomb lattice rather than using the double-layer kagome lattice. These objects govern the low-energy regime,, which can be guaranteed in the spinon model by fixing a chemical potential such that the corresponding bands exhibit a Fermi surface. Choosing additional basis elements perpendicular to the first ones, in order to correctly describe the full vector space, almost completes the model as it was shown that the exact hopping pattern matters only a little. Merely a second potential term has to be added to energetically separate the resulting new spin-1/2 objects from the previously encountered spin-3/2 objects. This relatively simple model is capable of well explaining many features that have been observed in the scattering experiment. Furthermore, it coincides with the results of a semi-classical study in which it was observed that spins undergo two different dynamical processes [120].

To cope with the deviations from a linear temperature dependency of the heat capacity, seen in the lowest temperature regime it is argued that spinons enter a pairing state. The geometry of an f-wave pairing seems most plausible as it yields the best fit and complies with the symmetry of the material. The corresponding pairing amplitude is too small to be identified in the neutron data and is therefore not explicitly included in the spinon model. However, conceptually it is of paramount importance as it breaks the invariance group from $U(1)$, which applies for the pure

hopping model, down to $\mathbb{Z}_2$. Only in the later case, one can a posteriori justify the neglect of visonic degrees of freedom, which were entirely neglected so far in the spinon model. This last bit of information completes the picture and indicates that $Ca_{10}Cr_7O_{28}$ is a $\mathbb{Z}_2$ quantum spin liquid which can be described by a mean-field theory resulting from a fermionic parton approach.

9. Projective symmetry group classifications of quantum spin liquids on the simple cubic, body centered cubic, and face centered cubic lattices

In this work, a projective symmetry group classification [5, 11] is carried out for several three-dimensional lattices. This chapter's underlying work has been published in [60].

PSG classifications have been made for multiple two-dimensional lattice groups [5, 129, 130, 131, 54, 61], but they remain scarce in three dimensions [132, 95, 133, 134, 135]. Interestingly, the best-known examples of three-dimensional space groups, namely the simple-, the body- and the face centered cubic lattices, have not been considered until now, although they show very rich phase diagrams of their classical Heisenberg models. For example, the classical antiferromagnetic Heisenberg model of the face centered cubic lattice exhibits already for first neighbor couplings only a subextensive ground state degeneracy which manifests itself via lines in reciprocal space [136]. Even though fluctuations become generally less important in higher dimensions, which naively would reduce the likelihood of finding quantum spin liquids phases, three-dimensional systems are actively studied in the context of frustrated magnetism, and it has been found that some geometries lead to a high degree of frustration, which in return increases the propensity of forming exotic quantum spin liquid states [137, 138, 139, 140, 141, 142, 143]. Most of these studies are based on numerical approaches for which it is hard to identify the underlying microscopic Hamiltonians describing the energetically low lying quasiparticles. Therefore, a PSG classification and the revealed symmetry group representations are important to construct possible symmetry obeying mean-field Hamiltonians. These effective models can help to connect the numerical results with a corresponding quantum Hamiltonian. Although these Hamiltonians cannot provide a complete description for the systems in question, they may, nevertheless, deliver valuable information on its own. As explained in Chapter 2, the main issue with such mean-field models is that they do not take the emergent gauge fields into account and thus neglecting visons, which are some fundamental excitations of the spin liquid state. However, in the case of a $\mathbb{Z}_2$ quantum liquid, these visons only appear above a certain energy

threshold, and if that is the case, the mean-field Hamiltonian do, in fact, provide an accurate low-energy description. Regardless whether these Hamiltonians correctly describe true $\mathbb{Z}_2$ states, their ground states can be employed as initial states for further variational Monte Carlo studies, or they may be enhanced via functional renormalization group methods as explained in Ref. [144].

This work might also be valuable from a material scientist's point of view. Recently, some materials have been identified as Mott insulators showing some of a quantum spin liquid's characteristic features. The relevant magnetic spin-1/2 ions in these candidates form cubic lattices. For example the Cu^{2+} ions of $Ca_3Cu_2GeV_2O_{12}$ sit on a body centered cubic lattice. Neutron scattering experiments on this compound could not reveal any sign of magnetic order down to 70 mK [145]. Such behavior might be explained by the proximity of this system to the phase transition point in the $J_1 - J_2$ antiferromagnetic Heisenberg model for which the transition point is at $J_2/J_1 \sim 0.7$ [146, 147]. Examples of the face centered cubic lattice may be realized through Ba_2CeIrO_6 [148] and the molecular antiferromagnet Cs_3C_{60} [149]. While the former shows a high degree of frustration for the second specific heat capacity measurements revealed the occurrence of both long-range antiferromagnetic order and a quantum paramagnetic state below 2.2 K.

In the first part, the PSG classifications, as introduced in Chapter 4 and 5, for the simple cubic, the body centered cubic, and the face centered cubic lattice are presented. These analyses reveal the relevant symmetry conditions which every symmetric *Ansatz* needs to fulfill. They further supply the irreducible representations of the relevant gauge transformations within the projective group setting. These results are used to construct all relevant short-range mean-field states for the body centered- and face centered cubic lattice. Starting with the first neighbor states, it will be shown how these states change by further adding up to third neighbor couplings. The magnetic coupling strengths J_1, J_2, J_3 are chosen such that the corresponding classical Heisenberg model is close to a phase transition point. In the vicinity of these points, large quantum fluctuations might enable the existence of a quantum liquid state [150, 151, 152, 147, 142]. The resulting mean-field models are treated by a self-consistent Hartree-Fock procedure in order to calculate the relevant hopping and pairing amplitudes, the multiplier fields, which guarantee single-occupation, at least, on average, and the corresponding mean-field ground state energies. The dispersion and the dynamical structure factor of these states are shown and discussed.

9.0.1. Simple cubic lattice

The octahedral point group O_h is built by the generators

$$\begin{aligned}
&\Pi_z(x,y,z) \to (-x,-y,z)\\
&\Pi_y(x,y,z) \to (-x,y,-z)\\
&\Pi_{xy}(x,y,z) \to (y,x,-z)\\
&I(x,y,z) \to (-x,-y,-z)\\
&P(x,y,z) \to (z,x,y).
\end{aligned} \tag{9.1}$$

The full space group includes translations

$$\begin{aligned}
&T_x(x,y,z) \to (x+1,y,z)\\
&T_y(x,y,z) \to (x,y+1,z)\\
&T_z(x,y,z) \to (x,y,z+1),
\end{aligned} \tag{9.2}$$

where x, y, z take integer values. This definition implies that the lattice constant of the cubic unit cell is unity $a = 1$, which will always be assumed in the following. As discussed in Chapter 5 time-reversal symmetry shall be included as well. The point group generators Eq. (9.1), except for the generator of rotations around the $(1,1,1)$-axis (which effectively permutes the entries of a vector therefore it is denoted by P), can be identified by cyclic subgroups of order two since they map onto the identity when applied twice. Only P forms a cyclic group of order three.

As discussed in Chapter 5 a valid group representation follows from the algebraic relations of the group itself. Thus a set of constraints on the representation can be formulated. To ensure that different representations are gauge inequivalent it is convenient to fix a gauge. Here the gauge is used in which all gauge transformation belonging to translations are represented by

$$\begin{aligned}
&G_{T_x}(\mathbf{r}) = \eta^z_{z_x}\eta^y_{y_x}\tau^0\\
&G_{T_y}(\mathbf{r}) = \eta^z_{z_y}\tau^0\\
&G_{T_z}(\mathbf{r}) = \tau^0.
\end{aligned} \tag{9.3}$$

The explicit construction can be found in Chapter 5. Note that the gauging of the $G_{T_\mu(\mathbf{r})}$ matrices does not fix the entire gauge freedom as global gauge transformations can be made without changing Eq. (9.3). Identifying the elements of the little group leads to determining equations. These conditions can be solved by decomposing the site-dependent gauge transformations into site-dependent sign factors $\eta^{f(\mathbf{r})}$, with f some function, and site-independent matrices g of the form $G(\mathbf{r}) = \eta^{f(\mathbf{r})}g$. One finds

thus that the PSG is defined by

$$
\begin{aligned}
&G_{T_z}(\mathbf{r}) = \tau^0, \quad G_{T_y}(\mathbf{r}) = \eta_X^z \tau^0, \quad G_{T_x}(\mathbf{r}) = \eta_X^{z+y} \tau^0, \\
&G_{\mathcal{T}}(\mathbf{r}) = \eta_{\mathcal{T}}^{x+y+z} g_{\mathcal{T}}, \quad g_{\mathcal{T}}^2 = \pm\tau^0, \\
&G_I(\mathbf{r}) = \eta_I^{x+y+z} g_I, \quad g_I^2 = \pm\tau^0, \\
&G_{\Pi_z}(\mathbf{r}) = \eta_\Pi^{x+y} g_{\Pi_z}, \quad g_{\Pi_z}^2 = \pm\tau^0, \\
&G_{\Pi_y}(\mathbf{r}) = \eta_\Pi^{x+z} g_{\Pi_y}, \quad g_{\Pi_y}^2 = \pm\tau^0, \\
&G_{\Pi_{xy}}(\mathbf{r}) = \eta_X^{xy} \eta_{\Pi_{xy}}^z g_{\Pi_{xy}}, \quad g_{\Pi_{xy}}^2 = \pm\tau^0, \\
&G_P(\mathbf{r}) = \eta_X^{x(y+z)} \eta_P^{x+y} g_P, \quad g_P^3 = \pm\tau^0, \\
&[g_{\mathcal{T}}, g_{\mathcal{O}}]_\pm = 0, \quad [g_I, g_{\mathcal{O}\neq I}]_\pm = 0, \quad \left[g_{\Pi_z}, g_{\Pi_y}\right]_\pm = 0, \\
&g_{\Pi_z} g_{\Pi_{xy}} g_{\Pi_y}^{-1} g_{\Pi_{xy}}^{-1} g_{\Pi_y} = \pm\tau^0, \quad g_{\Pi_z} g_P g_{\Pi_y}^{-1} g_P^{-1} = \pm\tau^0, \\
&g_P g_{\Pi_{xy}} g_P g_{\Pi_{xy}} g_{\Pi_y}^{-1} = \pm\tau^0, \quad \eta_\Pi \eta_{\Pi_{xy}} \eta_P = 1.
\end{aligned} \tag{9.4}
$$

The symbol $\mathcal{O}$ denotes the point group generators and $\eta = \pm 1$. The notation $[\ldots]_\pm$ represents either the commutator or the anti-commutator. A full set of gauge inequivalent g-matrices can be found in the Appendix A.4. To obtain the equations (9.4) an additional gauge transformation $W(\mathbf{r}) = \eta_{w_x}^x \eta_{w_y}^y \eta_{w_z}^z \tau^0$ was made. However, this gauge transformation does not change the previously obtained results as it acts on translations as $G_{T_\mu}(\mathbf{r}) \to \eta_{w_\mu} G_{T_\mu}(\mathbf{r})$. The resulting global sign can then be absorbed by redefining $G_{T_\mu}(\mathbf{r})$. It further commutes with most of the other transformations. Only P and Π_{xy} are affected. These two operations transform as $G_{\Pi_{xy}}(\mathbf{r}) \to \eta_{w_x}^{x+y} \eta_{w_y}^{x+y} G_{\Pi_{xy}}(\mathbf{r})$ and $G_P(\mathbf{r}) \to \eta_{w_x}^{x+z} \eta_{w_y}^{x+y} \eta_{w_z}^{y+z} G_P(\mathbf{r})$. By choosing the values η_{w_μ} one can hence eliminate some of the other sign factors of P and Π_{xy}. Concerning the algebraic conditions of the g-matrices one finds that only $g_{\Pi_z} = g_{\Pi_y} = \tau^0$ fulfills all conditions at once. The number of distinct PSGs can be calculated by counting the number of inequivalent g-matrices times two to the power of independent η values. Regarding $\eta_\Pi \eta_{\Pi_{xy}} \eta_P = 1$ shows that three different sign factors are mutually dependent, and thus, only two are counted as independent. The number of distinct PSGs on the simple cubic lattice is found to be $21 \cdot 2^5 = 672$. Since $\eta_{\mathcal{T}} = 1$ and $g_{\mathcal{T}} = \tau^0$ ultimately leads to a vanishing mean-field *Ansatz* the corresponding PSGs are excluded. One finds eventually that $21 \cdot 2^5 - 9 \cdot 2^4 = 528$ distinct mean-field *Ansätze* can be constructed on the simple cubic lattice.

9.1. Body centered cubic lattice

The results of the simple cubic lattice can be extended to the body centered cubic lattice. The difference is that an additional generator of the point group needs to

be taken care of. The action of this operator results in an additional translation

$$t(x, y, z) \to (x + 1/2, y + 1/2, z + 1/2). \tag{9.5}$$

By superposing two distinct simple cubic lattice which shall be called sub-lattice $A = \{(x, y, z)|x, y, z \in \mathbb{Z}\}$ and $B = \{(x + 1/2, y + 1/2, z + 1/2)|x, y, z \in \mathbb{Z}\}$ a body centered cubic lattice can be constructed. For each sub-lattice a complete description, besides the new generator t, of the symmetry representations is given by the equations (9.4). Yet there is an important difference since on sub-lattice B the invariant element, which is the origin $(0, 0, 0)$ on sub-lattice A, is $\mathbf{r}_0 = (1/2, 1/2, 1/2)$. That means that symmetry operations on sub-lattice B need to be modified such that $\mathbf{r}_0$ is indeed the invariant element under point group operations. Take inversion as an example for which the naive operations acting on sub-lattice B yields

$$I(x + 1/2, y + 1/2, z + 1/2) \to (-(x + 1/2), -(y + 1/2), -(z + 1/2)). \tag{9.6}$$

The modified operation given by

$$I'(x + 1/2, y + 1/2, z + 1/2) \to (-x + 1/2, -y + 1/2, -z + 1/2) \tag{9.7}$$

leaves $\mathbf{r}_0$ invariant. However, for the entire lattice, consisting of both sub-lattices, the center of inversion should be the zero vector. The inversion defined on sub-lattice B can be related to the naive inversion. This can be achieved by including translations T_μ

$$I' = T_x T_y T_z I. \tag{9.8}$$

which becomes

$$G_{I'} I' = G_{T_x} T_x G_{T_y} T_y G_{T_z} T_z G_I I. \tag{9.9}$$

for the representation matrices. Similarly, for the other generators Π_z, Π_y and Π_{xy}, which do not leave $\mathbf{r}_0$ invariant on sub-lattice B, one can identify the connections between these redefined operations and the naive ones given by

$$\begin{aligned} \Pi'_z &= T_x T_y \Pi_z \\ \Pi'_y &= T_x T_z \Pi_y \\ \Pi'_{xy} &= T_z \Pi_{xy}. \end{aligned} \tag{9.10}$$

Since lattice translations T_μ are defined for integer steps the exponents of the η values take only integer values regardless the sub-lattice. The new symmetry operation t connects both sub-lattices, and the algebraic relations that include t merge the two distinct representations into one, which is valid on the entire body centered cubic

lattice. In the following, the procedure will be explained using some concrete examples. Consider for instance the operation $T_x^{-1}tT_xt^{-1} = id$ which translates, starting from a given site $\mathbf{r}$, following a closed path back to site $\mathbf{r}$, thus belonging to the stabilizer group of $\mathbf{r}$. The requirement reads $T_x^{-1}(G_{T_x})^{-1}G_t t(G_{T_x})T_x t^{-1}(G_t)^{-1} \in IGG$ which then gives a condition on the representation

$$\begin{aligned}
&(G^A_{T_x})^{-1}(x+1,y,z)G^A_t(x+1,y,z)\times \\
&\times G^B_{T_x}(x+1/2,y-1/2,z-1/2)(G^A_t)^{-1}(x,y,z) = \eta^A_{t_x}\tau^0 \\
&\implies G^A_t(x,y,z) = (\eta^A_X\eta^B_X)^{y+z}\eta^A_{t_x}G^A_t(x+1,y,z).
\end{aligned} \tag{9.11}$$

Similarly, one finds conditions for the other directions

$$\begin{aligned}
G^A_t(x,y,z) &= (\eta^A_X\eta^B_X)^z\eta^A_{t_y}G^A_t(x,y+1,z) \\
G^A_t(x,y,z) &= \eta^A_{t_z}G^A_t(x,y,z+1).
\end{aligned} \tag{9.12}$$

For sub-lattice B a similar calculation yields

$$\begin{aligned}
&G^B_t(x+1/2,y+1/2,z+1/2) = \\
&(\eta^A_X\eta^B_X)^{y+z}\eta^B_{t_x}G^B_t(x+1+1/2,y+1/2,z+1/2) \\
&G^B_t(x+1/2,y+1/2,z+1/2) = \\
&(\eta^A_X\eta^B_X)^{z}\eta^B_{t_y}G^B_t(x+1/2,y+1+1/2,z+1/2) \\
&G^B_t(x+1/2,y+1/2,z+1/2) = \\
&\eta^B_{t_z}G^B_t(x+1/2,y+1/2,z+1+1/2).
\end{aligned} \tag{9.13}$$

Combining these facts indicates that a closed solution exists, if the condition $\eta^A_X = \eta^B_X \equiv \eta_X$ is met, which is given by

$$\begin{aligned}
G^A_t(\mathbf{r}) &= (\eta^A_{t_x})^x(\eta^A_{t_y})^y(\eta^A_{t_z})^z g^A_t \\
G^B_t(\mathbf{r}) &= (\eta^B_{t_x})^x(\eta^B_{t_y})^y(\eta^B_{t_z})^z g^B_t.
\end{aligned} \tag{9.14}$$

The sub-lattices A, B can be connected via $t^2 = T_zT_yT_x$, which yields that $\eta^A_{t_x} = \eta^B_{t_x} \equiv \eta_{t_x}$, $\eta^A_{t_y} = \eta_X\eta^B_{t_y} \equiv \eta_{t_y}$ and $\eta^A_{t_z} = \eta^B_{t_z} \equiv \eta_{t_z}$. The site-independent matrices need to fulfill $g^A_t g^B_t = \pm g^B_t g^A_t = \pm\tau^0$ such that one can define $g^A_t = \pm g^B_t \equiv g_t$ with $g_t^2 = \pm\tau^0$.

The inclusion of inversion leads to the algebraic relation combining inversion and the new translation as $I^{-1}t^{-1}I't = I^{-1}t^{-1}T_xT_yT_zIt = id$, which yields $\eta^A_I = \eta^B_I$, as a consequence that this equation should be independent of the x, z component of an initial site $\mathbf{r}$, and $\eta^A_{t_y}\eta^B_{t_y}\eta^A_I\eta^B_I = 1$, which results from independence of the y component. Gathering the previous results shows that $\eta_X = 1$. This means that all gauge transformations of translations are now trivially represented by τ^0. Importantly, this

further implies that the gauge transformations do no longer distinguish between the redefined and the naive operations. The relations $Pt = tP$ and $\Pi_{xy} T_z t^{-1} \Pi_{xy} t = id$ connect the sign factors of different directions $\eta_{t_x} = \eta_{t_y} = \eta_{t_z} \equiv \eta_t$. Regarding the matrix representations, one finds, in the case of inversion, that the matrices have to obey $g_t^{-1} g_I^A g_t = \pm g_I^B$. Similar results are obtained for all the other elements of the simple cubic lattice point group

$$\begin{aligned} g_t^{-1} g_I^A g_t &= \pm g_I^B \\ g_t^{-1} g_\mathcal{T}^A g_t &= \pm g_\mathcal{T}^B \\ g_t^{-1} g_{\Pi_{xy}}^A g_t &= \pm g_{\Pi_{xy}}^B \\ g_t^{-1} g_P^A g_t &= \pm g_P^B. \end{aligned} \tag{9.15}$$

For each sub-lattice, one can find an irreducible set of $g_\mathcal{S}$ representations. As these two sub-lattices are equivalent descriptions of the simple cubic lattice, the two sets are also equivalent. To fulfill equations (9.15) in the case of $g_\mathcal{S}^A \neq g_\mathcal{S}^B$ one would require a global transformation, which exchanges between two representations. However, this is not possible since they are gauge inequivalent by construction. As a result, it follows that $g_\mathcal{S}^A = \pm g_\mathcal{S}^B$. Yet the appearing sign can be eliminated by a proper definition. Luckily, it turns out that one can also use the results for the simple cubic lattice Eq. (9.4) to represent the generators of the body centered cubic lattice, whereas $\eta_X = 1$ and the additional generator $G_t(\mathbf{r})$ needs to be added

$$\begin{aligned} &G_t(\mathbf{r}) = \eta_t^{x+y+z} g_t, \quad g_t^2 = \pm \tau^0, \\ &[g_t, g_\mathcal{S}]_\pm = 0, \quad g_{\Pi_z} g_{\Pi_y} g_{\Pi_{xy}} g_P g_t g_{\Pi_{xy}} g_P = \pm g_t. \end{aligned} \tag{9.16}$$

It is important to remember that due to the different sub-lattices, the coordinates in the exponents depend on the simple cubic lattice's unit cell. Irreducible representations for the body centered cubic lattice are shown in Appendix A.4. The number of distinct PSGs for the body centered cubic lattice is $59 \cdot 2^5 = 1888$. Removing those PSGs that lead to vanishing mean-field matrices yields $59 \cdot 2^5 - 23 \cdot 2^4 = 1520$.

9.2. Face centered cubic lattice

Similarly to the body centered cubic lattice the face centered cubic lattice can be obtained from the simple cubic lattice by including additional symmetry generators. In this case, one has to add two additional translations

$$\begin{aligned} t_1(x, y, z) &\to (x, y + 1/2, z + 1/2) \\ t_2(x, y, z) &\to (x + 1/2, y + 1/2, z). \end{aligned} \tag{9.17}$$

This lattice can be constructed by superposing four distinct simple cubic lattices $A = \{(x,y,z)|x,y,z \in \mathbb{Z}\}$, $B = \{(x+1/2,y+1/2,z)|x,y,z \in \mathbb{Z}\}$, $C = \{(x+1/2,y,z+1/2)|x,y,z \in \mathbb{Z}\}$, and $D = \{(x,y+1/2,z+1/2)|x,y,z \in \mathbb{Z}\}$. As for the body centered lattice these four sub-lattices are connected by incorporating t_1, t_2. Using the same gauge as for the simple cubic lattice, in a similar treatment, as described above in the case of the body centered cubic lattice, one finds that the gauge transformations can be represented equally on all different sub-lattices $G_{\mathcal{S}}^A = G_{\mathcal{S}}^B = G_{\mathcal{S}}^C = G_{\mathcal{S}}^D$. The sign corresponding to translations must again be positive $\eta_X = +1$. The gauge transformations related to the new generators are determined by

$$\begin{aligned}
&G_{t_1}(\mathbf{r}) = \eta_t^{x+y+z} g_{t_1} \quad g_{t_1}^2 = \pm\tau^0, \\
&G_{t_2}(\mathbf{r}) = \eta_t^{x+y+z} g_{t_2} \quad g_{t_2}^2 = \pm\tau^0, \\
&(g_{t_1} g_{t_2})^2 = \pm\tau^0, \quad [g_{\mathcal{T}}, g_{t_1}]_{\pm} = 0, \quad [g_{\mathcal{T}}, g_{t_2}]_{\pm} = 0, \\
&[g_I, g_{t_1}]_{\pm} = 0, \quad [g_I, g_{t_2}]_{\pm} = 0, \quad \left[g_{\Pi_{xy}}, g_{t_2}\right]_{\pm} = 0, \\
&g_{t_2} g_{t_1} g_{\Pi_{xy}} g_{t_1} g_{\Pi_{xy}} = \pm\tau^0, \quad g_P g_{t_2} g_P^{-1} g_{t_1} = \pm\tau^0, \\
&g_{\Pi_{xy}} g_P g_{t_1} g_{\Pi_{xy}} g_P g_{t_1} = \pm\tau^0.
\end{aligned} \tag{9.18}$$

Note that there is only one possible sign factor η_t for both transformations. Contrary to the body centered cubic lattice one finds that in order to solve equations (9.18) t_1 as t_2 can only have a trivial matrix representation such that the corresponding gauge transformations are given by $G_{t_1}(\mathbf{r}) = G_{t_2}(\mathbf{r}) = \eta_t^{x+y+z}\tau^0$. As a reminiscence of this construction, four elements in the unit cell are labeled by the same coordinates leading to the same exponents of the sign values η. Gauge inequivalent matrix representations are shown in Appendix A.4. The total number of distinct PSGs is equivalent to the simple cubic lattice $21 \cdot 2^5 = 672$. This is because $g_{t_1} = g_{t_2} = \tau^0$ and that the sign factor η_X of the integer translations is replaced by the sign factor η_t of the new translations. This leads, after PSGs have been removed, which results in vanishing mean-field matrices, to $21 \cdot 2^5 - 9 \cdot 2^4 = 528$ possible mean-field models on the face centered cubic lattice.

9.3. Constructing a short-rang mean-field Ansatz

The PSG representations at hand, it is possible to construct mean-field *Ansätze* whose projected wave function will obey the desired symmetry relations. The entire construction is based on the PSG defining property Eq. (4.2) as explained in Chapter 4 and Chapter 5. The calculation of all mean-field models is too long as that it should be repeated here explicitly. In order to explains, nevertheless, the main procedure, a sketch of the construction for the nearest neighbor states

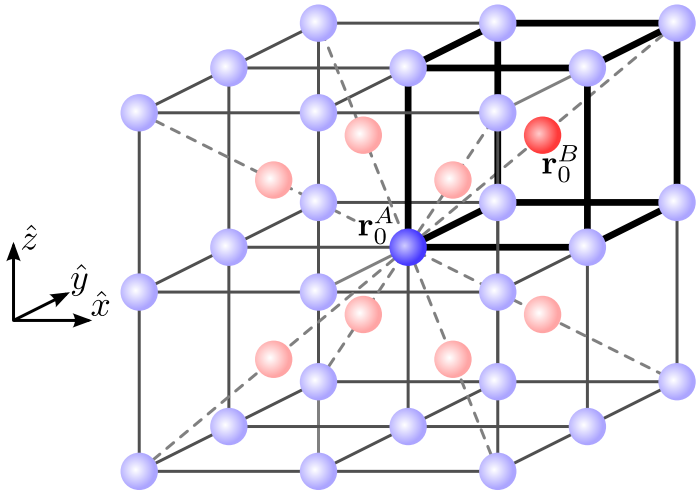

Figure 9.1.: In the upper right corner the first unit cell of the simple cubic lattice is drawn in bold lines. The Blue points indicate the A sub-lattice sites. The red points show the positions of sub-lattice B sites. The boldly drawn dots indicate the two sites belonging to the first unit cell. The first neighbors of site $\mathbf{r}_0^A$ are the eight depicted B sites. (The author gratefully received this figure from Johannes Reuther [60].)

of the body centered cubic lattice is given. The defining symmetry operators are $\mathcal{S} = \{T_x, T_y, T_z, t, \mathcal{T}, I, \Pi_z, \Pi_y, \Pi_{xy}, P\}$. Employing PSG equations (4.2) for all three lattices translations T_μ shows that

$$G^\dagger_{T_\mu}(T_\mu(\mathbf{r}))u_{T_\mu(\mathbf{r})T_\mu(\mathbf{r}')}G_{T_\mu}(T_\mu(\mathbf{r}')) = u_{\mathbf{r}+\hat{e}_\mu\mathbf{r}'+\hat{e}_\mu} = u_{\mathbf{r}\mathbf{r}'}, \tag{9.19}$$

in the second equality it was used that the corresponding representations for the body centered cubic lattice are all represented by the identity $G_{T_\mu}(\mathbf{r}) = \tau^0$. This translational invariance reduces the number of independent mean-field matrices, and it is sufficient to determine only the matrices that connect to the origin. In the considered case, one finds 8 first neighbors as shown in Fig. 9.1, which are assigned by the vectors $\delta\mathbf{r} = \{\pm 1/2, \pm 1/2, \pm 1/2\}$. For the following one defines $\delta\mathbf{r} = \mathbf{r}' - \mathbf{r}$ and fixes $\mathbf{r} = (0,0,0)$ to be the origin. The relevant coupling matrices are $u_{\mathbf{r}\mathbf{r}'} = u_{(0,0,0),\mathbf{r}'} \equiv u_{\delta\mathbf{r}}$. It will be convenient to expand them in terms of Pauli matrices

$$u_{\delta\mathbf{r}} = i\alpha^0_{\delta\mathbf{r}} + \sum_{i=1}^{3} \alpha^i_{\delta\mathbf{r}}\tau^i. \tag{9.20}$$

Among these matrices one picks $u_{(1/2,1/2,1/2)} \equiv u_{\delta\mathbf{r}_1}$. The remaining ones are derived according to the symmetry properties defined by the point group operators. Before connecting different $u_{\delta\mathbf{r}_i}$ some conditions dictate the general from of any possible

matrix. For instance, time-reversal invariance requires

$$\begin{aligned} &- G_{\mathcal{T}}^{\dagger}(\mathcal{T}(\mathbf{r}))u_{\mathbf{r}\mathbf{r}'}G_{\mathcal{T}}(\mathcal{T}(\mathbf{r}')) = u_{\mathbf{r}\mathbf{r}'} \\ &- \eta_{\mathcal{T}}^{x'+y'+z'} g_{\mathcal{T}}^{-1} u_{\delta\mathbf{r}} g_{\mathcal{T}} = u_{\delta\mathbf{r}}. \end{aligned} \tag{9.21}$$

This means $\delta\mathbf{r}_1 = (0,0,0)$ since $\mathbf{r}$ and $\mathbf{r}'$ lie in the simple cubic unit cell of the origin. Hence the sign factor $\eta_{\mathcal{T}}$ vanishes. Therefore, $u_{\delta\mathbf{r}_1}$ has to anti-commute with the representation matrix of $g_{\mathcal{T}}$. This matrix can either be represented by the identity, or by $i\tau^2$ (see Tab. A.2 in the Appendix A.4). This implies further that for any finite *Ansatz* the representation must be $g_{\mathcal{T}} = i\tau^2$. To anti-commute with this representation the coefficients $\alpha^0_{\delta\mathbf{r}_1} = \alpha^2_{\delta\mathbf{r}_1} = 0$ have to vanish. It follow that $(u_{\delta\mathbf{r}_1})^{\dagger} = u_{\delta\mathbf{r}_1}$. Generally, the effect of hermitian conjugation is given by $(u_{\mathbf{r}\mathbf{r}'})^{\dagger} = u^*_{\mathbf{r}'\mathbf{r}} = u^*_{-\delta\mathbf{r}}$. In this case one finds $u_{\delta\mathbf{r}_1} = u_{-\delta\mathbf{r}_1} = u_{(-1/2,-1/2,-1/2)}$. The corresponding coupling vector points from the origin to the simple cubic unit cell with the coordinates $(x,y,z) = (-1,-1,-1)$ such that the sign factor $\eta_{\mathcal{T}}$ does not vanish in Eq. (9.21). Consequently, only $\eta_{\mathcal{T}} = +1$ leads to a finite *Ansatz*. Combining hermitian conjugation and inversion leads to another criteria: Any coupling matrix has to comply with

$$\begin{aligned} &G_I^{\dagger}(I(\mathbf{r}))u_{I(\mathbf{r})I(\mathbf{r})}G_I(I(\mathbf{r}')) = u_{\mathbf{r}\mathbf{r}'} \\ &\eta_I^{I(x')+I(y')+I(z')} g_I^{-1} u_{-\delta\mathbf{r}} g_I = u_{\delta\mathbf{r}} \\ &\eta_I^{I(x')+I(y')+I(z')} g_I^{-1} \left(u_{\delta\mathbf{r}}\right)^{\dagger} g_I = u_{\delta\mathbf{r}}. \end{aligned} \tag{9.22}$$

In the case of $\delta\mathbf{r}_1$ this demands that $u_{\delta\mathbf{r}_1}$ has to commute with the representation matrix g_I. Since this must hold equally for $u_{-\delta\mathbf{r}_1}$ one finds that the corresponding sign factor can only be positive $\eta_I = +1$. Next consider the requirement dictated by permutation symmetry, which reads

$$\begin{aligned} &G_P^{\dagger}(P(\mathbf{r}))u_{P(\mathbf{r})P(\mathbf{r})}G_P(P(\mathbf{r}')) = u_{\mathbf{r}\mathbf{r}'} \\ &\eta_P^{P(x')+P(y')} g_P^{-1} u_{P(\delta\mathbf{r})} g_P = u_{\delta\mathbf{r}}. \end{aligned} \tag{9.23}$$

This operation leaves $\delta\mathbf{r}_1$ invariant, and the exponent vanishes in the case of $\delta\mathbf{r}_1$. It follows that $u_{\delta\mathbf{r}_1}$ has to commute with g_P, which can only by accomplished by a trivial representation $g_P = \tau^0$. Contrary to the cases above, the condition of $u_{-\delta\mathbf{r}_1}$, which also remains invariant under P, does not require that η_P has to be positive. The other point group operations can be used to connect between different $\delta\mathbf{r}$ according to

$$\eta_{\Pi}^{\Pi_z(x')+\Pi_z(y')} u_{\Pi_z(\delta\mathbf{r})} = u_{\delta\mathbf{r}} \tag{9.24}$$

$$\eta_{\Pi}^{\Pi_y(x')+\Pi_y(z')} u_{\Pi_y(\delta\mathbf{r})} = u_{\delta\mathbf{r}} \tag{9.25}$$

$$\eta_{\Pi_{xy}}^{\Pi_{xy}(z')} g_{\Pi_{xy}}^{-1} u_{\Pi_{xy}(\delta\mathbf{r})} g_{\Pi_{xy}} = u_{\delta\mathbf{r}}. \tag{9.26}$$

$\eta_{\mathcal{T}} g_{\mathcal{T}}$	$\eta_P g_P$	$\eta_I g_I$	$\eta_{\Pi_{xy}} g_{\Pi_{xy}}$	$\eta_t g_t$
$+i\tau^2$	$\pm\tau^0$	$+\tau^0$	$+\tau^0$	$+\tau^0$
$+i\tau^2$	$\pm\tau^0$	$+\tau^0$	$+i\tau^3$	$+\tau^0$
$+i\tau^2$	$\pm\tau^0$	$+\tau^0$	$+\tau^0$	$+i\tau^3$
$+i\tau^2$	$\pm\tau^0$	$+\tau^0$	$+i\tau^3$	$+i\tau^3$
$+i\tau^2$	$\pm\tau^0$	$+i\tau^3$	$+\tau^0$	$+\tau^0$
$+i\tau^2$	$\pm\tau^0$	$+i\tau^3$	$+\tau^0$	$+i\tau^3$
$+i\tau^2$	$\pm\tau^0$	$+i\tau^3$	$+i\tau^3$	$+\tau^0$
$+i\tau^2$	$\pm\tau^0$	$+i\tau^3$	$+i\tau^3$	$+i\tau^3$

Table 9.1.: Possible PSG representations for first neighbor *Ansätze* on the body centered cubic lattice.

Combining these rotations with inversion leads to further consistency conditions. For instance, one finds that $\Pi_{xy}(1/2, 1/2, -1/2) = (1/2, 1/2, 1/2) = \Pi_z(I(1/2, 1/2, -1/2))$, which yields $g_{\Pi_{xy}}^{-1} u_{\delta\mathbf{r}_1} g_{\Pi_{xy}} = g_I^{-1} u_{\delta\mathbf{r}_1} g_I$. Furthermore, from the relation $\Pi_{xy}(1/2, -1/2, 1/2) = I(1/2, -1/2, 1/2) = (-1/2, 1/2, -1/2)$ it follows that the sign factor belonging to Π_{xy} has to be positive $\eta_{\Pi_{xy}} = +1$. The sign constraint $\eta_{\Pi_{xy}} \eta_\Pi \eta_P = 1$ locks the remaining sign values $\eta_P = \eta_\Pi$. It remains to checked how t transforms the coupling matrices

$$G_t^\dagger(t(\mathbf{r})) u_{t(\mathbf{r})t(\mathbf{r}')} G_t(t(\mathbf{r}')) = u_{\mathbf{r}\mathbf{r}'}. \tag{9.27}$$

Acting on $u_{\delta\mathbf{r}_1}$ yields $\eta_t g_t^{-1} u_{\delta\mathbf{r}_1} g_t = u_{\delta\mathbf{r}_1}$, where the definition $\delta r = \mathbf{r}' - \mathbf{r}$, and the invariance under lattice translations $T_x, T_y T_z$ were used. Repeating the same procedure for $u_{-\delta\mathbf{r}_1}$ shows that $g_t^{-1} u_{\delta\mathbf{r}_1} g_t = u_{\delta\mathbf{r}_1}$. Thus it follows that $\eta_t = +1$ and that $u_{\delta\mathbf{r}_1}$ has to commute with g_t, which leaves τ^0 or $i\tau^3$ as possible representations. Putting everything together identifies all relevant PSG representations, which are shown in Table 9.1, and correspond to the eight different choices of g_I, $g_{\Pi_{xy}}$ and g_t, which can independently be represented by either τ^0 or $i\tau^3$. The representations of all but the first line in Table 9.1 demand that an *Ansatz* given by Eq. (9.20) has only finite coefficients belonging to τ^3. This yields $u_{\delta\mathbf{r}} = \alpha_{\delta\mathbf{r}}^3 \tau^3$ for all $\delta\mathbf{r}$. The requirements given by the PSG representation of the first line in Table 9.1 are less restrictive, and an *Ansatz* could be $u_{\delta\mathbf{r}} = \alpha_{\delta\mathbf{r}}^1 \tau^1 + \alpha_{\delta\mathbf{r}}^3 \tau^3$. However, since all matrices except for time-reversal are represented by the identity one can apply a global gauge transformation $W = e^{-i\theta\tau^2}$, with $\theta(\alpha_{\delta\mathbf{r}_1}^1, \alpha_{\delta\mathbf{r}_1}^3)$ denoting the angle within the plane spanned by τ^1 and τ^3, without altering the PSG representation. This rotation turns the coupling matrix along the τ^3 axis, and thus the coefficient along τ^1 vanishes $\alpha_{\delta\mathbf{r}}^1 = 0$. This is possible because the coefficients for different first neighbor $\delta\mathbf{r}$ are all locked such that the angle in the τ^1, τ^3-plane is the same for all $u_{\delta\mathbf{r}}$. Note that this is possible only for first neighbor couplings. Eventually, there are only two

distinct mean-field *Ansätze* on the body centered cubic lattice for nearest neighbor coupling. These two can be distinguished by the sign value η_P.

Before the full mean-field Hamiltonian can be written out, some comments about the multiplier fields are due. In order to make the Hamiltonian invariant these fields have to comply with all the symmetry requirements too, which is expressed by the equation

$$G_{\mathcal{S}}^{\dagger}(S(\mathbf{r}))a_\mu(\mathcal{S}(\mathbf{r}))\tau^\mu G_{\mathcal{S}}(S(\mathbf{r})) = a_\mu(\mathbf{r})\tau^\mu. \tag{9.28}$$

One immediately finds that $a_\mu(\mathbf{r}+\hat{e}_\nu) = a_\mu(\mathbf{r}) \equiv a_\mu$, for $\nu = \{x, y, z\}$ by taking advantage of translational invariance. Since the gauge transformation matrices multiplied from the left and right side are always on the same site $\mathbf{r}$ the η factors of any transformation will square and hence are irrelevant. For the remaining operations, $a_\mu\tau^\mu$ transforms according to

$$\begin{aligned} -g_{\mathcal{T}}^{-1}a_\mu\tau^\mu g_{\mathcal{T}} &= a_\mu\tau^\mu \\ g_{\mathcal{O}}^{-1}a_\mu\tau^\mu g_{\mathcal{O}} &= a_\mu\tau^\mu, \end{aligned} \tag{9.29}$$

while $\mathcal{O}$ can be any point group generator. This means that $a_\mu\tau^\mu$ has to anti-commute with the representation of $g_{\mathcal{T}}$ and has to commute with all other representation matrices $g_{\mathcal{O}}$.

The $u_{\delta\mathbf{r}}$ matrices and the multiplier field a_μ constructed according to the presented discussion yield the desired mean-field Hamiltonian. The matrix structure of $u_{\delta\mathbf{r}}$ is entirely fixed by the PSG. The remaining freedom is the value of the hopping amplitude $\alpha^3_{\delta\mathbf{r}_1} \equiv \chi_1$ and the chemical potential a_3. These values are calculated self-consistently as described in Chapter 2. In the following sections, the resulting mean-field states will be explained in detail for the body centered and face centered cubic lattice. Beginning at the first neighbor level up to third nearest neighbor couplings will be taken into account. Their construction follows the same scheme as it is discussed here and will therefore not be explained again.

9.4. Body centered cubic lattice

On the body centered cubic lattice the classification reveals that there are two distinct first neighbor states BCC 1 and BCC 2, which can be distinguished by the sign factor $\eta_P = \pm 1$.

9.4.1. BCC 1: $\eta_P = +1$ state

The mean-field Hamiltonian is given by a uniform hopping

$$\begin{aligned} \text{BCC 1 first}: \quad u_{\delta\mathbf{r}} &= \chi_1\tau^3, \quad \forall\delta\mathbf{r} \text{ first neighbors} \\ a_3 &\neq 0. \end{aligned} \tag{9.30}$$

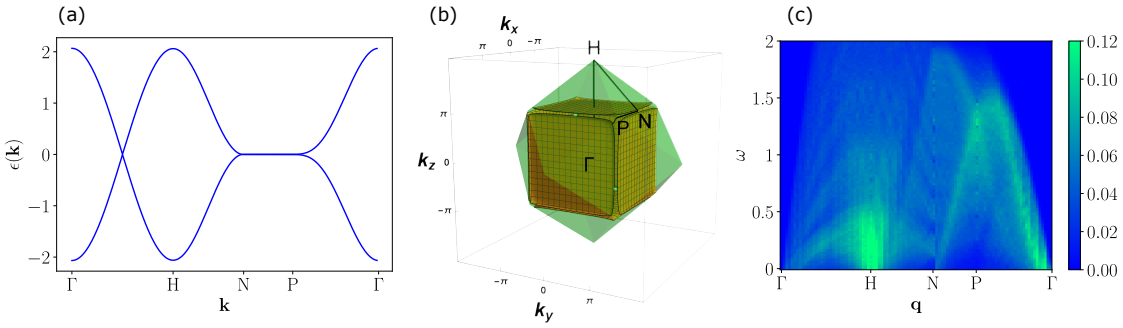

Figure 9.2.: First neighbor state "BCC 1 first" on the body centered cubic lattice. The high symmetry points are given by $H = (0, 0, 2\pi)$, $N = (0, \pi, \pi)$ and $P = (\pi, \pi, \pi)$ (a) shows the dispersion of Eq. (9.30) along a path through the Brillouin zone. The Fermi surface is depicted in (b) where the green region indicates the first Brillouin zone. Sub-figure (c) represents the dynamical structure factor along a path in reciprocal space. (Figure taken from [60])

Calculating the invariance group of this state, as explained in Chapter 5, reveals the $SU(2)$ character of this state. The self-consistently calculated hopping amplitude is found to be $\chi_1 = 0.129$ and the on-site term $a_3 = 0.003$. The resulting ground-state energy per site is determined as $\epsilon_1 = -0.149$. These values are obtained for a fixed coupling $J_1 = 1$ for all first neighbor $\delta\mathbf{r}$, while all other couplings are set to zero $J_2, J_3, \ldots = 0$. It is not expected that this state represents a quantum spin liquid state. The reason for this is that for nearest neighbor couplings only the underlying spin model on the body centered cubic lattice is not frustrated. The resulting ground state is given by a $\mathbf{q} = (2\pi, 0, 0)$ Néel order, shown in Fig. 9.3. However, as further neighbor couplings are included, it was found that the system can get into a magnetically disordered phase [147]. In this perspective, the first neighbor mean-field state is a starting point for extended models in which J_1 is the dominant coupling. These extended models, including second and third neighbor couplings, will be explained below. The dispersion of the first neighbor state is shown in Fig. 9.2. It exhibits a Fermi surface, illustrated in Fig. 9.2, which consists of almost parallel planes. The small curvature at the edges of these planes is due to the chemical potential term a_3. The dynamical structure factor, introduced in Chapter 6, can be seen in Fig. 9.2. It shows a high intensity around the H point. This signal can be understood by the form of the underlying Fermi surface in which two opposite planes are connected by a nesting vector $\mathbf{H} = (2\pi, 0, 0)$. A second characteristic is cone-like signals found around the Γ point. The opening angle of a cone can be linked to the slope of the dispersion and thus gives information about the Fermi velocity v_F. Comparing this angle for different directions departing from the Γ point shows that it is smaller on the line $\overline{\Gamma P}$ than it is on the line $\overline{\Gamma H}$ indicating

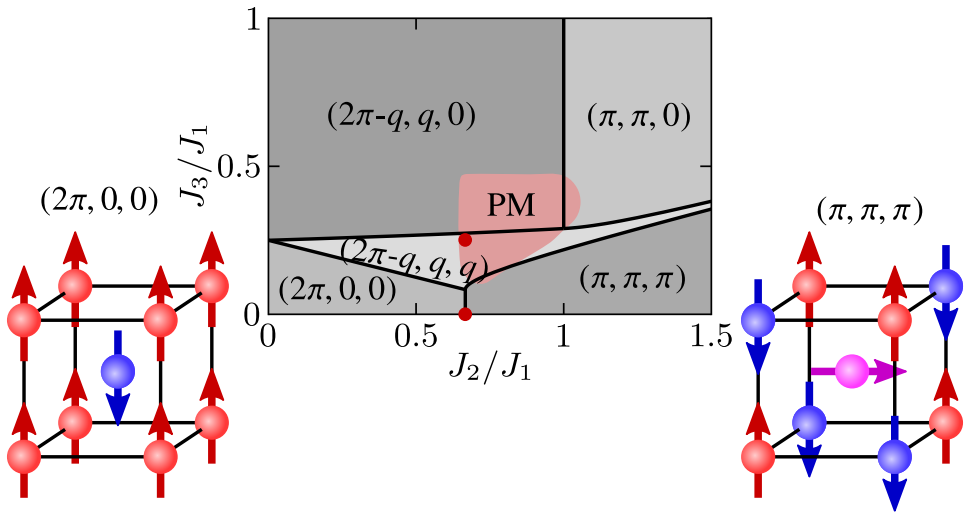

Figure 9.3.: Phase diagram of the classical $J_1 - J_2 - J_3$ Heisenberg model on the body centered cubic lattice. The region drawn in gray represent the classical phases for which the corresponding wave vector is given accordingly. The black lines denote the phase boundaries of the classical model. For the region drawn in red Ref. [147] identified a non magnetic phase. The red points denote the coupling strengths as they are used in the mean-field models. In the bottom left Néel order according to the wave vector $\mathbf{q} = (2\pi, 0, 0)$ is shown. In the bottom right one sees an image of the stripy ordered phase given by wave vector $\mathbf{q} = (\pi, \pi, \pi)$. Note that in this case sub-lattice B has the same spin configuration as the shown sub-lattice A yet with a relative phase shift of $\pi/2$. (The author gratefully received these figures from Johannes Reuther [60].)

a momentum dependency of the Fermi velocity.

The gauge transformation, which made an *Ansatz* belonging to the PSG defined by the first line in Tab. 9.1 equivalent to an *Ansatz* determined by the PSGs of the other lines, does generally not work for second and third neighbor states. The following discussion is, therefore, divided into two parts. The first one deals with the states corresponding to the PSG representation given by the first line in Tab. 9.1.

The second neighbor terms for this PSG representation can include uniform hopping and additionally uniform pairing terms

$$\begin{aligned} \text{BCC 1a second:} \quad & u_{\delta\mathbf{r}} = \chi_2 \tau^3 + \Delta_2 \tau^1, \\ & \forall \delta\mathbf{r} \text{ second neighbors.} \end{aligned} \tag{9.31}$$

The amplitudes and the ground state energy per site are calculated for a fixed ratio of $\frac{J_2}{J_1} = \frac{2}{3}$. At this point previous studies suggest (see Fig. 9.3) that the $J_1 - J_2$ antiferromagnetic Heisenberg model exhibits a phase transition between a $\mathbf{q} = (2\pi, 0, 0)$ Néel ordered and a $\mathbf{q} = (\pi, \pi, \pi)$ stripy long range antiferromagnetically ordered phase [150, 151]. At the transition fluctuations increase, which could lead to a quantum spin liquid phase [152, 147]. The numerical values are calculated as $\chi_1 = 0.116$, $\chi_2 = 0$, $\Delta_2 = -0.106$ and the chemical potential $a_3 = -0.001$. In principle, one could also include an additional Lagrange multiplier along the τ^1 axis, which is found to be redundant $a_1 = 0$. The energy is determined as $\epsilon_2 = -0.178$. The additional pairing term is responsible that a gap in the spectrum appears, as illustrated in Fig. 9.4. Including second neighbors allows for odd-numbered flux operators. This breaks the $SU(2)$ invariance group of the first neighbor state down to a $U(1)$ invariance group. The dynamical structure factor captures the gap in the

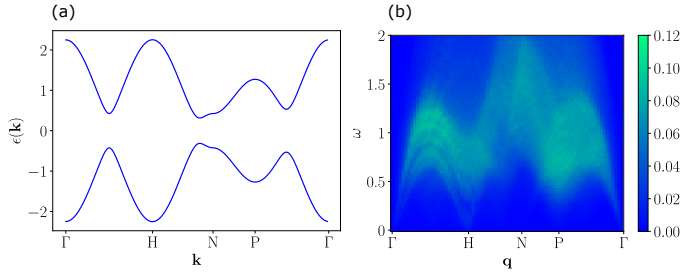

Figure 9.4.: Second neighbor state "BCC 1a second" on the body centered cubic lattice. (a) shows the dispersion of the Hamiltonian consisting of first neighbor terms Eq. (9.30) and second neighbor terms Eq. (9.31) along a path through the Brillouin zone. (b) illustrates the corresponding dynamical structure factor along a path in reciprocal space (see Fig. 9.2). (Figure taken from [60])

energy spectrum, and thus the cone-like signal at the Γ point disappears below a

threshold. The response can be divided into three arcs; one between the Γ, H points, the second between H, P points, and the third between P, Γ points. Inside the first and the third arc, the intensity is relatively homogeneous. The second one appears as a superposition of two slightly shifted ones. The arcs' maxima are at the minima positions of the dispersion.

The requirements of this projective representation for the third nearest neighbors can be satisfied by terms that, similar to the second neighbor case, consists of uniform hopping and pairing terms

$$\begin{aligned} \text{BCC 1a third:} \quad & u_{\delta\mathbf{r}} = \chi_3 \tau^3 + \Delta_3 \tau^1, \\ & \forall \delta\mathbf{r} \text{ third neighbors.} \end{aligned} \tag{9.32}$$

These terms can break the remaining invariance group down to $\mathbb{Z}_2$. The couplings are chosen as $\frac{J_2}{J_1} = \frac{2}{3}$ and $\frac{J_3}{J_1} = \frac{1}{4}$, which marks a point within a non-magnetic phase, as seen in Fig. 9.3. The calculation of the amplitudes yields $\chi_1 = 0.116$, $\chi_2 = 0$, $\Delta_2 = -0.105$, $\chi_3 = 0$ and $\Delta_3 = -0.014$, and vanishing chemical potentials $a_3 = 0$ and $a_1 = 0$. The ground state energy per site is $\epsilon_3 = -0.178$. The dispersion shows similar properties to the second neighbor state and has an energy gap. This applies also for the dynamical structure factor.

The second neighbor terms for the PSGs represented by the lines 2-8 of Tab. 9.1 can only be given by a uniform hopping between second neighbor sites

$$\begin{aligned} \text{BCC 1b second:} \quad & u_{\delta\mathbf{r}} = \chi_2 \tau^3, \\ & \forall \delta\mathbf{r} \text{ second neighbors.} \end{aligned} \tag{9.33}$$

The only consequence by adding these new terms to the Hamiltonian is a symmetry breaking of the $SU(2)$ gauge group down to a $U(1)$ group. The self-consistently determined amplitudes are $\chi_1 = 0.129$, $\chi_2 = -0.001$ and $a_3 = -0.002$. The energy per site is calculated as $\epsilon_2 = -0.149$. These values have been determined, as before, for $\frac{J_2}{J_1} = \frac{2}{3}$. In total, this extension does not change the qualities of the state, which still contains a Fermi surface. The dynamical structure factor also carries the characteristic of the first neighbor state (see Fig. 9.2).

The third neighbors can similarly be included by a uniform hopping between third neighbors

$$\text{BCC 1b third:} \quad u_{\delta\mathbf{r}} = \chi_3 \tau^3, \quad \forall \delta\mathbf{r} \text{ third neighbors.} \tag{9.34}$$

Adding third nearest neighbors has no significant impact, at least, if the third neighbor J_3 coupling is relatively small $\frac{J_3}{J_1} = 0.25$, which is the case for the considered non-magnetic point in the coupling parameter space (see Fig. 9.3). The exchange couplings for the second neighbors are again set to $\frac{J_2}{J_1} = \frac{2}{3}$. The self-consistently

obtained values for the amplitudes are $\chi_1 = 0.125$, $\chi_2 = 0.036$, $\chi_3 = -0.041$ and $a_3 = 0.095$. The energy per site is $\epsilon_3 = -0.152$.

In comparison between these two extensions (a, b), it is found that an *Ansatz* defined by the PSG of the first line in Tab. 9.1 yields the lower mean-field energies for the studied second and third neighbor cases. In this PSG, all representation matrices g_I, $g_{\Pi_{xy}}$, and g_t are given by τ^0, which allows for pairing terms; absent in the other mean-field model. These pairing terms bring a gain in energy, and they further break the invariance group down to $\mathbb{Z}_2$, at least for the third neighbor model.

9.4.2. BCC 2: $\eta_P = -1$ state

The second *Ansatz* is described by real hopping terms, which have a different sign structure induced by a non-trivial transformation of Π_z, Π_y, and P due to the negative factor $\eta_P = -1$. It can be constructed according to

$$\begin{aligned}
&\text{BCC 2 first:} \quad u_{(1/2,1/2,1/2)} = \chi_1\tau^3 = u_{(-1/2,-1/2,-1/2)} \\
&= u_{(1/2,-1/2,1/2)} = u_{(-1/2,1/2,-1/2)} \\
&= u_{(1/2,1/2,-1/2)} = u_{(-1/2,-1/2,1/2)} \\
&= -u_{(-1/2,1/2,1/2)} = -u_{(1/2,-1/2,-1/2)} \\
&a_3 \neq 0.
\end{aligned} \tag{9.35}$$

The invariance group of this *Ansatz* contains the full $SU(2)$ space. By fixing the exchange coupling $J_1 = 1$ the self-consistently calculated energy per site is given by $\epsilon_1 = -0.208$ while the amplitude is $\chi_1 = 0.152$ and the Lagrange multiplier $a_3 = -0.004$. Following the line of argument already made for the BCC 1 state, the first neighbor *Ansatz* is explained even though it has no direct relevance as a possible spin liquid state. The dispersion of this *Ansatz* is shown in Fig. 9.5. Like the other first neighbor state (BCC 1), it has a Fermi surface that has an entirely different form and does not contain any parallel planes. This is also reflected in the dynamical structure factor for which, in the absence of any nesting vectors, the signal's intensity appears fairly homogeneous and can be divided into two arc-like signals. The first arc reaches from the Γ point to the P point (on the momentum axis, including the H and N points) with its maxima roughly at the H point. The second arc, significantly less intense, emerges between the P and Γ point. Inside the first arc, two smaller domes appear in which the signal vanishes. The opening angle of the cone around the Γ point is constant for both directions $\overline{\Gamma H}$ and $\overline{\Gamma P}$. This indicates a constant Fermi velocity.

No second neighbor terms are compatible with the underlying symmetry requirements dictated by the PSG representations $\eta_\Pi = \eta_P = -1$.

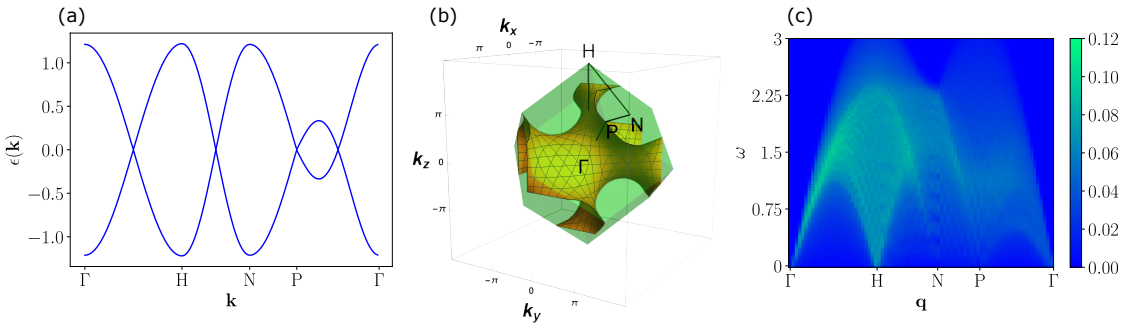

Figure 9.5.: First neighbor state "BCC 2 first" on the body centered cubic lattice. (a) shows the dispersion of Eq. (9.35) along a path through the Brillouin zone. The Fermi surface is depicted in (b) where the green region indicates the first Brillouin zone. Sub-figure (c) represents the dynamical structure factor along a path in reciprocal space. (Figure taken from [60])

Similar to the previously discussed state (BCC 1), the third neighbor can be incorporated in two different fashions, depending on the PSG representations, thus lifting the degeneracy of the first neighbor case where the *Ansätze* of different PSGs can be connected by a gauge transformation.

An *Ansatz* belonging to a PSG given by the first line of Tab. 9.1 can have third neighbor terms including hopping and pairing amplitudes

$$\begin{aligned}\text{BCC 2a third:}\quad & u_{(1,1,0)} = \chi_3\tau^3 + \Delta_3\tau^1 = u_{(-1,-1,0)} \\ &= u_{(0,1,1)} = u_{(0,-1,-1)} = u_{(1,0,-1)} = u_{(-1,0,1)} \\ &= -u_{(1,0,1)} = -u_{(-1,0,-1)} = -u_{(1,-1,0)} = -u_{(-1,1,0)} \\ &= -u_{(0,1,-1)} = -u_{(0,-1,1)}.\end{aligned} \tag{9.36}$$

Due to the absence of second neighbors, the point, which will be used here at $\frac{J_3}{J_1} = \frac{1}{4}$, lies in the vicinity of a triple point, as indicated in the phase diagram Fig. 9.3, between a Néel ordered phase with wave vector $\mathbf{q} = (2\pi, 0, 0)$, a spiral order given by $\mathbf{q} = (2\pi - q, q, 0)$, and a spiral ordered phase $\mathbf{q} = (2\pi - q, q, q)$. Fig. 9.6 illustrates the incommensurate spiral ordering. The self-consistent amplitudes are $\chi_1 = 0.151$, $\chi_3 = -0.001$ and $\Delta_3 = 0.028$. The chemical potential is found at $a_3 = -0.004$ and $a_1 = 0$ yielding an energy per site of $\epsilon_3 = -0.209$ slightly lower than the first neighbor state. The invariance group is broken down to $\mathbb{Z}_2$, and the dispersion has a nodal point at $P = (\pi, \pi, \pi)$, as shown in Fig. 9.7. The dynamical structure factor bears similar properties to the first neighbor state (BCC 2 first).

Possible third neighbors according to PSG representations given by lines 2-8 of

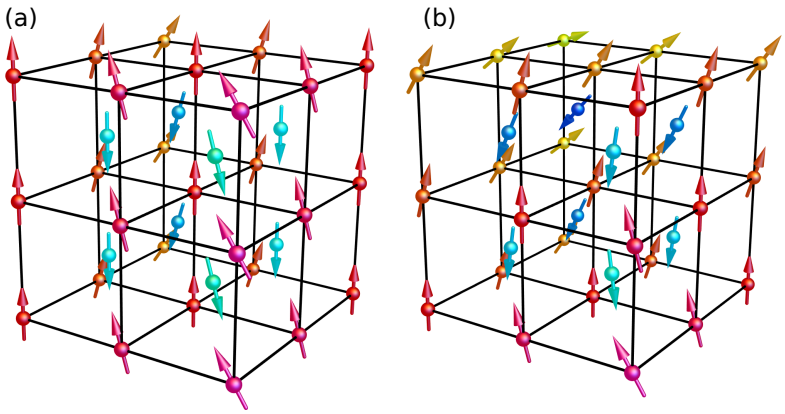

Figure 9.6.: Incommensurate spiral ordering at the triple point of the body centered cubic lattice (see Fig. 9.3) which is used for the thrid neighbor models (9.36),(9.37). Sub-figure (a) corresponds to $\mathbf{q} = (2\pi - q, q, 0)$ and (b) represents $\mathbf{q} = (2\pi - q, q, q)$. (The author gratefully received these figures from Pratyay Ghosh)

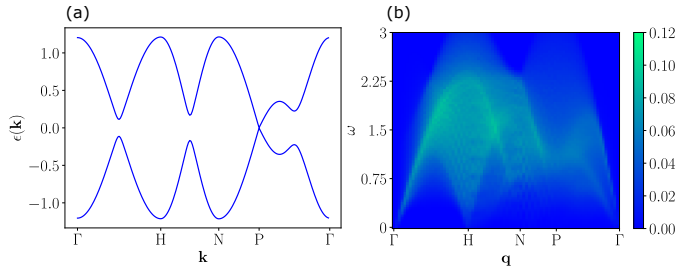

Figure 9.7.: Third neighbor state "BCC 2a third" on the body centered cubic lattice. (a) shows the dispersion of the Hamiltonian consisting of first neighbor terms Eq. (9.35) and third neighbor terms Eq. (9.36) along a path through the Brillouin zone. (b) illustrates the corresponding dynamical structure factor along a path in reciprocal space (see Fig. 9.2). (Figure taken from [60])

Tab. 9.1 can be included by

$$\begin{aligned}
&\text{BCC 2b third:} \quad u_{(1,1,0)} = \chi_3 \tau^3 = u_{(-1,-1,0)} \\
&= u_{(0,1,1)} = u_{(0,-1,-1)} \\
&= u_{(1,0,-1)} = u_{(-1,0,1)} \\
&= -u_{(1,0,1)} = -u_{(-1,0,-1)} \\
&= -u_{(1,-1,0)} = -u_{(-1,1,0)} \\
&= -u_{(0,1,-1)} = -u_{(0,-1,1)}.
\end{aligned} \tag{9.37}$$

The self-consistent amplitudes were calculated at $\frac{J_3}{J_1} = 0.25$ as $\chi_1 = 0.152$ and $\chi_3 = 0$ with an on-site term $a_3 = -0.004$ resulting in an energy per site $\epsilon_3 = -0.208$. For

non vanishing amplitudes the third neighbor state could break the invariance group to $U(1)$. Besides that it bears exactly the same properties as the corresponding first neighbor state BCC 2.

9.4.3. Summary BCC

On the body centered cubic lattice, two distinct $SU(2)$ nearest-neighbor states were identified labeled "BCC 1" and "BCC 2". Their mean-field Hamiltonians contain real uniform hopping terms in the first case and sign dependent real hopping terms in the second case. Both states have gapless excitations due to a Fermi surface in their spectra. Comparison of the ground state energy favors the "BCC 2", which is roughly 40% lower. The Fermi surface of "BCC 1" contains almost parallel planes, which implies nesting vectors. These nesting vectors produce a strong characteristic response in the dynamical structure factor. A second identifying feature for the state "BCC 1" is a momentum dependency of the Fermi velocity. This observation is based on the momentum dependency of the opening angle of a cone-like signal around the Γ point. For each state extending to higher neighbors can be done in two different, projective symmetry respecting, ways that are labeled "a" and "b". The "a" extension includes real hopping and real pairing terms. The extended states were calculated by fixing $\frac{J_2}{J_1} = \frac{2}{3}$ for the second neighbors and $\frac{J_3}{J_1} = \frac{1}{4}$ for the third neighbors. These couplings are suggested by classical studies of the corresponding Heisenberg system as they lie at a phase transition point or in a paramagnetic phase, respectively (see Fig. 9.3). The involved pairing terms are responsible for the opening of an energy gap for the "BCC 1a" state, and they break the invariance group down to $U(1)$ if the second nearest neighbors are included and to $\mathbb{Z}_2$ if the third nearest neighbors are present. The "b" extension only allows additional real hopping terms. This extension breaks the invariance group down to $U(1)$ irrespective of the included neighbors. The properties of the first neighbor state are maintained in this scenario. The "a" extension has an energetically advantage of about 19% over the "b" extension for second neighbors and approximately 17% if third neighbors are involved. The "BCC 2" state cannot include any second nearest neighbor terms. However, the third neighbor extensions can again be made by either including real hopping and real pairing "a" or by real hopping only "b". The "BCC 2a" state has a $\mathbb{Z}_2$ invariance group, and the Fermi surface is reduced to nodal points, thus preserving a gapless spectrum. The invariance group of the "BCC 2b" state is $U(1)$, and all other characteristics of the first neighbor state are unchanged. No difference in energy was found for the "BCC 2" states.

9.5. Face centered cubic lattice

The first neighbor states on the face centered cubic lattice can be classified by six different PSG representations, which are given in Tab. 9.2. As it has been encountered before, an *Ansatz* constructed according to the representations of the first line can be connected to one built according to lines $2-4$ by a gauge rotation around the τ^2 axis, which leaves all representations untouched. This, however, can be done only for the first neighbors. The representations given by the fifth and sixth line yield similar mean-field models in which merely the axes are relabeled by a permutation. Therefore, here only the state belonging to the PSG given in the fifth line is discussed. Summarizing, one can distinguish between two different states on a first neighbor level according to the representation $g_P = \tau^0$ or $g_P = e^{i\frac{\pi}{3}\tau^2}$.

$\eta_\mathcal{T} g_\mathcal{T}$	$\eta_P g_P$	$\eta_I g_I$	$\eta_{\Pi_{xy}} g_{\Pi_{xy}}$
$+i\tau^2$	$+\tau^0$	$+\tau^0$	$+\tau^0$
$+i\tau^2$	$+\tau^0$	$+i\tau^3$	$+\tau^0$
$+i\tau^2$	$+\tau^0$	$+\tau^0$	$+i\tau^3$
$+i\tau^2$	$+\tau^0$	$+i\tau^3$	$+i\tau^3$
$+i\tau^2$	$+e^{i\frac{\pi}{3}\tau^2}$	$+\tau^0$	$+i\tau^3$
$+i\tau^2$	$+e^{i\frac{2\pi}{3}\tau^2}$	$+\tau^0$	$+i\tau^3$

Table 9.2.: Possible PSG representations for first neighbor *Ansätze* on the face centered cubic lattice.

9.5.1. FCC 1: $g_P = \tau^0$ state

This *Ansatz* class, valid for the first to fourth line of Tab. 9.2 consists of a uniform hopping between first neighbor sites on the face centered cubic lattice

$$\begin{aligned} \text{FCC 1 first}: \quad u_{\delta\mathbf{r}} =& \chi_1 \tau^3, \quad \forall \delta\mathbf{r} \text{ first neighbors} \\ a_3 \neq& 0. \end{aligned} \tag{9.38}$$

The hopping amplitude $\chi_1 = 0.109$ and the chemical potential $a_3 = 0.204$ are self-consistently calculated by fixing the exchange coupling $J_1 = 1$ for all first neighbors. On the face centered cubic lattice already first neighbor couplings result in frustration of the classical Heisenberg model, and numerical studies found non-magnetic phases [153, 148]. This can be linked to energetically degenerate lines, which exist in reciprocal space and enhance quantum fluctuations [136, 142]. Such a ground state degeneracy of the classical model enhances the propensity for spin liquid formation. The corresponding ground state energy per site is $\epsilon_1 = -0.156$. The mean-field state exhibits a Fermi surface as shown in Fig. 9.8. The invariance group of this

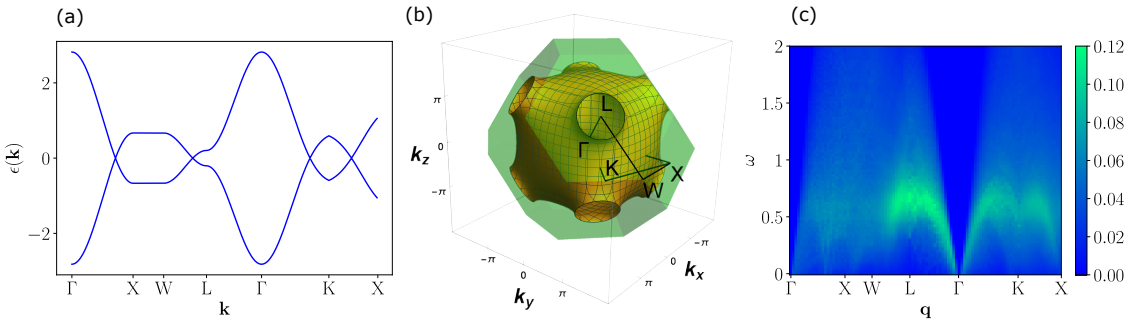

Figure 9.8.: First neighbor state "FCC 1" on the face centered cubic lattice. (a) shows the dispersion of Eq. (9.38) along a path through the Brillouin zone. The Fermi surface is depicted in (b) where the green region indicates the first Brillouin zone. Sub-figure (c) represents the dynamical structure factor along a path in reciprocal space. The high symmetry points are given by $X = (0, 2\pi, 0)$, $W = (\pi, 2\pi, 0)$, $L = (\pi, \pi, \pi)$, and $K = (\frac{3}{2}\pi, \frac{3}{2}\pi, 0)$. (Figure taken from [60])

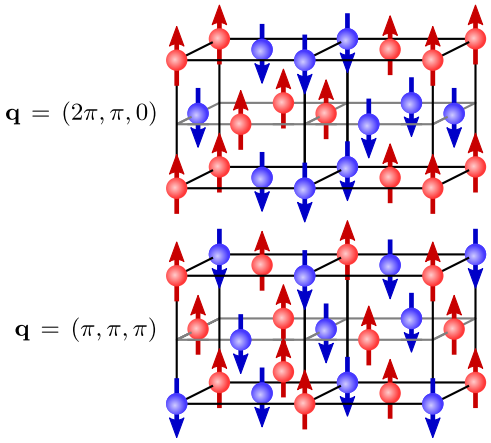

Figure 9.9: Two different magnetically ordered phases at the transition point $\frac{J_2}{J_1} = 0.5$ of the classical $J_1 - J_2$ Heisenberg model on the face centered cubic lattice. (The author gratefully received these figures from Johannes Reuther [60].)

state is $U(1)$. The dynamical structure factor illustrated in Fig. 9.8 shows a fairly homogeneous signal with small regions of higher intensities visible as the flanks of a cone around the Γ point. The opening angle of this cone is constant indicating a constant Fermi velocity.

For the second neighbors the J_1, J_2 couplings are fixed at $\frac{J_2}{J_1} = 0.5$. At this point the classical Heisenberg model undergoes a phase transition between a $\mathbf{q} = (2\pi, \pi, 0)$ order to a $\mathbf{q} = (\pi, \pi, \pi)$ order, as shown in Fig. 9.9. The line degeneracy, present in the J_1 model, even expands to a surface degenarcy for these couplings [142]. A second neighbor *Ansatz* built according to the PSG representations given by the first line of Tab. 9.2 can incorporate real hopping and real pairing terms

$$\begin{aligned} \text{FCC 1a second}: \quad & u_{\delta\mathbf{r}} = \chi_2 \tau^3 + \Delta_2 \tau^1, \\ & \forall \delta\mathbf{r} \text{ second neighbors.} \end{aligned} \tag{9.39}$$

Solving the self-consistent equations yields the amplitudes $\chi_1 = 0.106$, $\chi_2 = -0.075$ and $\Delta_2 = -0.059$. The chemical potential sits at $a_3 = 0.090$ satisfying single-occupancy. A further on-site term is symmetry permitted but vanishes $a_1 = 0$. The resulting energy per site is $\epsilon_2 = -0.185$. The ramification of an additional pairing term is twofold. It breaks the $U(1)$ invariant group of the first neighbor state down to $\mathbb{Z}_2$ and it opens a bandgap as shown in Fig. 9.10. The dynamical structure

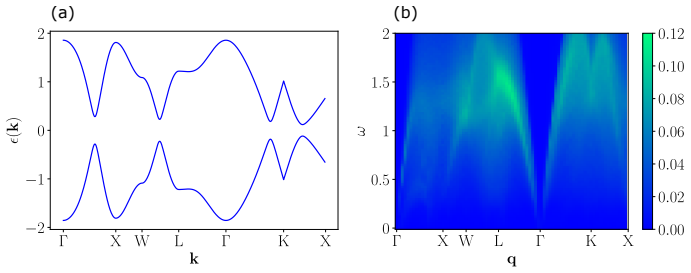

Figure 9.10.: Second neighbor state "FCC 1a second" on the face centered cubic lattice. (a) shows the dispersion of the Hamiltonian consisting of first neighbor terms Eq. (9.38) and second neighbor terms Eq. (9.39) along a path through the Brillouin zone. (b) illustrates the corresponding dynamical structure factor along a path in reciprocal space (see Fig. 9.8). (Figure taken from [60])

factor in Fig. 9.10 also indicates an energy gap. The cone at the Γ point does not appear below this gap. The maximal energy rises, and the entire signal appears more stretched compared to the first neighbor state. Especially the first two-thirds of the plotted momentum range show more structural features in the signal.

For the third neighbors, the Heisenberg couplings are considered at $\frac{J_2}{J_1} = 0.5$ and $\frac{J_3}{J_1} = 0.25$. The classical model shows a tricritical point between two magnetic phases given by the commensurate ordering vectors $\mathbf{q} = (2\pi, 0, 0)$ and $\mathbf{q} = (\pi, \pi, \pi)$, and a non-commensurate spiral order $\mathbf{q} = (q, 0, 0)$ [154]. Including third neighbors in the mean-field model can again be done by adding real hopping and real pairing terms

$$\begin{aligned} \text{FCC 1a third}: \quad & u_{\delta\mathbf{r}} = \chi_3 \tau^3 + \Delta_3 \tau^1, \\ & \forall \delta\mathbf{r} \text{ third neighbors.} \end{aligned} \tag{9.40}$$

The self-consistent amplitudes are found to be $\chi_1 = 0.106$, $\chi_2 = -0.066$, $\Delta_2 = 0.067$, $\chi_3 = -0.028$, $\Delta_3 = -0.013$ and the on-site term $a_3 = 0.093$. The ground state energy per site is $\epsilon_3 = -0.192$. The properties of this extended state do not alter compared to the second neighbor state.

The PSG representations given by line two to four in Tab. 9.2 are more restrictive than the previously discussed case, and second neighbors can only be included by

adding uniform hopping terms

$$\begin{aligned} \text{FCC 1b second}: \quad & u_{\delta\mathbf{r}} = \chi_2 \tau^3, \\ & \forall \delta\mathbf{r} \text{ second neighbors.} \end{aligned} \tag{9.41}$$

Amplitudes and chemical potential are calculated as $\chi_1 = 0.107$, $\chi_2 = -0.087$ and $a_3 = 0.067$, where the couplings were fixed $\frac{J_2}{J_1} = 0.5$, as explained above. The differences compared to the first neighbor state are only quantitative in nature, and all characteristics are maintained. The ground state energy per site is lowered to $\epsilon_2 = -0.183$.

A possible third neighbor extension can again include only a uniform hopping between third neighbors

$$\begin{aligned} \text{FCC 1b third}: \quad & u_{\delta\mathbf{r}} = \chi_3 \tau^3, \\ & \forall \delta\mathbf{r} \text{ third neighbors.} \end{aligned} \tag{9.42}$$

Fixing $\frac{J_2}{J_1} = 0.5$ and $\frac{J_3}{J_1} = 0.25$ at the tricritical point yields the amplitudes as $\chi_1 = 0.108$, $\chi_2 = -0.078$, $\chi_3 = -0.026$ and an on-site term $a_3 = 0.070$. The resulting energy per site is further lowered to $\epsilon_3 = -0.188$. Yet all characteristics remain the same regarding the first neighbor state.

Similar to the BCC states it is found that the higher neighbor extensions including pairing terms yield the lower mean-field ground state energies.

9.5.2. FCC 2: $g_P = e^{i\frac{\pi}{3}\tau^2}$ state

The *Ansatz* belonging to this PSG is built according to

$$\begin{aligned} u_{(1/2,1/2,0)} &= \chi_1 \tau^3 \\ &= u_{(1/2,-1/2,0)} = u_{(-1/2,1/2,0)} = u_{(-1/2,-1/2,0)}, \\ u_{(1/2,0,1/2)} &= \chi_1 \left(\frac{\sqrt{3}}{2}\tau^1 - \frac{1}{2}\tau^3 \right) \\ &= u_{(1/2,0,-1/2)} = u_{(-1/2,0,1/2)} = u_{(-1/2,0,-1/2)}, \\ u_{(0,1/2,1/2)} &= \chi_1 \left(-\frac{\sqrt{3}}{2}\tau^1 - \frac{1}{2}\tau^3 \right) \\ &= u_{(0,1/2,-1/2)} = u_{(0,-1/2,1/2)} = u_{(0,-1/2,-1/2)}. \end{aligned} \tag{9.43}$$

This state has an interesting property: choosing a gauge such that one direction is fixed to include only a hopping amplitude, the peculiar representation of permutation immediately induces pairing terms for other directions. Thus this state has already on the nearest neighbor level the invariance group broken down to $\mathbb{Z}_2$.

In momentum space, the action of time-reversal, followed by inversion $I\mathcal{T}$ maps any momentum back onto itself $\mathbf{k} \to \mathbf{k}$. In the corresponding PSG time-reversal is implemented by $g_{\mathcal{T}} = i\tau^2$, which combined with inversion $g_I = \tau^0$ yields a condition on the mean-field Hamiltonian $(g_I g_{\mathcal{T}})^\dagger H(\mathbf{k}) g_I g_{\mathcal{T}} = -H(\mathbf{k})$. It follows that the Hamiltonian has to anti-commute with the corresponding representation. Furthermore, for momenta that map back onto themselves under permutation $P(\mathbf{k}) = \mathbf{k}$, g_P provides an additional condition on the Hamiltonian: $g_P^\dagger H(\mathbf{k}) g_P = H(\mathbf{k})$. These two conditions collide since there cannot be any finite $H(\mathbf{k})$ that anti-commutes with $I\mathcal{T} = i\tau^2$ and commutes with $g_P = e^{i\theta\tau^2}$ at the same time. Indeed, one finds zero-energy modes in the spectrum shown in Fig. 9.11 along the lines $\overline{\Gamma L}$ and $\overline{LL'}$, invariant under P. One sees that additionally to the diagonal lines, a cube-like object at zero energy. This cube connects different L points in the Brillouin zone, and its existence is due to the small translations t_1 and t_2 of the face centered cubic lattice. Acting with these translations on the momentum representation of the mean-field matrices reveals that $u_{\mathbf{k}}$ has to vanish for momenta lying on the edges of the cube. This manifold of zero-energy modes, pervasive through the entire space, is protected by the projective symmetries.

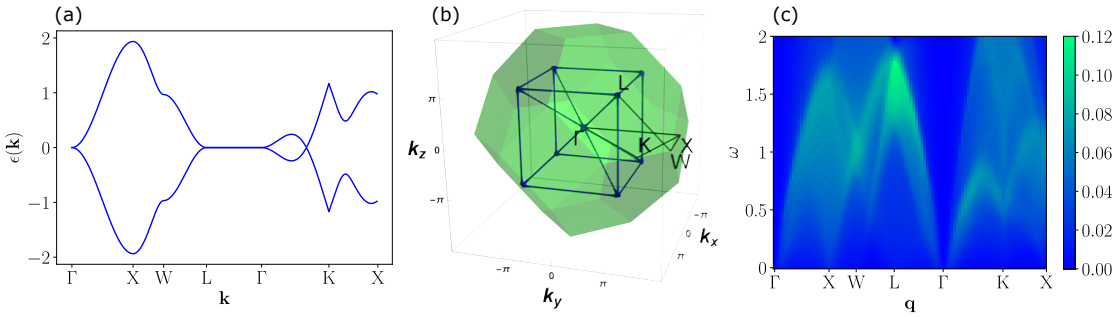

Figure 9.11.: First neighbor state "FCC 1" on the face centered cubic lattice. (a) shows the dispersion of Eq. (9.43) along a path through the Brillouin zone. The Fermi surface is depicted in (b) where the green region indicates the first Brillouin zone. Sub-figure (c) represents the dynamical structure factor along a path in reciprocal space. (Figure taken from [60])

To compute the self-consistent amplitudes $J_1 = 1$ is fixed for nearest neighbors (see discussion FCC 1) yielding $\chi_1 = 0.121$. There is no symmetry allowed Lagrange multiplier possible. The ground state energy per site is $\epsilon_1 = -0.198$. The dynamical structure factor illustrated in Fig. 9.11 shows the typical cone around the Γ-point with a constant opening angle. It also shows a feature that looks like a crossings at $\omega \approx 1$ at the W point. The edges of the cube, which appear at zero energy can be connected with nesting vectors $\mathbf{X} = (2\pi, 0, 0)$ (and other permutations). This leads to a characteristic signal in the spin structure factor. Since here only lines exist the

intensity of this signal is much lower, as compared to the BCC 1 state for which the Fermi surface includes entire planes.

Second neighbor terms cannot be included without violating any symmetry condition.

Third neighbor terms follow the description

$$\begin{aligned}
&u_{(1/2,1/2,1)} = \chi_3\tau^3 = u_{(-1/2,-1/2,-1)} \\
&= u_{(-1/2,-1/2,1)} = u_{(1/2,-1/2,-1)} = u_{(-1/2,1/2,-1)} \\
&= u_{(1/2,1/2,-1)} = u_{(-1/2,1/2,1)} = u_{(1/2,-1/2,1)}, \\
&u_{(1/2,1,1/2)} = \chi_3\left(\frac{\sqrt{3}}{2}\tau^1 - \frac{1}{2}\tau^3\right) = u_{(-1/2,-1,-1/2)} \\
&= u_{(-1/2,-1,1/2)} = u_{(1/2,-1,-1/2)} = u_{(-1/2,1,-1/2)} \\
&= u_{(1/2,1,-1/2)} = u_{(-1/2,1,1/2)} = u_{(1/2,-1,1/2)}, \\
&u_{(1,1/2,1/2)} = \chi_3\left(-\frac{\sqrt{3}}{2}\tau^1 - \frac{1}{2}\tau^3\right) = u_{(-1,-1/2,-1/2)} \\
&= u_{(-1,-1/2,1/2)} = u_{(1,-1/2,-1/2)} = u_{(-1,1/2,-1/2)} \\
&= u_{(1,1/2,-1/2)} = u_{(-1,1/2,1/2)} = u_{(1,-1/2,1/2)}.
\end{aligned} \tag{9.44}$$

The amplitudes for the fixed ratio $\frac{J_3}{J_1} = 0.25$ are found to be $\chi_1 = 0.121$ and $\chi_3 = -0.035$ yielding a ground state energy per site as $\epsilon_3 = -0.208$. The properties of the third neighbor state are similar to the first neighbor state which also includes the presence of the zero lines in the energy spectrum.

9.5.3. Summary FCC

The first neighbor states for the face centered cubic lattice can be grouped into two different *Ansatz* classes that are called "FCC 1" and "FCC 2". The mean-field Hamiltonian of "FCC 1" contains uniform real hopping terms between nearest neighbors. The resulting state has a $U(1)$ invariance group, and its dispersion contains a Fermi surface. The other possible state, "FCC 2", has an interesting structure combining real hopping and real pairing amplitudes directional dependent. The invariance group is broken down to $\mathbb{Z}_2$. The corresponding projective group representation protects some zero-energy nodal lines against any possible perturbation as long as the projective symmetries are respected. The ground state energy of the "FCC 2" state is about 27% lower than that of the "FCC 1" state. Including higher neighbors to the "FCC 1" state can be achieved by adding real hopping and real pairing terms "a" or by real hopping terms only "b". The J couplings were set to $\frac{J_2}{J_1} = \frac{1}{2}$ for the second neighbors and $\frac{J_3}{J_1} = \frac{1}{4}$ for the third neighbors. These couplings

relate to phase transitions points of the antiferromagnetic Heisenberg model. The "FCC 1a" acquires an excitation gap, and the invariance group is further broken down to $\mathbb{Z}_2$ by adding second nearest neighbors. Taking third neighbors into account does not qualitatively change these results. According to the "b" description, extending the first neighbor state has no qualitatively effect neither for the second nor the third neighbors. Comparing the resulting mean-field energies shows that "FCC 1a" is slightly lower than "FCC 1b". The difference is merely about 1% to 2% comparing the second or third neighbor states, respectively. For the "FCC 2" state, it was derived that no second neighbor terms respect the symmetries and are absent. Third neighbor terms have a similar structure to the first neighbor terms and do not qualitatively change any of the first neighbor state properties. The mean-field energy remains lower for the "FCC 2" state.

9.6. Conclusion

The classification of the simple cubic lattice revealed that there are 672 different algebraic PSGs. These PSGs can lead to 528 possible mean-field models. The resulting irreducible representations of gauge transformations, which are related to the symmetry generators, could be used to generalize this classification for the PSGs of the body- and face centered cubic lattice. It was found that for the BCC lattice 1888 algebraic PSGs exist yielding 1520 mean-field *Ansätze* and for the FCC lattice 672 algebraic PSGs leading to 528 *Ansätze*. The PSG representations for the body centered cubic and face centered cubic lattice were in the following used to construct all possible short-range mean-field states. It was found that despite the large number of algebraic PSGs, very few are, in fact, relevant for short-ranged states, which included couplings up to third nearest neighbors. For both lattices, it was found that for first nearest neighbor only two gauge inequivalent models exist: One which has a similar form for both lattices and is described by only a uniform hopping between nearest neighbors. The second scenario exhibits a particular sign structure of these hopping amplitudes in the case of the BCC lattice and a more complex structure, which also involves pairing amplitudes in the FCC lattice case. For both lattices, it was shown that, based on self-consistent calculations of the energy, the state which is not built by uniform hopping terms is energetically favorable. It was shown that including higher neighbor terms can be done in two different manners: (1) A possible extension includes further hopping terms of second and third nearest neighbors. (2) The extension incorporates hopping and pairing terms for second- and third nearest neighbors. These extensions are possible for all studied cases except for the FCC model, which already on the nearest neighbor level includes pairing terms. Comparing the resulting mean-field energies revealed that the extension, including

additional pairing terms, always yields lower energies.

Furthermore, for the energetically favorable state of the face centered cubic lattice, it could be shown that in the spectrum zero-energy lines exist protected by the representations of some projective symmetries.

10. Conclusion

This concluding chapter summarizes the three main research projects conducted during the author's doctoral studies. In the end, some unifying remarks are made, and an outlook is given.

Concerning the first project, the analysis made in Chapter 7 took up a study in which 1488 representation were identified in a PSG classification [54]. This precursory classification, calculated on the square lattice, explicitly took spin rotation symmetry breaking terms into account. These terms result in an extension of the spinor space, and the decoupling has to be done in additional triplet channels contrary to the usual mean-field approach, which considers only the singlet channel. In the course of this study, it was found that, in this enlarged setting, which expresses the effect of spin-orbit coupling, spinons can exhibit non-trivial band topologies.

In the follow-up study, the large number of possible PSGs could be reduced under the physically motivated assumption that the resulting mean-field models should contain only short-ranged coupling terms. Limiting these couplings to only first neighbors led to 28 possible PSG representations. It could be shown that the resulting spinon models can merely have topologically trivial bands. Loosening the first neighbor condition by including second nearest neighbors was found to be sufficient such that the resulting spinon models revealed topological band structures even under further restraining conditions. Two of these models were further studied. One of them could be identified as a spinon equivalent of the famous Bernevig-Hughes-Zhang (BHZ) model. Contrary to the electric model, the spinon model contains a $\cos k_x \cos k_y$ dependency of the effective mass, which drives the occurrence of a second band inversion resulting in an additional topological phase with Chern number $n_\uparrow = 2$. This phase and the second band inversion are absent in the BHZ model.

In the following, the effect of visons was studied. In this regard, the two topological second nearest neighbor models, as well as one topologically trivial first neighbor model, were extended in a manner that a resulting lattice model takes static configurations of a background gauge field into account. By choosing these background configurations, it is possible to mimic the effect of vison excitations. The first result confirmed that all spinon models represent a vison deconfining phase. The insertion of a pair of visons amounts to the cost of finite energy. However, the separation of an existing pair does not require significantly more energy. The responsible confin-

ing potential was observed to be short-ranged in nature and became irrelevant only after two elementary plaquette steps. It was further found that spinons and visons form composite objects that appear in the low-energy region of the spectrum. In the case of the topologically non-trivial spinon band models, it was found that these spinon-visons pair states are Majorana zero modes. This statement was supported by an exact mapping between the spinon-vison model to a continuum model, which was identified as the $p + ip$ Bogoliubiv-de Gennes Hamiltonian coupled to a vortex in the superconducting pairing field. For the later model, the existence of Majorana modes had already been rigorously established [56, 57]. The effect of a gas of visons was also considered. In order to imitate such a gas, visons were included on random lattice positions. These gases were created such that visons appeared on 0.6% and 2% of all plaquettes. These visons led to the occurrence of characteristic peaks in the low-energy spectrum. It was claimed that these peaks could be an experimental signature that reveals information on the spinon band topology.

The second project explained in Chapter . 8, was initiated shortly after the compound $Ca_{10}Cr_7O_{28}$ had been proposed as a quantum spin liquid candidate [50]. At the moment, such candidates are rare, and thus its discovery is a felicitous circumstance and enables the community of condensed matter theorists to affirm or refute existing theories. In the case of the fermionic mean-field theory, its correctness would imply that the material, if it is a veritable $\mathbb{Z}_2$ quantum spin liquid, should in the low-energy regime show properties of a free fermionic state. The spinon hopping model concocted in Chapter 8 showed precisely this. In a first step, reflecting the geometry of the magnetic couplings, the complexity was reduced by an effective description that was built upon a single layer honeycomb - instead of the original bilayer kagome lattice. This reduction introduced a new basis in which the low-energy degrees of freedom are described by emerging spin-3/2 objects. These objects can be identified as symmetric superpositions of three ferromagnetically coupled spins sitting on triangles. The full vector space required two additional perpendicular basis vectors, which correspond to spin-1/2 objects representing antisymmetric superpositions. These three basis vectors can be understood as the irreducible representations of the dihedral group D_3. From a technical point of view, in the spinon model, these components were energetically separated by choosing a suitable chemical potential. To reproduce the observed linear temperature dependency of the heat capacity the chemical potential of the energetically low sitting spin-3/2 objects was tuned such that a Fermi surface appeared. A second potential term raised the antisymmetric superposed objects in energy such that separation in the form of an energy gap occurred. Based on the overlap properties of the corresponding eigenstates, this simple model already explained some of the key features found in the neutron scattering data.

High-resolution data of the heat capacity in the lowest accessible temperature regime showed a small deviation from linearity. The new dependency appears to be quadratic in temperature. Therefore, it was argued that these deviations are not due to the, in the free fermion model neglected, visons, for which the expected behavior follows a $T^{2/3}$ law [127], but rather due to a spinon pairing mechanism. The pairing is most likely momentum dependent, which excludes a simple s-wave spinon superconductor. Fitting different pairing models to the available data and taking symmetry arguments into account suggested an f-wave pairing. The corresponding amplitude, however, appeared to be very small such that no attempt was made in order to include this feature into the spinon hopping model. The reason for this lies in the resolution of the scattering plots, which are too coarse to resolve such a small amplitude correctly. Yet conceptually, this mechanism is crucial as it breaks the invariance group and therefore completes the picture of a $\mathbb{Z}_2$ quantum spin liquid.

In the final project, PSG classifications explained in Chapter 9, were made for the simple-, body-, and face centered cubic lattice. The relevant PSG equations were identified which are given respectively in Eq. (9.4), Eq. (9.16) and Eq. (9.18), and the corresponding irreducible representations shown in Appendix A.4. It was found that despite the large numbers of possible PSG realizations for every lattice, only a few of them are, in fact, relevant for short-ranged spinon mean-field models. Based on these classifications such short-ranged mean-field Hamiltonians were constructed for the body- and face centered cubic lattice, including up to third nearest neighbors coupling. Using a Hartree-Fock self-consistency procedure, these models were further scrutinized by analyzing the spinon band dispersion and the dynamical spin structure factor. On the body centered cubic lattice, two different first neighbor states could be identified, which can be distinguished through the representation of the symmetry generator P. Both states result from mean-field models containing only real hopping amplitudes. For the state which was labeled "BCC 1", these amplitudes are spatially uniform, whereas the model resulting in the state "BCC 2" showed some sign patterns induced by a non-trivial symmetry representation P. The dispersions of both states contain a Fermi surface. The surface of the state "BCC 1" consists of nearly parallel planes leading to the existence of a Nesting vector. This vector evokes a characteristic signature in the dynamical structure factor. Comparison of the self-consistently calculated mean-field ground state energies suggested that the "BCC 2" state is more likely to be realized as it lies about 40% lower in energy. However, both models include a $SU(2)$ invariance group. Therefore, the effective low-energy models contain gapless fermionic modes and gapless gauge fields. This might spark some skepticism about the correctness of the mean-field approach. Besides that, the classical antiferromagnetic Heisenberg model does not develop any frustration, and the ground state is described by Néel order. Including second- and

third neighbors breaks this $SU(2)$ invariance to either $U(1)$ or $\mathbb{Z}_2$. The second and third neighbor models were respectively derived for fixed $J_1 = 1, \frac{J_2}{J_1} = \frac{2}{3}, \frac{J_3}{J_1} = \frac{1}{4}$ coupling constants. In the case of second neighbors, the corresponding classical Heisenberg model is at a phase transition point. The parameters for third neighbors lie in a non-magnetic phase [147]. The spatially extended models include in the $\mathbb{Z}_2$ scenario additional real hopping and real pairing terms while the later destroy the Fermi surface and open a bandgap. The extension resulting in the $U(1)$ state can consist of only further real hopping terms, which leads to the persistence of gapless fermionic modes. The self-consistently determined energies indicated that for the "BCC 1" state, the $\mathbb{Z}_2$ scenario is more favorable, whereas for "BCC 2" state, for which no second neighbor extensions are symmetry allowed, both scenarios yielded comparable energies.

On the face centered cubic lattice, it was similarly found that only two different states appear, which again can be classified according to the representation of P. The "FCC 1" state results from a uniform and real spinon hopping *Ansatz*. It has a Fermi surface of a circular shape, which is slightly deformed. The $U(1)$ invariance group of this first neighbor state can be broken by including real pairing terms of higher neighbor bonds. Such an extension would be energetically favorable compared to an extension of only further real hopping terms. These findings rely on self-consistent calculations of the respective mean-field energies with $J_1 = 1, \frac{J_2}{J_1} = \frac{1}{2}, \frac{J_3}{J_1} = \frac{1}{4}$ fixed. The second neighbor couplings are chosen at a phase transition point, and the third neighbors are at a triple point of the classical Heisenberg model. The second state, "FCC 2", has a more involved structure. Caused by a non-trivial representation of P, the first neighbor state already includes hopping and pairing terms, which immediately break the invariance group down to $\mathbb{Z}_2$. The corresponding amplitudes are symmetry-related and alternate for different spatial directions. It could be shown that in the spinon band dispersion, zero-energy lines exist, which are protected by different PSG elements. These zero-energy lines are pervasive through the entire momentum space. This state cannot contain any symmetry consistent second neighbor terms. Third neighbor terms show a similar pattern to the first neighbor terms, and qualitatively do not change the first neighbor state. The "FCC 2" state has a lower mean-field ground state energy than the "FCC 1" state.

Within this thesis, several aspects of the mean-field approach to antiferromagnetic Heisenberg systems have been considered. These mean-field theories are founded upon a rewriting of the spin operators in terms of fermionic operators, which can be linked to the fractionalized spinon excitations governing the low-energy regime of quantum spin liquid states. The usage of this formalism is twofold. In one way, it makes it possible to classify exotic phases which otherwise evade a conventional classification scheme. This is achieved using projective symmetry group represen-

tations. Knowledge of these group representations enables the construction of all possible symmetry allowed mean-field *Ansätze* for a given space group. In a second usage, the fermionic mean-field theory can be applied in order to build a phenomenological effective low-energy theory as it was explained for the quantum spin liquid candidate $Ca_{10}Cr_7O_{28}$. Regardless of the details of their derivation, such mean-field models can help to identify relevant quantum models. This is important since many numerical methods are powerful in calculating certain correlation functions, but deriving the fundamental microscopic models may be an obstacle. Furthermore, in the mean-field formalism, it is possible to directly access the dynamical spin structure factor, which can be immediately connected to experimental neutron scattering data. Numerical methods cannot always probe this quantity. Any given mean-field state may be readily improved as it provides a starting point for a variational method in the form of an initial *Ansatz*. An enhancement could also be obtained by including pseudofermion functional renormalized vertex functions [144]. Both methods take fluctuations into account, which are neglected in the bare mean-field theory. Concerning this last point, the mean-field theory can, on its own, be further improved. As explained in this work existing mean-field models that entirely exclude the emerging gauge fields can be generalized by incorporating static gauge field configuration. This method is still not capable of describing full dynamical gauge fields, but it may serve to study the mutual effect of spinon and vison excitations. In this context, an experiment was proposed that might reveal some information about the spinon band dispersion by measuring the energy-resolved density of states while changing the temperature. The basic idea behind this procedure is that thermal fluctuations can excite visons, which then bind spinon modes. These composite objects are expected to emerge in the spectrum at zero energy if the spinon bands are topologically non-trivial. In summary, this work showed that mean-field theory, if correctly applied, is, despite its flaws, a suitable analytic tool in order to study strongly correlated spin systems from the perspective of describing quantum spin liquid states.

A. Appendix

A.1. Point group generators and corresponding spin space representations for the square lattice

The square lattice is besides the two translations T_x, T_y defined by the following generators

$$\begin{aligned} \mathcal{P}_x &: \mathbf{r} \to (-x, y) \\ \mathcal{P}_y &: \mathbf{r} \to (x, -y) \\ \mathcal{P}_{xy} &: \mathbf{r} \to (y, x) \end{aligned} \tag{A.1}$$

This is further illustrated in Fig. A.1. In the case that spin rotational symmetry is broken the PSG classification needs to take a further operator into account, which acts as

$$\mathcal{P}_z : z \to -z. \tag{A.2}$$

These operators act on a spinor doublet $f_{\mathbf{r}} = (f_{\mathbf{r}\uparrow}, f_{\mathbf{r}\downarrow})$ according to

$$\begin{aligned} \mathcal{P}_x &: f_{\mathbf{r}} \to \exp(-\frac{i\pi}{2}\tau^1) f_{\mathcal{P}_x(\mathbf{r})} \\ \mathcal{P}_y &: f_{\mathbf{r}} \to \exp(-\frac{i\pi}{2}\tau^2) f_{\mathcal{P}_y(\mathbf{r})} \\ \mathcal{P}_{xy} &: f_{\mathbf{r}} \to \exp(-\frac{i\pi}{2}\tau^1) \exp(-\frac{i\pi}{4}\tau^3) f_{\mathcal{P}_{xy}(\mathbf{r})} \\ \mathcal{P}_z &: f_{\mathbf{r}} \to \exp(-\frac{i\pi}{2}\tau^3) f_{\mathbf{r}}. \end{aligned} \tag{A.3}$$

These relations can be used to determine the coefficients of the representation matrices $\mathcal{D}_{\mathcal{S}}$ which where defined in Chapter 5.

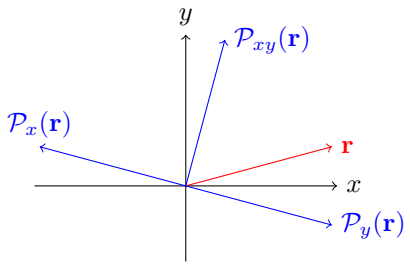

Figure A.1: The action of the generators given in Eq. (A.1) denoted in blue on a vector $\mathbf{r}$ drawn in red.

A.2. Projective symmetry conditions on the mean-field matrices $\tilde{u}_{\mathbf{r}\mathbf{r}'}$

This appendix shows for the square lattice the projective transformation properties of an *Ansatz* for all channels $u^X_{\mathbf{r}\mathbf{r}'}$ with $X = s, t_1, t_2, t_3$.

$$\begin{aligned}
-\eta_{\mathcal{T}}^{\delta x+\delta y} g_{\mathcal{T}}^{\dagger} u^{s}_{\delta\mathbf{r}} g_{\mathcal{T}} &= u^{s}_{\delta\mathbf{r}},\\
\eta_{\mathcal{P}_x}^{\delta x}\eta_{\mathcal{P}_y}^{\delta y} g_{\mathcal{P}_x}^{\dagger} u^{s}_{\mathcal{P}_x(\delta\mathbf{r})} g_{\mathcal{P}_x} &= u^{s}_{\delta\mathbf{r}},\\
\eta_{\mathcal{P}_y}^{\delta x}\eta_{\mathcal{P}_x}^{\delta y} g_{\mathcal{P}_y}^{\dagger} u^{s}_{\mathcal{P}_y(\delta\mathbf{r})} g_{\mathcal{P}_y} &= u^{s}_{\delta\mathbf{r}},\\
\eta^{\delta x\delta y} g_{\mathcal{P}_{xy}}^{\dagger} u^{s}_{\mathcal{P}_{xy}(\delta\mathbf{r})} g_{\mathcal{P}_{xy}} &= u^{s}_{\delta\mathbf{r}},\\
\eta_{\mathcal{P}_z}^{\delta x+\delta y} g_{\mathcal{P}_z}^{\dagger} u^{s}_{\delta\mathbf{r}} g_{\mathcal{P}_z} &= u^{s}_{\delta\mathbf{r}},\\
\eta^{\delta x\delta y} (u^{s})^{\dagger}_{-\delta\mathbf{r}} &= u^{s}_{\delta\mathbf{r}}
\end{aligned} \tag{A.4}$$

$$\begin{aligned}
-\eta_{\mathcal{T}}^{\delta x+\delta y} g_{\mathcal{T}}^{\dagger} u^{t_1}_{\delta\mathbf{r}} g_{\mathcal{T}} &= u^{t_1}_{\delta\mathbf{r}},\\
-\eta_{\mathcal{P}_x}^{\delta x}\eta_{\mathcal{P}_y}^{\delta y} g_{\mathcal{P}_x}^{\dagger} u^{t_1}_{\mathcal{P}_x(\delta\mathbf{r})} g_{\mathcal{P}_x} &= u^{t_1}_{\delta\mathbf{r}},\\
-\eta_{\mathcal{P}_y}^{\delta x}\eta_{\mathcal{P}_x}^{\delta y} g_{\mathcal{P}_y}^{\dagger} u^{t_1}_{\mathcal{P}_y(\delta\mathbf{r})} g_{\mathcal{P}_y} &= u^{t_1}_{\delta\mathbf{r}},\\
-\eta^{\delta x\delta y} g_{\mathcal{P}_{xy}}^{\dagger} u^{t_1}_{\mathcal{P}_{xy}(\delta\mathbf{r})} g_{\mathcal{P}_{xy}} &= u^{t_1}_{\delta\mathbf{r}},\\
\eta_{\mathcal{P}_z}^{\delta x+\delta y} g_{\mathcal{P}_z}^{\dagger} u^{t_1}_{\delta\mathbf{r}} g_{\mathcal{P}_z} &= u^{t_1}_{\delta\mathbf{r}},\\
\eta^{\delta x\delta y} (u^{t_1})^{\dagger}_{-\delta\mathbf{r}} &= u^{t_1}_{\delta\mathbf{r}}
\end{aligned} \tag{A.5}$$

$$\begin{aligned}
-\eta_{\mathcal{T}}^{\delta x+\delta y} g_{\mathcal{T}}^{\dagger} u^{t_2}_{\delta\mathbf{r}} g_{\mathcal{T}} &= u^{t_2}_{\delta\mathbf{r}},\\
-\eta_{\mathcal{P}_x}^{\delta x}\eta_{\mathcal{P}_y}^{\delta y} g_{\mathcal{P}_x}^{\dagger} u^{t_2}_{\mathcal{P}_x(\delta\mathbf{r})} g_{\mathcal{P}_x} &= u^{t_2}_{\delta\mathbf{r}},\\
\eta_{\mathcal{P}_y}^{\delta x}\eta_{\mathcal{P}_x}^{\delta y} g_{\mathcal{P}_y}^{\dagger} u^{t_2}_{\mathcal{P}_y(\delta\mathbf{r})} g_{\mathcal{P}_y} &= u^{t_2}_{\delta\mathbf{r}},\\
-i\eta^{\delta x\delta y} g_{\mathcal{P}_{xy}}^{\dagger} u^{t_2}_{\mathcal{P}_{xy}(\delta\mathbf{r})} g_{\mathcal{P}_{xy}} &= u^{t_3}_{\delta\mathbf{r}},\\
-\eta_{\mathcal{P}_z}^{\delta x+\delta y} g_{\mathcal{P}_z}^{\dagger} u^{t_2}_{\delta\mathbf{r}} g_{\mathcal{P}_z} &= u^{t_2}_{\delta\mathbf{r}},\\
-\eta^{\delta x\delta y} (u^{t_2})^{\dagger}_{-\delta\mathbf{r}} &= u^{t_2}_{\delta\mathbf{r}}
\end{aligned} \tag{A.6}$$

$$\begin{aligned}
-\eta_{\mathcal{T}}^{\delta x+\delta y} g_{\mathcal{T}}^{\dagger} u^{t_3}_{\delta\mathbf{r}} g_{\mathcal{T}} &= u^{t_3}_{\delta\mathbf{r}},\\
\eta_{\mathcal{P}_x}^{\delta x}\eta_{\mathcal{P}_y}^{\delta y} g_{\mathcal{P}_x}^{\dagger} u^{t_3}_{\mathcal{P}_x(\delta\mathbf{r})} g_{\mathcal{P}_x} &= u^{t_3}_{\delta\mathbf{r}},\\
-\eta_{\mathcal{P}_y}^{\delta x}\eta_{\mathcal{P}_x}^{\delta y} g_{\mathcal{P}_y}^{\dagger} u^{t_3}_{\mathcal{P}_y(\delta\mathbf{r})} g_{\mathcal{P}_y} &= u^{t_3}_{\delta\mathbf{r}},\\
i\eta^{\delta x\delta y} g_{\mathcal{P}_{xy}}^{\dagger} u^{t_3}_{\mathcal{P}_{xy}(\delta\mathbf{r})} g_{\mathcal{P}_{xy}} &= u^{t_2}_{\delta\mathbf{r}},\\
-\eta_{\mathcal{P}_z}^{\delta x+\delta y} g_{\mathcal{P}_z}^{\dagger} u^{t_3}_{\delta\mathbf{r}} g_{\mathcal{P}_z} &= u^{t_3}_{\delta\mathbf{r}},\\
\eta^{\delta x\delta y} (u^{t_3})^{\dagger}_{-\delta\mathbf{r}} &= u^{t_3}_{\delta\mathbf{r}}.
\end{aligned} \tag{A.7}$$

In each of these equations, the last line ensures hermiticity of the mean-field Hamiltonian.

A.3. Nearest neighbor coupling Z_2 mean-field Anstätze

All possible $\mathbb{Z}_2$ mean-field *Anstätze* for nearest neighbor coupling with fully broken SU(2) spin-rotation symmetry on the square lattice and their corresponding PSG representations are listed below:

$$\begin{aligned} &g_{\mathcal{P}_z} = \tau^0, \quad g_{\mathcal{T}} = \tau^0, \quad g_{\mathcal{P}_{xy}} = i\tau^3, \quad g_{\mathcal{P}_x} = i\tau^1, \quad g_{\mathcal{P}_y} = i\tau^1 \\ &\eta_{\mathcal{P}_z} = -1, \quad \eta_{\mathcal{T}} = -1, \quad \eta = \pm 1, \quad \eta_{\mathcal{P}_x} = 1, \quad \eta_{\mathcal{P}_y} = 1 \end{aligned} \tag{A.8}$$

$$\begin{aligned} &g_{\mathcal{P}_z} = \tau^0, \quad g_{\mathcal{T}} = \tau^0, \quad g_{\mathcal{P}_{xy}} = i\tau^3, \quad g_{\mathcal{P}_x} = i\tau^1, \quad g_{\mathcal{P}_y} = i\tau^1 \\ &\eta_{\mathcal{P}_z} = -1, \quad \eta_{\mathcal{T}} = -1, \quad \eta = \pm 1, \quad \eta_{\mathcal{P}_x} = -1, \quad \eta_{\mathcal{P}_y} = -1 \end{aligned} \tag{A.9}$$

$$\begin{aligned} &g_{\mathcal{P}_z} = i\tau^3, \quad g_{\mathcal{T}} = \tau^0, \quad g_{\mathcal{P}_{xy}} = i\tau^3, \quad g_{\mathcal{P}_x} = i\tau^1, \quad g_{\mathcal{P}_y} = i\tau^1 \\ &\eta_{\mathcal{P}_z} = 1, \quad \eta_{\mathcal{T}} = -1, \quad \eta = \pm 1, \quad \eta_{\mathcal{P}_x} = -1, \quad \eta_{\mathcal{P}_y} = -1 \end{aligned} \tag{A.10}$$

$$\begin{aligned} &g_{\mathcal{P}_z} = i\tau^2, \quad g_{\mathcal{T}} = \tau^0, \quad g_{\mathcal{P}_{xy}} = \tau^0, \quad g_{\mathcal{P}_x} = i\tau^3, \quad g_{\mathcal{P}_y} = i\tau^3 \\ &\eta_{\mathcal{P}_z} = 1, \quad \eta_{\mathcal{T}} = -1, \quad \eta = \pm 1, \quad \eta_{\mathcal{P}_x} = -1, \quad \eta_{\mathcal{P}_y} = -1 \end{aligned} \tag{A.11}$$

$$\begin{aligned} &g_{\mathcal{P}_z} = i\tau^2, \quad g_{\mathcal{T}} = \tau^0, \quad g_{\mathcal{P}_{xy}} = i\tau^3, \quad g_{\mathcal{P}_x} = \tau^0, \quad g_{\mathcal{P}_y} = \tau^0 \\ &\eta_{\mathcal{P}_z} = 1, \quad \eta_{\mathcal{T}} = -1, \quad \eta = \pm 1, \quad \eta_{\mathcal{P}_x} = 1, \quad \eta_{\mathcal{P}_y} = 1 \end{aligned} \tag{A.12}$$

$$\begin{aligned} &g_{\mathcal{P}_z} = i\tau^1, \quad g_{\mathcal{T}} = \tau^0, \quad g_{\mathcal{P}_{xy}} = i\tau^3, \quad g_{\mathcal{P}_x} = i\tau^1, \quad g_{\mathcal{P}_y} = i\tau^1 \\ &\eta_{\mathcal{P}_z} = 1, \quad \eta_{\mathcal{T}} = -1, \quad \eta = \pm 1, \quad \eta_{\mathcal{P}_x} = 1, \quad \eta_{\mathcal{P}_y} = 1 \end{aligned} \tag{A.13}$$

$$\begin{aligned} &g_{\mathcal{P}_z} = i\tau^2, \quad g_{\mathcal{T}} = \tau^0, \quad g_{\mathcal{P}_{xy}} = i\tau^3, \quad g_{\mathcal{P}_x} = \tau^0, \quad g_{\mathcal{P}_y} = \tau^0 \\ &\eta_{\mathcal{P}_z} = -1, \quad \eta_{\mathcal{T}} = -1, \quad \eta = \pm 1, \quad \eta_{\mathcal{P}_x} = 1, \quad \eta_{\mathcal{P}_y} = -1 \end{aligned} \tag{A.14}$$

$$\begin{aligned} &g_{\mathcal{P}_z} = i\tau^1, \quad g_{\mathcal{T}} = \tau^0, \quad g_{\mathcal{P}_{xy}} = i\tau^3, \quad g_{\mathcal{P}_x} = i\tau^1, \quad g_{\mathcal{P}_y} = i\tau^1 \\ &\eta_{\mathcal{P}_z} = -1, \quad \eta_{\mathcal{T}} = -1, \quad \eta = \pm 1, \quad \eta_{\mathcal{P}_x} = -1, \quad \eta_{\mathcal{P}_y} = 1 \end{aligned} \tag{A.15}$$

$$\begin{aligned} &g_{\mathcal{P}_z} = i\tau^2, \quad g_{\mathcal{T}} = \tau^0, \quad g_{\mathcal{P}_{xy}} = i\tau^3, \quad g_{\mathcal{P}_x} = i\tau^3, \quad g_{\mathcal{P}_y} = i\tau^3 \\ &\eta_{\mathcal{P}_z} = 1, \quad \eta_{\mathcal{T}} = -1, \quad \eta = \pm 1, \quad \eta_{\mathcal{P}_x} = -1, \quad \eta_{\mathcal{P}_y} = -1 \end{aligned} \tag{A.16}$$

$$\begin{aligned} &g_{\mathcal{P}_z} = i\tau^2, \quad g_{\mathcal{T}} = \tau^0, \quad g_{\mathcal{P}_{xy}} = i\tau^3, \quad g_{\mathcal{P}_x} = i\tau^1, \quad g_{\mathcal{P}_y} = i\tau^1 \\ &\eta_{\mathcal{P}_z} = 1, \quad \eta_{\mathcal{T}} = -1, \quad \eta = \pm 1, \quad \eta_{\mathcal{P}_x} = -1, \quad \eta_{\mathcal{P}_y} = -1 \end{aligned} \tag{A.17}$$

$$\begin{aligned} &g_{\mathcal{P}_z} = i\tau^1, \quad g_{\mathcal{T}} = \tau^0, \quad g_{\mathcal{P}_{xy}} = i\tau^3, \quad g_{\mathcal{P}_x} = i\tau^1, \quad g_{\mathcal{P}_y} = i\tau^1 \\ &\eta_{\mathcal{P}_z} = -1, \quad \eta_{\mathcal{T}} = -1, \quad \eta = \pm 1, \quad \eta_{\mathcal{P}_x} = -1, \quad \eta_{\mathcal{P}_y} = -1 \end{aligned} \tag{A.18}$$

$$\begin{aligned} &g_{\mathcal{P}_z} = i\tau^2, \quad g_{\mathcal{T}} = \tau^0, \quad g_{\mathcal{P}_{xy}} = i\tau^3, \quad g_{\mathcal{P}_x} = \tau^0, \quad g_{\mathcal{P}_y} = \tau^0 \\ &\eta_{\mathcal{P}_z} = -1, \quad \eta_{\mathcal{T}} = -1, \quad \eta = \pm 1, \quad \eta_{\mathcal{P}_x} = 1, \quad \eta_{\mathcal{P}_y} = 1 \end{aligned} \tag{A.19}$$

$$\begin{aligned} &g_{\mathcal{P}_z} = i\tau^2, \quad g_{\mathcal{T}} = \tau^0, \quad g_{\mathcal{P}_{xy}} = i\tau^3, \quad g_{\mathcal{P}_x} = \tau^0, \quad g_{\mathcal{P}_y} = \tau^0 \\ &\eta_{\mathcal{P}_z} = 1, \quad \eta_{\mathcal{T}} = -1, \quad \eta = \pm 1, \quad \eta_{\mathcal{P}_x} = -1, \quad \eta_{\mathcal{P}_y} = -1 \end{aligned} \tag{A.20}$$

$$\begin{aligned} &g_{\mathcal{P}_z} = i\tau^1, \quad g_{\mathcal{T}} = \tau^0, \quad g_{\mathcal{P}_{xy}} = i\tau^3, \quad g_{\mathcal{P}_x} = i\tau^1, \quad g_{\mathcal{P}_y} = i\tau^1 \\ &\eta_{\mathcal{P}_z} = 1, \quad \eta_{\mathcal{T}} = -1, \quad \eta = \pm 1, \quad \eta_{\mathcal{P}_x} = -1, \quad \eta_{\mathcal{P}_y} = -1 \end{aligned} \tag{A.21}$$

These representations in combination with the PSG equations of Appendix A.2 enable the construction of symmetric mean-field states on the square lattice.

A.4. Inequivalent PSG representations

Tab. A.1 lists a set of inequivalent representation matrices for the point group generators of the simple cubic lattice. The matrices for Π_z, Π_y can only be trivially represented $g_{\Pi_z} = g_{\Pi_y} = \tau^0$ without violating any of the algebraic conditions of Eq. (9.4). There are 21 different choices for the remaining matrices. For every possible set of matrices, a set of $\eta_{\mathcal{S}} = \pm 1$ sign factors complete the PSG representation, besides the case in which $g_{\mathcal{T}} = \tau^0$ where only $\eta_{\mathcal{T}} = -1$ is possible. In the face centered cubic lattice the additional symmetries can only have a trivial matrix representation $g_{t_1} = g_{t_2} = \tau^0$. The representation matrices are, therefore, the same as for the simple cubic lattice (see Tab. A.1). In the body centered cubic lattice gauge inequivalent choices are shown in Tab. A.2. Here are 51 different choices possible.

$g_{\mathcal{T}}$	g_P	g_I	$g_{\Pi_{xy}}$
τ^0	τ^0	τ^0	τ^0
τ^0	τ^0	$i\tau^2$	τ^0
τ^0	τ^0	τ^0	$i\tau^2$
τ^0	τ^0	$i\tau^2$	$i\tau^2$
τ^0	τ^0	$i\tau^2$	$i\tau^3$
τ^0	$e^{i\frac{\pi}{3}\tau^2}$	τ^0	$i\tau^3$
τ^0	$e^{i\frac{\pi}{3}\tau^2}$	$i\tau^2$	$i\tau^3$
τ^0	$e^{i\frac{2\pi}{3}\tau^2}$	τ^0	$i\tau^3$
τ^0	$e^{i\frac{2\pi}{3}\tau^2}$	$i\tau^2$	$i\tau^3$
$i\tau^2$	τ^0	τ^0	τ^0
$i\tau^2$	τ^0	$i\tau^2$	τ^0
$i\tau^2$	τ^0	$i\tau^3$	τ^0
$i\tau^2$	τ^0	τ^0	$i\tau^2$
$i\tau^2$	τ^0	τ^0	$i\tau^3$
$i\tau^2$	τ^0	$i\tau^2$	$i\tau^2$
$i\tau^2$	τ^0	$i\tau^3$	$i\tau^2$
$i\tau^2$	τ^0	$i\tau^3$	$i\tau^3$
$i\tau^2$	$e^{i\frac{\pi}{3}\tau^2}$	τ^0	$i\tau^3$
$i\tau^2$	$e^{i\frac{\pi}{3}\tau^2}$	$i\tau^2$	$i\tau^3$
$i\tau^2$	$e^{i\frac{2\pi}{3}\tau^2}$	τ^0	$i\tau^3$
$i\tau^2$	$e^{i\frac{2\pi}{3}\tau^2}$	$i\tau^2$	$i\tau^3$

Table A.1.: Projective representation matrices for the simple cubic and face centered cubic lattice.

$g_{\mathcal{T}}$	g_P	g_I	$g_{\Pi_{xy}}$	g_t
$\tau^0/i\tau^2$	τ^0	τ^0	τ^0	τ^0
$\tau^0/i\tau^2$	τ^0	$i\tau^2$	τ^0	τ^0
$\tau^0/i\tau^2$	τ^0	τ^0	$i\tau^2$	τ^0
$\tau^0/i\tau^2$	τ^0	τ^0	τ^0	$i\tau^2$
$\tau^0/i\tau^2$	τ^0	τ^0	$i\tau^2$	$i\tau^2$
$\tau^0/i\tau^2$	τ^0	$i\tau^2$	$i\tau^2$	τ^0
$\tau^0/i\tau^2$	τ^0	$i\tau^2$	τ^0	$i\tau^2$
$\tau^0/i\tau^2$	τ^0	$i\tau^2$	$i\tau^2$	$i\tau^2$
$\tau^0/i\tau^2$	τ^0	$i\tau^2$	$i\tau^3$	τ^0
$\tau^0/i\tau^2$	τ^0	$i\tau^2$	τ^0	$i\tau^3$
$\tau^0/i\tau^2$	τ^0	τ^0	$i\tau^2$	$i\tau^3$
$\tau^0/i\tau^2$	τ^0	$i\tau^2$	$i\tau^3$	$i\tau^3$
$\tau^0/i\tau^2$	τ^0	$i\tau^2$	$i\tau^2$	$i\tau^3$
$\tau^0/i\tau^2$	τ^0	$i\tau^2$	$i\tau^3$	$i\tau^2$
$\tau^0/i\tau^2$	τ^0	$i\tau^2$	$i\tau^3$	$i\tau^1$
$i\tau^2$	τ^0	$i\tau^3$	τ^0	τ^0
$i\tau^2$	τ^0	τ^0	$i\tau^3$	τ^0
$i\tau^2$	τ^0	τ^0	τ^0	$i\tau^3$
$i\tau^2$	τ^0	τ^0	$i\tau^3$	$i\tau^3$
$i\tau^2$	τ^0	τ^0	$i\tau^3$	$i\tau^1$
$i\tau^2$	τ^0	$i\tau^3$	$i\tau^2$	τ^0
$i\tau^2$	τ^0	$i\tau^3$	τ^0	$i\tau^2$
$i\tau^2$	τ^0	$i\tau^3$	$i\tau^2$	$i\tau^2$
$i\tau^2$	τ^0	$i\tau^3$	$i\tau^3$	τ^0
$i\tau^2$	τ^0	$i\tau^3$	τ^0	$i\tau^3$
$i\tau^2$	τ^0	$i\tau^3$	$i\tau^3$	$i\tau^3$
$i\tau^2$	τ^0	$i\tau^3$	$i\tau^3$	$i\tau^1$
$i\tau^2$	τ^0	$i\tau^3$	$i\tau^1$	$i\tau^1$
$\tau^0/i\tau^2$	$e^{i\frac{\pi}{3}\tau^2}$	τ^0	$i\tau^3$	τ^0
$\tau^0/i\tau^2$	$e^{i\frac{\pi}{3}\tau^2}$	τ^0	$i\tau^3$	$i\tau^2$
$\tau^0/i\tau^2$	$e^{i\frac{\pi}{3}\tau^2}$	$i\tau^2$	$i\tau^3$	τ^0
$\tau^0/i\tau^2$	$e^{i\frac{\pi}{3}\tau^2}$	$i\tau^2$	$i\tau^3$	$i\tau^2$
$\tau^0/i\tau^2$	$e^{i\frac{2\pi}{3}\tau^2}$	τ^0	$i\tau^3$	τ^0
$\tau^0/i\tau^2$	$e^{i\frac{2\pi}{3}\tau^2}$	τ^0	$i\tau^3$	$i\tau^2$
$\tau^0/i\tau^2$	$e^{i\frac{2\pi}{3}\tau^2}$	$i\tau^2$	$i\tau^3$	τ^0
$\tau^0/i\tau^2$	$e^{i\frac{2\pi}{3}\tau^2}$	$i\tau^2$	$i\tau^3$	$i\tau^2$

Table A.2.: Projective representation matrices for the body centered cubic lattice. The notation $\tau^0/i\tau^2$ indicated that $g_{\mathcal{T}}$ can either be represented by τ^0 or $i\tau^2$.

Bibliography

[1] L.D. Landau and E.M Lifschitz. *Statistical Physics - Course of Theoretical Physics*, volume 5. Elsevier - Butterworth Heinemann, Oxford, 1980.

[2] John W. Negele and Henri Orland. *Quantum Many-Particle Systems*. Westview Press, Advanced Book Program, 1998.

[3] D. C. Tsui, H. L. Stormer, and A. C. Gossard. Two-dimensional magnetotransport in the extreme quantum limit. *Phys. Rev. Lett.*, 48:1559–1562, May 1982.

[4] R. B. Laughlin. Anomalous quantum hall effect: An incompressible quantum fluid with fractionally charged excitations. *Phys. Rev. Lett.*, 50:1395–1398, May 1983.

[5] Xiao-Gang Wen. Quantum orders and symmetric spin liquids. *Phys. Rev. B*, 65:165113, Apr 2002.

[6] Leon Balents. Spin liquids in frustrated magnets. *Nature (London)*, 464(7286):199–208, 03 2010.

[7] M. R. Norman. Colloquium: Herbertsmithite and the search for the quantum spin liquid. *Rev. Mod. Phys.*, 88:041002, Dec 2016.

[8] Yi Zhou, Kazushi Kanoda, and Tai-Kai Ng. Quantum spin liquid states. *Rev. Mod. Phys.*, 89:025003, Apr 2017.

[9] Lucile Savary and Leon Balents. Quantum spin liquids: a review. *Rep. Prog. Phys.*, 80:016502, 2017.

[10] Xiao-Gang Wen. Quantum order: a quantum entanglement of many particles. *Physics Letters A*, 300(2):175 – 181, 2002.

[11] Xiao-Gang Wen. *Quantum Field Theory of Many-body Systems: From the Origin of Sound to an Origin of Light and Electrons*. Oxford University Press; Reissue edition, Oxford Graduate Texts, 2007.

[12] N F Mott. The basis of the electron theory of metals, with special reference to the transition metals. *Proceedings of the Physical Society. Section A*, 62(7), 1949.

[13] Assa Auerbach. *Interacting Electrons and Quantum Magnetism*. Springer-Verlag New York, 1 edition, 1994.

[14] Eduardo Fradkin. *Field Theories of Condensed Matter Physics*. Cambridge University Press, 2 edition, 2013.

[15] P.W. Anderson. Resonating valence bonds: A new kind of insulator? *Mater. Res. Bull.*, 8(2):153 – 160, 1973.

[16] J. G. Bednorz and K. A. Müller. Possible high T_c superconductivity in the Ba-La-Cu-O system. *Zeitschrift für Physik B Condensed Matter*, 64, 1986.

[17] M. K. Wu, J. R. Ashburn, C. J. Torng, P. H. Hor, R. L. Meng, L. Gao, Z. J. Huang, Y. Q. Wang, and C. W. Chu. Superconductivity at 93 k in a new mixed-phase Y-Ba-Cu-O compound system at ambient pressure. *Phys. Rev. Lett.*, 58:908–910, Mar 1987.

[18] J. E. Hirsch. Attractive interaction and pairing in fermion systems with strong on-site repulsion. *Phys. Rev. Lett.*, 54:1317–1320, Mar 1985.

[19] Ian Affleck and J. Brad Marston. Large-n limit of the heisenberg-hubbard model: Implications for high-T_c superconductors. *Phys. Rev. B*, 37:3774–3777, Mar 1988.

[20] G. Baskaran, Z. Zou, and P.W. Anderson. The resonating valence bond state and high-tc superconductivity a mean field theory. *Solid State Communications*, 63, 1987.

[21] Patrick A. Lee, Naoto Nagaosa, and Xiao-Gang Wen. Doping a mott insulator: Physics of high-temperature superconductivity. *Rev. Mod. Phys.*, 78:17–85, Jan 2006.

[22] G. Baskaran and P. W. Anderson. Gauge theory of high-temperature superconductors and strongly correlated fermi systems. *Phys. Rev. B*, 37:580–583, Jan 1988.

[23] Ian Affleck, Z. Zou, T. Hsu, and P. W. Anderson. Su(2) gauge symmetry of the large-u limit of the hubbard model. *Phys. Rev. B*, 38:745–747, Jul 1988.

[24] L. B. Ioffe and A. I. Larkin. Gapless fermions and gauge fields in dielectrics. *Phys. Rev. B*, 39:8988–8999, May 1989.

[25] G Baskaran. Gauge theory of high temperature superconductivity. *Physica Scripta*, T27:53–59, jan 1989.

[26] X. G. Wen. Mean-field theory of spin-liquid states with finite energy gap and topological orders. *Phys. Rev. B*, 44:2664–2672, Aug 1991.

[27] Patrick A. Lee and Naoto Nagaosa. Gauge theory of the normal state of high-t_c superconductors. *Phys. Rev. B*, 46:5621–5639, Sep 1992.

[28] A. A. Abrikosov. Electron scattering on magnetic impurities in metals and anomalous resistivity effects. *Physics Physique Fizika*, 2:5–20, Sep 1965.

[29] Naoto Nagaosa and Patrick A. Lee. Normal-state properties of the uniform resonating-valence-bond state. *Phys. Rev. Lett.*, 64:2450–2453, May 1990.

[30] T. Senthil and Matthew P. A. Fisher. Z_2 gauge theory of electron fractionalization in strongly correlated systems. *Phys. Rev. B*, 62:7850–7881, Sep 2000.

[31] Alexei Kitaev. Anyons in an exactly solved model and beyond. *Annals of Physics*, 321(1):2 – 111, 2006.

[32] Frank Wilczek. Magnetic flux, angular momentum, and statistics. *Phys. Rev. Lett.*, 48:1144–1146, Apr 1982.

[33] Daniel Arovas, J. R. Schrieffer, and Frank Wilczek. Fractional statistics and the quantum hall effect. *Phys. Rev. Lett.*, 53:722–723, Aug 1984.

[34] X. G. Wen, Frank Wilczek, and A. Zee. Chiral spin states and superconductivity. *Phys. Rev. B*, 39:11413–11423, Jun 1989.

[35] Kenneth G. Wilson. Confinement of quarks. *Phys. Rev. D*, 10:2445–2459, Oct 1974.

[36] Claudine Lacrois, Philippe Mendels, and Frédéric Mila. *Introduction to Frustrated Magnetism*. Springer-Verlag Berlin Heidelberg, Springer Series in Solid-State Science 164, 2011.

[37] Frank Wilczek. Quantum mechanics of fractional-spin particles. *Phys. Rev. Lett.*, 49:957–959, Oct 1982.

[38] N. Read and B. Chakraborty. Statistics of the excitations of the resonating-valence-bond state. *Phys. Rev. B*, 40:7133–7140, Oct 1989.

[39] Steven Kivelson. Statistics of holons in the quantum hard-core dimer gas. *Phys. Rev. B*, 39:259–264, Jan 1989.

[40] A.Yu. Kitaev. Fault-tolerant quantum computation by anyons. *Annals of Physics*, 303(1):2 – 30, 2003.

[41] Chetan Nayak, Steven H. Simon, Ady Stern, Michael Freedman, and Sankar Das Sarma. Non-abelian anyons and topological quantum computation. *Rev. Mod. Phys.*, 80:1083–1159, Sep 2008.

[42] Subir Sachdev. Kagome- and triangular-lattice heisenberg antiferromagnets: Ordering from quantum fluctuations and quantum-disordered ground states with unconfined bosonic spinons. *Phys. Rev. B*, 45:12377–12396, Jun 1992.

[43] J. S. Helton, K. Matan, M. P. Shores, E. A. Nytko, B. M. Bartlett, Y. Yoshida, Y. Takano, A. Suslov, Y. Qiu, J.-H. Chung, D. G. Nocera, and Y. S. Lee. Spin dynamics of the spin-1/2 kagome lattice antiferromagnet $ZnCu_3(OH)_6Cl_2$. *Phys. Rev. Lett.*, 98:107204, Mar 2007.

[44] Tian-Heng Han, Joel S. Helton, Shaoyan Chu, Daniel G. Nocera, Jose A. Rodriguez-Rivera, Collin Broholm, and Young S. Lee. Fractionalized excitations in the spin-liquid state of a kagome-lattice antiferromagnet. *Nature*, 492:406 EP –, 12 2012.

[45] J. A. Sears, M. Songvilay, K. W. Plumb, J. P. Clancy, Y. Qiu, Y. Zhao, D. Parshall, and Young-June Kim. Magnetic order in α-$RuCl_3$: A honeycomb-lattice quantum magnet with strong spin-orbit coupling. *Phys. Rev. B*, 91:144420, Apr 2015.

[46] A. Banerjee, C. A. Bridges, J. Q. Yan, A. A. Aczel, L. Li, M. B. Stone, G. E. Granroth, M. D. Lumsden, Y. Yiu, J. Knolle, S. Bhattacharjee, D. L. Kovrizhin, R. Moessner, D. A. Tennant, D. G. Mandrus, and S. E. Nagler. Proximate kitaev quantum spin liquid behaviour in a honeycomb magnet. *Nature Materials*, 15:733 EP –, 04 2016.

[47] Seung-Hwan Do, Sang-Youn Park, Junki Yoshitake, Joji Nasu, Yukitoshi Motome, Yong Seung Kwon, D. T. Adroja, D. J. Voneshen, Kyoo Kim, T. H. Jang, J. H. Park, Kwang-Yong Choi, and Sungdae Ji. Majorana fermions in the kitaev quantum spin system α-$RuCl_3$. *Nature Physics*, 13:1079 EP –, 09 2017.

[48] Arnab Banerjee, Jiaqiang Yan, Johannes Knolle, Craig A. Bridges, Matthew B. Stone, Mark D. Lumsden, David G. Mandrus, David A. Tennant, Roderich Moessner, and Stephen E. Nagler. Neutron scattering in the proximate quantum spin liquid α-$RuCl_3$. *Science*, 356(6342):1055–1059, 2017.

[49] Christian Balz, Paula Lampen-Kelley, Arnab Banerjee, Jiaqiang Yan, Zhilun Lu, Xinzhe Hu, Swapnil M. Yadav, Yasu Takano, Yaohua Liu, D. Alan Tennant, Mark D. Lumsden, David Mandrus, and Stephen E. Nagler. Finite field

regime for a quantum spin liquid in $\alpha-\mathrm{rucl}_3$. *Phys. Rev. B*, 100:060405, Aug 2019.

[50] Christian Balz, Bella Lake, Johannes Reuther, Hubertus Luetkens, Rico Schönemann, Thomas Herrmannsdörfer, Yogesh Singh, A. T. M. Nazmul Islam, Elisa M. Wheeler, Jose A. Rodriguez-Rivera, Tatiana Guidi, Giovanna G. Simeoni, Chris Baines, and Hanjo Ryll. Physical realization of a quantum spin liquid based on a complex frustration mechanism. *Nature Physics*, 12:942 EP –, 07 2016.

[51] Christian Balz, Bella Lake, A. T. M. Nazmul Islam, Yogesh Singh, Jose A. Rodriguez-Rivera, Tatiana Guidi, Elisa M. Wheeler, Giovanna G. Simeoni, and Hanjo Ryll. Magnetic hamiltonian and phase diagram of the quantum spin liquid $Ca_{10}Cr_7O_{28}$. *Phys. Rev. B*, 95:174414, May 2017.

[52] Christian Balz, Bella Lake, Manfred Reehuis, A T M Nazmul Islam, Oleksandr Prokhnenko, Yogesh Singh, Philip Pattison, and Sándor Tóth. Crystal growth, structure and magnetic properties of $Ca_{10}Cr_7O_{28}$. *Journal of Physics: Condensed Matter*, 29(22):225802, apr 2017.

[53] Jonas Sonnenschein and Johannes Reuther. Topological spinon bands and vison excitations in spin-orbit coupled quantum spin liquids. *Phys. Rev. B*, 96:235113, Dec 2017.

[54] Johannes Reuther, Shu-Ping Lee, and Jason Alicea. Classification of spin liquids on the square lattice with strong spin-orbit coupling. *Phys. Rev. B*, 90:174417, Nov 2014.

[55] B. Andrei Bernevig, Taylor L. Hughes, and Shou-Cheng Zhang. Quantum spin hall effect and topological phase transition in HgTe quantum wells. *Science*, 314(5806):1757–1761, 2006.

[56] R. Jackiw and P. Rossi. Zero modes of the vortex-fermion system. *Nuclear Physics B*, 190(4):681 – 691, 1981.

[57] N. Read and Dmitry Green. Paired states of fermions in two dimensions with breaking of parity and time-reversal symmetries and the fractional quantum hall effect. *Phys. Rev. B*, 61:10267–10297, Apr 2000.

[58] V. Gurarie and L. Radzihovsky. Zero modes of two-dimensional chiral p-wave superconductors. *Phys. Rev. B*, 75:212509, Jun 2007.

[59] Jonas Sonnenschein, Christian Balz, Ulrich Tutsch, Michael Lang, Hanjo Ryll, Jose A. Rodriguez-Rivera, A. T. M. Nazmul Islam, Bella Lake, and Jo-

hannes Reuther. Signatures for spinons in the quantum spin liquid candidate $Ca_{10}Cr_7O_{28}$. *Phys. Rev. B*, 100:174428, Nov 2019.

[60] Jonas Sonnenschein, Aishwarya Chauhan, Yasir Iqbal, and Johannes Reuther. Projective symmetry group classifications of quantum spin liquids on the simple cubic, body centered cubic, and face centered cubic lattices. *Phys. Rev. B*, 102:125140, Sep 2020.

[61] Samuel Bieri, Laura Messio, Bernard Bernu, and Claire Lhuillier. Gapless chiral spin liquid in a kagome heisenberg model. *Phys. Rev. B*, 92:060407(R), Aug 2015.

[62] Steven Weinberg. *The Quantum Theory of Fields*, volume 1. Cambridge University Press, 1995.

[63] Steven Weinberg. *The Quantum Theory of Fields*, volume 2. Cambridge University Press, 1996.

[64] L. D. Faddeev and V. N. Popov. Feynman diagrams for the Yang-Mills field. *Physics Letters B*, 25(1):29–30, July 1967.

[65] David J. Gross and André Neveu. Dynamical symmetry breaking in asymptotically free field theories. *Phys. Rev. D*, 10:3235–3253, Nov 1974.

[66] Franz J. Wegner. Duality in generalized ising models and phase transitions without local order parameters. *Journal of Mathematical Physics*, 12(10):2259–2272, 1971.

[67] X. G. Wen. Topological orders in rigid states. *International Journal of Modern Physics B*, 04(02):239–271, 1990.

[68] John B. Kogut. An introduction to lattice gauge theory and spin systems. *Rev. Mod. Phys.*, 51:659–713, Oct 1979.

[69] Michael A. Levin and Xiao-Gang Wen. String-net condensation: A physical mechanism for topological phases. *Phys. Rev. B*, 71:045110, Jan 2005.

[70] A.M. Polyakov. Quark confinement and topology of gauge theories. *Nuclear Physics B*, 120(3):429 – 458, 1977.

[71] Igor F. Herbut, Babak H. Seradjeh, Subir Sachdev, and Ganpathy Murthy. Absence of $U(1)$ spin liquids in two dimensions. *Phys. Rev. B*, 68:195110, Nov 2003.

[72] Igor F. Herbut and Babak H. Seradjeh. Permanent confinement in the compact QED_3 with fermionic matter. *Phys. Rev. Lett.*, 91:171601, Oct 2003.

[73] Michael Hermele, T. Senthil, Matthew P. A. Fisher, Patrick A. Lee, Naoto Nagaosa, and Xiao-Gang Wen. Stability of $U(1)$ spin liquids in two dimensions. *Phys. Rev. B*, 70:214437, Dec 2004.

[74] Flavio S. Nogueira and Hagen Kleinert. Quantum electrodynamics in $2 + 1$ dimensions, confinement, and the stability of $u(1)$ spin liquids. *Phys. Rev. Lett.*, 95:176406, Oct 2005.

[75] Ciarán Hickey and Simon Trebst. Emergence of a field-driven $U(1)$ spin liquid in the kitaev honeycomb model. *Nature Communications*, 10(1):530, 2019.

[76] Eugene Paul Wigner. *Gruppentheorie und ihre Anwendung auf die Quantenmechanik der Atomspektren*. Springer Fachmedien Wiesbaden GmbH, 1931.

[77] Anthony Zee. *Group Theory in a Nutshell for Physicists*. Princeton University Press, 2016.

[78] J. J. Sakurai and Jim Napolitano. *Modern Quantum Mechanics*. Cambridge University Press, 2 edition, 2017.

[79] Henrik Bruus and Karsten Flensberg. *Many-Body Quantum Theory in Condensed Matter Physics: An Introduction*. Oxford Graduate Texts, 1 edition, 2004.

[80] K. v. Klitzing, G. Dorda, and M. Pepper. New method for high-accuracy determination of the fine-structure constant based on quantized hall resistance. *Phys. Rev. Lett.*, 45:494–497, Aug 1980.

[81] R. B. Laughlin. Quantized hall conductivity in two dimensions. *Phys. Rev. B*, 23:5632–5633, May 1981.

[82] F. D. M. Haldane. Model for a quantum hall effect without landau levels: Condensed-matter realization of the "parity anomaly". *Phys. Rev. Lett.*, 61:2015–2018, Oct 1988.

[83] C. L. Kane and E. J. Mele. Z_2 topological order and the quantum spin hall effect. *Phys. Rev. Lett.*, 95:146802, Sep 2005.

[84] Markus König, Steffen Wiedmann, Christoph Brüne, Andreas Roth, Hartmut Buhmann, Laurens W. Molenkamp, Xiao-Liang Qi, and Shou-Cheng Zhang. Quantum spin hall insulator state in HgTe quantum wells. *Science*, 318(5851):766–770, 2007.

[85] Alexander Altland and Martin R. Zirnbauer. Nonstandard symmetry classes in mesoscopic normal-superconducting hybrid structures. *Phys. Rev. B*, 55:1142–1161, Jan 1997.

[86] Ching-Kai Chiu, Jeffrey C. Y. Teo, Andreas P. Schnyder, and Shinsei Ryu. Classification of topological quantum matter with symmetries. *Rev. Mod. Phys.*, 88:035005, Aug 2016.

[87] N. Read and Subir Sachdev. Large-n expansion for frustrated quantum antiferromagnets. *Phys. Rev. Lett.*, 66:1773–1776, Apr 1991.

[88] Dmytro Pesin and Leon Balents. Mott physics and band topology in materials with strong spin-orbit interaction. *Nat. Phys.*, 6(5):376–381, 05 2010.

[89] Stephan Rachel and Karyn Le Hur. Topological insulators and mott physics from the hubbard interaction. *Phys. Rev. B*, 82:075106, Aug 2010.

[90] Gil Young Cho, Yuan-Ming Lu, and Joel E. Moore. Gapless edge states of background field theory and translation-symmetric Z_2 spin liquids. *Phys. Rev. B*, 86:125101, Sep 2012.

[91] Andreas Rüegg and Gregory A. Fiete. Topological order and semions in a strongly correlated quantum spin hall insulator. *Phys. Rev. Lett.*, 108:046401, Jan 2012.

[92] Matthias Punk, Debanjan Chowdhury, and Subir Sachdev. Topological excitations and the dynamic structure factor of spin liquids on the kagome lattice. *Nat. Phys.*, 10(4):289–293, 04 2014.

[93] Robert Schaffer, Subhro Bhattacharjee, and Yong Baek Kim. Spin-orbital liquids in non-kramers magnets on the kagome lattice. *Phys. Rev. B*, 88:174405, Nov 2013.

[94] Tyler Dodds, Subhro Bhattacharjee, and Yong Baek Kim. Quantum spin liquids in the absence of spin-rotation symmetry: Application to herbertsmithite. *Phys. Rev. B*, 88:224413, Dec 2013.

[95] Biao Huang, Yong Baek Kim, and Yuan-Ming Lu. Interplay of nonsymmorphic symmetry and spin-orbit coupling in hyperkagome spin liquids: Applications to $Na_4Ir_3O_8$. *Phys. Rev. B*, 95:054404, Feb 2017.

[96] Jason Alicea. New directions in the pursuit of majorana fermions in solid state systems. *Reports on Progress in Physics*, 75(7):076501, 2012.

[97] M. Z. Hasan and C. L. Kane. Colloquium: Topological insulators. *Rev. Mod. Phys.*, 82:3045–3067, Nov 2010.

[98] Xiao-Liang Qi, Taylor L. Hughes, S. Raghu, and Shou-Cheng Zhang. Time-reversal-invariant topological superconductors and superfluids in two and three dimensions. *Phys. Rev. Lett.*, 102:187001, May 2009.

[99] Xiao-Liang Qi, Taylor L. Hughes, and Shou-Cheng Zhang. Topological invariants for the fermi surface of a time-reversal-invariant superconductor. *Phys. Rev. B*, 81:134508, Apr 2010.

[100] Xiao-Liang Qi and Shou-Cheng Zhang. Topological insulators and superconductors. *Rev. Mod. Phys.*, 83:1057–1110, Oct 2011.

[101] Rahul Roy. Z_2 classification of quantum spin hall systems: An approach using time-reversal invariance. *Phys. Rev. B*, 79:195321, May 2009.

[102] Liang Fu. Topological crystalline insulators. *Phys. Rev. Lett.*, 106:106802, Mar 2011.

[103] Robert-Jan Slager, Andrej Mesaros, Vladimir Juricic, and Jan Zaanen. The space group classification of topological band-insulators. *Nat. Phys.*, 9(2):98–102, 02 2013.

[104] R. Moessner, S. L. Sondhi, and Eduardo Fradkin. Short-ranged resonating valence bond physics, quantum dimer models, and ising gauge theories. *Phys. Rev. B*, 65:024504, Dec 2001.

[105] Ville Lahtinen, Andreas W. W. Ludwig, Jiannis K. Pachos, and Simon Trebst. Topological liquid nucleation induced by vortex-vortex interactions in kitaev's honeycomb model. *Phys. Rev. B*, 86:075115, Aug 2012.

[106] Ville Lahtinen, Andreas W. W. Ludwig, and Simon Trebst. Perturbed vortex lattices and the stability of nucleated topological phases. *Phys. Rev. B*, 89:085121, Feb 2014.

[107] J. Knolle, D. L. Kovrizhin, J. T. Chalker, and R. Moessner. Dynamics of fractionalization in quantum spin liquids. *Phys. Rev. B*, 92:115127, Sep 2015.

[108] Stephan Rachel, Lars Fritz, and Matthias Vojta. Landau levels of majorana fermions in a spin liquid. *Phys. Rev. Lett.*, 116:167201, Apr 2016.

[109] Meng Cheng, Roman M. Lutchyn, Victor Galitski, and S. Das Sarma. Splitting of majorana-fermion modes due to intervortex tunneling in a $p_x + ip_y$ superconductor. *Phys. Rev. Lett.*, 103:107001, Aug 2009.

[110] Satoshi Yamashita, Yasuhiro Nakazawa, Masaharu Oguni, Yugo Oshima, Hiroyuki Nojiri, Yasuhiro Shimizu, Kazuya Miyagawa, and Kazushi Kanoda. Thermodynamic properties of a spin-1/2 spin-liquid state in a κ-type organic salt. *Nature Physics*, 4:459 EP –, 04 2008.

[111] Neil W. Ashcroft and N. David Mermin. *Solid State Physics*. Holt, Rinehart and Winston, 6 edition, 1976.

[112] Zhihao Hao and Oleg Tchernyshyov. Fermionic spin excitations in two- and three-dimensional antiferromagnets. *Phys. Rev. Lett.*, 103:187203, Oct 2009.

[113] B. Normand and Z. Nussinov. Fermionic spinon and holon statistics in the pyrochlore quantum spin liquid. *Phys. Rev. B*, 93:115122, Mar 2016.

[114] Tian-Heng Han, M. R. Norman, J.-J. Wen, Jose A. Rodriguez-Rivera, Joel S. Helton, Collin Broholm, and Young S. Lee. Correlated impurities and intrinsic spin-liquid physics in the kagome material herbertsmithite. *Phys. Rev. B*, 94:060409(R), Aug 2016.

[115] Yao Shen, Yao-Dong Li, Hongliang Wo, Yuesheng Li, Shoudong Shen, Bingying Pan, Qisi Wang, H. C. Walker, P. Steffens, M. Boehm, Yiqing Hao, D. L. Quintero-Castro, L. W. Harriger, M. D. Frontzek, Lijie Hao, Siqin Meng, Qingming Zhang, Gang Chen, and Jun Zhao. Evidence for a spinon fermi surface in a triangular-lattice quantum-spin-liquid candidate. *Nature*, 540:559 EP –, 12 2016.

[116] Joseph A. M. Paddison, Marcus Daum, Zhiling Dun, Georg Ehlers, Yaohua Liu, Matthew B. Stone, Haidong Zhou, and Martin Mourigal. Continuous excitations of the triangular-lattice quantum spin liquid $YbMgGaO_4$. *Nature Physics*, 13:117 EP –, 12 2016.

[117] Yao Shen, Yao-Dong Li, H. C. Walker, P. Steffens, M. Boehm, Xiaowen Zhang, Shoudong Shen, Hongliang Wo, Gang Chen, and Jun Zhao. Fractionalized excitations in the partially magnetized spin liquid candidate $YbMgGaO_4$. *Nature Communications*, 9(1):4138, 2018.

[118] Arnab Banerjee, Paula Lampen-Kelley, Johannes Knolle, Christian Balz, Adam Anthony Aczel, Barry Winn, Yaohua Liu, Daniel Pajerowski, Jiaqiang Yan, Craig A. Bridges, Andrei T. Savici, Bryan C. Chakoumakos, Mark D. Lumsden, David Alan Tennant, Roderich Moessner, David G. Mandrus, and Stephen E. Nagler. Excitations in the field-induced quantum spin liquid state of α-$RuCl_3$. *npj Quantum Materials*, 3(1):8, 2018.

[119] Zhenyue Zhu, P. A. Maksimov, Steven R. White, and A. L. Chernyshev. Disorder-induced mimicry of a spin liquid in $YbMgGaO_4$. *Phys. Rev. Lett.*, 119:157201, Oct 2017.

[120] R Pohle, H. Yan, and N. Shannon. How many spin liquids are there in $Ca_{10}Cr_8O_{28}$? *arXiv:1711.03778*, 2017.

[121] Sounak Biswas and Kedar Damle. Semiclassical theory for liquidlike behavior of the frustrated magnet $Ca_{10}Cr_8O_{28}$. *Phys. Rev. B*, 97:115102, Mar 2018.

[122] A. Kshetrimayum, C. Balz, B. Lake, and J. Eisert. Tensor network investigation of the double layer kagome compound $Ca_{10}Cr_7O_{28}$. *arXiv:1904.00028*, 2019.

[123] Jad C. Halimeh and Matthias Punk. Spin structure factors of chiral quantum spin liquids on the kagome lattice. *Phys. Rev. B*, 94:104413, Sep 2016.

[124] Laura Messio, Samuel Bieri, Claire Lhuillier, and Bernard Bernu. Chiral spin liquid on a kagome antiferromagnet induced by the dzyaloshinskii-moriya interaction. *Phys. Rev. Lett.*, 118:267201, Jun 2017.

[125] B. Fåk, S. Bieri, E. Canévet, L. Messio, C. Payen, M. Viaud, C. Guillot-Deudon, C. Darie, J. Ollivier, and P. Mendels. Evidence for a spinon fermi surface in the triangular $s = 1$ quantum spin liquid $Ba_3NiSb_2O_9$. *Phys. Rev. B*, 95:060402(R), Feb 2017.

[126] Walter Rantner and Xiao-Gang Wen. Spin correlations in the algebraic spin liquid: Implications for high-T_c superconductors. *Phys. Rev. B*, 66:144501, Oct 2002.

[127] Olexei I. Motrunich. Variational study of triangular lattice spin-1/2 model with ring exchanges and spin liquid state in κ-$(ET)_2Cu_2(CN)_3$. *Phys. Rev. B*, 72:045105, Jul 2005.

[128] M. Tinkham. *Introduction to superconductivity.* McGraw Hill, 2 edition, 1996.

[129] Ting-Pong Choy and Yong Baek Kim. Classification of quantum phases for the star-lattice antiferromagnet via a projective symmetry group analysis. *Phys. Rev. B*, 80:064404, Aug 2009.

[130] Yuan-Ming Lu, Ying Ran, and Patrick A. Lee. Z_2 spin liquids in the $s = \frac{1}{2}$ heisenberg model on the kagome lattice: A projective symmetry-group study of schwinger fermion mean-field states. *Phys. Rev. B*, 83:224413, Jun 2011.

[131] Yuan-Ming Lu and Ying Ran. z_2 spin liquid and chiral antiferromagnetic phase in the hubbard model on a honeycomb lattice. *Phys. Rev. B*, 84:024420, Jul 2011.

[132] Kevin O'Brien, Maria Hermanns, and Simon Trebst. Classification of gapless Z_2 spin liquids in three-dimensional kitaev models. *Phys. Rev. B*, 93:085101, Feb 2016.

[133] Biao Huang, Wonjune Choi, Yong Baek Kim, and Yuan-Ming Lu. Classification and properties of quantum spin liquids on the hyperhoneycomb lattice. *Phys. Rev. B*, 97:195141, May 2018.

[134] Chunxiao Liu, Gábor B. Halász, and Leon Balents. Competing orders in pyrochlore magnets from a Z_2 spin liquid perspective. *Phys. Rev. B*, 100:075125, Aug 2019.

[135] Hui-Ke Jin and Yi Zhou. Classical and quantum order in hyperkagome antiferromagnets. *Phys. Rev. B*, 101:054408, Feb 2020.

[136] D. Ter Haar, M. E. Lines, and Brebis Bleaney. A molecular-field theory of anisotropic ferromagnetica. *Philosophical Transactions of the Royal Society of London. Series A, Mathematical and Physical Sciences*, 254(1046):521–555, 1962.

[137] Manuel Laubach, Darshan G. Joshi, Johannes Reuther, Ronny Thomale, Matthias Vojta, and Stephan Rachel. Quantum disordered insulating phase in the frustrated cubic-lattice hubbard model. *Phys. Rev. B*, 93:041106, Jan 2016.

[138] Yasir Iqbal, Ronny Thomale, Francesco Parisen Toldin, Stephan Rachel, and Johannes Reuther. Functional renormalization group for three-dimensional quantum magnetism. *Phys. Rev. B*, 94:140408, Oct 2016.

[139] Yasir Iqbal, Tobias Müller, Kira Riedl, Johannes Reuther, Stephan Rachel, Roser Valentí, Michel J. P. Gingras, Ronny Thomale, and Harald O. Jeschke. Signatures of a gearwheel quantum spin liquid in a spin-$\frac{1}{2}$ pyrochlore molybdate heisenberg antiferromagnet. *Phys. Rev. Materials*, 1:071201, Dec 2017.

[140] Yasir Iqbal, Tobias Müller, Pratyay Ghosh, Michel J. P. Gingras, Harald O. Jeschke, Stephan Rachel, Johannes Reuther, and Ronny Thomale. Quantum and classical phases of the pyrochlore heisenberg model with competing interactions. *Phys. Rev. X*, 9:011005, Jan 2019.

[141] T. Müller et al. P. Ghosh, Y. Iqbal. Breathing chromium spinels: a showcase for a variety of pyrochlore heisenberg hamiltonians. *npj Quantum Mater*, 4:63, Dec 2019.

[142] Péter Balla, Yasir Iqbal, and Karlo Penc. Affine lattice construction of spiral surfaces in frustrated heisenberg models. *Phys. Rev. B*, 100:140402, Oct 2019.

[143] H.O. Jeschke et al. S. Chillal, Y. Iqbal. Evidence for a three-dimensional quantum spin liquid in $PbCuTe_2O_6$. *Nature Communications*, 11:2348, May 2020.

[144] Max Hering, Jonas Sonnenschein, Yasir Iqbal, and Johannes Reuther. Characterization of quantum spin liquids and their spinon band structures via functional renormalization. *Phys. Rev. B*, 99:100405, Mar 2019.

[145] Joey A Lussier, Brooke N Richtik, Cole Mauws, Jeffrey W Lynn, and Chris R Wiebe. Absence of magnetic ordering in the spin liquid candidate $Ca_3Cu_2GeV_2O_{12}$. *Journal of Physics: Condensed Matter*, 32(13):134001, dec 2019.

[146] J. Oitmaa and Weihong Zheng. Phase diagram of the bcc $s = \frac{1}{2}$ heisenberg antiferromagnet with first and second neighbor exchange. *Phys. Rev. B*, 69:064416, Feb 2004.

[147] Pratyay Ghosh, Tobias Müller, Francesco Parisen Toldin, Johannes Richter, Rajesh Narayanan, Ronny Thomale, Johannes Reuther, and Yasir Iqbal. Quantum paramagnetism and helimagnetic orders in the heisenberg model on the body centered cubic lattice. *Phys. Rev. B*, 100:014420, Jul 2019.

[148] A. Revelli, C. C. Loo, D. Kiese, P. Becker, T. Fröhlich, T. Lorenz, M. Moretti Sala, G. Monaco, F. L. Buessen, J. Attig, M. Hermanns, S. V. Streltsov, D. I. Khomskii, J. van den Brink, M. Braden, P. H. M. van Loosdrecht, S. Trebst, A. Paramekanti, and M. Grüninger. Spin-orbit entangled $j = \frac{1}{2}$ moments in Ba_2CeIrO_6: A frustrated fcc quantum magnet. *Phys. Rev. B*, 100:085139, Aug 2019.

[149] Y. Kasahara, Y. Takeuchi, T. Itou, R. H. Zadik, Y. Takabayashi, A. Y. Ganin, D. Arčon, M. J. Rosseinsky, K. Prassides, and Y. Iwasa. Spin frustration and magnetic ordering in the $s = \frac{1}{2}$ molecular antiferromagnet $\mathrm{fcc} - \mathrm{cs_3c_{60}}$. *Phys. Rev. B*, 90:014413, Jul 2014.

[150] Ken-ichi Utsumi and Takeo Izuyama. Possible Spin Ordering in BCC Solid 3He: Role of Four Particle Exchanges in Heisenberg Antiferromagnet. *Progress of Theoretical Physics*, 58(1):44–58, 07 1977.

[151] R. Schmidt, J. Schulenburg, J. Richter, and D. D. Betts. Spin-$\frac{1}{2}J_1-J_2$ model on the body-centered cubic lattice. *Phys. Rev. B*, 66:224406, Dec 2002.

[152] D. J. J. Farnell, O. Götze, and J. Richter. Ground-state ordering of the J_1-J_2 model on the simple cubic and body-centered cubic lattices. *Phys. Rev. B*, 93:235123, Jun 2016.

[153] E. V. Kuz'min. Quantum spin liquid in the fcc lattice. *Journal of Experimental and Theoretical Physics*, 96:129, Jan 2003.

[154] Péter Balla, Yasir Iqbal, and Karlo Penc. manuscript in preparation.

Acknowledgments

First of all, I would like to thank Johannes Reuther, who gave me the opportunity to perform my doctoral studies. It was he who offered me a position in his group and who guided me towards interesting research topics. He was a great supervisor, and I'm happy to have worked with him during the last years. I would also like to thank my collaborators for the fantastic teamwork. Among them a special thanks goes to Yasir Iqbal, who invited me to his institution in India, which was definitely a lifetime experience. I further acknowledge the CRC 183, which provided the financial support and through which we, as doctoral students, were able to participate and organize annual and magnificent summer schools. I'm grateful for the bureaucratic support from our group secretaries Gabriele Hermann and especially Marietta Wissmann. With finishing this Ph.D., I pursued, so far, my entire academical career at the Freie University of Berlin. During these years, I found many good colleagues and some close friends. As with the time many gorgeous people came and went, I will not try to name them all. In this regard, I would like to thank the entire *Fachbereich Physik* and, most of all, the present and former members of the Dahlem Center for Complex Quantum Systems.

I'm very thankful to my family, who supported me throughout the entire time. Last but not least, thank you Céline for your patience and your perpetual moral support!